University of Crete

Nitride Polariton Lasers

by

Emmanouil A. Amargianitakis

submitted to

Department of Materials Science and Technology

in fulfillment of the requirements
for the degree of Doctor of Philosophy

Supervisor

Prof. Nikolaos T. Pelekanos

December, 2020

Heraklion, Greece

University of Crete

Nitride Polariton Lasers

by

Emmanouil A. Amargianitakis

submitted to

Department of Materials Science and Technology

in fulfillment of the requirements
for the degree of Doctor of Philosophy

Supervisor

Prof. Nikolaos T. Pelekanos

December, 2020

Heraklion, Greece

Nitride Polariton Lasers

Thesis author : Emmanouil A. Amargianitakis

Principal advisor : Prof. Nikolaos T. Pelekanos

Examination committee : Prof. George Kioseoglou
: Dr. Eva Monroy
: Prof. Alexandros Georgakilas
: Prof. George Kopidakis
: Dr. George Konstantinidis
: Dr. George Deligeorgis

Department of Materials Science and Technology

University of Crete

December, 2020

Heraklion, Greece

Funded by H.F.R.I. Hellenic Foundation for Research & Innovation

ΙΣΝ/SNF ΙΔΡΥΜΑ ΣΤΑΥΡΟΣ ΝΙΑΡΧΟΣ STAVROS NIARCHOS FOUNDATION

Επιχειρησιακό Πρόγραμμα Ανάπτυξη Ανθρώπινου Δυναμικού, Εκπαίδευση και Διά Βίου Μάθηση

Ειδική Υπηρεσία Διαχείρισης Με τη συγχρηματοδότηση της Ελλάδας και της Ευρωπαϊκής Ένωσης

ΕΣΠΑ 2014-2020

Towards a brighter
UV future...

Περίληψη

Ο κύριος σκοπός της διδακτορικής διατριβής πραγματεύεται την καινοτόμα ανάπτυξη μικροκοιλοτήτων βασισμένες σε Νιτρίδια του Γαλλίου ως ενεργό υλικό καθώς και τη χρήση διηλεκτρικών καθρεφτών εκατέρωθεν των δυο πλευρών τους για τη μείωση της πυκνότητας ενέργειας κατωφλίου σε λειτουργία σύμφωνης και μονοχρωματικής εκπομπής φωτός υπό οπτική άντληση σε θερμοκρασία δωματίου για τη θέσπιση τεχνολογικών θεμελίων και τη μεταγενέστερη κατασκευή ηλεκτρικά αντλούμενων δομών. Η διάταξη μιας μικροκοιλότητας μας προσφέρει τη δυνατότητα να γίνει μελέτη της ισχυρής αλλελεπίδρασης μεταξύ του φωτός και της ύλης με την ίδια ενέργεια και ορμή, και έτσι, μας επιτρέπει να εξερευνήσουμε τις δυνατότητες ενός μη τετριμένου φυσικού συστήματος καθώς και την αξιοποίηση του σε μελοντικές οπτοηλεκτρονικές συσκευές και εφαρμογές. Στην παρούσα εργασία, ως δομικά συστατικά της ύλης χρησιμοποιούνται τα ζεύγοι ηλεκτρονίου-οπής, γνωστά στη βιβλιογραφία ως εξιτόνια, όπου παρατηρούνται σε μη-οργανικά (όπως η παρούσα μελέτη) καθώς και σε οργανικά ημιαγωγικά υλικά. Εαν η αλληλεπίδραση φωτός-ύλης είναι αρκετά ισχυρή, όπου είναι εφικτό όταν οι συνολικές απώλειες του συστήματος είναι μειωμένες, η διάκριση των αρχικών καταστάσεων χάνεται και δημιουργούνται νέες οιονεί-καταστάσεις με τις ιδιότητες των εξιτονίων και των φωτονίων. Σε αυτή τη περίπτωση, το σύστημα λειτουργεί υπό το λεγόμενο "καθεστώς ισχυρής σύζευξης" και τα παραγόμενα σωματίδια ονομάζονται "πολαριτόνια". Η αυθόρμητη συλλογική συμφωνία αυτών των σωματιδίων επιτρέπει τη συμπύκνωση τους στην θεμελιώδη κατάσταση, όπου αναφέρεται στη βιβλιογραφία ως πολαριτονικό λέϊζερ χωρίς να γίνεται αναστροφή των πληθυσμών, ενώ επιτρέπει τη παρατήρηση και άλλων φυσικών φαινομένων όπως η παραμετρική σκέδαση, η υπερρευστότητα κτλ. εξαιτίας των μη συνηθισμένων χαρακτηριστικών τους να είναι μισό-φως/μισό-εξιτόνιο σε συσχέτιση με την οιονεί-μποσονική τους φύση. Παρόλα αυτά, η παρατήρηση των φαινομένων αυτών παραμένει ένα απαιτητικό έργο όταν ανεβαίνει η θερμοκρασία, ενώ ο τελικός στόχος να είναι εφικτή η λειτουργία τους σε συνθήκες περιβάλλοντος έχει δυσκολέψει πολλά ερευνητικά εργαστήρια για πολλά χρόνια. Προοφανώς, ο κύριος λόγος είναι η

γρήγορη αποδιέγερση των εξιτονικών οντοτήτων εξαιτίας της πεπερασμένης δεσμικής ενέργειας τους σε ανόργανους ημιαγωγούς, η οποία δεν τους επιτρέπει να "ζήσουν" παρά μόνο σε κρυογενικές συνθήκες. Η κβαντική μηχανική έχει δείξει ότι ο περιορισμός των φορέων μέσα σε κβαντικά πηγάδια ενισχύει τη δεσμική ενέργεια ενός ζεύγους ηλεκτρονίου-οπής, όπως και τη δύναμη ταλάντωσης της οπτικής μετάβασης. Προηγούμενες εργασίες σε υλικά μεγάλου ενεργειακού χάσματος, όπως το Νιτρίδιο Γαλλίου, έχουν δείξει την ικανότητα να υπερνικήσουν, το λιγότερο εν μέρη, τους προηγούμενους περιορισμούς, εφόσον οι εξιτονικές καταστάσεις κατέχουν δεσμικές ενέργειες οι οποίες είναι συγκρίσιμες του k_BT σε θερμοκρασία δωματίου, ενώ μπορεί να είναι πολύ μεγαλύτερες όταν το υλικό χρησιμοποιείται σε λεπτά κβαντικά πηγάδια. 'Οσον αφορά το φωτονικό περιορισμό, η κατασκευή περιλαμβάνει υψηλής ποιότητας ανακλαστικούς καθρέπτες οι οποίοι τις περισσότερες φορές είναι κατασκευασμένοι από κατανεμημένους ανακλαστήρες Μπραγκ σε επίπεδη διάταξη. Αυτοί οι καθρέπτες είναι βασικά μια στοίβα από εναλλασόμενα υλικά με μεγάλο και μικρό δείκτη διάθλασης που τοποθετούνται και από τις δύο μεριές του ενεργού υλικού.

Μια σημαντική περίπτωση, ενδιαφέροντος στην επικείμενη εργασία, είναι όταν διηλεκτρικοί καθρέπτες χρησιμοποιηθούν σαν πάνω και κάτω κάτοπτρα, εξαιτίας του αυξημένου φωτονικού περιορισμού που προσφέρουν με με πολύ μικρότερο αριθμό εναλλασόμενων ζευγών. Οπότε ο κύριος στόχος είναι να βελτιωθούν προηγούμενες επίπεδες συσκευές μικροκοιλοτήτων, με το να κατασκευαστούν υπέρλεπτα φιλμ Νιτριδίου του Γαλλίου με μικρή επιφανειακή τραχύτητα, χρησιμοποιώντας την τεχνική της φωτο-ηλεκτροχημικής εγχάραξης όπου γίνεται επιλεκτική αφαίρεση ενός στρώματος Νιτριδίου Ινδίου Γαλλίου. Ο οπτικός σχεδιασμός και η προσομοίωση των διηλεκτρικών μικροκοιλοτήτων έγινε με τη χρήση λογισμικού σε υπολογιστή ώστε να επιτευχθεί ο επιθυμητός συντονισμός ανάμεσα στο οπτικό τρόπο ταλάντωσης και στην εξιτονική κατάσταση μέσα στην ενεργό περιοχή. Η ανάπτυξη έγινε με τη τεχνική μοριακής επίταξης υποβοηθούμενη με πλάσμα σε πολικά υποστρώματα Νιτριδίου Γαλλίου πάνω σε Σάπφειρο για τις πολικές δομές και πάνω σε μη-πολικά υποστρώματα Νιτριδίου Γαλλίου για τις μη-πολικές δομές από συνεργαζόμενο φορέα στη Γαλλία. 'Ολα τα δείγματα μελετήθηκαν από ένα εύρος τεχνικών για να εκτιμηθεί η ποιότητα και τα

χαρακτηριστικά τους. Συγκεκριμένα, στο κεφάλαιο 1, δίνεται το θεωρητικό υπόβαθρο των III-νιτριδίων υλικών και της πολαριτονικής φυσικής. Στο κεφάλαιο 2, η μελέτη εστιάζεται στο να κατασκευαστούν υπερ-λείες υπό του μήκους κύματος μεμβράνες Νιτριδίου του Γαλλίου με το να γίνει φωτο-ηλεκτροχημική εγχάραξη ενός στώματος Νιτριδίου Ινδίου Γαλλίου, διευκολύνοντας τη μελέτη του συντελεστής απορρόφησης των μεμβρανών με βάση μετρήσεων μικρο-διαπερατότητας και λαμβάνοντας υπ'όψη τα φαινόμενα στάσιμου κύματος. Το κεφάλιο 3 περιγράφει τη χρησιμοποιηθήσα μεθοδολογία για να κατασκευαστούν εξ-ολοκλήρου διηλεκτρικές μικροκοιλότητες κατασκευασμένες από τα οξείδια Πυριτίου και Ταντάλου, όπου παρουσιάζουν μια μεγάλη αντίθεση στο δείκτη διάθλασης, και πολικές μεμβράνες αποτελούμενες από νιτρίδια Γαλλίου και Αλουμινίου Γαλλίου, όπου επιτρέπουν την παρατήρηση καλά καθορισμένων πολαριτονικών καταστάσεων στον ανάστροφο χώρο με τη χαρακτηριστική αντι-τεμνόμενη συμπεριφορά, καθώς και,την αξιοσημείωτη σύμφωνη εκμπομπή φωτονίων από πολαριτόνια (πολαριτονικό λέϊζερ) σε θερμοκρασία δωματίου με τη χρήση μόνο τεσσάρων εναλλασσόμενων ζευγών στον πάνω καθρέπτη. Στο κεφάλαιο 4, η ίδια προσέγγιση εφαρμόστηκε και στην μη-πολική διεύθυνση για τη κατασκευή διηλεκτρικών μικροκοιλοτήτων από υψηλής ποιότητας μη-πολικές μεμβράνες νιτριδίων Γαλλίου και Αλουμινίου Γαλλίου για πρώτη φορά. Ο υπό διερεύνηση τελευταίας τεχνολογίας σχηματισμός μικροκοιλότητας επέδειξε ενδιαφέροντα πολαριτονικά χαρακτηριστικά εξαιτίας της επίπεδης ανισοτροπίας του υλικού, ενώ θέτει νέο ρεκόρ κατωφλίου ενός πολαριτονικού λέϊζερ εξαιτίας της εξάλειψης των εσωτερικών πεδίων. Τελικά, για να ξεπεραστούν περιορισμοί στην εναπόθεση των διηλεκτρικών καθρεφτών εξαιτίας της μεγάλης θερμικής τάσης που δρα σε λεπτά φίλμ όταν αυτά κρυώσουν από τη θερμοκρασία της εναπόθεσης, το κεφάλαιο 5 εισάγει μια νέα κατασκευή μικροκοιλοτήτων με τη χρήση μεταφερόμενων καθρεφτο-μεμβρανών από οξείδια για τη χρήση τους σαν πάνω καθρέπτες, των οποίων η λειτουργία επιτεύχθηκε σε $\lambda/2$ (μόνο οξείδια) και $3\lambda/2$ (πολαριτονικές) κοιλότητες.

Abstract

The major aim of this doctoral thesis involved the novel development of all-dielectric GaN-based planar microcavity structures for the reduction of polariton lasing threshold at room temperature operation when the device is optically excited, while setting also the fundamentals of subsequent electrically injected polariton lasing structures. The microcavity configuration offers the potential to study the strong interaction of confined light and matter with the same energy and momentum, and hence, allows us to explore the capabilities of a non-trivial physical system and utilize it in future optoelectronic devices and applications. Here, the matter component of polaritons regards electron-hole pairs, known in literature as excitons, which are observed in either inorganic (as in this work) or organic semiconducting materials. If the light-matter interaction is strong enough, which is usually possible when suppressing the overall losses in the system, the distinction of the original states is lost and new quasi-states are formed, thus, sharing properties of both the excitons and the photons. In such case, the system is operating in the so-called "strong coupling regime" and the produced particles are called "polaritons". The spontaneous collective coherence of those particles allows for their condensation at the ground state, referred to as inversionless polariton lasing, while enable other intriguing physical phenomena such as parametric scattering, superfluidity etc. due to their extraordinary composite characteristics of being half-photons/half-excitons along with their quasi-bosonic nature. Nevertheless, the observation of these phenomena remains a challenging task when going to elevated temperatures, while the final goal to reach ambient conditions has troubled many research groups for many years. Apparently, the main reason is the fast decay of the exciton entities due to the finite binding energy in most inorganic semiconductors, which restricts them to "live" only at cryogenic temperatures. Quantum mechanics has shown that confinement of carriers inside quantum wells can enhance the binding energy of an electron-hole pair, as well as the oscillator strength of the optical transition.

Previous works on wide bandgap materials, such as GaN, have demonstrated the ability to surpass, at least in part, the previous limitations, since the exciton states possess binding energies which are comparable to k_BT at room temperature in the bulk, while they can be much higher when the material is in the form of thin quantum wells. As concerns photon confinement, the necessary configuration involves highly reflective mirrors which in most of cases are made by distributed Bragg reflectors (DBRs) in a planar configuration. These mirrors are basically a stack of alternating high and low refractive index materials that are placed on both sides of the active material.

An important case, of interest in this work, is when dielectric mirrors are used as top and bottom DBRs, due to the increased photon confinement they offer with a reduced number of alternating pairs. Hence, a main goal of this work is to improve further the previous all-dielectric planar microcavity devices, by fabricating GaN-based sub-wavelength films with low roughness, using the photo-electrochemical etching (PEC) technique based on the selective removal of an InGaN layer. The optical design and simulation of the all-dielectric III/V microcavity structures was made with the use of a computer software, in order to achieve the desired resonance between the cavity mode and the exciton state within the active region. The epitaxial growth was made by plasma-assisted molecular beam epitaxy on c-GaN/Sapphire for the polar-oriented structures and on m-plane GaN substrates for the non-polar ones at INAC, CEA. All the samples were studied by a range of techniques to assess their quality and characteristics. Specifically, in Chapter 1 is given the theoretical background of III-nitride materials and principles of polariton physics. In Chapter 2, the study focuses on producing ultra-smooth subwavelength-thin GaN membranes by photo-electrochemically etching an InGaN sacrificial layer, enabling therefore to extract the absorption coefficient of bare membranes, based on μ-transmittance measurements and taking into account the standing wave effects. Chapter 3 describes the utilized methodology to fabricate all-dielectric DBR microcavities made by the oxides SiO_2 and Ta_2O_5, which illustrate a high refractive-index

contrast, and polar GaN/AlGaN membranes allowing for the observation of well-resolved polariton branches in the reciprocal lattice (k -space) with the characteristic anti-crossing behavior, as well as, remarkable polariton lasing at room temperature with the use of only 4 alternating pairs in the top DBR. In Chapter 4, the same approach was applied to the m-plane orientation in order to produce all-dielectric microcavities with high-quality non-polar GaN/AlGaN membranes for the first time. The investigated state-of-the-art microcavity structure exhibited intriguing polariton characteristics attributed to the in-plane anisotropy while set a new record for the ultra-low polariton lasing threshold due to the elimination of the internal build-in fields. Finally, to overcome limitations in the DBR evaporation based on the large thermal strain acting on thin films when cooled from deposition to room temperature, Chapter 5 introduces a new concept in the development of microcavities with the use of oxide-based "*transferrable*" DBR membranes (*t*-DBR) as top mirrors, whose successful operation was confirmed in $\lambda/2$ (only oxide) and $3\lambda/2$ (polariton) cavities.

Acknowledgments

First of all, I would like to express the deepest appreciation and gratitude to Prof. Nikolaos T. Pelekanos for giving me the opportunity to perform novel research in the field of III-V polariton structures, as well as, the support and constant supervision all the years of my PhD studies. In addition, I am highly indebted to Prof. George Kioseoglou and Dr. Eva Monroy for their continuous guidance and who accepted to be in my three-member committee. Furthermore, Dr. Eva Monroy provided the as-grown high-quality III-N structures utilized in this thesis, fabricated epitaxially by the Plasma-Assisted Molecular Beam Epitaxy in INAC, CEA in Grenoble. Sincere thanks also to the other members of my examination committee consisting of Prof. Alexandros Georgakilas, Prof. George Kopidakis, Dr. George Konstantinidis and Dr. George Deligeorgis and for their insightful comments during the correction of my manuscript. Dr. George Konstantinidis provided me also with valuable advices in the fabrication of the micro/nano structures and access in the processing facilities.

I am thankful to Dr. Rahul Jayaprakash and Dr. Fotis Kalaitzakis, former members of our group, for the theoretical and technical guidance in GaN-based polariton technology. Additional thanks to Rahul for providing me his Matlab code to design my samples. I would like to acknowledge the contribution of Mr. Eric Delamadeleine who fabricated with e-beam deposition the dielectric materials utilized in this work in INAC, CEA in Grenoble and Dr. Stelios Kazazis for performing Spectroscopic Ellipsometry in the micro-electronic facilities in Crete to deduce their refractive indices. Many thanks to Dr. George Doundoulakis and Dr. Fabrice Iacovella for their aid with the processing skills. Moreover, I thank a lot Ms. Foteini Miziou, a master student which I supervised during my studies, who helped me perform several photo-electrochemical etching experiments. I would like to extend my special thanks to Ms. Maria Androulidaki for her assistance with the optical setups - equipment and who allowed me to make a mess of the lab-space available to me until I managed to make the

optical setups operational. Moreover, the help of Ms. Katerina Tsagaraki in characterizing the nitride and dielectric samples with X-Ray Diffraction, Scanning Electron Microscopy and Atomic Force Microscopy has been a major part of this work which gave me precious feedback.

To continue, I would like to thank Mr. Athanasios Kostopoulos for the fabrication of mesas on the nitride samples and Mr. George Stavrinidis for his support in making the appropriate processing for the transferrable DBR membranes. I am thankful also to Dr. Maria Kaliva for providing me with the KOH solution utilized in the etching experiments. I thank Dr. Adam Adikimenakis and Dr. Ilias Aperathitis for providing me with liquid nitrogen in emergency cases where the CCD camera of the Photoluminescence setup had to stay cool. I appreciate also the aid of Mr. Nikos Papadakis and Mr. Michalis Sfendourakis for their technical support and advices in repairing the utilized instrumentation which sometimes was either not fully-operational or needed an upgrade. My gratitude to Prof. Eleftherios Iliopoulos and Dr. George Deligeorgis for allowing me to utilize their lab facilities and the rest of the colleagues of the Microelectronics Research Group lab for the beneficial and fun time we spent together during my doctoral studies. The minor or major contribution by all of you allowed me to finally achieve the state-of-the-art work presented in this thesis. It has been a great experience and pleasure working with each one of you all these years.

A special word of gratitude to Prof. Gregor Weihs who allowed me to spend three months in his lab facilities in Innsbruck, Austria, as well as his students and secretary who provided me with more help than I expected during my stay there. Also, I would like to express my deep gratitude to my dear family and close friends for the continuous encouragement and belief in me which gave me strength to finally complete my doctoral studies. Last but not least, the completion of this project would not have been possible without the financial support by ELIDEK - GSRT, Stavros Niarchos Foundation and EDVM, and therefore, is gratefully acknowledged.

Contents

List of Figures

Chapter 1

Microcavity engineering based on nitrides

In this chapter, it is introduced the family of III-nitride semiconductors which has played a significant role to today's opto-electronic technology due to their superior characteristics for a series of applications. Towards this end, the fundamental concepts and the unique properties are presented here for the design of novel polariton devices by utilizing them as active material in microcavities.

1.1 Introduction

After the pioneering realization of the first LASER (**L**ight **A**mplification by **S**timulated **E**mission of **R**adiation) in 1960 by T. H. Maiman [1, 2], which is practically a device emitting coherent monochromatic radiation, there was a tremendous boost of laser applications which are vital in today's life applications. Towards this route, seeking of lasing devices with reduced energy consumption has been the subject by a large number of research groups following the original demonstration. The progress in fabrication of novel or higher quality materials has enabled the production of superior lasing devices in comparison to the initial realizations in this field. The outcome of this investigation paved the production of ultra-compact lasing devices made by semiconducting materials [3, 4]. The principles of operation for all the conventional semiconductor lasing devices is based on the inversion of carrier populations. The latter simply means that a large amount of electrons must occupy the conduction band rather than the valence band of the semiconductor. Experimentally, this can be accomplished by optical or electrical excitation. Succeeding this inversion, it occurs stimulated emission of decayed photons which are identical in phase and wavelength and in

turn stimulate further the transition of the system in an cascade way, and above a critical limit, bring the system to a steady lasing state. When this happens, the stimulated decay of electron carriers, or in other words the stimulated electron-hole recombination, leads to light amplification and to lasing action. Under this operation, when the electron-hole pair (exciton) and cavity states remain unchanged, the system is said to operate in the "weak coupling" regime and the photons have a finite probability to escape outside the microcavity without getting re-absorbed by the valence band electrons.

In comparison to the weak interaction, subsequent observations have shown that it is possible to obtain lasing emission in semiconductor microcavity devices operating in the so-called "strong coupling" regime [5–7], where population inversion is no longer a prerequisite condition to fulfill [9]. In this case, the decayed photons from the active medium are trapped inside the cavity long enough due to the highly reflective cavity mirrors, increasing thus, the probability of the photons to be re-absorbed by the medium before escaping the cavity. This strong interaction of photons and excitons, creates two new quasi-states, named as lower and upper polariton branches [6,8] where the carriers have hybrid exciton-photon properties. The successful fabrication of polariton microcavities has been the key solution to observe lasing at much lower injection densities as opposed to the conventional lasing devices [10]. Under this regime, the polariton lasing action is triggered by certain relaxation mechanisms which are enhanced by the excitonic part of the polariton quasi-particle and basically rely on polariton-polariton and polariton-phonon interactions, leading above a critical polariton density (or below a critical value of temperature) to their condensation at the lowest energetically polariton state with zero wavevector [9, 11], similar to the Bose-Einstein condensation [12,13] of non-interacting particles with integer spin. As follows from this intriguing possibility, someone can state that the major goal is to produce polariton lasers operating successfully at ambient conditions with reduced energy consumption. Macroscopic polariton condensation at elevated temperatures is possible due to the considerably low

mass ($10^{-5}m_e$) of exciton-photon polaritons in comparison to eg. atoms ($10^4 m_e$), where the transition temperature is limited to μK [14, 15]. Another example of condensation that the research community is actively working on is the exciton condensation with $M_{exc} \approx m_e$. So far, there have been many difficulties in providing a clear demonstration of exciton condensation, mainly related to the strong Coulomb interaction between excitons which tends to ionize them to e-h plasma before reaching above unity occupation numbers [16, 17].

An advantageous system for polariton technology is the utilization of the direct bandgap Gallium Nitride (GaN) semiconductor, which has led up to now to attractive optical and electrical devices such as Light Emitting Diodes (LEDs) [18], Vertical Cavity Surface Emitting Lasers (VCSELs) [19], power electronic devices [20] etc., used in a variety of applications. Its relatively high bandgap (3.437 eV at room temperature and 3.510 eV at zero Kelvin [21]), along with the high exciton binding energy and oscillator strength, GaN excitons have the ability to sustain high temperatures, enabling thus the observation of strong light-matter interaction up to room temperature [22, 23] something that is not feasible to Gallium Arsenide (GaAs) or Cadmium Telluride (CdTe) where polaritons do not "survive" up to ambient conditions [24, 25]. Compared to other systems that are considered excitonic such as ZnO, where it is also possible to observe polaritons at RT [26, 27], GaN has a clear technological advantage in the sense that it can be electrically injected [28], unlike ZnO where p-type doping is not available. Furthermore, the increased efficiency of GaN to conduct electrons at a fast rate reduces in part the power loss that is transformed into heat. Moreover, even though there have been made a series of works regarding the general performance enhancement, it is believed that there is still enough space for improvements in the design and fabrication of new type of devices, which can benefit from the properties of nitrides, and lead to novel technological achievements. As can be seen from the engineer's scope, all these properties make GaN an ideal candidate for obtaining robust strong coupling at RT and be the holy grail of the future polariton technology breakthroughs.

1.2 Properties of GaN, AlN, InN and their alloys

In the thermodynamic equilibrium, III-nitride semiconductors crystallize in the hexagonal wurtzite (WZ) structure [29] while they can also crystallize in a zincblende (ZB) [30] or a rocksalt (RS) [31] phase. Notably, Gallium Nitride (GaN), which is the main material utilized in this work, consists of two inter-penetrating hexagonal close-packed (hcp) sublattices, each with one type of atom, with an offset along the c-axis of 5/8 of the cell height. The biatomic stacking sequence is AaBbAa... in the [0001] (polar) orientation with 6 atoms in the hexagonal unit cell contained in it and is described by two lattice constants α and c. The minimum of the conduction band lies at the Γ-point (k = 0), meaning the center of the brillouin zone, with a Γ_7 symmetry (C_{6v}) and a quantum number $J_7 = 1/2$, labeled as Γ_{7c}. Regarding the valence band, the maximum point is also at the Γ-point, thereby making these materials direct bandgap semiconductors. More specifically, the valence band splits in three sub-bands, Γ_{9v}, Γ_{7uv} and Γ_{7lv} due to crystal-field and spin-orbit coupling of C_{6v} states and creates three individual band-to-band transitions, known as A, B and C [32, 33] (Figure 1.1(a)), with emission of GaN in the ultra-violet (UV) wavelength range due to its large bandgap (Figure 1.1(b)).

Apart from the above, a significant property which characterizes these materials is the lack of an inversion plane perpendicular to the c-axis in WZ phase. Since the hexagonal lattice is non centrosymmetric, the [0001] and [000$\bar{1}$] directions are not equal. In the GaN bond perpendicular to the {0001} plane, the vector pointing from Ga to N is identified arbitrarily as the [0001] direction. If the material is grown along this direction then it is called "Ga-polar" while if is grown in the opposite direction it is called "N-polar". The product of $u \cdot c$, with u (= 3/8) being the internal parameter, corresponds to the length of the anion (N^{3-}) - cation (Ga^{3+}) bonds parallel to the growth direction. The electrostatic interactions, arising from the large ionicity, reduce the interlayer anion - cation distances A-b and B-a, and result in increased values of u, larger than the ideal

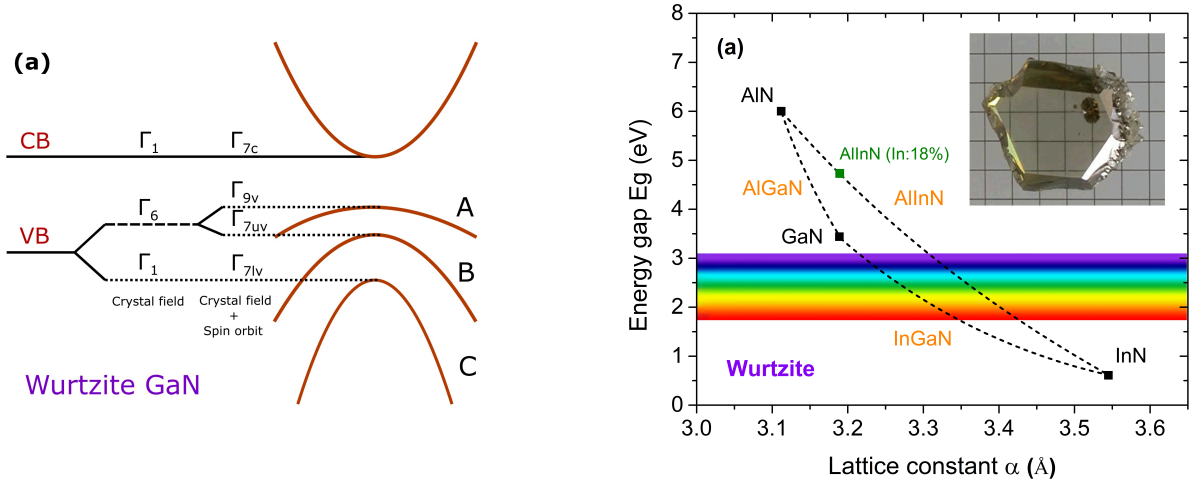

Figure 1.1: (a) Energy bandgap diagram of wurtzite GaN at zero k of the Γ-point due to valence band splitting [33]. (b) Energy bandgap of the III-V wurtzite binaries as a function of the lattice parameter α [21]. Inset depicts an optical image of a GaN crystal [34].

value of 3/8 (= 0.375). In addition, if the materials are strained, due to lattice mismatch and/or an applied external stress on the crystal, large polarization induced piezoelectric fields arise that should be also taken into consideration.

More analytically, the relative displacement of atoms induces permanent spontaneous polarization (P_{sp}) while the strain induces piezoelecric polarization (P_{piez}) vertically to the material layer, resulting to bound charge concentrations (σ_{polar}) at the interfaces of the materials [35–37].

$$\vec{P}_{polar}.\hat{n} = \underbrace{P_{piez,\perp}}_{lattice\ mismatch} + \underbrace{P_{spont,\perp}}_{crystal\ symmetry} = +\sigma_{polar} \tag{1.1}$$

Temperature contribution should also be taken into consideration in case of an accurate modeling. These effects result in large built-in electrostatic fields ($\sim$ MV/cm [38]) inside quantum wells and are responsible for the separation of the electron-hole wavefunctions and a redshift in the transitions due to band bending [39]. By adding strain effects, the conduction and the valence band edges for wurtzite GaN should be calculated based on the model of ref. [40]. In addition, it is important to point out that the nitride-based heterostructures

exhibit large exciton binding energies (E_B) [41, 42], which for the A_{GaN} bulk GaN exciton is around 25 - 27 meV [43] much larger in comparison to other III-V semiconductors (eg. 4 - 5 meV for GaAs [44]). This high value of E_B in nitrides is of major importance for obtaining strong light-matter coupling in microcavities at room temperature (RT) since it is comparable to the thermal energy at RT (k_BT = 26 meV). Therefore, the electron-hole pairs, named as excitons, are still attracted to each other without dissociating.

Similar to GaN, Aluminum Nitride (AlN) and Indium Nitride (InN) are also interesting materials due to the higher (E_g^{AlN}: 6.00 eV) and lower (E_g^{InN}: 0.61 eV) than GaN's bandgap energy (E_g^{GaN}: 3.437 eV) at RT, and thus, can form various alloys with emission in the whole visible spectrum (Figure 1.1(b)). The main properties of GaN, AlN and InN can be found elsewhere [29, 45, 46]. By adjusting the concentration of Al, one can synthesize alloys of $Al_xGa_{1-x}N$ by combining AlN and GaN characteristics to obtain a range of wide bandgap semiconductors, which are widely utilized as barriers in nitride quantum well structures. Indium Nitride is not as famous as its two other relatives, since its lower band gap energy denotes that it is not practical for UV applications. Hence, its applications are mainly limited to form InGaN and InAlN alloys. The energy bandgap of the alloys to a first approximation is described by the well known Vegard's law [47], while a curvature term [48] is usually added to simulate the parabolic compositional dependence (Figure 1.1(b)).

The characteristic dependence of the bandgap shrinkage as a function of temperature, holding for nearly all the semiconductors due to phonon-induced renormalization of electron states, follows the Varshni's semi-empirical relation [49–52] given by

$$E(T) = E(0) - \frac{\alpha T^2}{\beta + T} \tag{1.2}$$

where E(0) is the expected value for energy bandgap at T = 0 K, while α = 0.909 meV/K and β = 830 K are the empirical Varshni parameters for GaN [45].

In addition, the exciton full width at half maximum (FWHM) is affected by the inhomogeneous and homogeneous broadening mechanisms. The latter depends on temperature due to interaction with acoustic and optical phonons. The overall exciton linewidth is often described as follows

$$\Gamma(T) = \Gamma_o + \gamma_{ac}T + \frac{\Gamma_{LO,1}}{e^{\frac{E_{LO,1}}{k_B T}} - 1} \tag{1.3}$$

where Γ_o accounts for temperature-independent inhomogeneous effects such as the alloy composition fluctuations, lateral thickness variation, imperfections in the crystal and backround impurities, while γ_{ac} and Γ_{LO} represent the coupling strength due to inelastic scattering of electron-hole pairs with acoustic-phonons and LO-phonons, with the latter term having the characteristic Bose-Einstein thermal distribution. The exponential term corresponds to the first LO-phonon mode ($E_{LO,1}$ = 91.7 meV) with $\Gamma_{LO,1}$ = 375 meV indicating a large exciton coupling with LO-phonons, while typical values for the rest terms are Γ_o = 10 meV and $\gamma_{AC} = 15\ \mu eV$ [53].

1.3 Excitons in quantum wells

Semiconductor quantum wells (QWs) are 2D structures which are utilized as trap-potentials for electrons and holes. Ideally, the excited carriers should find it difficult to escape out of the wells. Their fabrication corresponds to a semiconductor of a lower bandgap energy (well) that is encapsulated on both sides by semiconductors of higher bandgap energy (barriers). Similar to bulk semiconductors, the excitonic peaks are observed in the optical spectra below the characteristic band-edge states and their properties depend on the material and quantum well parameters such as well thickness, barrier height etc. These states play a significant role in various photonic devices since they have much more pronounced optical signature. Therefore, by utilizing a quantum well structure, the quantum confinement strongly enhances the overlap between the

electron-hole pair wavefunctions, which in turn increases the oscillator strength of the exciton transitions [54] as well as their binding energy [55], permitting thus, the fabrication of photonic devices with enhanced excitonicity.

In general, exciton peaks can be clearly observed at low temperatures, while at higher temperatures thermal effects induce broadening of the exciton states. Moreover, if the thermal energy is comparable to the exciton binding energy, it occurs ionization of the e-h pair into the respective bands. Wide bandgap materials, like the GaN under study, have a large exciton binding energy that allows for the exciton observation up to room temperature conditions [56] in spite of the significant line broadening. Quantum wells can be grown by epitaxial techniques such as plasma-assisted molecular beam epitaxy (PAMBE) or metal organic chemical vapor phase epitaxy (MOVPE) on a substrate which for polar orientation is usually a GaN template on Al_2O_3. Combining all III-nitride family materials and adjusting the growth parameters, it is possible to fabricate QWs of various thicknesses and energy bandgaps ranging from UV to FIR [57, 58]. Additionally, QWs can be made by using a ternary alloy of different mole composition i.e. $Al_yGa_{1-y}N/Al_xGa_{1-x}N/Al_yGa_{1-y}N$, hence completing any gaps in the radiation spectrum [59, 60]. Typically, the QWs have structural non-uniformities that usually occur during growth, therefore, the emission spectra of QW-excitons consist of the superposition of non-identical emitted photons often called as inhomogeneous broadening of the photoluminescence lines.

For a QW structure grown along the c-axis, as depicted in Figure 1.2, it exhibits huge polarization built-in fields inside the wells due to strain effects, leading thus, to a modification in the shape of the energy bands [58, 61, 62]. This modification is the cause of a low electron-hole wavefunction overlap, and therefore, a reduced oscillator strength [63,64]. In many cases, this band-bending leads also to dissociation of the exciton pair [65]. In the case of an infinite superlattice, the amplitude of the built-in electric field inside the QW [66, 67] is

$$F_{well} = -\frac{\Delta P}{\varepsilon_o}\frac{L_{barrier}}{\varepsilon_{r,w}L_{barrier} + \varepsilon_{r,b}L_{well}},\ \Delta P = \Delta P_{piez} + \Delta P_{spont} \qquad (1.4)$$

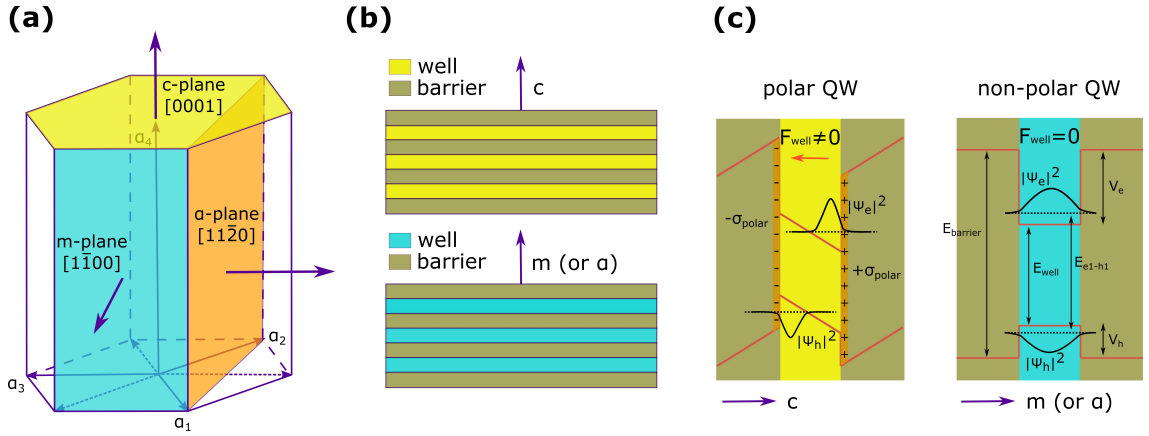

Figure 1.2: (a) Hexagonal unit cell of wurtzite GaN crystal. (b) Geometrical superlattice engineering for the polar (c-axis) and the non-polar (m- and α-axis) orientations. (c) The corresponding valence and conduction band profiles of a single QW for the two cases to depict the effect of internal built-in electric fields in the polar-oriented QW, leading to reduced electron/hole wavefunction overlap. On the other hand, in a non-polar structure, the energy bands remain unaffected due to elimination of polarization discontinuities and thus the electron-hole bonding is enhanced.

where ε_o, ε_r are the vacuum and relative permittivities, L denotes the thickness and ΔP is the difference in polarization, introducing thus a redshift of QW energy bands by a factor of $-eF_{well}L_{well}$. The most promising solution to this problem is to grow the QW-structure along a non-polar direction (m- or α-) (Figure 1.2), where there are no built-in fields along the growth direction and the energy bands are maintained flat [39, 68]. In the past years, most of the significant works concerned the polar growth of thin quantum wells [66, 67, 69], since in the manufactured non-polar samples there was poor quality. Nowdays, low-defect non-polar GaN substrates are commercially available and have boosted remarkably the radiative efficiencies of the realized devices with respect to the polar ones, taking advantage of the absence of the built-in fields and the overall enhancement of structural quality. Semi-polar structures [70], which are exhibiting lower polarization built-in fields, can also be fabricated but in this work we did not decide to produce any samples as we found the non-polar alternative to be a better research challenge for our needs.

Regarding modeling, it is possible to mathematically describe the exciton entity by solving Schrödinger's equation for the relative motion of the e-h pair,

taking into consideration the Coulomb interactions and the confining potentials (energy barriers). For a flat-band quantum well, within the effective mass approximation [71] (parabolic dispersion near the band edges), the model yields

$$[-\frac{\hbar^2\nabla_e^2}{2m_e^*}-\frac{\hbar^2\nabla_h^2}{2m_h^*}+V_e^{conf}(\vec{z}_e)+V_h^{conf}(\vec{z}_h)-\frac{e^2}{4\pi\varepsilon_r\varepsilon_o|\vec{r}_e-\vec{r}_h|}]\psi(\vec{r}_e,\vec{r}_h)=E_{exc}^{2D}\psi(\vec{r}_e,\vec{r}_h) \tag{1.5}$$

where $\psi(\vec{r}_e,\vec{r}_h)$ describes the exciton wavefunction. The resulting eigen-energies of the system are given by

$$E_{exc}^{2D}=\underbrace{E_g+E_e^{conf}+E_h^{conf}}_{E_{e-h,n}}-\underbrace{\frac{R_y^*}{(n-\frac{1}{2})^2}}_{E_{b,n}}+\underbrace{\frac{\hbar^2K_{//}^2}{2M_{exc}}}_{E_{disp}},\quad n=1,..,\infty \tag{1.6}$$

where $E_{e-h,n}$ and $E_{b,n}$ are the photon energy and the exciton binding energy respectively, of the e_n-h_n exciton state of the quantum well, E_{disp} is the kinetic energy of the exciton with $K_{//}$ the in-plane wavevector, $R_y^*=\frac{\mu_r}{m_e\varepsilon_r^2}\times 13.6$ eV is the effective (exciton) Rydberg energy with $\mu_r=\frac{m_e^*m_h^*}{m_e^*+m_h^*}$ the reduced exciton mass, $M_{exc}=m_e^*+m_h^*$ is the exciton translational mass with m_e^* and m_h^* the effective masses of the electron and hole, while m_e is the free electron mass. Considering the following values for GaN, $\varepsilon_r=8.9$, $m_e^*=0.18m_e$ and $m_h^*=0.8m_e$ (heavy hole), we obtain an effective Rydberg energy $R_y^*\approx 26$ meV [72].

When dealing with QW structures, the density of states (DOS) is modified with respect to that of the bulk material. By considering again a parabolic approximation for the energy bands, the DOS for a 2D structure [73] becomes

$$\rho_{2D}=\sum_{i=1}^{n}\frac{\mu_r}{\pi\hbar^2}H(E-E_{exc}^{2D}) \tag{1.7}$$

where $H(E)$ is the Heavyside function. In the case where the device consists of N similar QWs close to each other, we have to multiply the density of states

with the number of the QWs. A change in the DOS entails that there will be a change in the optical transition rate, governed by the Fermi's Golden Rule [74], which for the first order transitions is given by

$$W_{i\to f} = \frac{2\pi}{\hbar}\sum_{f,i}|\langle f|\hat{H'}|i\rangle|^2\rho_{2D} \tag{1.8}$$

where i, f initial and final states with energies E_i and E_f, respectively, and $\hat{H'}$ = -e$\vec{r}_{e-h}.\vec{E}_{ph}$ is the interaction Hamiltonian with e being the charge of the electron, $\vec{r}_{e-h}$ the relative motion of electron-hole pair and $\vec{E}_{ph}$ the electric field of the photon. The square of the transition matrix element $M_{fi} = \langle f|\hat{H'}|i\rangle$ describes the probability of a transition from an initial state $|i\rangle$ to a final state $|f\rangle$ and vice verca. In the case of exciton transitions, the initial and final states regard the ground and the excited states of the e-h pairs..

A vital parameter of great importance is the oscillator strength which gives the strength of the optical transition. For QW excitons, this strength is defined per unit surface according to the relation

$$\frac{f_{exc}}{S} = \frac{2N\omega_{fi}}{\varepsilon_o\hbar}|\langle f|\hat{H'}|i\rangle|^2 \tag{1.9}$$

where N is the number of oscillators, ω_{fi} is the transition frequency and ε_o the vacuum permittivity. The confinement of carriers in QWs increases the overlapping of the electron-hole wavefunctions and leads to higher oscillator strengths for the exciton entities. The dielectric response describing the bulk or QW exciton resonances can be simulated by the Drude-Lorentz damping oscillator model [75, 76] considering a homogeneous broadening term for the exciton decay (γ_{exc}). For a number of non-identical oscillators near the same frequency caused by the random inhomogeneities [77] in the produced devices, a Gaussian distribution should be applied for an appropriate representation of the excitonic broadening (Appendix A).

1.4 Fabry-Pérot resonator

A Fabry-Perot resonator, is a photonic device which has the ability to create standing waves of trapped light due to multiple reflections of the photons between two eg. metallic mirrors with peak reflectivities R_1 and R_2, as depicted in Figure 1.3(a). Apart from the mentioned reflectivity values, the efficient confinement of the electromagnetic (E/M) field depends on the wavelength of light and the distance (L_{cav}) of the mirrors. This can be succeeded by utilizing a mirror distance equal to

$$L_{cav} = m\frac{\lambda_o}{2n_{cav}} \tag{1.10}$$

where m is a positive integer, λ_o the "design" wavelength of the cavity in air and n_{cav} is the average refractive index of the cavity medium at the designed wavelength ($\lambda_{cav} = \frac{\lambda_o}{n_{cav}}$) [78]. The above condition is fulfilled for a periodic number of frequencies (Figure 1.3(b)) and the frequency separation between adjacent modes, named as free spectral range ($\Delta\nu_{FSR}$), is given by

$$\Delta\nu_{FSR} = \frac{c}{2L_{cav}n_g} \tag{1.11}$$

where c is the speed of light in vacuum while n_g is the group refractive index of the medium. An important conclusion from the previous relation is that by utilizing a sub-wavelength thickness for the resonator, it is possible to create modes inside the Fabry-Perot cavity that are distanced far away from each other. Therefore, in micron-sized cavities, similar to this work, the light confinement usually refers to only one of these modes. The ratio of the $\Delta\nu_{FSR}$ to the resonant linewidth ($\Delta\nu_{FHWM}$) is called Finesse (F) and depends strongly on the mirror reflectivities R_1, R_2 [71]. Increased values of Finesse are desirable in order to produce sharp cavity modes such as the green ones given in Figure 1.3(b).

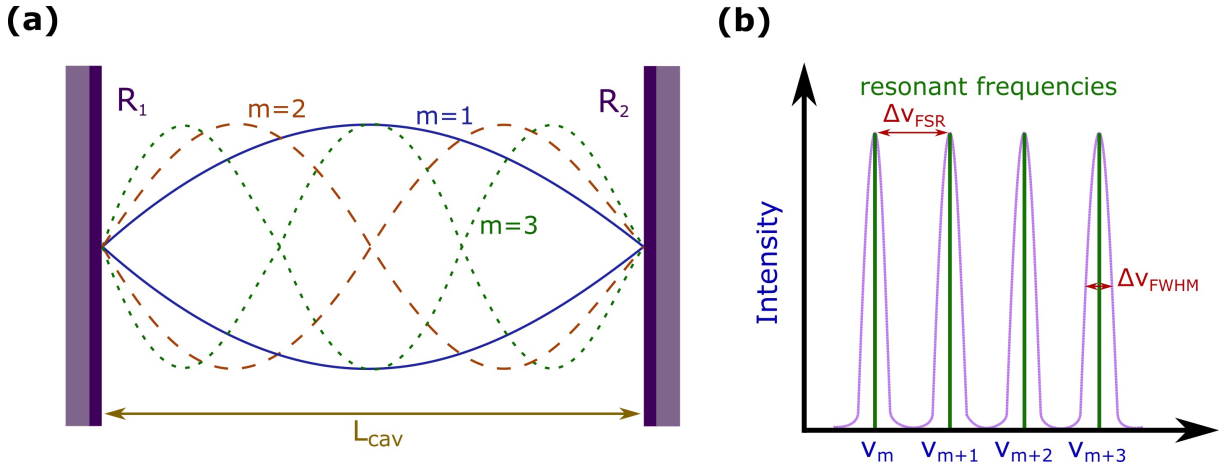

Figure 1.3: Illustration of (a) the standing waves for m = 1, 2 and 3 in a Fabry-Perot resonator made by metallic mirrors with side mirror reflectivities R_1 and R_2 distanced L_{cav}, while in (b) the graph shows the transmitted intensity versus the frequency. The allowed resonant frequencies inside the resonator are distanced by $\Delta\nu_{FSR}$.

An additional parameter which characterizes a microcavity is the escape rate of the trapped photons, known as quality factor Q [71], and corresponds to the energy dissipated in the system as a function of time. The Q-factor is related to the Finesse parameter by the relation $Q = mF$, where m is the cavity mode order. Moreover, by solving the time-dependent decay problem, we end up to the following relation

$$Q = \frac{E_{cav}}{\Delta E} = \frac{\lambda_{cav}}{\Delta\lambda} = \frac{2\pi c\tau_{cav}}{\lambda_o} \tag{1.12}$$

where in the numerator E_{cav} (λ_{cav}) is the resonant energy (wavelength) of the cavity mode, while in the denominator is the full width at half maximum of the resonant peak in energy ΔE or wavelength $\Delta\lambda$. In essence, this relation represents the average lifetime of cavity photons (τ_{cav}) and depends critically on the top and bottom mirror reflectivities R_1 and R_2. Higher reflectivities, as they provide a smaller FWHM values of the photonic mode, they tend to increase the Q-factor, and hence, the photon lifetime in the cavity ($\sim$ ps). Regarding the fabrication of such a resonator, the mirrors can be made either by a metallic coating or for instance by a periodic structure of materials operating also as reflectors and discussed next.

1.5 Distributed Bragg Reflectors

A distributed Bragg Reflector (DBR) is a multilayered stack of high (n_H) and low (n_L) refractive index materials (Figure 1.4(a)), with a quarter-wavelength ($\lambda_o/4n_i$) thickness in each layer, where λ_o is the wavelength of central maximum reflectivity and n_i the refractive index of the i^{th} layer [71]. It should be noted that the material with the lower refractive index will always have a larger thickness. The principle of operation relies on the constructive interference of the incoming and outgoing waves based on their phase. Due to this composite nature of this periodic structure, a large number of repeated alternating pairs, results to high reflectance, which can reach close to unity values ($R_{max} = 1$) as shown in Figure 1.4(b). The major advantage for utilizing DBR mirrors is their ability to exhibit high reflectivity values at any desired wavelength of the electromagnetic radiation spectrum by merely adjusting the thicknesses of the individual layers. For mechanical stability and operation, the DBR stack is usually deposited on a thick substrate.

The way to measure reflectivity is by illuminating a fabricated DBR mirror with white light and measuring the reflected intensity, normalized to a reference signal. Their ratio, referred to as reflectance, typically results in an optical response with very high values of reflectivity in a wavelength window called "stopband" or "forbidden" region and less pronounced values outside the main stopband (Figure 1.4(b)). At normal incidence, the description of the maximum reflectivity [79] and the bandwidth [80] of the stopband are given by the following relations

$$R_{stopband} = \left[\frac{n_i(n_H)^{2N} - n_s(n_L)^{2N}}{n_i(n_H)^{2N} + n_s(n_L)^{2N}}\right]^2 \tag{1.13}$$

$$\Delta\lambda_{stopband} = \frac{4\lambda_o}{\pi} arcsin\Big(\frac{|n_H - n_L|}{n_H + n_L}\Big) \tag{1.14}$$

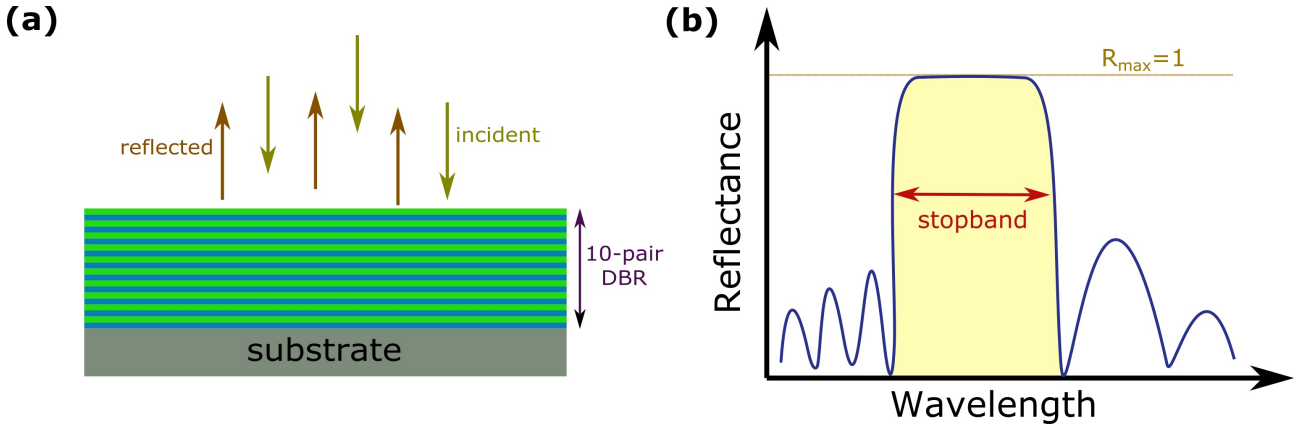

Figure 1.4: Schematic of (a) normal incident and reflected photons on a 10-pair DBR mirror deposited on a thick substrate for mechanical stability, (b) the respective reflectance spectrum of the mirror, reaching unity ($R_{max} = 1$) at the main "stopband" region. At higher and lower wavelengths there are less pronounced peaks as expected also from theory.

where n_i, n_s are the refractive indices of the incident and substrate mediums, N is the number of alternating pairs, n_H / n_L are the high and low refractive indices of the DBR materials and λ_o is the central wavelength of the stopband. The methodology can be easily extended to higher angles of reflection, producing thus, an angle dependent variation in the reflected wavelengths respectively.

The above characteristics make DBR structures ideal light reflectors in planar microcavities, obtaining high Q-factors with narrow spectral width of the escaped light (low losses in the system), which is one of the fundamental conditions for achieving lasing action. Considering the dispersion of the real part of the refractive index of the materials, which is described by the Sellmeier relation (Appendix A), it is possible to simulate the reflectivity spectrum of a DBR structure with the use of a transfer matrix model (TMM) (Appendix B), assuming in many cases for simplicity that the media are homogeneous and isotropic while the interfaces between the media are taken totally flat. The mathematical formulation can be obtained by utilizing a 2×2 matrix describing the amplitudes and phases of the left and right propagating waves. The change in amplitude, when light passes from one medium to another, is given by the Fresnel's reflection and transmission coefficients [81], as results from the boundary conditions in order to satisfy energy and momentum conservation,

while the change in phase occurs due to the optical path difference. When the medium has a thickness comparable to the wavelength of light, interference is more prominent and gives rise to standing wave effects.

1.6 Photon dispersion inside a cavity

As concerns microcavity fabrication, DBR mirrors have to be utilized on both sides of an active layer to create a photonic mode inside the cavity [82] as the one depicted in Figure 1.5(a). It is important to note that the low refractive index of the DBR materials should be the initial layer attached on either side of the active medium for successful operation while both of materials should have lower refractive index than the active medium. In such configuration, the active medium works in essence as a defect layer in comparison to the rest of the periodic structure, creating thus a mode with a considerably lower reflectivity, observed as a dip within the stopband of the reflectance spectrum (Figure 1.5(b)). The photons of this mode can escape out of the cavity with a fast or a slow rate, depending on the previously mentioned Q-factor.

Based on the work of Savona et al. [7], both DBR mirrors are penetrated by the electric field of the cavity mode, hence, the effective Fabry-Pérot cavity length is actually given by

$$L_{eff} = L_{cav} + L_{DBR}^{top} + L_{DBR}^{bottom} \tag{1.15}$$

where L_{cav} is the length of the cavity layer and

$$L_{DBR} = \frac{\lambda_o}{4n_{cav}} \frac{n_L n_H}{|n_H - n_L|} \tag{1.16}$$

is the effective length in each DBR reflector due to penetration of the electric field. The variables λ_o and n_{cav} are the wavelength of the cavity mode (in free space) and the refractive index of the active material in the cavity, n_H and

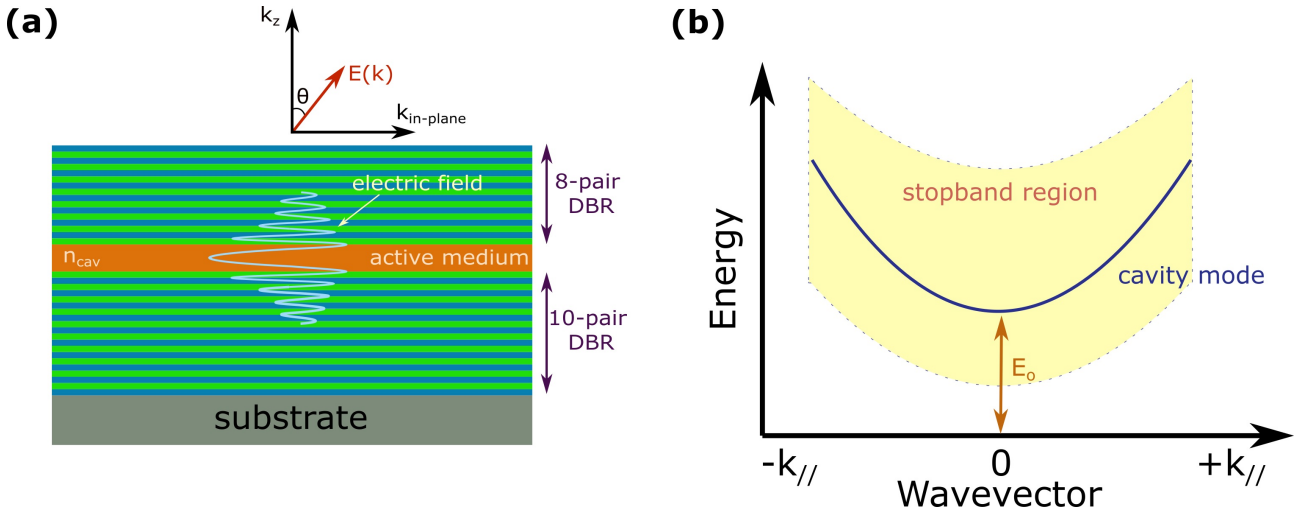

Figure 1.5: Design of (a) a λ-thick microcavity structure with an 8-pair top DBR and a 10-pair bottom DBR mirror deposited on a substrate, (b) the resulting energy dispersion versus the emission angle ($k_{//}$) of the cavity mode which is observed as a dip inside the stopband region in the analyzed reflectance spectrum.

n_L represent the high (H) and low (L) refractive indices of the two dielectric materials utilized in the DBR mirrors.

Considering a planar microcavity grown along z-axis, there is a quantization in the allowed photon modes due to the refractive index difference between the active layer and the DBR mirrors. An oxide cavity can also be formed by using only a top and a bottom DBRs, where the cavity region is made by a $\lambda/2n$ oxide layer (without exciton emitters). The energy dispersion of the cavity photons can be described by starting the analysis from the quantized wavevector

$$\vec{k}_z = \frac{2\pi}{\lambda_{cav}}\hat{z} = \frac{m\pi}{L_{eff}}\hat{z}. \tag{1.17}$$

where m is the quantum number similar to Fabry-Pérot resonator. After replacing the wavevector $|\vec{k}|$ $(= \sqrt{k_z^2 + k_{//}^2})$ in the relation for the cavity photon energy $(E_{cav} = \hbar\omega_{cav} = \hbar u_{cav}|\vec{k}|)$ and expanding in Taylor series, it yields

$$E_{cav} = \frac{\hbar c}{n_{cav}}\sqrt{(\frac{m\pi}{L_{eff}})^2 + k_{//}^2} \approx \frac{\hbar c}{n_{cav}}(\frac{m\pi}{L_{eff}}) + \frac{\hbar c}{2n_{cav}}\frac{k_{//}^2}{(\frac{m\pi}{L_{eff}})} = E_o + \frac{\hbar^2 k_{//}^2}{2m_{cav}} \tag{1.18}$$

As presented in Figure 1,5(b), the above equation gives a parabolic dispersion

around a quantized value E_o with increasing in-plane momentum ($k_{//}$), similar to an exciton state given in Section 1.3. Here, the dispersion can be described by an effective mass for the cavity photons as

$$m_{cav} = \frac{m\pi\hbar n_{cav}}{cL_{eff}} \approx 10^{-5} m_e \;\; or \;\; 10^{-4} M_{exc} \tag{1.19}$$

where the cavity photons seem to be 5 orders of magnitude lighter than electrons (or 4 orders lighter compared to excitons) [83]. This means that the energy dispersion of an exciton resonance ($E_{exc}(k_{//})$) looks flat in the same $k_{//}$ range of the cavity mode, and hence, E_{exc} can be simply represented by a constant value in polariton simulations.

The corresponding relation connecting the in-plane wavevector ($k_{//}$) and the external angle of theta (θ_{ext}) of photons escaping the microcavity is

$$k_{//} = \frac{E}{\hbar c} sin\theta_{ext} \tag{1.20}$$

where the approximation is valid if $k_z \gg k_{//}$. The photon decay rate ($1/\tau_{cav}$) of the microcavity due to mirror losses [7] can be estimated by

$$\frac{1}{\tau_{cav}} = \frac{1 - \sqrt{R_1 R_2}}{\sqrt[4]{R_1 R_2}} \frac{c}{n_{cav} L_{eff}} \tag{1.21}$$

where R_1, R_2 are the mirror reflectivities in the microcavity. Furthermore, for oblique angles (θ), the respective relations should be utilized depending on the electric field orientation of a propagating E/M wave. As results from theory [84], but observed also experimentally, two cavity modes are distinguished at higher angles denoted as s / TE polarized ($\vec{E}$ normal to the plane of incidence) or p / TM polarized ($\vec{E}$ parallel to the plane of incidence). Such a difference can affect also the polariton branches as will be shown in the experimental part of this thesis and should be taken into account for a detailed description of the modes.

1.7 Polaritons in semiconductor microcavities

All the previous considerations were neccessary in order to introduce the polariton states. A cavity polariton is a superposition of quantum states formed by light and matter inside an optical Fabry-Pérot microcavity (Figure 1.6(a)), where their distinction disappears due to the increased light-matter interaction and the system is said to operate in "strong coupling" regime [82, 85, 86]. In particular, the coupling of the two modes occurs due to the high probability of a QW exciton (absorbing emitter) to reabsorb a photon that was previously decayed by the same or another exciton having the same wavevector as the photon (momentum conservation). This is possible if the cavity photon stays long enough inside the microcavity due to the multiple reflections from the highly reflective side mirrors. This interaction occurs particularly fast, with a Rabi frequency ($\Omega_{Rabi} = \Delta E_{Rabi}/\hbar$), and gives rise to new dispersions of quasi-states, named as upper (UPB) and lower (LPB) polariton branches, which are hybrid states of light and matter. This is illustrated in Figure 1.6(b) where the energy dispersion of polaritons behaves differently from uncoupled light or matter excitations. Historically, polariton states were observed experimentally for the first time by Weisbuch et al. in 1992, when studying a GaAs microcavity [6], demonstrating thus their novel capabilities in the field of optoelectronics.

Due to dual nature, polariton engineering is possible by controlling the light and matter density of states in order to alternate their characteristics, and thus, affect the polariton optical properties. Depending on the detuning, the LPB, at low in-plane wavevectors is more photonic while at larger $k_{//}$ more excitonic. The opposite holds for the UPB. The exciton / photon percentage in each branch can be altered by moving the relative energy position of the cavity and exciton states. This is usually accomplished by changing the lattice temperature, where the GaN excitons redshift from zero up to RT in the range of 50 - 60 meV), whereas the cavity mode remains almost unaffected. From the relative position of the cavity and exciton states, a positive, zero or negative detuning (δ) can be

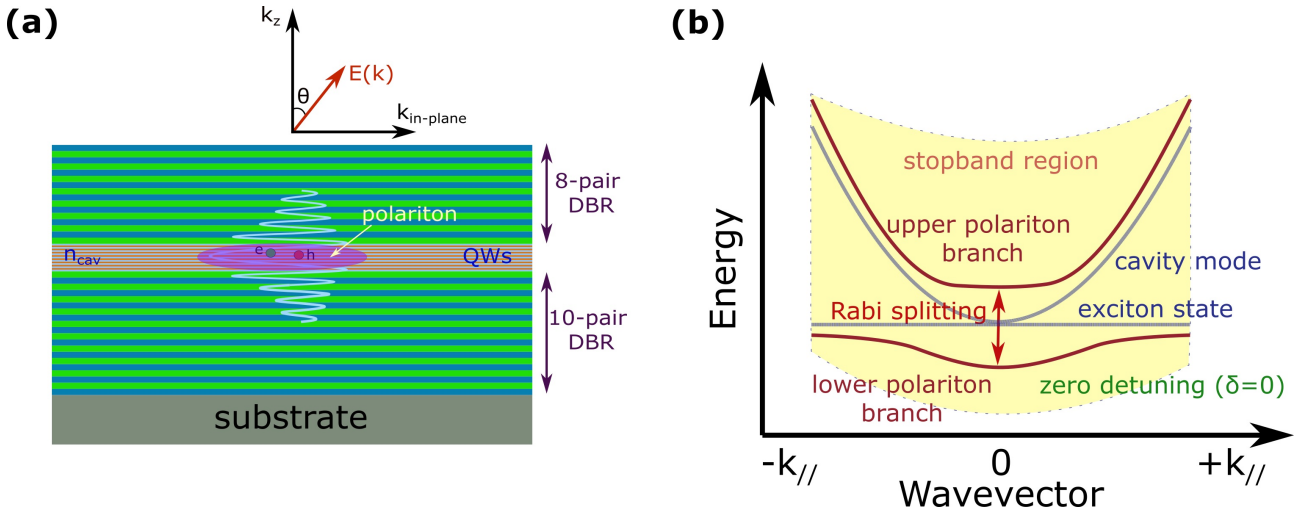

Figure 1.6: (a) A complete λ-thick microcavity structure with QWs embedded in the active region with an 8-pair top DBR and a 10-pair bottom DBR mirror made on top of a substrate, (b) the resulting energy dispersion spectrums of the lower and upper polariton branches in the case of strong coupling in respect to the exciton state and cavity mode (dashed-lines). The energy difference at the anticrossing point of the two branches (here at $k_{//} = 0$) is called Rabi splitting ($\hbar\Omega_{Rabi}$), while the zero detuning refers to the energy difference of the uncoupled states at $k_{//} = 0$.

achieved. Experimentally, all the information about the cavity, exciton and/or polariton branches can be easily extracted from the emitted photons escaping the cavity, providing hence, an accurate diagnostic tool of all the quantum states inside the microcavity.

As will be discussed in this thesis, the "matter" component in the cavity regards excitons inside quantum wells, which exhibit a much higher oscillator strength and binding energy compared to the bulk excitons. These parameters are crucial for a successful strong-coupling up to room temperature where e-h pairs need still to be bound. In order to accomplish a sufficient interaction between excitons and photons, it is important that the exciton-photon coupling strength (g_o) is larger than the linewidths (γ_{exc}, γ_{cav}) in the system. These linewidths as explained earlier derive from the cavity lifetime for a photon state and the broadening mechanisms for an exciton state. The major consideration is that this strong interaction enables some very intriguing phenomena such as polariton lasing [9, 22, 23], parametric scattering [87–90], superfluidity [91, 92] etc.

The quantum theory describes the strong coupling dynamics of a simple

system with a single exciton and cavity photon state in a linear Hamiltonian model using the rotating wave approximation, in the second quantization form, [7, 93] as

$$\hat{H} = \underbrace{\sum_{k_{//}} E_{cav,k_{//}}(\hat{a}^{\dagger}_{k_{//}}\hat{a}_{k_{//}})}_{\hat{H}_{cav}} + \underbrace{\sum_{k_{//}} E_{exc,k_{//}}(\hat{b}^{\dagger}_{k_{//}}\hat{b}_{k_{//}})}_{\hat{H}_{exc}} + \underbrace{\sum_{k_{//}} g_o(\hat{a}^{\dagger}_{k_{//}}\hat{b}_{k_{//}} + \hat{a}_{k_{//}}\hat{b}^{\dagger}_{k_{//}})}_{\hat{H}_{int}} \tag{1.22}$$

where $\hat{a}^{\dagger}_{k_{//}}$, $\hat{b}^{\dagger}_{k_{//}}$ are the creation, and $\hat{a}_{k_{//}}$, $\hat{b}_{k_{//}}$ the annihilation operators for cavity photons and excitons having an in plane wavevector $k_{//}$, while g_o is the exciton-photon coupling strength directly affecting the energy splitting of the polariton states occurring at the anticrossing point. As a result, for $g_o = 0$ there is no interaction between the photons and excitons and the states remain are uncoupled (weak coupling). For $g_o \neq 0$, the system is said to operate in the "strong coupling" regime, and new mixed states arise. As will be stated later on, there is also the situation where the two regimes can coexist in a cavity. Analyzing the system in a matrix formalism and taking also into consideration the damping parameters of the two states arising from exciton broadening and optical losses of the cavity, the Hamiltonian can be represented as

$$\hat{H} = \begin{bmatrix} E_{cav,k_{//}} - i\gamma_{cav} & g_o \\ g_o* & E_{exc,k_{//}} - i\gamma_{exc} \end{bmatrix} \tag{1.23}$$

where $E_{exc,k_{//}}$ and $E_{cav,k_{//}}$ are the exciton and photon energies, while γ_{exc} and γ_{cav} are the finite widths of the two states describing the decay / escape rates. Note that the above Hamiltonian can be expanded to include more exciton states or cavity modes in case of a more complicated system [94, 95].

Regarding g_o, it is referred to as the coupling strength between the exciton and photon states, representing the overlap of the wavefunctions. For a cavity

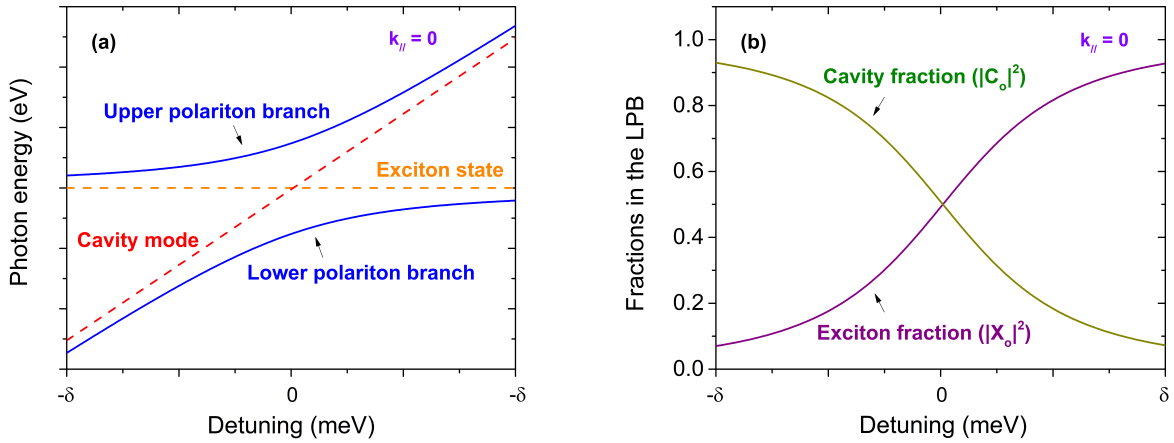

Figure 1.7: The graphs show (a) the characteristic anticrossing behavior of an exciton and a cavity mode energy states (dashed lines) versus the detuning at zero in-plane wavevector ($\delta_{k_{//}=0}$) with the creation of an upper and a lower polariton branch (solid lines). In (b) are depicted the exciton $|X_o|^2$ and photon $|C_o|^2$ fractions in the lower polariton branch versus detuning.

with a high Q-factor (R_1, $R_2 = 1$), g_o is given by

$$g_o = \hbar\sqrt{\frac{e^2 N_{eff}^{QW} f_{exc}/S}{2m_e\varepsilon_o n_{eff}^2 L_{eff}}} \tag{1.24}$$

where e is the charge of the electron, m_e the free electron mass, ε_o the vacuum permittivity, N_{eff}^{QW} corresponds to the active number of quantum wells that overlap with the antinodes of the intensity profile of the photonic mode, therefore, contributing to the coupling, f_{exc}/S the oscillator strength of the QW per unit area, $n_{eff} = \sqrt{\varepsilon_r}$ the effective refractive index of the active region, and L_{eff} the effective length of the cavity. The contribution of the DBR mirror in the effective length is an important parameter which tends to reduce the Rabi splitting.

To move on, by diagonalizing the previous Hamiltonian for a given in-plane wavevector ($k_{//}$), the quasi energy states of the upper and lower polariton branches can be obtained:

$$E_{UP,k_{//}} = \frac{1}{2}[E_{exc,k_{//}} + E_{cav,k_{//}} - i(\gamma_{exc} + \gamma_{cav}) + \sqrt{4g_o^2 + (\delta_{k_{//}} - i(\gamma_{exc} - \gamma_{cav}))^2}] \tag{1.25}$$

$$E_{LP,k_{//}} = \frac{1}{2}[E_{exc,k_{//}} + E_{cav,k_{//}} - i(\gamma_{exc} + \gamma_{cav}) - \sqrt{4g_o^2 + (\delta_{k_{//}} - i(\gamma_{exc} - \gamma_{cav}))^2}] \tag{1.26}$$

where $\delta_o = E_{exc,o} - E_{cav,o}$ is the detuning at $k_{//} = 0$ (Figure 1.6(b)). In literature, the case in which $\delta_o < 0$ (or $\delta_o > 0$) is often called negative (or positive) detuning. An example, of the energy splitting for a range of detunings considering a coupling constant $g_o \neq 0$ and a zero in-plane wavevector is visible in Figure 1.7(a). The corresponding exciton and photon fractions ($|X_o|^2$, $|C_o|^2$) of the lower polariton branch versus the detuning at $k_{//} = 0$ are shown in Figure 1.7(b). The description of the mixed states can be found in Appendix C. Another parameter of major role, called the Rabi splitting ΔE_{Rabi} ($= \hbar\Omega_{Rabi}$) (Figure 1.6(b)), gives the energy splitting at the anti-crossing point of the polariton states. Considering zero detuning (δ_o =0), where $E_{exc} = E_{cav}$ and $\gamma_{aver} = \frac{\gamma_{exc}+\gamma_{cav}}{2}$ being the average polariton linewidth, we obtain

$$\hbar\Omega_{Rabi} = 2\sqrt{g_o^2 - \frac{(\gamma_{exc} - \gamma_{cav})^2}{4}} \tag{1.27}$$

which shows that to obtain the strong coupling regime the coupling constant is not the only parameter which plays a role. Instead, the condition $4g_o^2 > (\gamma_{exc} - \gamma_{cav})^2$ must be satisfied.

It should be noted that the specific relation does not give any boundaries for the exciton or cavity linewidths. Therefore, considering the work of [7] for the $\hbar\Omega_{Rabi}^{Abs}$, we can deduce three cases defined as weak, intermediate, and strong coupling regimes shown in the graph of Figure 1.8(a), where the limits are given by the blue lines [96]. Here, we are interested in the orange colored region where the distinction of the initial states is lost due to the strong interaction. In this regime, there is an ultra-fast (fs) periodic energy exchange rate between the cavity photons and excitons (prior to any loss), due to which there is a

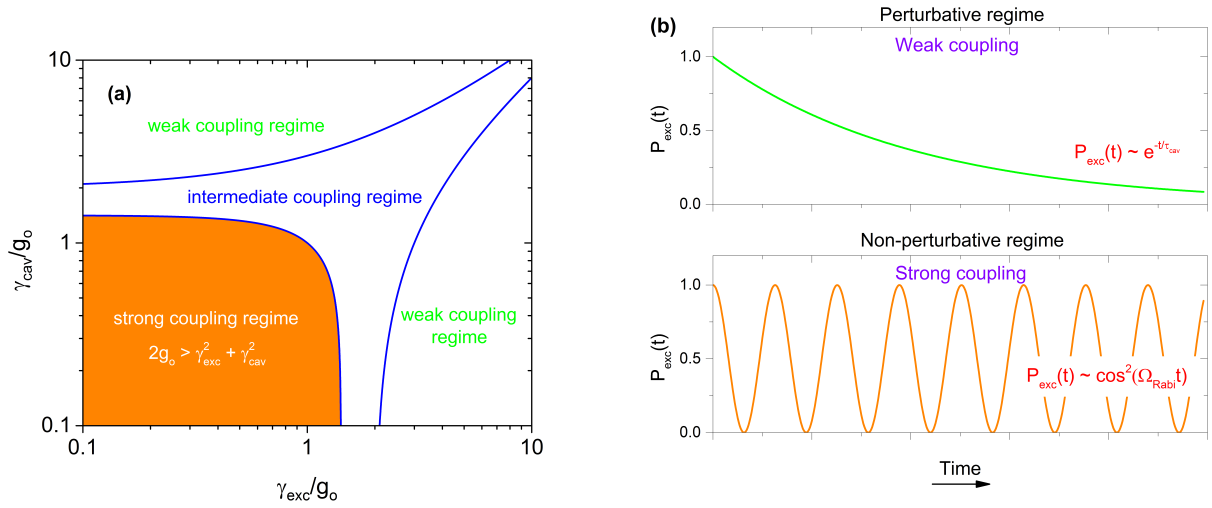

Figure 1.8: Graph (a) depicts the condition for the weak, intermediate and strong coupling regime (reproduced from ref. [96]) while graph shows (b) probability of photons to re-excite electrons at the exciton state before leaving the microcavity in the weak and strong coupling regimes [98].

modification in the energy bands, and new hybrid states govern inside the microcavity. In the weak coupling regime, known also as Purcell effect [97], the square root of Equation 1.27 becomes imaginary and corresponds to the operation of a light emitting diode (LED) under low carrier injection or of a vertical cavity surface emitting laser (VCSEL) under high carrier injection. For devices operating in the strong coupling regime, we have the fabrication of a "polariton LED" under low carrier injection and "polariton LASER" under high carrier injection. The intermediate region in Figure 1.8(a) is a situation between the weak and strong coupling regimes where the coupling condition is satisfied but without any visible splitting. Figure 1.8(b) shows the difference of the temporal evolution in a weakly and a strongly coupled system regarding the probability of photons to re-excite excitons before escaping the microcavity [98].

It can be understood up to this point that in order to succeed strong coupling two routes can be followed, either increasing the coupling between the two states or reducing the losses of the system as much as possible. The first can be made by placing many emitters with high oscillator strength at the antinodes of the field in the cavity and by decreasing the mode volume. On the other hand, the total losses of the system can be described as $\gamma_{cav}(\gamma_{cav}^{inhom}$,

γ_{cav}^{hom}) and $\gamma_{exc}(\gamma_{exc}^{inhom}, \gamma_{exc}^{hom})$. Practically, the homogeneous photon decay can be decreased by increasing the number of the DBR pairs, while the inhomogeneous broadening is related to the in-plane inhomogeneities of the mirrors. As concerns excitons, the reduction of the homogeneous exciton decay can be obtained by decreasing the temperature of the microcavity device. The inhomogeneous broadening is again related to the in-plane inhomogeneities in the QWs. Both inhomodeneous decay rates are difficult to be avoided since they are related to the fabrication of the mirrors and the quantum well layers, respectively. The common description is based on a Gaussian distribution, while homogeneous decay rates follow Lorentzian statistics. Another description can be performed by utilizing their combination. This can be accomplished by their convolution with the use of a Voigt function (Appendix A).

As already referred, in the weak coupling regime, it is possible to obtain stimulated emission (light amplification) if there is a sufficient number of carriers in the excited state with respect to the ground one. In quantum wells, the density of states is analogous to the effective mass of the excitons (Equation 1.7), which gives a high limit of the critical density in GaN-based wells which in terms of inversion of populations requires an increased energy consumption. On the contrary, as will be explained in the next section, the underlying physics for lasing operation in the strong coupling regime does not require inversion of populations. Therefore, an ultra-low energy consumption can be achieved, highlighting the need for further research and optimization in such structures. It should be pointed out that in the case of very large negative detunings, the lower polariton branch is affected by the so-called "bottleneck" effect. In this case, a large number of polaritons is stuck at higher $|k_{//}|$ values, having it difficult to reach the $k_{//} = 0$ states since there is no efficient relaxation mechanism, involving accoustic phonons, due to the steep slope of the branch. This is observed in photoluminescence experiments where the emitted intensity is much higher at non-zero in-plane wavevectors ($|k_{//}^{bott}|$). As can be understood, all the physical restrictions should be balanced for the best performance.

1.8 Bose Einstein condensation

To explain Bose Einstein condensation (BEC) [99,100], a critical parameter is the thermal wavelength λ_{DB} defined by Louis de Broglie [101], which describes the wave nature of massive particles and is expressed as follows

$$\lambda_{DB} = \frac{h}{\sqrt{2\pi m k_B T}} \tag{1.28}$$

where h is the Planck's constant, m the mass of the particle, k_B Boltzmann's constant and T the temperature. Having a particle with a huge mass at a high temperature the above relation shows that the λ_{DB} will go to zero as the rest of the parameters are constant. On the other hand, for a light particle at low temperatures, the λ_{DB} will tend to increase at a finite value. In the ideal case of a boson gas, when the de Broglie wavelength reaches a value comparable to the mean interparticle distance ($\lambda_{DB} \approx d_{int}$) in conjunction with a critical temperature (T_{crit}) there will be, based on quantum mechanics, overlap due to the spatial extent of their symmetric wavefunction tending to condense them. Moreover, if $\lambda_{DB} \gg d_{int}$ and T $\leq T_{crit}$, the boson gas will occupy the ground state of the system due to the constructive interference [12, 13]. The corresponding behavior for fermionic particles is opposite since they are described by an anti-symmetric wavefunction which tends to repel them from being close to each other (Pauli's exclusion principle).

The mentioned T_{crit} in the case of an ideal 3D Bose gas is given by

$$T_{crit} = \frac{2\pi\hbar^2}{m k_B} \left(\frac{n}{2.612}\right)^{3/2} \tag{1.29}$$

where m is the mass and n the density of boson particles. The admixed polariton quasi-particles, since they consist of bosons (photons and excitons) with integer spin, they are also characterized by a bosonic nature described by a symmetric

wavefunction. At low densities, the specific symmetry allows for the polaritons to be very close to each other, and after a critical density (or below T_{crit}), the particles can undergo a phase transition due to mutual overlap, tending to gather polaritons all together and create a coherent state named as polariton condensation. Considering the Bose-Einstein distribution [99, 100], polariton statistics is described by the following equation

$$f_{bos}(k_{//}, T, \mu) = \frac{1}{e^{\frac{E(k_{//})-E(0)-\mu}{k_B T}} - 1} \tag{1.30}$$

where $k_{//}$ is the polariton's in-plane wavevector, $E(k_{//})$ the dispersion relation, $E(0)$ the ground state, k_B Boltzmann's constant, and μ the energy that has to be compensated for a particle to enter the system, named as chemical potential. The massive occupation of the lower polariton branch at $k_{//} \approx 0$ is possible even at room temperature, due to the extremely light effective mass of polaritons ($10^{-5} m_e$). On the contrary, atoms having a much larger effective mass ($10^4 m_e$) are limited to condense at temperatures lower than μK [14, 15], while exciton condensation ($M_{exc} \sim m_e$) is thwarted by saturation and exchange effects [16, 17], as well as localization in structural defects which has a strong impact on the inhomogeneous exciton broadening. On the other extreme, cavity photons despite the small effective mass ($10^{-5} m_e$) do not form easily a condensate due to the negligible particle-particle interaction.

From the previous statements, it can be seen that for the above three cases it is hard to fulfill all the appropriate conditions in order to obtain room temperature condensation. Therefore, within certain criteria, the successful coherent emission in the strong coupling regime and possibility of low operating thresholds of exciton polaritons comes from the composite properties, combining the photon and exciton characteristics in one entity, and playing a significant role in their condensation at the lowest energy site ($k_{//} = 0$) of the lower polariton branch (LPB) which is actually behaving like a trap (Figure 1.9(a)). It should be remarked that due to the low effective mass of polaritons, the LPB

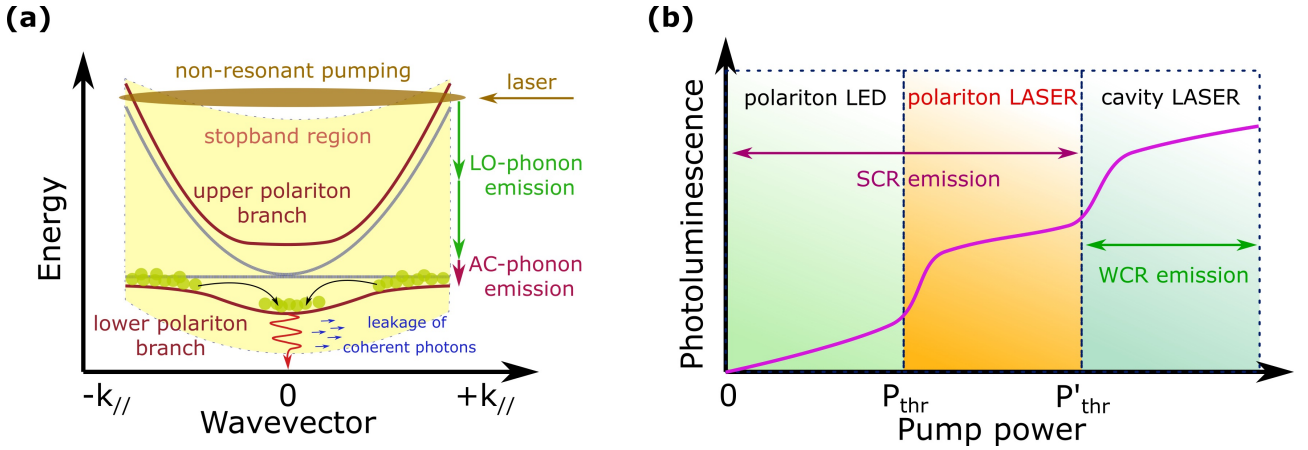

Figure 1.9: (a) Schematic showing the stimulated emission of polaritons under non-resonant excitation and the leakage of coherent photons. (b) Photoluminescence as a function of the pump power excitation (in log scale) where they are visible the three experimental cases in the emission.

ground state has a very low effective density of states which reduces the critical density that is necessary for their condensation. To demonstrate polariton lasing experimentally, non-resonant optical excitation is utilized for this purpose where the exciton particles are being excited to form an e-h plasma. Gradually, they lose their excess in energy as well as their coherence through scattering processes with lattice vibrations (LO/AC phonons) until they finally reach the upper part of lower polariton branch, often called "exciton reservoir", which allows them to become again excitons and then polaritons if they manage to relax down to the LPB as depicted in Figure 1.9(a). The radiative coupling of excitons at large wavevectors is limited to those that are within the light cone.

Depending on the relaxation dynamics of polaritons inside the cavity, two polariton lasing regimes are distinguished. The first is called the "thermodynamic regime", where the relaxation time (τ_{rel}) of polaritons is faster than the polariton radiative decay (τ_{pol}), while the second is the case where $\tau_{pol} << \tau_{rel}$ referred to as the "kinetic regime". The relaxation mechanism concerns polariton-polariton scattering which is enhanced by the excitonic fraction of polaritons (Appendix C) and acts as a stimulated process for polaritons to reach the bottom of the LPB trap, triggering thus the amplification. Based on relative reports [102], moving from the thermodynamic to the kinetic regime and vice verca can be in practice accomplished by tuning the lower polariton branch to be more

excitonic ($\delta > 0$) or more photonic ($\delta < 0$). In either regime, leakage of coherent photons from the macroscopic state occurs mainly from the top DBR, which is designed from the start to have a slightly lower reflectivity compared to the bottom mirror. It should be noted here that the suppression of the "bottleneck effect" [103, 104] in less negatively detuned structures is also an important parameter that needs to be taken into consideration. Moreover, when moving to a high density regime, the fermionic nature of polaritons takes over, therefore above a critical density named as Mott transition or saturation density (n_{sat}), the anti-symmetric wavefunction of large number of exciton polaritons [105] generates exciton-exciton scattering through exchange and phase space filling effects [106–108], weakening the exciton coupling, and hence the polariton states.

Apart from the high exciton binding energy (E_B) and oscillator strength (f) in GaN, the Mott carrier density needed to create ionization of excitons toward an e-h plasma is of the order of 10^{13} cm^{-2} [23, 102, 103, 109], which is higher than other semiconductors due to the small exciton Borh radius ($r_{exc} \sim 3$ nm). Therefore, the critical density of polaritons for condensation inside the LPB trap should be lower than the Mott transition density (n_{sat}). Under polariton lasing conditions, if the density of polaritons exceeds the saturation limit, the strong coupling is lost and lasing occurs from the cavity mode, prompting the term "cavity" or "photon" lasing where basically the system operates in the weak coupling regime (Figure 1.9(b)). An additional non-linear property of polaritons is the parametric scattering where polariton-polariton scattering is stimulated and results to the generation of a "*signal*" and an "*idler*" polariton by conserving the total energy and momentum in connection with the initial polariton state [87,88,110–113]. The photons issued from these polaritons enable the possibility to be utilized as entangled photon pairs in quantum computing devices [114,115]. Under all the circumstances, the ability to have robust polariton branches at room temperature conditions can provide novel demonstrations in the polariton physics that were previously limited to cryogenic temperatures and could allow for their use in new quantum-optical applications.

1.9 Photo-electrochemical etching process

Unlike previous research where the DBR mirrors and the active region are fabricated by the same materials (fully-epitaxial) [116] or bottom epitaxial and top dielectric (hybrid) [23, 55], here, we implement a nitride microcavity by embedding a strain-free high quality GaN-based membrane in between two dielectic mirrors (all-dielectric DBRs) [117, 118]. This context offers much more compact devices with enhanced optical confinement and reduced absorption near or at the stopband region. In addition, there is direct compatibility in case of employing electrical injection into the specific configuration. Several processing techniques have been utilized in the literature for substrate removal such as laser-induced lift-off (LLO) [119, 120], chemo-mechanical polishing (CMP) [121] or wet / dry etching [122]. In this work, this is accomplished with the use of a photo-electrochemical (PEC) wet etching process which allows for the separation of GaN material in a membrane form [123, 124] by etching an InGaN layer [125]. The PEC technique was developed by Minsky et al. [126] in order to etch the III-nitride family semiconductors at room temperature conditions and the major characteristics are the minimal damage to surrounding areas, rapid etch rates, lateral, anisotropic and bandgap selective etching relative to the direction and the wavelength of the photo-excitation used. Other wet-etching methods are isotropic and generally non-selective while dry-etching methods have failed to give the desired result due to ion induced damages resulting in poor material quality and rough surfaces. An adequate roughness for microcavity fabrication is when having an almost epitaxial quality which is in the range of lower than 1 nm. Higher surface roughness induces significant scattering of light, and thereby reducing strongly the Q-factor of the cavity.

Following the work of Jayaprakash et al. [124], the PEC-etching was carried out in an electrochemical cell at ambient conditions, where the electrolytic solution had a content of $4{\cdot}10^{-4}$ M KOH diluted in deionized (DI) water, resulting to PH of around 10.6. It should be noted that the work function of the electrolyte

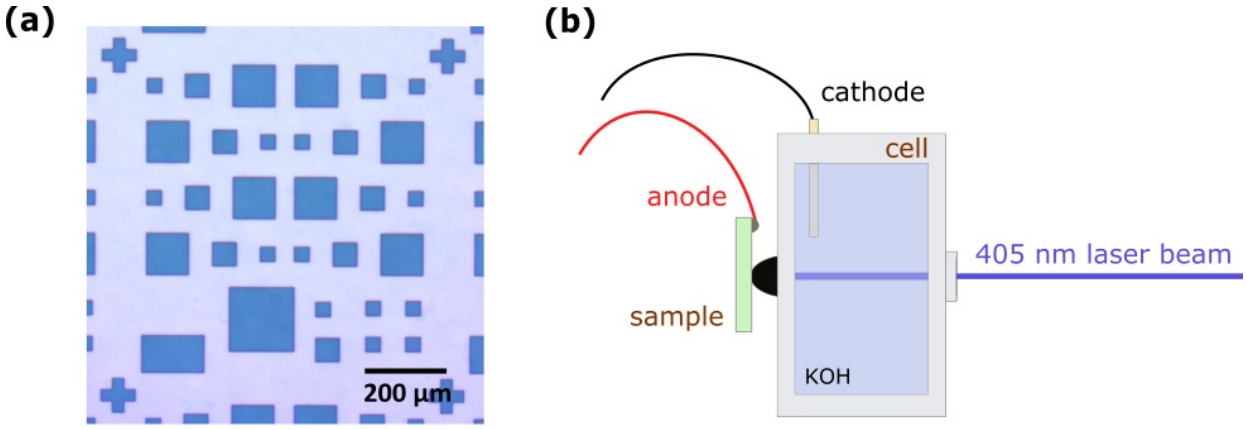

Figure 1.10: (a) Optical image depicting one of the utilized for PEC-etching mesa grid pattern. (b) Configuration of the PEC-etching and position of the sample when attached on the electrochemical cell.

depends on the PH value of the solution. In Figure 1.10(a) is presented the optical image of one of the grid patterns with mesas of various sizes fabricated by photolithography and reactive ion etching (RIE) processing steps. The patterned sample is positioned on the backside of an electrochemical cell where the only contact between surface of the sample and the cell is with the use of a cone-shaped rubber pinhole as illustrated in the PEC-etching setup given in Figure 1.10(b). In this way, the etching occurs at a pre-determined area of $7.8{\cdot}10^{-3}\ cm^2$ and several tens of membranes are etched in a single run. In order to create a Schottky-type barrier, the semiconductor needs to be in contact with the conductive KOH electrolyte acting as a cathode, while the sample is acting as an anode. To inject current from a Keithley 6517A power source (Appendix E), a dipped Platinum (Pt) electrode is placed inside the electrolyte KOH solution for the connection with the cathode while an Indium contact is made on one of the top-side edge-regions for the anode. The optical excitation is made with the use of a cw diode laser emitting at 405 nm (Appendix E), having a photon energy slightly above the InGaN's bandgap, but considerably below the absorption of the GaN crystal ($E_{InGaN} < E_{405nm} < E_{GaN}$). To adjust the output power of the diode laser, a Neutral Density (ND) filter is placed in the optical path before the cell's entrance.

As seen in the energy band diagram of Figure 1.11(a), the Schottky barrier

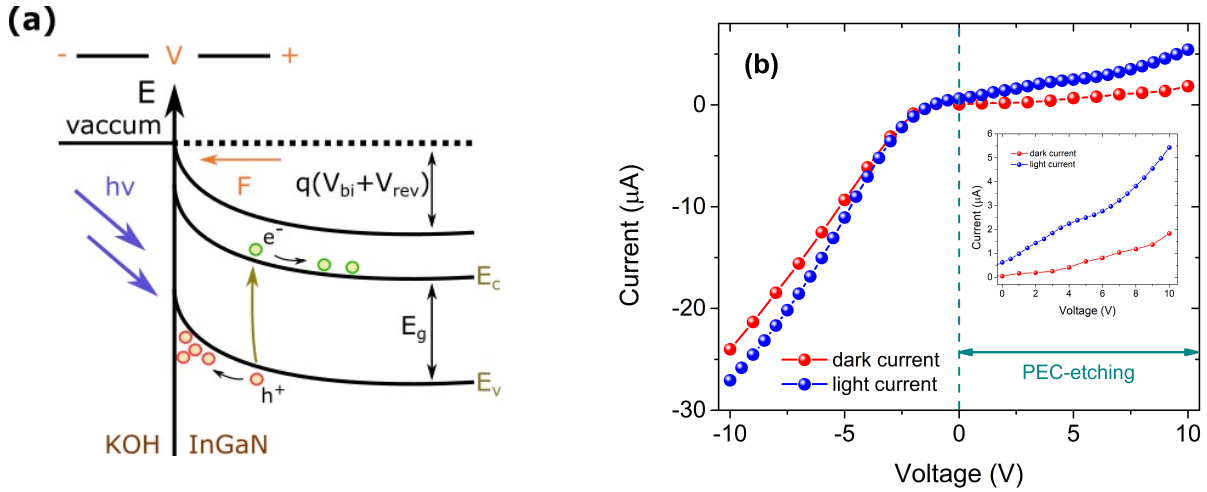

Figure 1.11: (a) Illustration depicting the hole accumulation at the interface of InGaN with the KOH due to electric field, which is the crucial mechanism for the etching. (b) Plot of current versus voltage under no light (red-curve) and light (blue-curve) illumination.

is utilized to confine the generated holes under illumination with light, at the interface of the sacrificial layer with the KOH electrolyte solution. For additional enhancement of the etching process, a reverse dc bias (V_{rev}) is applied to confine even more the holes at the electrolyte / semiconductor interface due to increased band bending. Hole accumulation is essential to PEC-etching, since the presence of a hole at the surface works essentially as a broken chemical bond. As a result, the holes facilitate oxidation and dissolution of the semiconductor by the electrolyte. The chemical reaction [124] for oxide formation is thus the following

$$2InGaN + 6h^{+} + 6OH^{-} \Rightarrow (In, Ga)_2O_3 + 3H_2O + N_2 \tag{1.31}$$

while the chemical reaction for the oxide dissolution is

$$(In, Ga)_2O_3 + 6OH^{-} \Rightarrow 2(In, Ga)_2O_3{}^{-3} + 3H_2O \tag{1.32}$$

The holes at the surface of the semiconductor, in our case of the InGaN, combine with the OH^{-} of the electrolyte, thus causing oxidation of InGaN, with nitrogen

and water as byproducts. Therefore, it is important after every etching to perform a cleaning with deionized water to remove any residual oxides. The referred residual oxides can form large particles (fast etching) or be barely visible (slow etching) depending on the etching conditions utilized in the experiment.

Figure 1.11(b) presents the characteristic current (I) versus voltage (V) curve without (red-curve) and with (blue-curve) illumination of the sample. As indicated, the etching occurs at reverse bias (0 - 10 V), where there is an increase in the overall current due to the induced photo-current ($I = I_{rev} + I_{phot}$) compared to no illumination ($I = I_{rev}$), as expected for the specific diode configuration [95]. To control and record the current versus voltage or time, the Keithley power source is connected to a computer through an Agilent GPIB cable and the whole setup runs through a script in the Agilent VEE software. The latter permits also to plot the data in real time, helping us to observe any mishappenings that could occur during the etching process. As concerns the I - t graph, the acquired data of current show an exponential-like decay versus time due to the reduced contact occurring from the etching of the InGaN layer as it is wanted. Hence, this is the basic indication that PEC operates at this stage. After PEC finishes, we look carefully the etched regions under an optical microscope in combination a scanning electron microcope (SEM), to confirm or not if PEC was successful and that the desired result is achieved. Adjusting the KOH solution along with the low etching rates and high extent in time, it is possible to induce appropriate lateral etching conditions to the InGaN sacrificial layer and create ultra-smooth bottom surfaces in the fabricated GaN-based membranes. The illuminated light is kept at low intensity levels to control the etching rate and avoid damage of the etched region. As has been observed by our group, for an optimal etching, there is an interplay between the applied bias, the optical power, the KOH concentration and the exposure time. As a result, it is important to adjust all these parameters accordingly so that the system will allow for an optimal etching with a low root-mean-square (RMS) roughness on the etched surfaces which can go even below 1 nm.

1.10 Focus of current work

The investigation of this work mainly focuses on a series of experimental observations made by employing the PEC-etching methodology on GaN samples grown in polar (c-) and non-polar (m-) crystal orientations for the fabrication and characterization of novel ultra-smooth free-standing GaN-based membranes. Next, the high quality membranes were utilized as active material by their subsequent implementation in all-dielectic microcavities for the fabrication of robust polaritonic devices for room temperature operation. Initially, in Chapter 2, is described a comprehensive methodology to extract the oscillator strength in polar GaN membranes with sub-wavelength thickness by analyzing the exciton peaks in micro-transmittance measurements. Moreover, the particular analysis can be applied also to ultra-thin membranes with embedded-QWs. In Chapter 3, is designed and developed a fully-operational microcavity configuration for the investigation of the strong coupling regime and polariton lasing with polar GaN/AlGaN QWs as the active material and SiO_2 / Ta_2O_5 as top and bottom DBRs. In Chapter 4, the polariton study is extended to the m-plane GaN/AlGaN QWs due to the advantageous elimination of the quantum confined stark effect (QCSE) which allowed the observation of an even lower polariton lasing threshold. Finally, Chapter 5 introduces an innovative way to minimize thermal / strain effects, induced during mirror deposition, by producing *transferrable* oxide-based DBRs (*t*-DBRs) for their use as top mirrors in all-dielectric microcavities.

Bibliography

[1] T. H. Maiman. *"Stimulated Optical Radiation in Ruby"*, Nature 187, 493 (1960).

[2] A. L. Schawlow and C. H. Townes. *"Infrared and Optical Masers"*, Phys. Rev. 112, 1940 (1958).

[3] W. W. Chow and S. W. Koch. *"Semiconductor-Laser fundamentals"*, Springer, (2011).

[4] L. A. Coldren, S. W. Corzine, and M. L. Mashanovitch. *"Diode Lasers and Photonic Integrated Circuits"*, Wiley-Interscience (1995).

[5] J. J. Hopfield. *"Theory of the Contribution of Excitons to the Complex Dielectric Constant of Crystals"*, Phys. Rev. 112, 1555 (1958).

[6] C. Weisbuch, M. Nishioka, A. Ishikawa, and Y. Arakawa. *"Observation of the coupled exciton-photon mode splitting in a semiconductor quantum microcavity"*, Phys. Rev. Lett. 69, 3314 (1992).

[7] V. Savona, L. C. Andreani, P. Schwendimann and A. Quattropani. *"Quantum well excitons in semiconductor microcavities: Unified treatment of week and strong coupling regimes"* Solid State Commun. 93, 733 (1995).

[8] M. S. Skolnick, A. I. Tartakonvskii, R. Butté, D. M. Whittaker, and R. M. Stevenson. *"High-occupancy effects and stimulation phenomena in semiconductor microcavities"* IEEE J. Sel. Top. Quant. 8, 1060 (2002).

[9] A. Imamoglu, R. J. Ram, S. Pau, and Y. Yamamoto. *"Nonequilibrium condensates and lasers without inversion: exciton-polariton lasers"*, Phys. Rev. A. 53, 4250 (1996).

[10] H. Deng, G. Weihs, D. Snoke, J. Bloch and Y. Yamamoto. *"Polariton lasing vs. photon lasing in a semiconductor microcavity"*, Proc. Natl. Acad. Sci. U. S. A., 100, 15318 (2003).

[11] J. Kasprzak, M. Richard, S. Kundermann, A. Baas, P. Jeambrun, J. M. J. Keeling, F. M. Marchetti, M. H. Szymańska, R. André, J. L. Staehli, V. Savona, P. B. Littlewood, B. Deveaud, and L. S. Dang. *"Bose-Einstein condensation of exciton polaritons"*, Nature 443, 409 (2006).

[12] A. Einstein. *"Quantentheorie des einatomigen idealen Gases"*, Albert Einstein: Akademie-Vorträge, Wiley-VCH Verlag GmbH & Co. KGaA, Weinheim, 237 (2006).

[13] A. Einstein. *"On the Bose-Einstein Condensation"*, Phys. Rev. 54, 947 (1938).

[14] M. H. Anderson, J. R. Ensher, M. R. Matthews, C. E. Wieman, and E. A. Cornell. *"Observation of Bose-Einstein Condensation in a Dilute Atomic Vapor"*, Science 269, 198 (1995).

[15] K. Davis, M. Mewes, M. Andrews, N. van Druten, D. Durfee, D. Kurn, and W. Ketterle. *"Bose-Einstein Condensation in Gas of Sodium Atoms"*, Phys. Rev. Lett. 75, 3969 (1995).

[16] J. M. Blatt, K. W. Böer, and W. Brandt. *"Bose-Einstein Condensation of Excitons"*, Phys. Rev. 126, 1691 (1962).

[17] J. L. Lin and J. P. Wolfe. *"Bose-Einstein Condensation of paraexcitons in stressed Cu2O"*, Phys. Rev. Lett. 71, 1222 (1993).

[18] H. Amano, M. Kito, K. Hiramatsu, and I. Akasaki. *"P-Type Conduction in Mg-Doped GaN Treated with Low-Energy Electron Beam Irradiation (LEEBI)"*, Jpn. J. Appl. Phys. 28, L2112 (1989).

[19] I. Akasaki, H. Amano, S. Sota, H. Sakai, T. Tanaka, and M. Koike. *"Stimulated Emission by Current Injection from an AlGaN/GaN/GaInN Quantum Well Device"*, Jpn. J. Appl. Phys. 34, L1517 (1995).

[20] X. Ding, Y. Zhou, and J. Cheng. *"A Review of Gallium Nitride Power Device and Its Applications in Motor Drive"*, CES TEMS 3, 54 (2019).

[21] J. Piprek. *"Nitride Semiconductor Devices: Principles and Simulation"*, Wiley-VCH Verlag GmbH & Co. KGaA (2007).

[22] S. Christopoulos, G. B. H. von Högersthal, A. J. D. Grundy, P. G. Lagoudakis, A. V. Kavokin, J. J. Baumberg, G. Christmann, R. Butté, E. Feltin, J.-F. Carlin, and N. Grandjean. *"Room-Temperature Polariton Lasing in Semiconductor Microcavities"*, Phys. Rev. Lett. 98, 126405 (2007).

[23] G. Christmann, R. Butté, E. Feltin, J.-F. Carlin,and N. Grandjean. *"Room temperature polariton lasing in a GaN/AlGaN multiple quantum well microcavity"*, Appl. Phys. Lett. 93, 051102 (2008).

[24] S. I. Tsintzos, N. T. Pelekanos, G. Konstantinidis, Z. Hatzopoulos, and P. G. Savvidis. *"A GaAs polariton light emitting diode operating near room temperature"*, Nature 453, 372 (2008).

[25] R. Huang, Y. Yamamoto, R. Andre, J. Bleuse, M. Muller, and H. Ulmer-Tuffigo. *"Exciton-polariton amplification based on exciton-exciton scattering in a CdTe quantum well"*, Technical Digest. Summaries of papers presented at the Quantum Electronics and Laser Science Conference. Postconference Technical Digest (IEEE Cat. No.01CH37172) 65, 1 (2001).

[26] F. Rahman. *"Zinc oxide light-emitting diodes: a review"*, Opt. Eng. 58, 010901 (2019).

[27] T. Guillet, M. Mexis1, J. Levrat, G. Rossbach, C. Brimont1, T. Bretagnon1, B. Gil1, R. Butté, N. Grandjean, L. Orosz, F. Réveret, J. Leymarie, J. Zúñiga-Pérez, M. Leroux, F. Semond, and S. Bouchoule. *"Polariton lasing in a hybrid bulk ZnO microcavity"*, Appl. Phys. Lett. 99, 161104 (2011).

[28] P. Bhattacharya, T. Frost, S. Deshpande, M. Z. Baten, A. Hazari, and A. Das. *"Room Temperature Electrically Injected Polariton Laser"*, Phys. Rev. Lett. 112, 236802 (2014).

[29] S. Strite and H Morkoç. *"GaN, AlN and InN: A review"*, J. Vac. Sci. Technol. B 1237, 10, (1992).

[30] T. Lei, M. Fanciulli, R. J. Molnar, T. D. Moustakas, R. J. Graham, and J. Scanlon. *"Epitaxial growth of zinc blende and wurtzitic gallium nitride thin films on (001) silicon"*, Appl. Phys. Lett. 59, 944 (1991).

[31] P. E. Van Camp, V. E. Van Doren, and J. T.Devreese. *"High pressure structural phase transformation in gallium nitride"*, Solid State Commun. 81, 23 (1992).

[32] K. Kornitzer, T. Ebner, M. Grehl, K. Thonke, R. Sauer, C. Kirchner, V. Schwegler, M. Kamp, M. Leszczynski, I. Grzegory, and S. Porowski. *"High-Resolution Photoluminescence and Reflectance Spectra of Homoepitaxial GaN layers"*, Phys. Stat. Sol. B, 216, 5 (1999).

[33] D. N. Papadimitriou. *"Calibration of Polarization Fields and Electro-Optical Response of Group-III Nitride Based c-Plane Quantum-Well Heterostructures by Application of Electro-Modulation Techniques"*, Appl. Sci. 10, 232 (2020).

[34] *"https://el.m.wikipedia.org"*.

[35] F. Bernardini and V. Fiorentini. *"Spontaneous Polarization and Piezoelectric Constants of III-V Nitrides"*, Phys. Rev. B 56, R10024 (1997).

[36] F. Bernardini, V. Fiorentini, and D. Vanderbilt. *"Accurate Calculation of Polarization-Related Quantities in Semiconductors"*, Phys. Rev. B 63, 193201 (1997).

[37] O. Ambacher, B. Foutz, J. Smart, J. Shealy, N. Weimann, K. Chu, M. Murphy, A. Sierakowski, W. Schaff, L. Eastman, R. Dimitrov, A. Mitchell, and M. Stutzmann. *"Two-Dimensional Electron Gases Induced by Spontaneous and Piezoelectric Polarization in Undoped and Doped AlGaN/GaN Heterostructures"*, J. Appl. Phys. 87, 334 (2000).

[38] F. D. Sala, A. D. Carlo, P. Lugli, F. Bernardini, V. Fiorentini, R. Scholz, and J.-M. Jancu. *"Free-carrier screening of polarization fields in wurtzite GaN/InGaN laser structures"*, Appl. Phys. Lett. 74, 2002 (1999).

[39] J. S. Speck and S. F. Chichibu. *"Nonpolar and Semipolar Group III Nitride-Based Materials"*, MRS Bull. 34, 304 (2009).

[40] S. L. Chuang and C. S. Chang. *"k.p method for strained wurtzite semiconductors"*, Phys. Rev. B 54, 2491 (1996).

[41] S. Chichibu, T. Azuhata, T. Sota, and S. Nakamura. *"Excitonic emission from hexagonal GaN epitaxial layers"*, Jpn. J. Appl. Phys. 36, 1976 (1997).

[42] W. Shan, B. D. Little, A. J. Fischer, J. J. Song, B. Goldenberg, W. G. Perry, M. D. Bremser, and R. F. Davis. *"Binding energy for the intrinsic excitons in wurtzite GaN"*, Phys. Rev. B 54, 16369 (1996).

[43] K. Kornitzer, T. Ebner, K. Thonke, R. Sauer, C. Kirchner, V. Schwegler, M. Kamp, M. Leszczynski, I. Grzegory, and S. Porowski. *"Photoluminescence and reflectance spectroscopy of excitonic transitions in high-quality homoepitaxial GaN films"*, Phys. Rev. B 60, 1471 (1999).

[44] S. B. Nam, D. C. Reynolds, C. W. Litton, R. J. Almassy, T. C. Collins, and C. M. Wolfe. *"Free-exciton energy spectrum in GaAs"*, Phys. Rev B 13, 761 (1976).

[45] I. Vurgaftman and J. R. Meyer. *"Band parameters for nitrogen-containing semiconductors"*, J. Appl. Phys. 94, 3675 (2003).

[46] F. Bernardini, V. Fiorentini, and D. Vanderbilt. *"Polarization-Based Calculation of the Dielectric Tensor of Polar Crystals"*, Phys. Rev. Lett. 79, 3958 (1997).

[47] L. Vegard. *"Die Konstitution der Mischkristalle und die Raumfüllung der Atome"*, Z. Physik 5, 17 (1921).

[48] Z. Dridi, B. Bouhafs, and P. Ruterana. *"First-principles investigation of lattice constants and bowing parameters in wurtzite $Al_xGa_{1-x}N$, $In_xGa_{1-x}N$ and $In_xAl_{1-x}N$ alloys"*, Semicond. Sci. Technol. 18, 850 (2003).

[49] Y. P. Varshni. *"Temperature dependence of the energy gap in semiconductors"*, Physica (Utrecht) 34, 149 (1967).

[50] I. Vurgaftman, J. R. Meyer, and L. R. Ram-Mohan. *"Band Parameters for III-V Compound Semiconductors and Their Alloys"*, J. Appl. Phys. 89, 5815 (2001).

[51] Q. Guo and A. Yoshida. *"Temperature Dependence of Band Gap Change in InN and AlN"*, Jpn. J. Appl. Phys., 33, 2453 (1994).

[52] W. Walukiewicz, S. X. Li, J. Wu, K. M. Yu, J. W. Ager, E. E. Haller, H. Lu, and W. J. Schaff. *"Optical Properties and Electronic Structure of InN and In-Rich Group III-Nitride Alloys"*, J. Cryst. Growth 269, 119 (2004).

[53] A. J. Fischer, W. Shan, J. J. Song, Y. C. Chang, R. Horning, and B. Goldenberg. *"Temperature-dependent absorption measurements of excitons in GaN epilayers"*, Appl. Phys.Lett. 71, 1981 (1997).

[54] M. A. Khan, R. A. Skogman, J. M. Van Hove, S. Krishnankutty, and R. M. Kolbas. *"Photoluminescence characteristics of AlGaN-GaN-AlGaN quantum wells"*, Appl. Phys. Lett. 56, 1257 (1990).

[55] G. Christmann, R. Butté, E. Feltin, A. Mouti, P. A. Stadelmann, A. Castilia, J.-F. Carlin, and N. Grandjean. *"Large vacuum Rabi splitting in a multiple quantum well GaN-based microcavity in the strong-coupling regime"*, Phys. Rev. B 77, 085310 (2008).

[56] J. F. Muth, J. H. Lee, I. K. Shmagin, R. M. Kolbas, H. C. Casey Jr., B. P. Keller, U. K. Mishra, and S. P. DenBaars. *"Absorption coefficient, energy gap, exciton binding energy, and recombination lifetime of GaN obtained from transmission measurements"*, Appl. Phys. Lett. 71, 2572 (1997).

[57] E. Feltin, D. Simeonov, J.-F. Carlin, R. Butté, and N. Grandjean. *"Narrow UV emission from homogeneous GaN / AlGaN quantum wells"*, Appl. Phys. Lett. 90, 021905 (2007).

[58] I. Gorczyca, T. Suski, N. E. Christensen, and A. Svane. *"Theoretical study of nitride short period superlattices"*, J. Phys.: Condens. Matter 30, 063001 (2018).

[59] E. A. Shevchenko, D. V. Nechaev, V. N. Jmerik, V. Kh. Kaibyshev, S. V. Ivanov, and A. A. Toropov. *"Enhanced photoluminescence efficiency in AlGaN quantum wells with gradient-composition AlGaN barriers"*, J. Phys. Conf. Ser. 741, 012118 (2016).

[60] T. Kim, B. So, J. Lee, and O. Nam. *"Effect on optical, structural and electrical properties by the AlGaN/AlGaN multi quantum wells with different well and barrier thicknesses"*, Thin Solid Films 680, 31 (2019).

[61] S. L. Chuang and C. S. Chang. *"A band-structure model of strained quantum-well wurtzite semiconductors"*, Semicond. Sci. Technol. 12, 252 (1997).

[62] C. Bulutay, N. Dagli, and Imamoglu. *"Characterization of excitons in wurtzite GaN quantum wells under valence band mixing, strain and piezoelectric field"*, IEEE J. Quant. Electr. 35, 590 (1999).

[63] J. Wang, J. B. Jeon, Y. M. Sirenko, and K. W. Kin. *"Piezoelectric effect on optical properties of pseudomorphically strained wurtzite GaN quantum wells"*, IEEE Photon. Technol. Lett. 9, 728 (1997).

[64] J. S. Im, H. Kollmer, J. Off, A. Sohmer. F. Scholz, and A. Hangleiter. *"Reduction of oscillator strength due to piezoelectric fields in $GaN/Al_xGa_{1-x}N$ quantum wells"*, Phys. Rev. B 57, R9435 (1998).

[65] H. S. Kim, J. Y. Lin, H. X. Jiang, W. W. Chow, A. Botchkarev and H. Morkoç. *"Piezoelectric effects on the optical properties of $GaN/Al_xGa_{1-x}N$ multiple quantum wells"*, Appl. Phys. Lett. 73, 3426 (1998).

[66] A. Bonfiglio, M. Lomascolo, G. Traetta, R. Cingolani, A. Di Carlo, F. Della Sala, P. Lugli, A. Botchkarev and H. Morkoç. *"Well-width dependence of the ground level emission of GaN/AlGaN quantum wells"*, J. Appl. Phys. 87, 2289 (2000).

[67] N. Grandjean, B. Damilano, S. Dalmasso, M. Leroux, M. Laügt, and J. Massies. *"Built-in electric-field effects in wurtzite AlGaN/GaN quantum wells"*, J. Appl. Phys. 86, 3714 (1999).

[68] E. Kuokstis, C. Q. Chen, M. E. Gaevski, W. H. Sun, J. W. Yang, G. Simin, M. Asif Khan, H. P. Maruska, D. W. Hill, M. C. Chou, J. J. Gallagher, and B. Chai. *"Polarization effects in photoluminescence of C- and M-plane GaN/AlGaN multiple quantum wells"*, Appl. Phys. Lett. 81, 4130 (2002).

[69] F. Natali, D. Byrne, M. Leroux, B. Damilano, F. Semond, A. Le Louarn, S. Vezian, N. Grandjean, and J. Massies. *"Inhomogeneous broadening of $Al_xGa_{1-x}N/GaN$ quantum wells"*, Phys. Rev. B 71, 075311 (2005).

[70] Y.-R. Wu, C.-Y. Huang, Y. Zhao, J. Speck. *"Nonpolar and semipolar LEDs"*, Nitride Semiconductor Light-Emitting Diodes (LEDs), Woodhead Publishing (2018).

[71] A. Kavokin, J. J. Baumberg, G. Malpuech, and F. P. Laussy. *"Microcavities"*, Oxford University Press (2017).

[72] S. Chichibu, H. Okumura, S. Nakamura, G. Feuillet, T. Azuhata, T. Sota, and S. Yoshida. *"Exciton Spectra of Cubic and Hexagonal GaN Epitaxial Films"*, Jpn. J. Appl. Phys. 36, 1976 (1997).

[73] S. Glutsch. *"Excitons in Low-Dimensional Semiconductors: Theory Numerical Methods Applications"*, Springer-Verlag GmbH, Berlin (2004).

[74] M. Fox, R. Ispasoiu. *"Springer Handbook of Electronic and Photonic Materials"*, Springer, Cham (2017).

[75] Y. Zhu, D. J. Gauthier, S. E. Morin, Q. Wu, H. J. Carmichael, and T. W. Mossberg. *"Vacuum Rabi splitting as a feature of linear-dispersion theory: Analysis and experimental observations"*, Phys. Rev. Lett. 64, 2499 (1990).

[76] R. Houdré, R. P. Stanley, U. Oesterle, and M Ilegems. *"Room-temperature cavity polaritons in a semiconductor microcavity"*, Phys. Rev. B 49, 16761 (1994).

[77] L. C. Andreani, G. Panzarini, A. V. Kavokin, and M. R. Vladimirova. *"Effect of inhomogeneous broadening on optical properties of excitons in quantum wells"*, Phys. Rev. B 57, 4670 (1998).

[78] N. Hodgson and H. Weber. *"Optical resonators: Fundamentals, Advanced Concepts and Applications"*, Springer-Verlag, London (1997).

[79] C. J. R. Sheppard. *"Approximate calculation of the reflection coefficient from a stratified medium"*, Pure Appl. Opt. 4, 665 (1995).

[80] H. Li and K. Iga. *"Vertical-Cavity Surface-Emitting Laser Devices"*, Springer, Berlin (2003).

[81] M. Born and E. Wolf. *"Principles of Optics"*, Pergamon Press, Oxford (1970).

[82] M. S. Skolnick, T. A. Fisher, and D. M. Whittaker. *"Strong coupling phenomena in quantum microcavity structures"*, Semicond. Sci. Technol. 13, 645 (1998).

[83] D. M. Whittaker, P. Kinsler, T. A. Fisher, M. S. Skolnick, A. Armitage, A. M. Afshar, M. D. Sturge, and J. S. Roberts. *"Motional Narrowing in Semiconductor Microcavities"*, Phys. Rev. Lett. 77, 4792 (1996).

[84] S. A. Furman and A. V. Tikhonravov. *"Spectral Characteristics of Multilayer Coatings: Theory"*, Basics of Optics of Multilayer Systems, Atlantica Séguier Frontières, Gifsur-Yvette, France (1992).

[85] V. Savona, Z. Hradil, A. Quattropani, and P. Schwendimann. *"Quantum theory of quantum-well polaritons in semiconductor microcavities"*, Phys. Rev. B 49, 8774 (1994).

[86] J. Levrat, R. Butté, G. Christmann, E. Feltin, J.-F. Carlin, and N. Grandjean. *"Tailoring the strong coupling regime in III-nitride based microcavities for room temperature polariton laser applications"*, Phys. Status Solidi C 6, 2820 (2009).

[87] P. G. Savvidis, J. J. Baumberg, R. M. Stevenson, M. S. Skolnick, D. M. Whittaker, and J. S. Roberts. *"Angle-Resonant Stimulated Polariton Amplifier"*, Phys. Rev. Lett. 84, 1547 (2000).

[88] P. G. Savvidis, J. J. Baumberg, R. M. Stevenson, M. S. Skolnick, D. M. Whittaker, and J. S. Roberts. *"Off-branch polaritons and multiple scattering in semiconductor microcavities"*, Phys. Rev. B 64, 075311 (2001).

[89] C. Ciuti, P. Schwendimann, and A. Quattropani. *"Theory of polariton parametric interactions in semiconductor microcavities"*, Semicond. Sci. Technol. 18, 165305 (2003).

[90] J. M. Zajac and W. Langbein. *"Parametric scattering of microcavity polaritons into ghost branches"*, Phys. Rev. B 92, 165305 (2015).

[91] A. Amo, J. Lefrère, S. Pigeon, C. Adrados, C. Ciuti, I. Carusotto, R. Houdré, E. Giacobino, and A. Bramati. *"Superfluidity of polaritons in semiconductor microcavities"*, Nat. Phys. 5, 805 (2009).

[92] G. Lerario, A. Fieramosca, F. Barachati, D. Ballarini, K. S. Daskalakis, L. Dominici, M. De Giorgi, S. A. Maier, G. Gigli, S. Kéna-Cohen, and D. Sanvitto. *"Room-temperature superfluidity in a polariton condensate"*, Nat. Phys. 13, 837 (2017).

[93] J. Ciers, J. G. Roch, J.-F. Carlin, G. Jacopin, R. Butté, and N. Gradjean. *"Propagating Polaritons in III-Nitride Slab Waveguides"*, Phys. Rev. App. 7, 034019 (2017).

[94] G. Christmann. *"III-nitride Based Microcavities: Towards Polariton Condensation at Room Temperature"*, PhD Thesis, École polytechnique fédérale de Lausanne (2009).

[95] R. Jayaprakash. *"Novel approaches for robust polaritonics"*, PhD Thesis, University of Crete (2015).

[96] R. Butté, G. Christmann, E. Feltin, A. Castiglia, J. Levrat, G. Cosendey, J.-F. Carlin, and N. Grandjean. *"Room temperature polariton lasing in III-nitride microcavities, a comparison with blue GaN-based vertical cavity surface emitting lasers"*, SPIE Int. Soc. Opt. Eng. 7216, 721619-1 (2009).

[97] E. M. Purcell. *"Proceedings of the American Physical Society: Spontaneous Emission Probabilities at Ratio Frequencies"*, Phys. Rev. 69, 681 (1946).

[98] K. Lagoudakis. *"The Physics of Exciton-Polariton Condensates"* EPFL, Lausanne (2013).

[99] A. Einstein. *"Quantum theory of ideal monoatomic gases"*, Sitz. Ber. Preuss. Akad. Wiss. 23, 3 (1925).

[100] F. Rief. *"Fundamentals of Statistical and Thermal Physics"*, McGraw-Hill Science, NewYork (1965).

[101] L. de Broglie. *"Recherches sur la théorie des quanta"*, Thesis (Paris), (1924); Ann. Phys. (Paris) 3, 22 (1925).

[102] J. Levrat, R. Butté, E. Feltin, J.-F. Carlin, N. Grandjean, D. Solnyshkov, and G. Malpuech. *"Condensation phase diagram of cavity polaritons in GaN-based microcavities: Experiment and theory"*, Phys. Rev. B 81, 125305 (2010).

[103] G. Malpuech, A. Di Carlo, A. Kavokin, J. J. Baumberg, M. Zamfirescu, and P. Lugli. *"Room-temperature polariton lasers based on GaN microcavities"*, Appl. Phys. Lett. 81, 412 (2002).

[104] F. Stokker-Cheregi, A. Vinattieri, F. Semond, M. Leroux, I. R. Sellers, J. Massies, D. Solnyshkov, G. Malpuech, M. Colocci, and M. Gurioli. *"Polariton relaxation bottleneck and its thermal suppression in bulk GaN microcavities"*, Appl. Phys. Lett. 92, 042119 (2008).

[105] F. Tassone and Y. Yamamoto. *"Exciton-exciton scattering dynamics in a semiconductor microcavity and stimulated scattering into polaritons"*, Phys. Rev. B 59, 10830 (1999).

[106] S. Schmitt-Rink, D. S. Chemla, and D. A. B. Miller. *"Theory of transient excitonic optical nonlinearities in semiconductor quantum-well structures"*, Phys. Rev. B 32, 6601 (1985).

[107] R. Zimmermann. *"Nonlinear Optics and the Mott Transition in Semiconductors"*, Phys. Status Solidi B 146, 371 (1988).

[108] S. Hunsche, K. Leo, H. Kurz, and K. Köhler. *"Exciton absorption saturation by phase-space filling: Influence of carrier temperature and density"*, Phys. Rev. B 49, 16565 (1994).

[109] G. Christmann, R. Butté, E. Feltin, A. Mouti, P. A. Stadelmann, A. Castilia, J.-F. Carlin, and N. Grandjean. *"Large vacuum Rabi splitting in a multiple quantum well GaN-based microcavity in the strong-coupling regime"*, Phys. Rev. B 773, 085310 (2008).

[110] Y. Yamamoto. *"Half-matter, half-light amplifier"*, Nature 405, 629 (2000).

[111] D. Ehrenstein. *"Amplifier from half-breed particles"*, Phys. Rev. Focus 5, story 6 (2000).

[112] R. Butté, M. Emam-Ismail, A. Lemaître, R.M. Stevenson, M. S. Skolnick, D. M. Whittaker, A. I. Tartakovskii, J. J. Baumberg, P. G. Savvidis, and J. S. Roberts. *"Pump Angle and Laser Energy Dependence of Stimulated Scattering in Microcavities"*, Phys. Status Solidi A 190, 333 (2002).

[113] M. Saba, C. Ciuti, S. Kundermann, J. L. Staehli, and B. Deveaud. *"Towards a room-temperature polariton amplifier"*, Semicond. Sci. Technol. 18, S325 (2003).

[114] S. Portolan, O. Di Stefano, S. Savasta, and V Savona. *"Emergent entanglement of microcavity polaritons"*, J. Phys.: Conf. Ser. 210, 012033 (2010).

[115] L. Einkemmer, Z. Vörös, G. Weihs, and S. Portolan. *"Polarization entanglement generation in microcavity polariton devices"*, Phys. Status Solidi B 252, 1749 (2015).

[116] J.-F. Carlin, J. Dorsaz, E. Feltin, R. Butté, N. Grandjean, M. Ilegems, and M. Laügt. *"Crack-free fully epitaxial nitride microcavity using highly reflective AlInN/GaN Bragg mirrors"*, Appl. Phys. Lett. 86, 031107 (2005).

[117] K. S. Daskalakis, P. S. Eldridge, G. Christmann, E. Trichas, R. Murray, E. Iliopoulos, E. Monroy, N. T. Pelekanos, J. J. Baumberg, and P. G. Savvidis. *"All-dielectric GaN microcavity: Strong coupling and lasing at room temperature"*, Appl. Phys. Lett. 102, 101113, (2013).

[118] R. Jayaprakash, F. G. Kalaitzakis, G. Christmann, K. Tsagaraki, M. Hocevar, B. Gayral, E. Monroy, and N. T. Pelekanos. *"Ultra-low threshold polariton lasing at room temperature in a GaN membrane microcavity with a zero-dimensional trap"*, Sci. Rep. 7, 5542 (2017).

[119] M. K. Kelly, O. Ambacher, R. Dimitrov, R. Handschuh, and M. Stutzmann. *"Optical Process for Liftoff of Group III-Nitride Films"*, Phys. Status Solidi A 159, R3 (1997).

[120] Y. Higuchi, K. Omae, H. Matsumura, and T. Mukai. *"Room-Temperature CW Lasing of a GaN-Based Vertical-Cavity Surface-Emitting Laser by Current Injection"*, Appl. Phys. Express 1, 121102 (2008).

[121] D. Kasahara, D. Morita, T. Kosugi, K. Nakagawa, J. Kawamata, Y. Higuchi, H. Matsumura, and T. Mukai. *"Demonstration of Blue and Green GaN-Based Vertical-Cavity Surface-Emitting Lasers by Current Injection at Room Temperature"*, Appl. Phys. Express 4, 072103 (2011).

[122] S. J. Pearton, C. R. Abernathy, F. Ren, J. R. Lothian, P. W. Wisk, and A. Katz. *"Dry and wet etching characteristics of InN, AlN, and GaN deposited by electron cyclotron resonance metalorganic molecular beam epitaxy"*, J. Vac. Sci. Technol. A 11, 1772 (1993).

[123] E. Trichas, N. T. Pelekanos, E. Iliopoulos, E. Monroy, K. Tsagaraki, A. Kostopoulos, and P. G. Savvidis. *"Bragg polariton luminescence from a GaN membrane embedded in all dielectric microcavity"*, Appl. Phys. Lett. 98, 221101 (2011).

[124] R. Jayaprakash, F. G. Kalaitzakis, M. Kayambaki, K. Tsagaraki, E. Monroy, and N. T. Pelekanos. *"Ultra-smooth GaN membranes by photo-electrochemical etching for photonic applications"*, J. Mater. Sci. 49, 4018 (2014).

[125] E. D. Haberer, R. Sharma, A. R. Stonas, S. Nakamura, and S. P. DenBaars. *"Removal of thick (>100nm) InGaN layers for optical devices using band-gap-selective photoelectrochemical etching"*, Appl. Phys. Lett. 85, 762 (2004).

[126] M. S. Minsky, M. White, and E. L. Hu. *"Room-temperature photoenhanced wet etching of GaN"*, Appl. Phys. Lett. 68, 1531 (1996).

Chapter 2

Optical absorption in ultra-thin GaN membranes

Here, it is presented a comprehensive methodology for the analysis of the absorption coefficient in ultra-thin ultra-smooth polar GaN membranes by accounting for the standing wave effect that is introduced in any sub-wavelength structure due to interference of light. Based on this approach, it is also possible to obtain the oscillator strength in such thin-films.

2.1 Introduction

The most straightforward and non-destructive technique to characterize a film, and more specifically a semiconductor crystal, is by illuminating it with radiation and measuring its optical response. If white light is utilized for the illumination at the front surface of a lossy medium, and the measurement is performed on the transmitted intensity for all the wavelengths of the incident spectrum, then it is possible to determine its optical absorption which is a characteristic signature, depending on the material's intrinsic properties. This optical attenuation is mathematically described by the imaginary part of the complex refractive index of a material and provides valuable information about a semiconductor's electronic band structure. Therefore, based on the accurate interpretation of an absorption spectrum, it is possible to know by how much and at which spectral range a material absorbs. The knowledge of a material's optical properties is a powerful tool and allows for the optical modeling and engineering of novel optoelectronic devices.

In most experimental cases, the investigation by means of transmittance and reflectance measurements is employed on thick crystals, where the coherence in the counter-propagating E/M waves is reduced. Nevertheless, when moving from

thick planar samples to ultra-thin ones, someone may face strong interference effects that alter the optical response by adding a sinusoidal-like signal. The reason lies in the significant contribution of the counter-propagating waves to add their phase, leading therefore, to destructive or constructive interference. In the case of thin-films, due to the close proximity of the sidewalls, the reflected electric field will have a comparable amplitude to the one coming from the counter front-side. When these fields interfere, it results to a sinusoidal intensity with maxima and minima inside the film. Hence, the measured transmittance is an overall combination of both the absorption in the layer and the interference caused by the multiple reflections of coherent waves at the film's sidewalls. Omitting interference effects in the analysis can lead to a wrong interpretation and to large errors in the deduced absorption coefficients. In most cases, since it is inevitable to avoid this "background" signal, the correct explanation and analysis of the measured transmittance data can be a difficult task.

An extensive number of theoretical approaches have been developed by many research groups to reproduce the optical response of transmittance, but most of them consider in their analysis either the case of relatively thick films [1], since fabrication of subwavelength films with low rms roughness on the two surfaces has been quite difficult up to now, or they develop mathematical tools to study heterogeneous samples, including the transparent template utilized for their growth [2,3]. However, both efforts present several drawbacks, discouraging someone to perform an in-depth analysis and understanding. A review paper on previous research in the field, given by Poelman and Smet, can be found in reference [4].

For all the above reasons, a valid methodology is introduced here to derive the absorption in thin film materials from first principles via a simplified way, considering that all the necessary criteria are satisfied. In the applied method there is a full consideration, both theoretically and experimentally, of all these effects in order to successfully extract intrinsic optical parameters of the materials such as the absorption coefficient. Towards this end, we have fabricated polar

GaN membranes of high-quality from three different samples, with successive $\frac{\lambda}{4}$nm-thick difference in thickness, from which it was possible to extract the absorption coefficient by measuring the ratio of the normal transmitted to the normal incident intensity of the beam. As it was observed experimentally, and confirmed later by the theory, including the interference effects in the analysis, the overall absorbance appeared to exhibit an oscillating behavior with varying the film's thickness d, which could not be explained in any other way.

2.2 Theoretical considerations regarding transmittance

Before starting the analysis, a few concepts have to be introduced for a better understanding of the standing wave effect. Since we have to deal with light, the initial point is to utilize James Clerk Maxwell's [5] electromagnetic equations in their compact form, given by Oliver Heaviside [6]. Then, it is possible to solve Faradays's law from which the wave equation of the electric field is deduced. In the case of a planar thin-film, the analysis of the problem is simplified to the solution of the one-dimensional wave equation since the propagation is limited to one direction. By considering a Cartesian coordinate system, where the film lies in the x-y plane, then the wave moves along the z-axis. The wave equation in absorbing homogeneous media is given by

$$\Big[\frac{\partial^2}{\partial z^2} - \frac{\tilde{n}^2}{c^2}\frac{\partial^2}{\partial t^2}\Big]\vec{E}(z,t) = 0 \tag{2.1}$$

where $c = 1/\sqrt{\varepsilon_o \mu_o}$ is the velocity of light in free space with ε_o and μ_o the electric permittivity and magnetic permeability in vacuum, while $\tilde{n}$ is the complex refractive index of the material [7] (Appendix A). The commonly used solutions for the electric field, satisfying the above equation for propagation in the z direction, take the form of an infinite monochromatic plane wave as

$$\vec{E}(z,t) = E_o e^{i(\tilde{k}z - \omega t + \phi)}\hat{x} \tag{2.2}$$

where E_o is the electric field amplitude, while $\tilde{k} = 2\pi\tilde{n}/\lambda_o$ the wavevector and $\omega = 2\pi\nu$ the angular frequency. The exponential term $i(\tilde{k}z - \omega t + \phi)$ represents the wave propagation in the z direction with a velocity u $(= \frac{c}{n})$ and an initial arbitary phase ϕ.

The above solution for the electric field follows the superposition principle where the linear combination of two or more solutions is also solution of the wave equation. It should be noted at this point that only the real part of complex solution describes the true field. In a similar manner, by solving Ampere's law, one can obtain the plane wave solutions for the magnetic field $\vec{H}(z,t)$. The cross product of electric $\vec{E}$ and magnetic $\vec{H}$ fields, gives us a parameter of major importance named as Poynting vector $\vec{S}$ $(= \vec{E} \times \vec{H})$ [8,9], describing the power flow of an electromagnetic wave propagating thought a perpendicular surface. The time-averaged value of $\vec{S}$ parameter is known as intensity (I) or energy flux density with units W/m^2 and is expressed as

$$| < \vec{S} >_t | \ = I = \frac{1}{2} nc\varepsilon_o |\vec{E}|^2 \tag{2.3}$$

where n the real refractive index of the medium, c is the velocity of light in free space, ε_o the electric permittivity and $\vec{E}$ the electric field [9,10]. Based on this definition, the absorbed (I_A), reflected (I_R) and transmitted (I_T) intensities normalized to the incident (I_o) radiation give the absorbance (A), reflectance (R) and transmittance (T) in a material and fulfill the following relation A = 1 - T - R. It should be pointed that the above parameters have a wavelength dependence due to the dispersion of light inside media as well as a dependence on the film's overall thickness. For example, a transmittance spectrum for a film of thickness d = 200 nm is defined as T(λ, d = 200 nm)).

When measuring ultra-thin absorbing films, where the thicknesses are a fraction of the wavelength of light, it is not correct to consider just an initial intensity I_o with a decaying $e^{-\alpha z}$ term and a reflectivity coefficient R', to describe

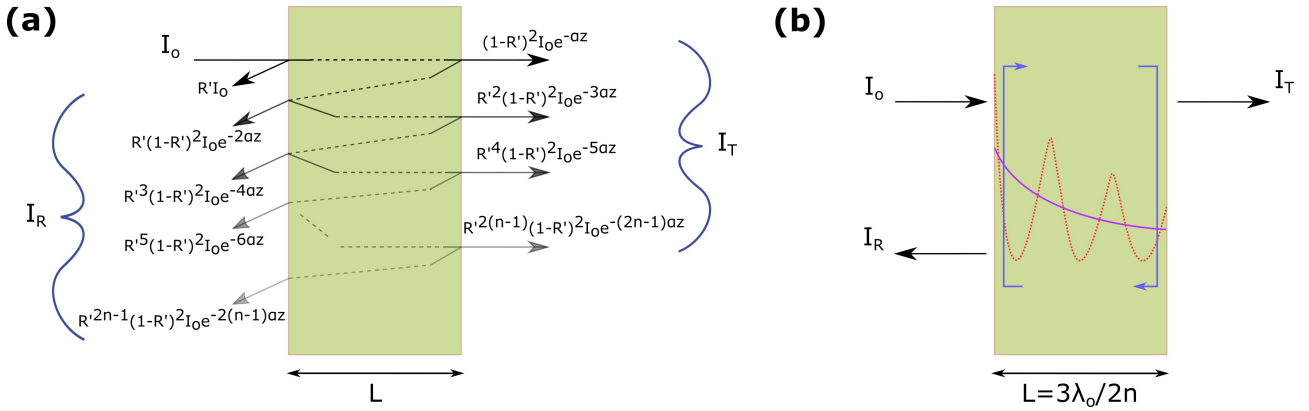

Figure 2.1: (a) Multiple internal reflections occurring inside a planar film [11] and (b) electric field intensity profile for an ultra-thin GaN film of $3\lambda_o/2n$ thickness by accounting for multiple reflections of either incoherent waves represented by a decaying intensity (purple solid line) or coherent waves represented by maxima and minima in the intensity (red dashed line).

the intensity profile along with the corresponding multiple reflections [11], as shown analytically in Figure 2.1(a). It is necessary to include the contribution of the wave's total phase θ in the calculations that accounts for the interference effect. As will be seen later on, the term that affects this phase has the form of $ikz = \frac{i2\pi nz}{\lambda_o}$. Therefore, after calculating transmittance inside a film, someone can conclude that the condition sin(kz) = 0 for constructive interference results to be $\frac{m\lambda_o}{2n}$ with m = 1,2,3, .., ∞, while the respective relation for destructive interference is $\frac{(2m'+1)\lambda_o}{4n}$ with m′ = 0,1,2,3, .., ∞ [9]. In order to follow the correct way, one has to sum the electric fields of the waves traveling back and forth after being reflected (blue arrows) at the film's sidewalls, depicted in Figure 2.1(b) for a film with thickness L = $3\lambda/2$. The square of sum will provide the overall intensity of the electric field in the medium. The purple solid line shows the produced intensity profile where incoherent multiple reflections are considered (similar to the case in Figure 2.1(a)), while the red dashed line describes the intensity profile where there are coherent multiple reflections resulting in the discussed interference effect. Hence, it can be seen that this is not a simple problem and interference effects should be included into the model in order to accurately extract the real value of the absorption coefficient in the investigated thin film. For this purpose, the main subject of this chapter is to establish the relevant methodology with the intention to be comprehensive and easy to apply.

2.3 Earlier absorption measurements

Previous research efforts regarding the absorption coefficient in GaN were made on relatively thin (< 1 μm) GaN films, epitaxially grown on Sapphire substrates [12–15] in order to maintain the transmittance signal above noise level. However, it is well known that such relatively thin GaN films on Sapphire suffer from pronounced stacking disorder and high dislocation densities, owing to the 14.6 % lattice mismatch between the two materials [16] which affect adversely their optoelectronic properties [17]. In addition, these films present significant residual strain values of the order of 0.1 %, altering the energy position and relative intensities of the A_{GaN} and B_{GaN} exciton lines [18]. Similarly, due to opacity reasons of the GaN templates typically used for growth, there is a void in the literature of reliable absorption measurements on nitride alloys and heterostructures around the energy gap of GaN, as for instance, GaN/AlGaN quantum wells (QWs).

2.4 Progress in fabrication by our group

Our work is based on recent developments in our group fabricating high optical quality GaN membranes of subwavelength thickness with atomically smooth surfaces, relying on the highly selective photo-electrochemical (PEC) wet etching of a thin InGaN sacrificial layer [19]. This approach allows for the detachment (in membrane form) of GaN-based films and heterostructures, which are coherently grown onto thick GaN/Al_2O_3 templates or bulk GaN substrates of superior crystalline quality. Using this PEC-etching technique, our group has recently demonstrated ultrasmooth GaN-based membranes with only 0.65 nm root-mean-square (rms) roughness of the etched N-face surface over an area of 10 μm $\times$ 10 μm [20].

Achieving similar results with alternative techniques to fabricate thin GaN nano-membranes would not be a trivial task, considering for instance that in

conductivity-selective electrochemical etching method [21,22] the rms roughness of the GaN etched surfaces remains considerably high, around 5 nm [23]. Likewise, removing the substrate in GaN/Si [24] and GaN/ZnO [25] heterostructures by selective wet-etching would lead to relatively low quality GaN nanomembranes based on the defective heterogeneous growth of GaN on Si or ZnO.

Accordingly, in this work, we employ the PEC etching approach and perform micro-transmittance (μ-T) experiments on high-quality free-standing bulk GaN membranes with a varying film thickness in the range from 160 to 230 nm. Considering the subwavelength thickness of the films, we develop a methodology taking into account the formation of standing waves inside the membranes, in order to turn the μ-T curves into actual absorption coefficient data. The method has the possibility to be extended to any subwavelength structure such as for instance the case were QWs are embedded in the membranes. The latter will be shown in the following chapters for polar and non-polar QW-containing membranes.

2.5 Optical characterization of the as-grown samples

As mentioned earlier, in this study, we have fabricated ultra-thin membranes of polar bulk GaN films from three different samples. Their growth was along the [0001] direction by plasma-assisted molecular beam epitaxy on commercial 8-μm-thick n-type c-axis GaN/Al_2O_3 templates. The basic epitaxial structure consists of a GaN active layer with varying nominal thickness of about "161", "194", and "226" nm, separated from the GaN/Al_2O_3 template by a 5-nm-thick $In_{0.14}Ga_{0.86}N$ sacrificial layer. The above thicknesses differ by about $\lambda_o/4$n, where λ_o and n are the emission wavelength and refractive index at the gap of GaN, respectively, while the "194" nm thickness corresponds to approximately a $3\lambda_o/2$n structure. The three bulk GaN layer designs are illustrated in Figure 2.2 where their thickness calculation was based on the standing wave condition. The reason for utilizing a thickness range in the produced membranes above 150

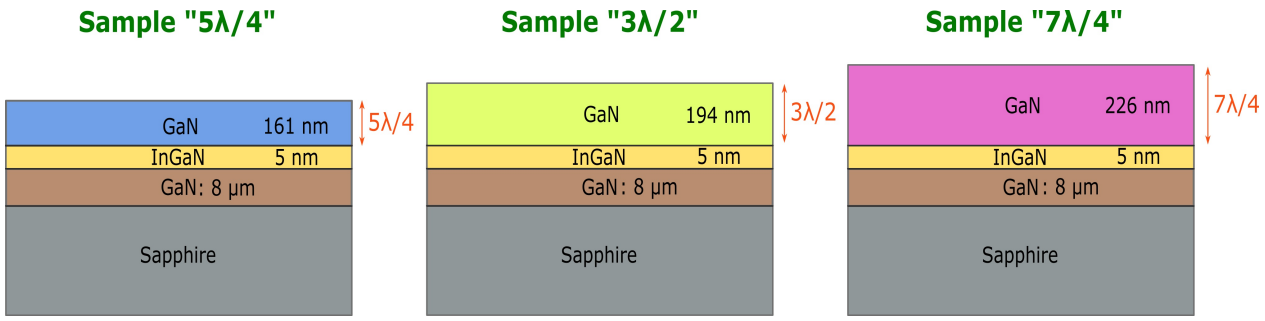

Figure 2.2: Illustration depicting the three thickness designs for the epitaxial growth of the GaN's layer. The three thicknesses were deduced from the condition for the standing wave effect in order to have a reduced absorbance ($5\lambda/4$ and $7\lambda/4$) and increased absorbance ($3\lambda/2$).

nm was just for the mechanical stability during the transfer of membranes on other substrates.

For their initial characterization, photoluminescence (PL) and reflectivity (RFL) spectroscopy was performed from low up to room temperature conditions. The discrimination between the two techniques is that in a PL measurement the excitation is performed by a laser with photon energy above the semiconductor's bandgap and the emitted secondary radiation is recorded, while for RFL a white light source is utilized and the reflected light is then recorded and analyzed. Both of the techniques photo-excite the electrons of the crystal with light and the emitted or reflected signal is analyzed with a monochromator that is connected to a CCD camera for data recording. Details of the equipment utilized in this study are given in Appendix F. A single PL spectrum is typically not enough to provide full identification of all the optically active transitions. Therefore, these two techniques complement each other and provide an advanced research tool which can reveal about the possible electronic states (such as energy gap, exciton levels, defect levels etc.) of the fabricated GaN material, and hence, its crystal quality and purity.

This can be observed in Figure 2.3(a) where the two spectra are plotted in the same graph. As can be seen, at 35 K, the major PL signal comes from localized states (donor-bound excitons) denoted as L_{GaN} at slightly lower energies 3.4793 eV. On the other hand, among the two main GaN free-exciton transitions recognized by the characteristic double sharp features in RFL, only

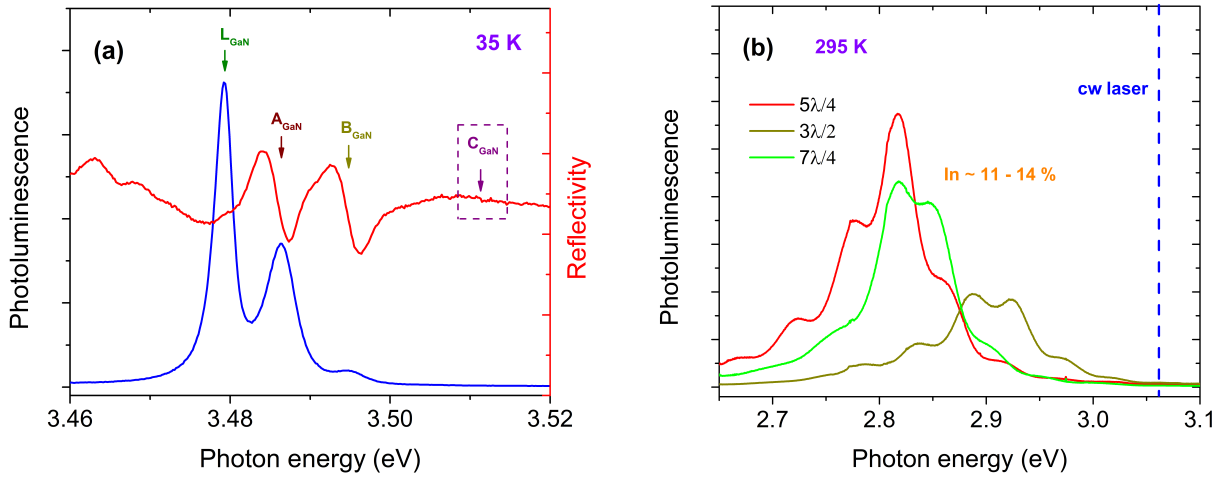

Figure 2.3: (a) PL and RFL data at 35 K. Arrows indicate the excitonic A_{GaN}, B_{GaN} bulk-GaN transitions as observed in RFL and PL spectra. The strongest PL emission is due to a D^oX transition in GaN (denoted here as L_{GaN}). (b) RT photoluminescence spectra at the InGaN region of the produced samples.

A_{GaN} located at 3.4864 eV is filled with enough carriers while B_{GaN} positioned at 3.4948 eV has a barely visible contribution in emission. C_{GaN} exciton cannot be identified here while we believe that its position is within the marked region depicted in Figure 2.3(a). It should be pointed out that the particular PL and RFL exciton observation belong to both the designed GaN membrane layer and the 8 μm-thick GaN buffer layer. Therefore, since they consist of the same material, they both contribute to the same exciton features (eg. $PL_{total} = PL_{buffer} + PL_{layer}$) without any discrimination at this stage. Nevertheless, the optical characterization by the two techniques marks, based on the acquired data, the ability to observe pronounced exciton features in the as-grown samples. Additionally, in Figure 2.3(b) are presented the photoluminescence spectra of the InGaN layers in the three as-grown samples obtained at room temperature conditions. It is clear that the small variation in photoluminescence is due to the slightly different In-composition in each structure 11 - 14 %. The In-composition was also checked by XRD which led to an average Indium percentage of 12 - 14 % in agreement with PL emission. This concentration, as can be seen from the bandgap energy of InGaN 2.8 - 2.9 eV, is sufficient for the PEC-etching method ($E_{InGaN} < E_{laser} = 3.061$ eV at 405 nm).

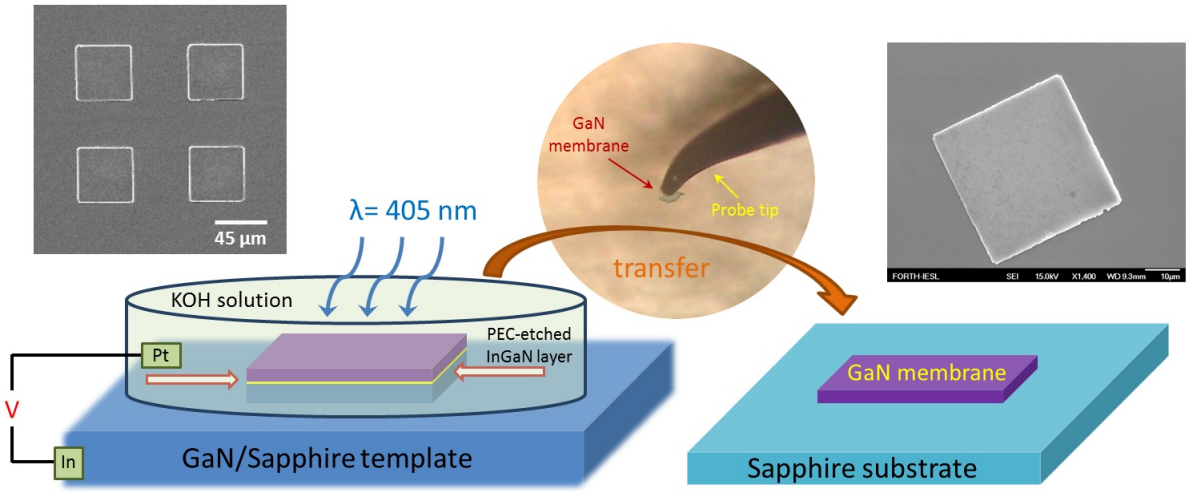

Figure 2.4: Schematic illustration depicting the GaN membrane fabrication by etching laterally an InGaN sacrificial layer with a PEC-etching process and its individual transfer on other substrates using a probe tip. The SEM image on the left presents a patterned mesa on the surface of the as-grown sample, formed by reactive ion etching, while the one on the right shows a transferred membrane on Sapphire.

2.6 Fabrication of ultra-smooth GaN membranes

In order to produce GaN membranes, the as-grown samples were patterned into 1-μm-deep square mesas with typical dimensions of 45 μm x 45 μm, using a lithography and reactive ion etching (RIE) steps, to expose the lateral facets and enable selective photo-electrochemical (PEC) etching of the InGaN sacrificial layer. The PEC etching method was performed, with a reverse bias of 3.5 V and under 3.5 mW illumination by a 405-nm diode laser for 30 min, to produce free-standing GaN membranes of high optical quality and an ultra-smooth etched surface with sub-nanometer rms roughness.

After the successful etching, it was possible to transfer the free-standing GaN membranes one by one on 300-μm-thick double-side polished Sapphire substrates for optical characterization. In Figure 2.4, a schematic depicts the GaN membrane fabrication and its individual transfer on other substrates using a probe tip. The SEM image on the left shows a patterned mesa on the surface of the as-grown sample while the one on the right comes from a transferred membrane on Sapphire. The dry-transfer process of membranes was developed within the framework of this phd work. In Figure 2.5, they are presented the

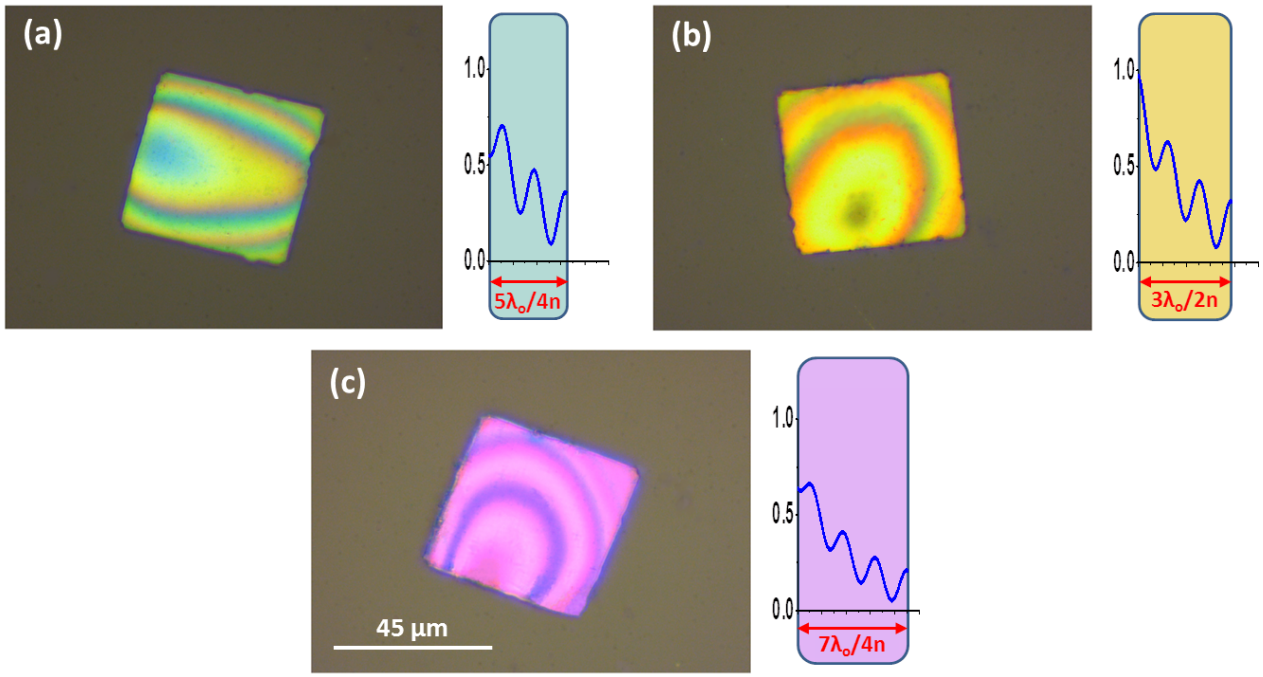

Figure 2.5: Optical images of transferred GaN membranes with thickness of (a) 163 nm, (b) 191 nm and (c) 230 nm obtained in an optical microscope under front illumination. Next to each one is depicted the simulated intensity profiles inside the membranes, normalized to the intensity beam.

top-view optical images of GaN membranes of variable thickness that were transferred on Sapphire substrates. Their distinct color is directly related to their thickness and is consistent with the results of reflectance as obtained from simulations. In the same figure are also depicted the simulated intensity profiles of the electric field inside the different membranes. These profiles are shown in a single plot in Figure 2.10(b).

In Figure 2.6 is illustrated the utilized μ-transmittance (μ-T) experimental setup, where the collimated light of a Xenon lamp is directed with UV-VIS mirrors. In order to reduce the noise in the measurements from any random background signal, the normal-incidence beam from the lamp is focused on the sample and the transmitted signal is imaged with $\times 20$ magnification onto a 100 μm diameter pinhole at the entrance of the spectrograph. To correct for the lamp's spectral response, a transmission spectrum was recorded next to each membrane and was used as a reference signal. For a better evaluation and statistics in the overall results, the same process was performed for a number of membranes.

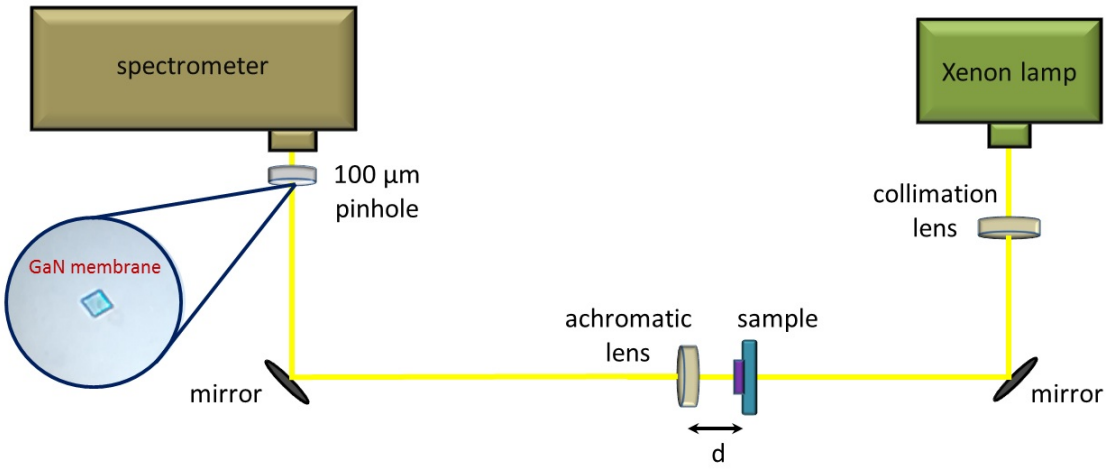

Figure 2.6: Schematic of the μ-transmittance setup, where collimated white light from a Xenon lamp illuminates the sample and an achromatic lens, placed at a distance d from the membrane, is utilized to magnify the membrane by a factor of 20 on a 100 μm pinhole at the entrance of the spectrograph. The pinhole is utilized for spatial filtering, as well as to drastically reduce the scattered light entering the spectrograph.

2.7 μ-Transmittance results and analysis

The division of the transmitted by the reference signal in each case provided us with the data presented in Figure 2.7 for each membrane thickness. For each membrane, the thickness is precisely determined by fitting the Fabry-Perot oscillations in the transparent part of the μ-T spectra. The fitting curve is based on a transfer matrix model (see Appendix B) assuming a free-standing non-absorbing GaN layer and is very sensitive to the GaN thickness, which is the only adjustable parameter. The refractive index of GaN below the band gap is taken by fitting Sellmeier's equation to the data reported in reference [26], while for simplicity the refractive index is taken constant above the band gap. The membrane is considered as free-standing based on the excellent fit of the transparent region of the μ-T spectra obtained under the assumption of an air / GaN / air structure. This is illustrated in Figure 2.7(c), where we observe that the simulated air / GaN / Sapphire curve fails to reproduce the "depth" of the Fabry-Perot oscillations, unlike the air / GaN / air configuration which provides a perfect fit.

Further evidence that the GaN membranes are actually free-standing is

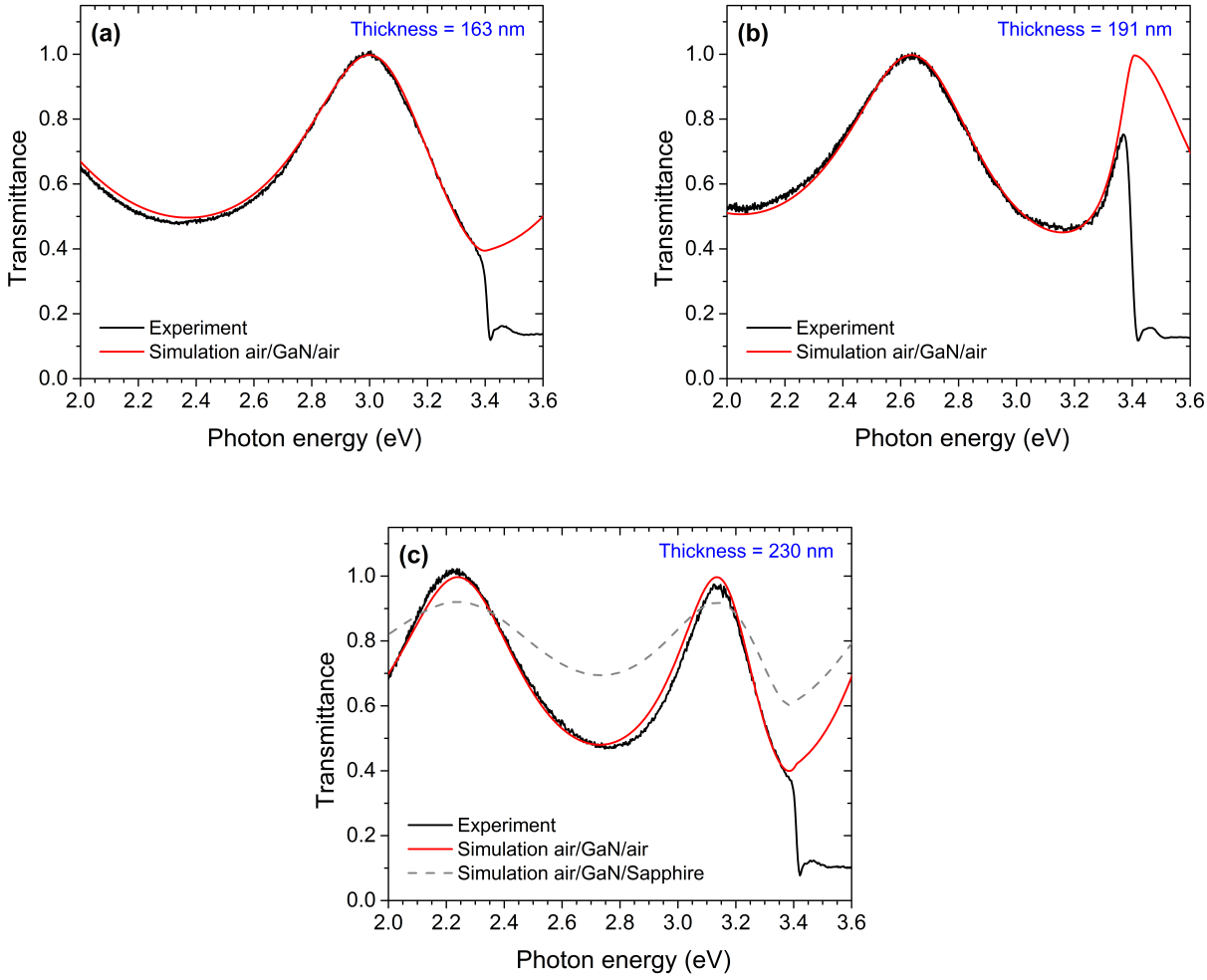

Figure 2.7: Micro-transmittance spectra obtained at room temperature from GaN membranes with thicknesses (a) 163 nm, (b) 191 nm and (c) 230 nm, as determined by fitting the transparent part of the spectra based on a transfer matrix model neglecting absorption, assuming an air / GaN / air configuration and using the thickness of GaN as the sole adjustable parameter. The grey-dashed curve in (c), corresponding to an air / GaN / Sapphire configuration, fails to reproduce the experimental curve.

provided by scanning electron microscopy images of GaN membranes transferred to Sapphire, such as the one shown in Figure 2.8(a), where it is clear that the GaN membrane is kept at a distance from the substrate most likely due to processing-related residues preventing a close contact. Aside from the excellent agreement between simulated and experimental curves for wavelengths below the band gap energy, all μ-T spectra in Figure 2.7 are marked by a pronounced GaN excitonic absorption dip, centered at 362.3 nm (3.422 eV). In Figure 2.8(b) is shown a zoom of the μ-T spectrum along with the corresponding absorption

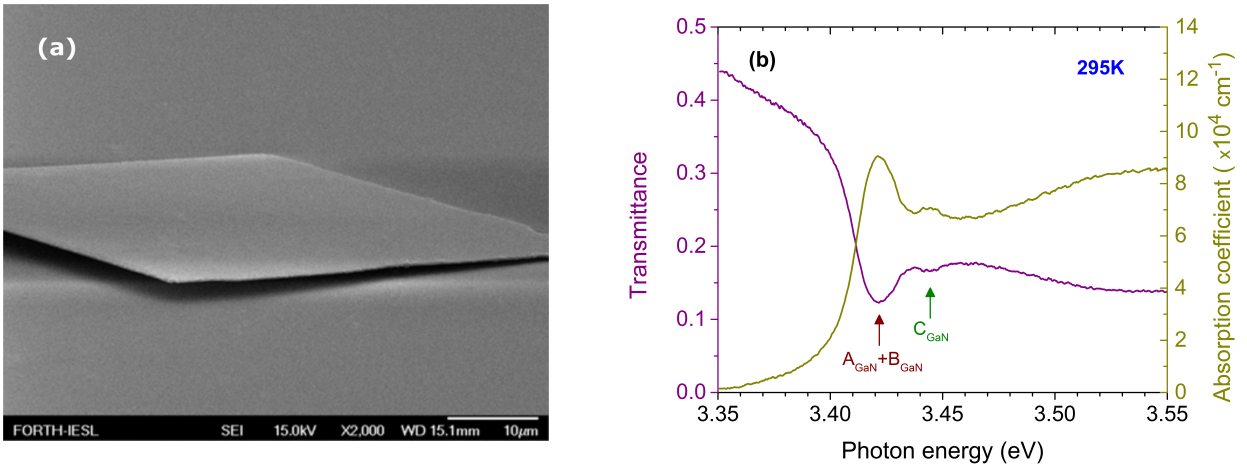

Figure 2.8: (a) μ-Transmittance spectrum at room temperature from a $5\lambda/4$ (163 nm) GaN membrane in the spectral region around the GaN gap. The main dip indicated by arrow is due to absorption by A_{GaN} and B_{GaN} excitons, while the weaker dip at shorter wavelengths is due to C_{GaN} excitons.

coefficient in the GaN band gap spectral region that was obtained from the "163-nm-thick" membrane at RT. The main dip in μ-T corresponds to a merged A_{GaN}+B_{GaN} exciton absorption peak and its energy position is in excellent agreement with the A_{GaN} and B_{GaN} exciton energies reported in unstrained homo-epitaxial GaN thin films [27] and in fully-relaxed GaN nanowires [28]. The weaker dip at higher energies corresponds to the C_{GaN} exciton.

Interestingly, the excitonic dip of the "191-nm-thick" membrane ($3\lambda/2$) in μ-T appears significantly more pronounced compared to the other two GaN thicknesses in Figure 2.7. This characteristic behavior has been confirmed on several membranes of each thickness. If we analyze these results in terms of the Beer-Lambert's law stated in the introduction, assuming as T_o the transmittance level, either 5 nm below the excitonic dip or at the first transmittance maximum, we end up with a thickness-dependent absorption coefficient. This is clearly an unrealistic result for a homogeneous film, illustrating the inadequacy of Beer-Lambert's law in ultra-thin films where interference effects can be important.

In order to include the standing wave effect in our analysis of the optical absorption, considering the sub-wavelength ($d \leq \lambda$) thickness of the membranes, a first approach is solving a three-layer Fabry-Perot structure of the type medium

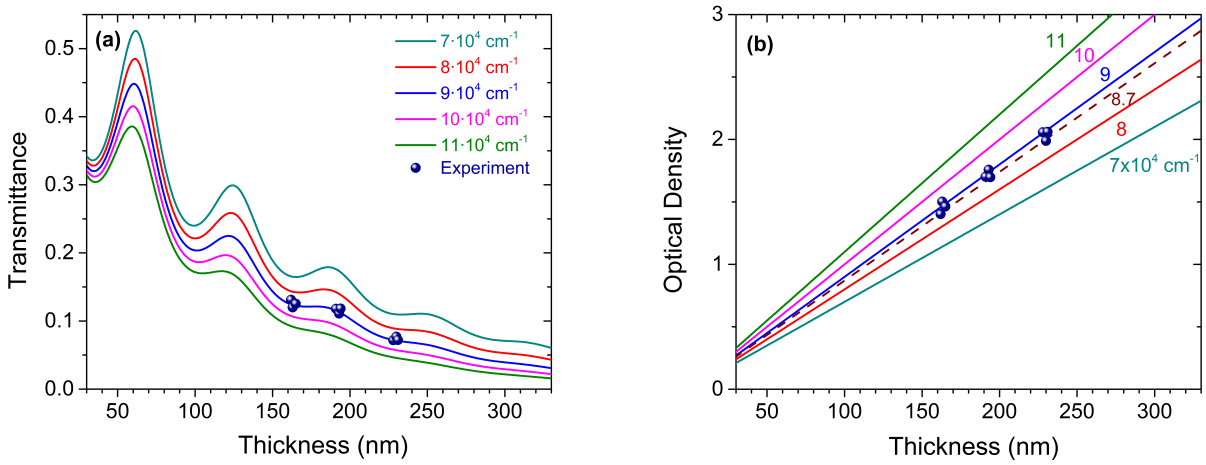

Figure 2.9: (a) Simulated transmittance at the A_{GaN}+B_{GaN} exciton position of GaN as a function of membrane thickness, estimated for various absorption coefficient values. (b) Optical density of the fabricated bulk GaN membranes vs thickness and comparison with linear curves corresponding to different absorption coefficient values.

1/GaN/medium 2 of thickness d under normal incidence. Using a transfer matrix model, the expressions for the transmittance (T) and reflectance (R) [29] are as follows:

$$T(\lambda, d) = \frac{(1-R_1)(1-R_2)e^{-\alpha d}}{(1-R''e^{-ad})^2 + 4R''e^{-\alpha d}sin^2(\beta d)} \tag{2.4}$$

$$R(\lambda, d) = \frac{(\sqrt{R_1} - \sqrt{R_2}e^{-\alpha d})^2 + 4R''e^{-ad}sin^2(\beta d)}{(1-R''e^{-\alpha d})^2 + 4R''e^{-\alpha d}sin^2(\beta d)} \tag{2.5}$$

where α is the absorption coefficient of GaN at wavelength λ, d is the thickness of GaN, $R_1(\lambda)$ and $R_2(\lambda)$ are the reflection coefficients at the interfaces of GaN with medium 1 and medium 2, respectively, $R'' = \sqrt{R_1 R_2}$, and $\beta = 2\pi \mathrm{Re}(\tilde{n})/\lambda$.

In Figure 2.9(a) is plotted the calculated transmittance at the A_{GaN}+B_{GaN} exciton position of 362.3 nm, for a symmetric air / GaN / air structure as a function of GaN thickness and for various values of the absorption coefficient. The T-curves, which exhibit an oscillatory behavior due to the standing wave effect, can reproduce the experimental values measured on several membranes

using a single absorption coefficient at the A_{GaN}+B_{GaN} exciton peak, namely α = 9·10^4 cm^{-1}. This value is in agreement with previous reports on the absorption coefficient of GaN [14, 15]. From Equation 2.4, the optical density, OD = $\alpha \cdot$ d, can be readily approximated as follows,

$$OD(\lambda, d) \approx ln[\frac{(1-R_1)(1-R_2)}{T(\lambda, d)} - 4R''sin^2(\beta d) + 2R''] \tag{2.6}$$

Introducing the experimental values of T(λ = 362.3 nm, d) and the respective refractive index of GaN [26] in Equation 2.6, we find the expected linear dependence of the optical density at the given wavelength on the film thickness, illustrated in Figure 2.9(b), with the experimental data points following closely the line with slope α = 9·10^4 cm^{-1}. On the other hand, if we introduce in Equation 2.6 the T(λ) spectra for a given d, and the dispersion of the GaN refractive index, we can extract the OD(λ) spectrum for the given thickness, and thereby the absorption coefficient $\alpha_{GaN}(\lambda)$ of the GaN membrane, as shown in Figure 2.8(b) with solid-brown line for the "163-nm-thick" GaN membrane.

2.8 Absorbance in GaN membranes

Next, we deduce for each membrane the absorbance (A = 1 - T - R) at the A_{GaN}+B_{GaN} exciton position, by estimating R through Equation 2.5, using α = 9·10^4 cm^{-1}. In Figure 2.10(a), there is a comparison of the obtained experimental values of absorbance with various theoretical models. Excellent agreement is observed with those models that take into account interference effects, such as the transfer matrix model discussed above (solid curve) and an alternative approach proposed by Ohta et al. [30] (dot-dashed curve). In the latter model, the absorbance A is calculated using Poynting's theorem and is related to the normalized beam intensity profile I(z) inside the film, according to:

$$A = \int_0^d \alpha(z) I(z) dz \tag{2.7}$$

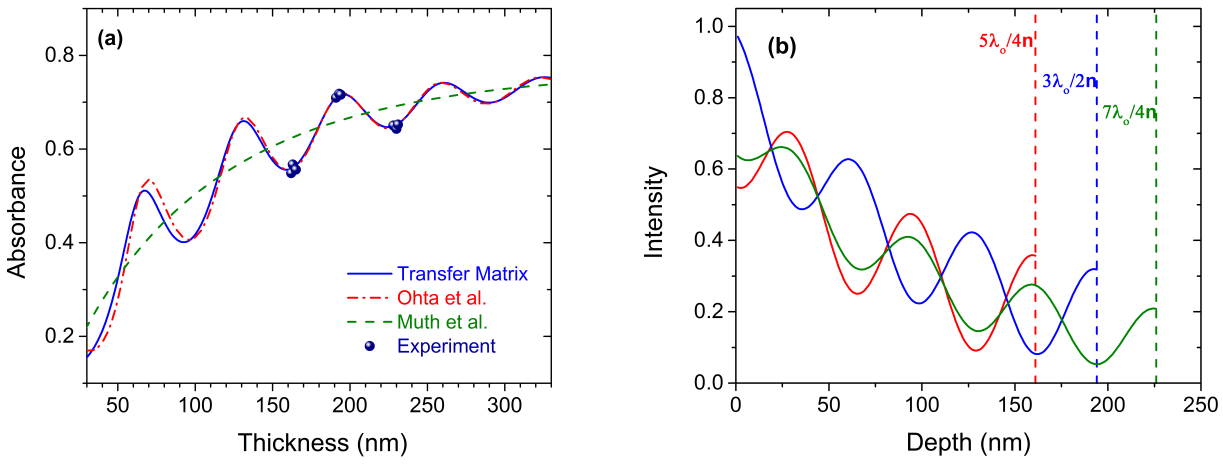

Figure 2.10: (a) Experimental absorbance compared to theoretical absorbance curves obtained using $\alpha = 9{\cdot}10^4\ cm^{-1}$ in the transfer matrix model equations, the model proposed by Ohta and Ishida [30, 31], and the model used by Muth et al. [15] (b) Normalized beam intensity profiles inside GaN membranes with varying thickness of $5\lambda_o/4n$, $3\lambda_o/2n$, and $7\lambda_o/4n$, where n is the refractive index of GaN and $\lambda_o = 362.3$ nm, calculated following the work of K. Ohta and H. Ishida, assuming an absorption coefficient $\alpha = 9{\cdot}10^4\ cm^{-1}$. The intensity is normalized based on the incident beam.

For a homogeneous film, similar to GaN membranes, α is assumed to be constant in the whole extent and A becomes proportional to the particular absorption coefficient and to the integral of I(z) inside the film. The normalized intensity profiles can be estimated as a function of film thickness following reference [31].

As an example, is shown in Figure 2.5(a-c) the intensity profile for each of the three types of GaN membranes studied in this work. For comparison purposes, these profiles are represented on the same graph in Figure 2.10(b). It is important to note that the integral of the $3\lambda_o/2n$-profile is larger than the integrals of the $5\lambda_o/4n$- and $7\lambda_o/4n$-profiles, accounting for the higher absorbance of the $3\lambda_o/2n$-thick membranes. The calculated integral values of intensity for the successive thicknesses are 62.8, 79.7, and 72.7 nm, respectively. The intensity profile is normalized to the intensity of the incident beam. Finally, the dashed curve in Figure 2.10(a), obtained considering multiple reflections but ignoring interference [15], clearly fails to reproduce the experimental results, illustrating thus, the crucial role of the standing wave effect in our structures.

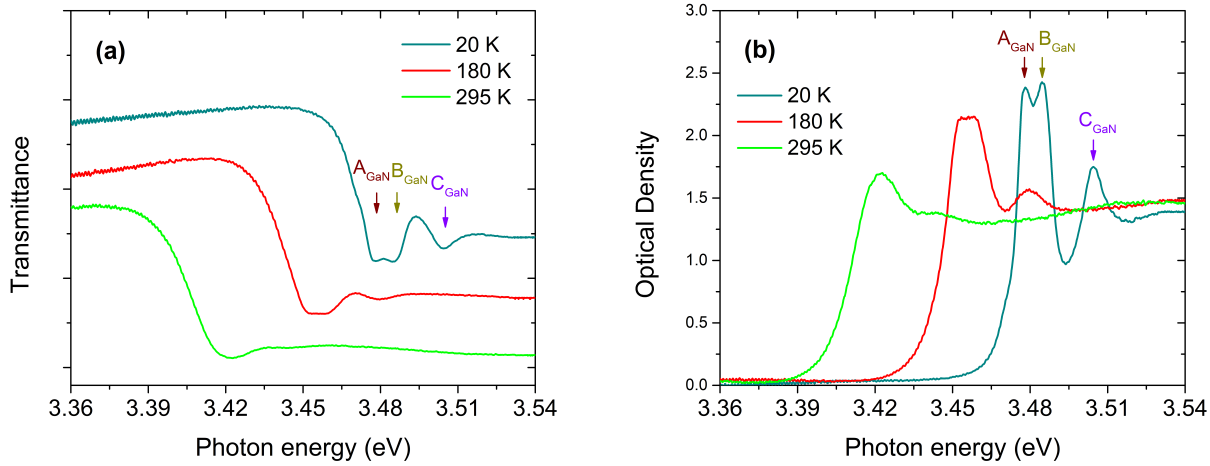

Figure 2.11: (a) Experimental micro-tranmsittance in a $3\lambda/2$ thick (191 nm) GaN membrane and (b) the deduced optical density profiles at the temperatures 20 K, 180 K and 295 K.

2.9 Optical density profile vs temperature

By utilizing the closed-cycle Helium cryostat in our lab, it was possible to perform μ-T measurements as a function of temperature. Nevertheless, due to the huge vibrations in the specific cryostat system there is a non-negligible uncertainty in the measured spectra. At any rate, in Figure 2.11(a) are given the normalized transmittance spectra, while in Figure 2.11(b) the extracted optical density profiles of the $3\lambda_o/2n$-thick (191 nm) membrane. In the μ-T spectra at Figure 2.11(a), a constant offset has been added between successive spectra for better visibility. In the 20 K spectra, the A_{GaN} peak is positioned at 3.478 eV and the B_{GaN} peak at 3.485 eV. The excitons are observed as separate dips / peaks in the two plots with an energy difference of around 7 meV, while the difference based on fitting with two Gaussians was 8 meV. The same fitting gave also a FWHM of 8 meV at 20 K for the two main exciton states.

The C_{GaN} exciton peak, which has also a relatively strong signature at low temperatures, is distanced by approximately 27 and 20 meV from the A_{GaN} and B_{GaN} excitons, respectively. These values are similar to the ones for unstrained hexagonal GaN reported in [32, 33]. Moving at higher temperatures, the two major excitons gradually merge into a single peak, while C_{GaN} fades away. With

the rise of the temperature, all the exciton states are affected by homogeneous broadening due to the interactions with LO phonons, and thus, have a weaker maximum peak-value and a much broader linewidth (around 22 meV fitted for each exciton at RT) in accordance with previous works [33]. Nevertheless, as confirmed based on the fittings, the exciton oscillator strength remains almost unaffected with temperature, since it is proportional to the integrated region below the exciton peak. This is further discussed in the proceeding section.

2.10 Bulk GaN exciton oscillator strength

By successfully obtaining the accurate absorption spectrum at ambient conditions in a GaN film and by considering the theoretical work of Y. Yamamoto et al. [34], it is then possible to extract the oscillator strength per unit volume of the A_{GaN}+B_{GaN} exciton line by utilizing the following expression:

$$\frac{f_{bulk}}{V} = \frac{2\varepsilon_o n_{GaN} m_e c}{\pi e^2 \hbar} \cdot \frac{\int OD(E)dE}{d} \tag{2.8}$$

where ε_o is the vacuum permittivity, n_{GaN} is the real refractive index of GaN at the exciton region, e and m_e are the charge and mass of the electron, c is the velocity of light, $\hbar$ is the Planck's constant and d the thickness of the film. Basically, the term $\frac{\int OD(E)dE}{d}$ here equals to $\int \alpha(E)dE$. Therefore, to be able to perform the calculation based on the above relation, the absorption coefficient integral is estimated by fitting the A_{GaN}+B_{GaN} main GaN exciton peak showed in Figure 2.8(b) with two equal-weight Lorentzians, corresponding to the A_{GaN} and B_{GaN} excitons and distanced by 8 meV. Then, the oscillator strength per unit volume for the bulk GaN (A_{GaN}+B_{GaN}) exciton is then obtained to have the value of $8.5{\cdot}10^{19}$ cm^{-3}. As will be described later on, the same process is possible to be applied in QW-containing membranes where the appropriate understanding of the oscillator strength is critical for the simulation of polariton branches.

2.11 Conclusion

In summary, a new approach is established here for measuring absorption coefficients and exciton oscillator strengths in nitride films and heterostructures, circumventing possible substrate-related limitations such as low quality or even opacity. The method relies on accurate micro-transmittance measurements on ultra-smooth GaN-based membranes, which are detached following a highly selective lateral etching step with the use of the PEC method. Interference effects, which are crucial in these sub-wavelength structures, are explicitly taken into account in the simulations. It is demonstrated, thus, the importance of the optical artifacts induced by the standing wave effects in understanding absorption experiments performed in such ultra-thin films. As examples of the described methodology, we deduced here the room temperature absorption coefficient spectra and oscillator strength per unit volume at the A_{GaN}+B_{GaN} exciton peak of polar GaN films. Moreover, the optical density profile of GaN is evaluated at various T's by performing the corresponding μ-T measurements.

Bibliography

[1] J. Bhattacharyya, S. Ghosh, B. M. Arora, O. Brandt, and H. T. Grahn. *"Optical polarization properties of M-plane GaN films investigated by transmittance anisotropy spectroscopy"*, Appl. Phys. Lett. 91, 251913 (2007).

[2] S. W. King and M. Milosevic. *"A method to extract absorption coefficient of thin films from transmission spectra of the films on thick substrates"*, J. Appl. Phys. 111, 073109 (2012).

[3] R. Swanepoel. *"Determination of the thickness and optical constants of amorphous silicon"*, J. Phys. E: Sci. Instrum. 16, 1214 (1983).

[4] D. Poelman and P. F. Smet. *"Methods for the determination of the optical constants of thin films from single transmission measurements: a critical review"*, J. Phys. D: Appl. Phys. 36, 1850 (2003).

[5] J. C. Maxwell. *"A treatise on Electricity and Magnetism"*, Clarendon Press, (1873).

[6] O. Heaviside. *"Electrical Papers Vol. 1 and 2"*, Cambridge University Press, Cambridge, New York, Melbourne (1892).

[7] B. E. A. Saleh and M. C. Teich. *"Fundamentals of Photonics"*, Wiley, New York (1991).

[8] J. H. Poynting. *"On the transfer of energy in the electromagnetic field"*, Philos. Trans. R. Soc. Lond. 175, 343 (1884).

[9] N. Hodgson and H. Weber. *"Optical Resonators: Fundamentals, Advanced Concepts and Applications"*, Springer-Verlag Berlin Heidelgerg New York (1997).

[10] D. J. Griffiths. *"Introduction to Electrodynamics"*, Cambridge University Press (2017).

[11] J. I. Pankove. *"Optical Processes in Semiconductors"*, Englewood Cliffs, New Jersey, Prentice-Hall (1971).

[12] H. Amano, N. Watanabe, N. Koide, and I. Akasaki. *"Room-Temperature Low-Threshold SurfaceStimulated Emission by Optical Pumping from $Al_{0.1}Ga_{0.9}N/GaN$ Double Heterostructure"*, Jpn. J. Appl. Phys. 32, L1000 (1993).

[13] M. O. Manasreh. *"Optical absorption near the band edge in GaN grown by metalorganic chemical-vapor deposition"*, Phys. Rev. B 53, 16425 (1996).

[14] A. J. Fischer, W. Shan, J. J. Song, Y. C. Chang, R. Horning, and B. Goldenberg. *"Temperature-dependent absorption measurements of excitons in GaN epilayers"*, Appl. Phys. Lett. 71, 1981 (1997).

[15] J. F. Muth, J. H. Lee, I. K. Shmagin, R. M. Kolbas, H. C. Casey Jr., B. P. Keller, U. K. Mishra, and S. P. DenBaars. *"Absorption coefficient, energy gap, exciton binding energy, and recombination lifetime of GaN obtained from transmission measurements"*, Appl. Phys. Lett. 71, 2572 (1997).

[16] X. H. Wu, L. M. Brown, D. Kapolnek, S. Keller, B. Keller, S. P. DenBaars, and J. S. Speck. *"Defect structure of metal-organic chemical vapor deposition-grown epitaxial (0001) GaN/Al_2O_3"*, J. Appl. Phys. 80, 3228 (1996).

[17] S. Nakamura. *"The Roles of Structural Imperfections in InGaN-Based Blue Light-Emitting Diodes and Laser Diodes"*, Science 281, 956 (1998).

[18] A. Shikanai, T. Azuhata, T. Sota, S. Chichibu, A. Kuramata, K. Horino, and S. Nakamura. *"Biaxial strain dependence of exciton resonance energies in wurtzite GaN"*, J. Appl. Phys. 81, 417 (1997).

[19] E. Trichas, M. Kayambaki, E. Iliopoulos, N. T. Pelekanos, and P. G. Savvidis. *"Resonantly enhanced selective photochemical etching of GaN"*, Appl. Phys. Lett. 94, 173505 (2009).

[20] R. Jayaprakash, F. G. Kalaitzakis, M. Kayambaki, K. Tsagaraki, E. Monroy, and N. T. Pelekanos. *"Ultra-smooth GaN membranes by photo-electrochemical etching for photonic applications"*, J. Mater. Sci. 49, 4018 (2014).

[21] S. H. Park, G. Yuan, D. Chen, K. Xiong, J. Song, B. Leung, and J. Han. *"Wide Bandgap III-Nitride Nanomembranes for Optoelectronic Applications"*, Nano Lett. 14, 4293 (2014).

[22] K. Xiong, S. H. Park, J. Song, G. Yuan, D. Chen, B. Leung, and J. Han. *"Single Crystal Gallium Nitride Nanomembrane Photoconductor and Field Effect Transistor"*, Adv. Funct. Mater. 24, 6503 (2014).

[23] D. Chen and J. Han. *"High reflectance membrane-based distributed Bragg reflectors for GaN photonics"*, Phys. Lett. 101, 221104 (2012).

[24] Y. Mei, D. J. Thurmer, C. Deneke, S. Kiravittaya, Y.-F. Chen, A. Dadgar, F. Bertram, B. Bastek, A. Krost, J. Christen, T. Reindl, M. Stoffel, E. Coric, and O. G. Schmidt. *"Fabrication, Self-Assembly, and Properties of Ultrathin AlN/GaN Porous Crystalline Nanomembranes: Tubes, Spirals, and Curved Sheets"*, ACS Nano 3, 1663 (2009).

[25] J. Wang, E. Song, C. Yang, L. Zheng, and Y. Mei. *"Fabrication and whispering gallery resonance of self-rolled up gallium nitride microcavities"*, Thin Solid Films 627, 77 (2017).

[26] S. A. Kazazis, E. Papadomanolaki, M. Androulidaki, M. Kayambaki, and E. Iliopoulos. *"Optical properties of InGaN thin films in the entire composition range"*, J. Appl. Phys. 123, 125101 (2018).

[27] K. Kornitzer, T. Ebner, K. Thonke, R. Sauer, C. Kirchner, V. Schwegler, M. Kamp, M. Leszczynski, I. Grzegory, and S. Porowski. *"Photoluminescence and reflectance spectroscopy of excitonic transitions in high-quality homoepitaxial GaN films"*, Phys. Rev. B 60, 1471 (1999).

[28] R. Jayaprakash, D. Ajagunna, S. Germanis, M. Androulidaki, K. Tsagaraki, A. Georgakilas, and N. T. Pelekanos. *"Extraction of absorption coefficients from as-grown GaN nanowires on opaque substrates using all-optical method"*, Opt. Express 22, 19555 (2014).

[29] L. A. Coldren and S. W. Corzine. *"Diode Lasers and Photonic Integrated Circuits"*, Wiley-Interscience (1995).

[30] K. Ohta and H. Ishida. *"Matrix formalism for calculation of the light beam intensity in stratified multilayered films, and its use in the analysis of emission spectra"*, Appl. Opt. 29, 2466 (1990).

[31] K. Ohta and H. Ishida. *"Matrix formalism for calculation of electric field intensity of light in stratified multilayered films"*, Appl. Opt. 29, 1952 (1990).

[32] B. Monemar, J. P. Bergman, I. A. Buyanova, W. Li, H. Amano, and I. Akasaki. *"Free Excitons in GaN"*, MRS Internet J. Nitride Semicond. Res. 1, e2 (1996).

[33] S. Chichibu, H. Okumura, S. Nakamura, G. Feuillet, T. Azuhata, T. Sota, and S. Yoshida. *"Exciton spectra of Cubic and Hexagonal GaN Epitaxial Films"*, Jpn. J. Appl. Phys. 36, 1976 (1997).

[34] Y. Yamamoto, F. Tassone, and H. Cao. *"Semiconductor Cavity Quantum Electrodynamics"*, Springer (2010).

Chapter 3

Strong coupling in polar GaN/AlGaN microcavities

This chapter demonstrates the fabrication process to realize a semiconductor microcavity, by utilizing a polar GaN-based membrane with embedded few or many GaN/AlGaN QWs as the active material in between two dielectric DBR mirrors, for the successful operation in the strong coupling regime at room temperature conditions. Furthermore, in the produced membranes, it was possible to extract the optical density, and thus the oscillator strength of the QW-excitons.

3.1 Introduction

The GaN semiconductor system is considered to be ideal for the fabrication of robust polaritonic devices, as it combines a mature technological platform with the large exciton oscillator strengths of nitrides, leading to devices with enhanced strong-coupling characteristics at ambient conditions. Up to now, several nitride polariton devices operating at 300 K have been demonstrated with predominant realization the polariton lasing emission [1–4]. From these results, it has become clear that a key issue in developing an optimized GaN polariton device is how to enclose a high quality active medium in between efficient top / bottom distributed Bragg reflectors (DBRs). Several pioneer works in the field reported nitride microcavities with all-dielectric DBRs following separation of the initial as-grown template, using either laser lift-off [5,6] or etching of an InAlN sacrificial layer [7]. Other realizations that relied on direct growth of the active medium on highly mismatched silicon substrates [8], or on strongly disordered AlInN/AlGaN DBRs [9] were limited by the moderate optical quality of the active layers. Recently, our group demonstrated an alternative approach to fabricate a GaN polariton laser with remarkably low threshold. The latter was achieved in

a microcavity made by an ultra-smooth GaN-based membrane embedded in between two dielectric DBR reflectors [10]. This significant achievement is believed to play a key role in making ultra-efficient and high optical quality microcavity devices.

3.2 Innovations regarding this work

Compared to the earlier work, a number of improvements are reported in this thesis in the design and fabrication of an all-dielectric polariton structure. First, an alternative membrane design is developed that enhances strong coupling by increasing the number of active GaN/AlGaN QWs in the whole membrane region. Previous microcavity fabrication involved a membrane containing $\times 33$ $GaN/Al_{0.05}Ga_{0.95}N$ (2.7 nm/2.7 nm) QWs with a 25-nm-thick GaN spacer, where the latter was found to participate in the strong coupling. Second, in order to reduce the threshold power density for polariton lasing, structures with QWs only at the two antinodes of the electric field in the $3\lambda_o/2$n cavity, have been fabricated where λ_o is the emission wavelength and n is the effective refractive index of the cavity. Third, a dry transfer method of the etched membranes was utilized during the fabrication process, to eliminate any residual absorption related to transfer residues in the earlier used wet transfer of membranes. Fourth, to minimize strain effects during the e-beam deposition of the top DBR, the total number of SiO_2/Ta_2O_5 layers was limited to only four pairs. In the earlier work, the top-mirror of the cavity was a 10-pair HfO_2/Al_2O_3 DBR deposited by Atomic Layer Deposition (ALD). In general, ALD technique minimizes thermal strain in the deposited layers but the growth rates are very low for the specific application. Finally, due to the novel design and successful membrane fabrication, μ-T experiments on such QW-containing membranes transferred onto double-side polished Sapphire substrates allowed to extract the optical density, and hence, the exciton oscillator strength in $GaN/Al_{0.07}Ga_{0.93}N$ QWs, by following the methodology of Chapter 2.

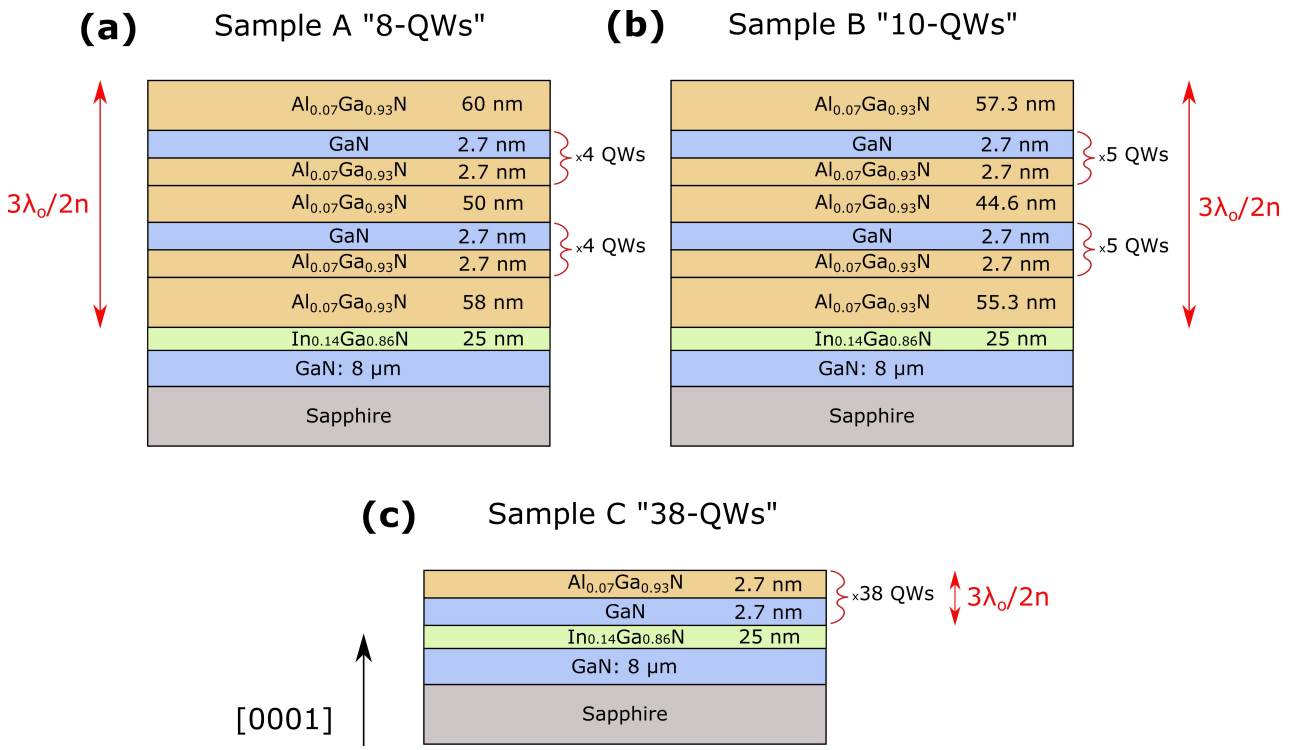

Figure 3.1: Illustration depicting the sample design along [0001]-orientation consisting of (a) "8 QWs", (b) "10 QWs" at the antinodes of the electric field and (c) "38 QWs" in the whole range of the active region. InGaN is utilized as sacrificial layer to release the designed $3\lambda_o/2n$ structures after PEC-etching in a membrane form.

3.3 Design and fabrication of c-plane GaN/AlGaN QWs

For the design of the active region, the transfer matrix model (see Appendix B) was utilized to simulate the structure layers for the maximum absorption, and thus coupling with light, accounting for the standing wave effect within the membranes similar to the theory discussed in Chapter 2. In the particular simulation, only the real part of the refractive index of the materials is taken into account, ignoring absorption at this stage. The cavity region is designed to have an approximately 200-nm-thick QW-containing active layer, which constitutes a $3\lambda_o/2n$ structure, satisfying thus the standing wave principle for maximum absorption and having a cavity mode close to the QW-exciton state which is near 360 nm (3.4440 eV) at room temperature. Thinner membranes fulfilling the same condition ($\lambda_o/2n$ or λ_o/n), as discussed in Chapter 2, can be in principle also fabricated but they will not be mechanically stable. In a first (A) and second (B) sample, as depicted in Figure 3.1(a-b), the active layer consists of $Al_{0.07}Ga_{0.93}N$,

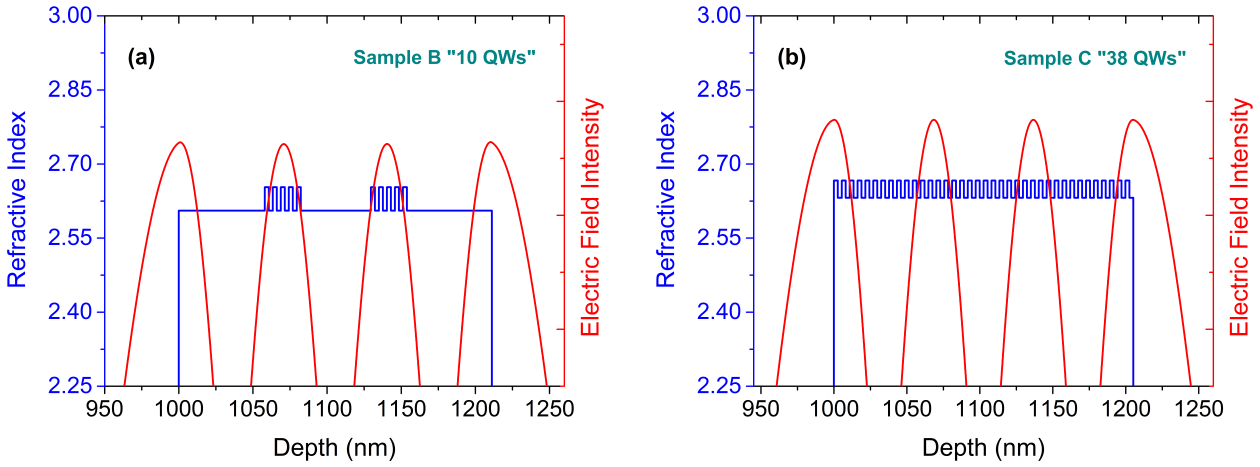

Figure 3.2: Refractive index and electric field intensity profile in a microcavity with (a) "10 QWs" located at the two antinodes and (b) "38 QWs" spanned in the whole range of the membrane layer. (The two DBR mirrors are not shown).

containing "8" and "10" GaN/$Al_{0.07}Ga_{0.93}N$ ($2.7nm/2.7nm$) QWs, respectively, centered at the two antinodes of the electric field intensity inside the $3\lambda_o/2n$ cavity. The simulated field intensity profile for the "10 QW" sample is depicted in Figure 3.2(a). In a third (C) sample, as presented in Figure 3.1(c), the active region consists of "38" $GaN/Al_{0.07}Ga_{0.93}N$ ($2.7nm/2.7nm$) QWs, spanning the whole $3\lambda_o/2n$ active region. As illustrated in Figure 3.2(b), the field intensity in this case does not couple with all the QWs but only with those that overlap with the antinodes of the electric field. However, in this particular configuration, if the two fabricated mirrors are not designed correctly at the desired operating wavelength or there is a non-negligible deviation in the thickness of the produced membrane, affecting again the position of the cavity mode, the field will always be able to find QWs to couple. On the other hand, the "absorption strength" will be weakened or enhanced depending on the standing wave condition as already explained. Experimentally, the mentioned deviations can arise at the fabrication stage where there is a difficulty in obtaining the exact nominal thicknesses. As a result, a careful control and feedback at every stage is important for the best outcome. As depicted in Figure 3.2, due to a small shift in the average refractive index [11, 30], the active region thickness varies slightly in the two designs.

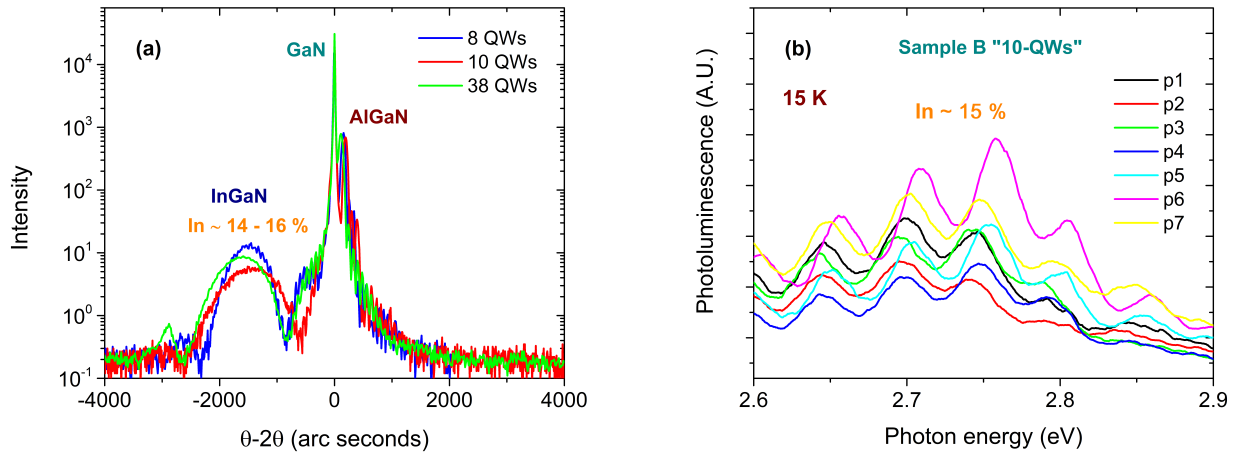

Figure 3.3: (a) XDR as acquired from all the three samples (b) PL emission from the "10 QW" sample at the InGaN spectral region.

Regarding the QW-fabrication, the GaN/AlGaN samples were grown by plasma-assisted molecular beam epitaxy on commercial 8-μm-thick n-type c-axis GaN/Al_2O_3 templates, along the [0001] crystallographic direction of the wurtzite structure. In this polar orientation, the structures inherit polarization induced build-in fields across the quantum wells, leading to a reduced electron-hole wavefunction overlap due to band-bending (Stark Effect) which increases the probability of exciton dissociation (Section 1.3). For these reasons, in the specific growth orientation ([0001]), thin quantum wells ($\approx$ 2.6 nm [12,13]) are necessary to balance the influence of the Stark effect, while preserving a PL above the bandgap of GaN with a reduced inhomogeneous broadening. An additional hint in favor of thin QWs is the observation of polariton lasing with even thinner QWs, reported in [2]. Moreover, despite their low Aluminum concentration (7 %), the AlGaN material provides sufficiently high energy barriers, which are in the range of 100 meV in our samples, as will be independently deduced later on by temperature-dependent photoluminescence spectra. Last but not least, as presented in Figure 3.1, for the needs of PEC-etching the active region is separated from the GaN/Al_2O_3 template by a 25-nm-thick $InGaN$ sacrificial layer, whose thickness and 14 - 16 % In-composition was independently confirmed by X-ray diffraction (XRD) in a θ-2θ scan Figure 3.3(a). Furthermore, a PL

mapping at the InGaN emission region is performed to verify the In-content in combination with the XRD measurements. An example for the sample with "10-QWs" is given in Figure 3.3(b) where the seven spots under illumination were distanced less than 0.5 cm. The emission of InGaN is mainly at 2.755 eV (450 nm) indicating an In composition of around 15 %. Again, as in the bulk GaN samples, these values are satisfying the criteria for the PEC-etching method ($E_{InGaN} < E_{laser} = 3.061$ eV at 405 nm). It should be noted here that InGaN's optical and morphological quality are very important for efficient membrane separation with ultra-smooth surfaces when applying the PEC-etching approach.

3.4 Optical properties in few and multiple QWs

Prior to any processing, apart from XRD, all the samples are optically characterized by photoluminescence (PL) and reflectance (RFL) as a function of temperature to assess the intrinsic properties of the produced QWs. In Figure 3.4(a-b) are given the combined PL and RFL spectra at 15 K for the "10" and "38" QWs samples. The sample with "8 QWs" had similar behavior with the "10 QWs" therefore its spectra are not shown here. As concerns the "10 QW" sample, apart from the localized QW-exciton (L_{QW}) emission at 3.5045 eV, it exhibits an additional PL peak at 3.6131 eV originating from localized excitons in the AlGaN barrier (L_{AlGaN}), which occupies most of the active region. The energy difference between the two PL peaks gives a barrier height of 110 meV, which is distributed in part in the conduction and the valence band (Figure 1.2(c)). By taking into account the RFL spectra and considering a localization energy of 15.7 meV according to Figure 3.4(c), the A_{QW} exciton is positioned at 3.5202 eV while B_{QW} at 3.5315 eV, having thus an energy difference of 11.3 meV. As concerns the C_{QW}, based on RFL it is positioned at 3.5493 eV, which is 29 meV above the A_{QW} exciton position. Furthermore, the AlGaN exciton (X_{AlGaN}) is located at about 3.63 eV in the RFL spectrum. On the other hand, in the multi-QW sample, there is no visible PL contribution from the AlGaN barriers

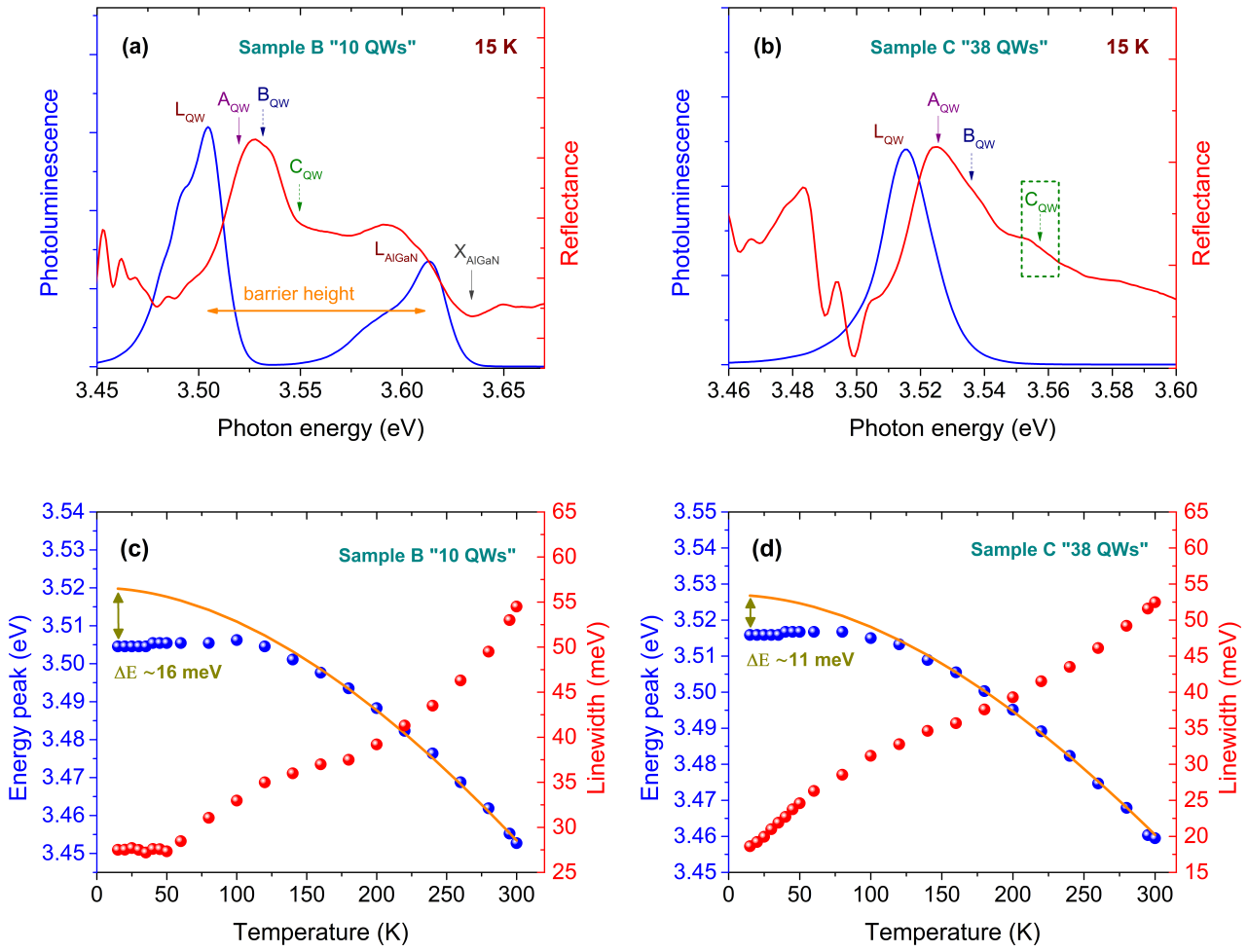

Figure 3.4: PL and RFL of as-grown structures with (a) few (×10) and (b) multi (×38) GaN/AlGaN QWs at the temperature of 15 K. Energy peak along with PL linewidth versus temperature for (c) the ×10 QWs and (d) the ×38 QWs. The orange curves in the graphs are obtained based on the Varshni model.

due to the superlattice structure. In the latter sample, the strong emission comes again from localized exciton states (L_{QW}) centered at 3.5150 eV, while based on a localization energy of 10.7 meV from Figure 3.4(d), the main A_{QW} and B_{QW} excitons are positioned at 3.5255 eV and 3.5360 eV, respectively, in the RFL spectrum of Figure 3.4(b). The energy difference between the latter two values is 10.5 meV which is again consistent for this system. Even thought not visible, the C_{QW} is considered to be within the dashed-square in Figure 3.4(d).

As already discussed, in the low temperature regime, the PL emission is dominated by localized excitons in regional potential traps arising from quantum well thickness and/or alloy fluctuations. This is a known effect in semiconductors

[14] and in order to verify it, the standard method is to plot the PL energy peak value (Figures 3.5(a-b)) as a function of temperature (T), where an "S-shape" (red-blue-red-shift) behavior is extracted as presented in Figures 3.4(c-d) for the two cases. The meaning of the S-like behavior is that there are potential minima from which carriers, as the temperature rises, are gradually delocalized into the free exciton states of the quantum well, resulting thus in a blueshifted PL emission. Due to the temperature-induced shrinkage of the bandgap, the photoluminescence peak redshifts again at elevated temperatures. The values of the PL energy peak are fitted with the Varshni model (Equation 1.2) [15]. Extrapolating for the "10 QW" sample the Varshni curve at low T's (orange curve in Figure 3.4(c)), we obtain a free-exciton bandgap energy at zero Kelvin (Eg(0K)) of 3.520 eV, while the corresponding α and β Varshni parameters are 0.88 meV/K and 890 K, respectively. Moreover, at low temperatures there is a localization energy of around 16 meV. Regarding the fitting of the "38-QW" sample (orange curve in Figure 3.4(d)), the model gives an Eg(0K) of 3.527 eV, while α and β remained the same. Concerning the localization energy here is found to be near 11 meV. The Varshni-fitting parameters are in very good agreement with the ones for bulk GaN in [16]. By comparing the Varshni curves with the PL peak energies, we see that there is significant deviation below about 100 ± 20 K, implying that above 100 K the PL emission is essentially due to "delocalized" excitons, while below 100 K we are in the localized exciton regime.

Furthermore, in the same plots for each sample, we give the FWHM of the PL emission (Figures 3.5(a-b)) as a function of temperature. Below the temperature of 100 K, we distinguish two different cases. Regarding the "10 QWs", from 15 K up to 50 K, the FWHM linewidth remains constant at 27.5 meV, while in the range between 50 K and 100 K, there is a linear-like increase in the linewidth up to 35 meV as we pass from the localized to the delocalized exciton emission. On the other hand, for the "38 QWs", where the low-T linewidth is only 18.6 meV, the linewidth increases continuously between 0 and 100 K, reaching a value of very close to 35 meV at 100 K, as in the "10-QW"

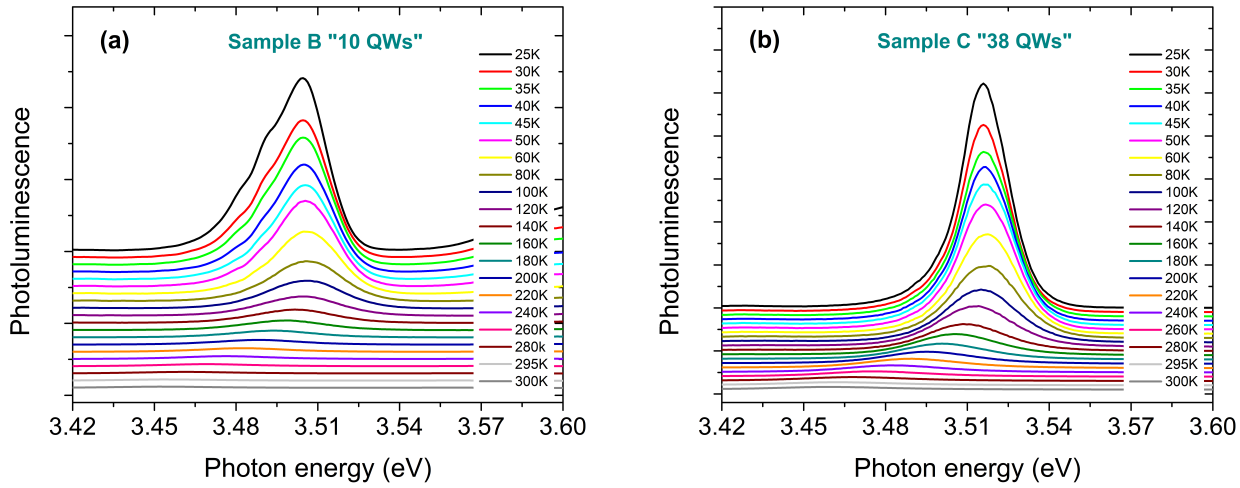

Figure 3.5: Photoluminescence at the exciton region for the temperatures 25 - 300 K of (a) the "10 QWs" and (b) the "38-QWs".

sample. After the temperature of 100 K up to ambient, we observe in both samples the phonon-assisted broadening in the PL emission, characterized by a linear acoustic-phonon term and by an exponential-like LO-phonon term [17], contributing homogeneously to the linewidth. As shown in Figures 3.4(c-d), both of the as-grown structures were found to have a similar FWHM at room temperatures of about 55 meV. It should be noted that this PL linewidth contains contributions from all A, B, and C excitons of the QWs. Figure 3.5 illustrates the PL emission of the QW-excitons in the few- and multi-QWs from cryogenic up to room temperature. The particular set of data were utilized to deduce the values given in Figures 3.4(c-d). Comparing the two graphs, it can be observed that as the temperature increases the photoluminescence is quenched much faster in the case of the few QWs. Regarding the FWHM, it is obvious that in the "38 QWs" the emission is narrower at low temperatures demonstrating the low inhomogeneity in the specific sample.

3.5 Time-resolved photoluminescence in polar QWs

An additional characterization of the as-grown samples was performed by time-resolved photoluminescence (TRPL) (Appendix D), which gives us the

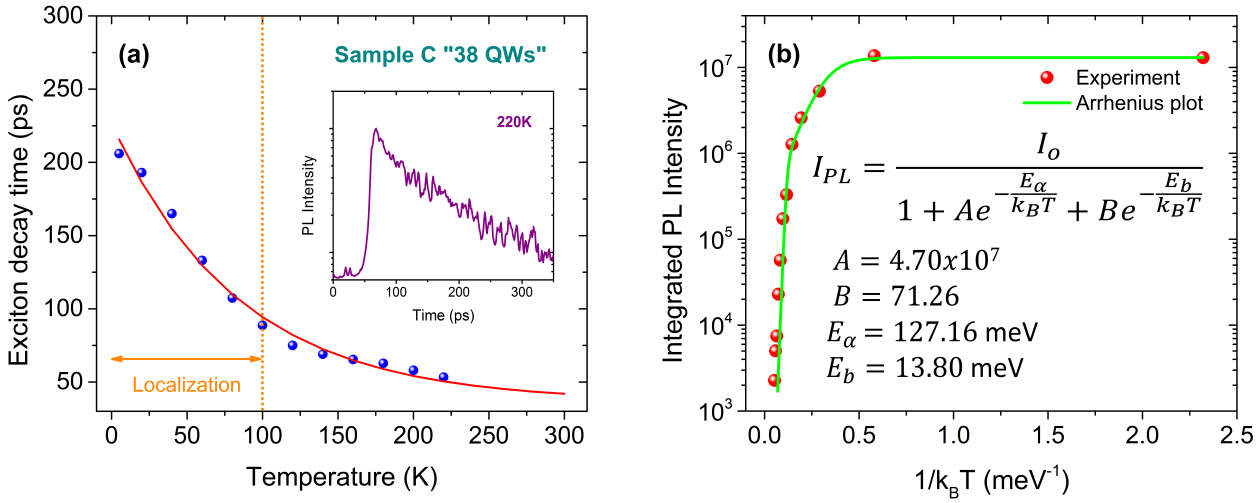

Figure 3.6: (a) Exciton decay times extracted from the time-resolved PL measurements as a function of temperature (the inset graph shows the recorded TRPL data at 220 K) and (b) the integrated PL emission versus $1/k_BT$ for the 38 GaN/AlGaN QWs.

lifetime of the QW-excitons as a function of the temperature. The PL signal from the "few-QW" samples decreased rapidly with temperature and for this reason only the TRPL results for the "multi-QW" sample are presented here, which exhibited enhanced emission but we followed up to 220 K. The deduced exciton decays based on the recorded TRPL spectra are depicted in Figure 3.6(a). Initially, at the temperature of 5 K, there is an exciton decay time of around 206 ps, but as the temperature increases there is a strong reduction reaching a decay time of 53 ps at 220 K, highlighting the significant contribution of non-radiative channels in this sample, already at cryogenic temperatures. By fitting the time decays with an exponential curve and extrapolating up to RT (red line), we obtain an exciton lifetime of about 42 ps at 300 K. The inset image shows the PL decay curve at 220 K. In Figure 3.6(b), an Arrhenious plot is presented of the integrated PL versus $1/k_BT$. From the graph, it follows that the PL emission has fallen approximately 4 orders of magnitude already at 220 K. A way to extract valuable information about the non-radiative mechanisms is by fitting the data with an Arrhenius curve. Here, two activation energies were considered, for which the model gives an activation energy of $E_\alpha = 127.16$ meV and another of $E_b = 13.80$ meV. It can be seen that the first value is very close to the bandgap

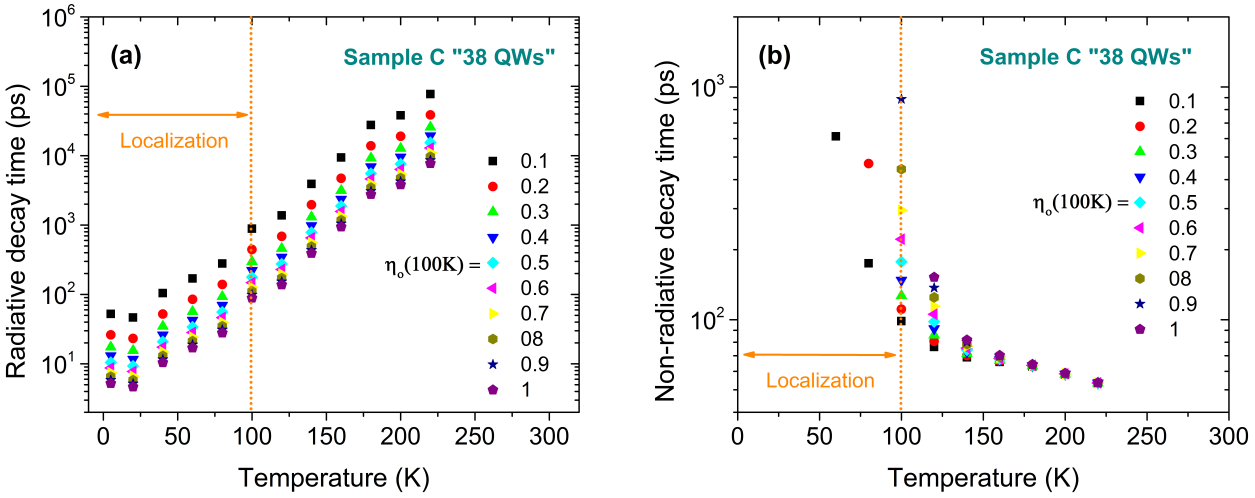

Figure 3.7: The deduced (a) radiative and (b) non-radiative decay times versus temperature for the 38 GaN/AlGaN QWs. The orange dashed line indicated the 100 K temperature for which the integrated PL value utilized instead of the one at 5 K.

difference between GaN and AlGaN barrier while the second agrees well with the localization energy as determined by the S-like behavior in Figure 3.4(d).

By analyzing the recorded exciton decay times of Figure 3.6(a) into the radiative and non-radiative components according to reference [18], we obtained the values presented in Figure 3.7. In the model, we use as an adjustable parameter the radiative efficiency (n_o) at 100 K, since the excitons have complete delocalization at this temperature (Figure 3.4(d)) and have become free-excitons (orange dashed line in Figure 3.6(a)). In our estimates of τ_r and τ_{nr}, the values for the radiative efficiency at 100 K ($\eta_o(100K)$) were ranging from 0.1 up to 1. As depicted in Figure 3.7, the exciton radiative decay time at 220 K reaches an average value of around 15.5 ns for $\eta_o(100K) = 0.5$, while the non-radiative decay converges at 53 ps in all cases. Regarding the latter, along with the fitting showed in Figure 3.6(a), we can safely assume that at RT the exciton decay is dominated by non-radiative channels with a lifetime of 42 ps, which is relatively low compared to previously studied samples [10], where we have measured τ_{nr} at RT close to 275 ps. In general, high exciton decay times are desired at RT, illustrating the high quality of the device due to suppression of the non-radiative channels.

3.6 Bottom and top DBR mirror design

For the growth of the DBR mirrors in this work, we decided to turn our attention to the electron-gun deposition, which was found to provide good quality dielectric mirrors for our purposes. The design of the two mirrors is based on the alternating pairs of Silicon Dioxide (SiO_2) and Tantalum Pentoxide (Ta_2O_5). These two oxides represent the low and high refractive index materials, exhibiting a remarkable refractive index-contrast, in comparison to nitride-based DBR layers [19], necessary for the fabrication of highly reflective DBR mirrors with reduced number of pairs. In particular, several demonstrations by other groups [20–22] have shown that the specific pair is one of the best for applications in the ultra-violet (UV) wavelength region, similar to this work. To characterize the oxide layers by spectroscopic ellipsometry (SE) and atomic force microscopy (AFM), 200-nm-thick SiO_2 and Ta_2O_5 layers were evaporated on Si substrates at 150 $^{\circ}C$ and 300 $^{\circ}C$. During deposition, an oxygen flow was continuously supplied at a rate of approximately 2 sccm, while the pressure in the chamber was around $5{\cdot}10^{-4}$ mbar. For SiO_2 and Ta_2O_5, the deposition rates were 5 $\mathring{A}$/s and 1 $\mathring{A}$/s, respectively. The surface morphology of the films deposited at 300 $^{\circ}C$ revealed a root-mean-square (RMS) roughness of 0.85 nm for SiO_2 and 1.23 nm for Ta_2O_5, measured by AFM over an area of 4 μm x 4 μm. For the films deposited at 150 $^{\circ}C$, the corresponding values for a 3 μm x 3 μm area were 0.79 nm for SiO_2 and 0.88 nm for Ta_2O_5. These low values of RMS roughness, independent of the deposition temperature, are important to reduce the light scattering losses at the surface and interfaces of the DBR layers.

Measuring accurately the refractive indices of our oxides is vital for an optimal design of the DBR mirrors and a reliable simulation of the photonic devices. Thus, spectroscopic ellipsometry measurements were performed on each oxide layer in order to extract their refractive indices, as depicted in Figure 3.8. By inspection, the investigated oxides presented a compelling refractive index difference of 0.85 (or $\Delta n/n \approx 0.37$) near the GaN exciton gap, making

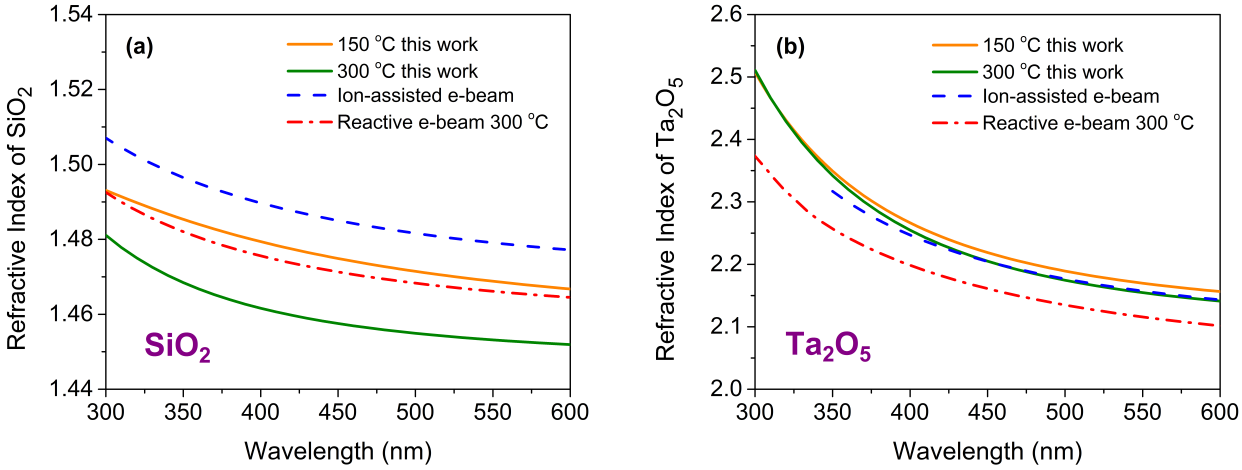

Figure 3.8: Ellipsometric data of the refractive index of (a) SiO_2 and (b) Ta_2O_5, deposited by electron beam evaporation at 150°C and 300°C (solid curves) along with values reported in the literature (dashed and dot-dashed curves) [23–25].

them excellent candidates for efficient DBR mirrors in GaN-based VCSEL and polariton devices. Moreover, the refractive indices of SiO_2 and Ta_2O_5 fabricated by ion-assisted electron-beam deposition [23, 24] or by reactive electron-beam evaporation at 300 °C [25], are also shown for comparison. The relatively small dissimilarity between the data reported here and the above works is likely due to differences in the deposition conditions. From the data of Figure 3.8, it is possible to derive the respective Sellmeier relations (Appendix A), describing the wavelength dispersion of the oxides, which were utilized in the reflectivity calculations of the bottom / top DBRs and for the complete microcavity with the use of a transfer matrix model (details in Appendix B). By performing the calculation of $\lambda/4n$, the quarter wave thicknesses of the two alternating oxide layers, in order to have a high reflectivity at the GaN/AlGaN QW-exciton position at RT ($\sim$ 360 nm), should be in the range of 60-nm-thick for the SiO_2 and 40-nm-thick for the Ta_2O_5, respectively.

In Figure 3.9, are presented the simulated reflectance spectra for different number of SiO_2/Ta_2O_5 pairs for (a) a bottom and (b) a top DBR mirror on an Si template. The calculations were based on the previously referred thicknesses for the two oxides. For the simulation with the transfer matrix model of the bottom

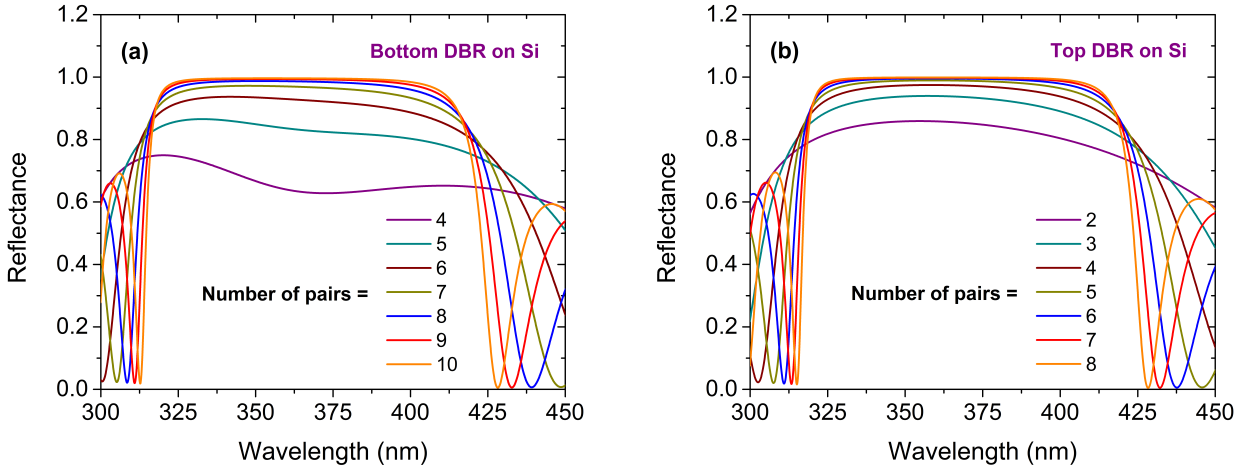

Figure 3.9: Simulation of reflectance for a various number of alternating pairs for (a) a bottom and (b) a top DBR mirror on Si template with thicknesses $t_{SiO_2} = 60$ nm and $t_{Ta_2O_5} = 40$ nm, considering the refractive indices of the oxides at the deposition temperature of 300 $^{\circ}C$ for the bottom mirror and 150 $^{\circ}C$ for the top mirror.

mirror we utilized the refractive indices of oxides at the deposition temperature of 300 $^{\circ}C$, while for the top mirror the ones at 150 $^{\circ}C$. In the first graph, it can be seen that with 10 alternating pairs in the bottom mirror the reflectance can reach unity, while having a remarkably large stopband of 110 nm. As concerns the top mirror in the second plot, it can be observed that only 4 pairs are enough to obtain a considerably high reflectivity (above 97 %) and a stopband of around 130 nm. Utilization of a lower deposition temperature in the top mirror is important in occasions similar to this research where the thermally-induced strain effects in the produced microcavities need to be kept at minimum levels. On the other side, the use of lattice-matched nitride-based mirrors gives less than 50 nm stopbands [19], making thus the nitride-pairs non-ideal for strong coupling observation where the upper and lower polariton branch range is comparable, or even larger, to that of the stopband range.

To confirm the theoretically predicted spectra with the experimental ones, we fabricated a 10-pair bottom DBR at 300 $^{\circ}C$ and a 4-pair top DBR at 150 $^{\circ}C$ on Si substrate. As explained, the use of a lower deposition temperature in the top DBR mirror was applied to induce less thermal strain in the deposited layers, since final goal is to be deposited on top of the produced subwavelength-thick

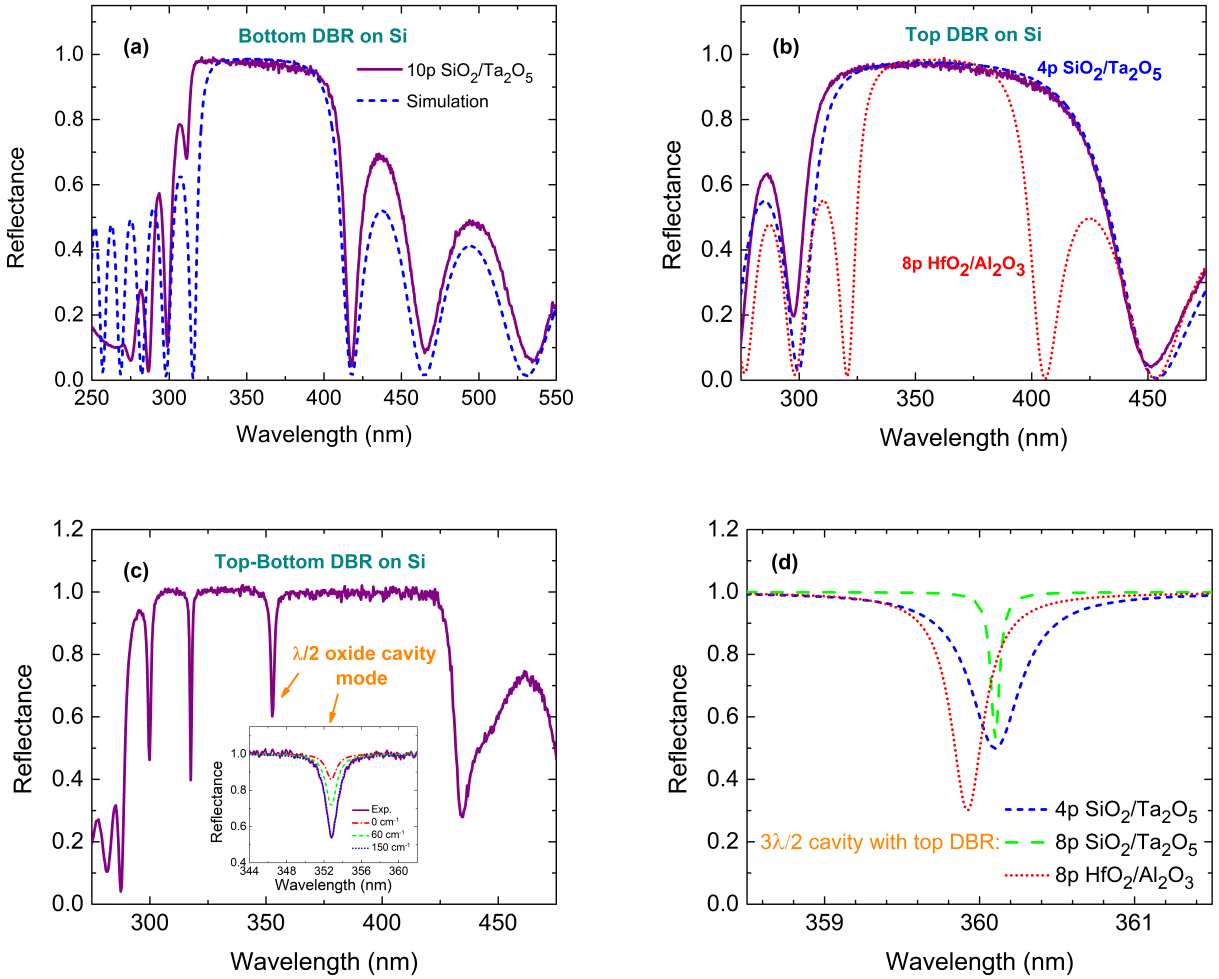

Figure 3.10: Experimental reflectance along with the simulated curve for a (a) 10-pair bottom and (b) 4-pair top DBR mirror on Si template. The simulated curve for an 8-pair HfO_2/Al_2O_3 top DBR is also shown in (b). (c) Experimental reflectance from a $\lambda/2$ oxide cavity along with theoretical curves. (d) Simulated cavity modes for a variety of top DBRs, for a $3\lambda/2$ QW-containing cavity with a 10-pair SiO_2/Ta_2O_5 as bottom DBR.

membranes. Depositing at higher temperature, the larger values of thermal strain can induce severe damage in the membranes, thwarting the formation of a fully-operational microcavity device. Figure 3.10(a) depicts the reflectance spectrum of a 10-pair SiO_2/Ta_2O_5 bottom DBR while Figure 3.10(b) of a 4-pair SiO_2/Ta_2O_5 top DBR deposited on Si. Both reflectance values seem to be in excellent agreement with the theoretically predicted spectra, as indicated by the dashed curves in each mirror. Moreover, in Figure 3.10(b), the simulated reflectance (dotted) curve of an 8-pair HfO_2/Al_2O_3 ($\Delta n/n \approx 0.19$ [26, 27]) top DBR mirror is also shown for comparison, confirming our initial statement that

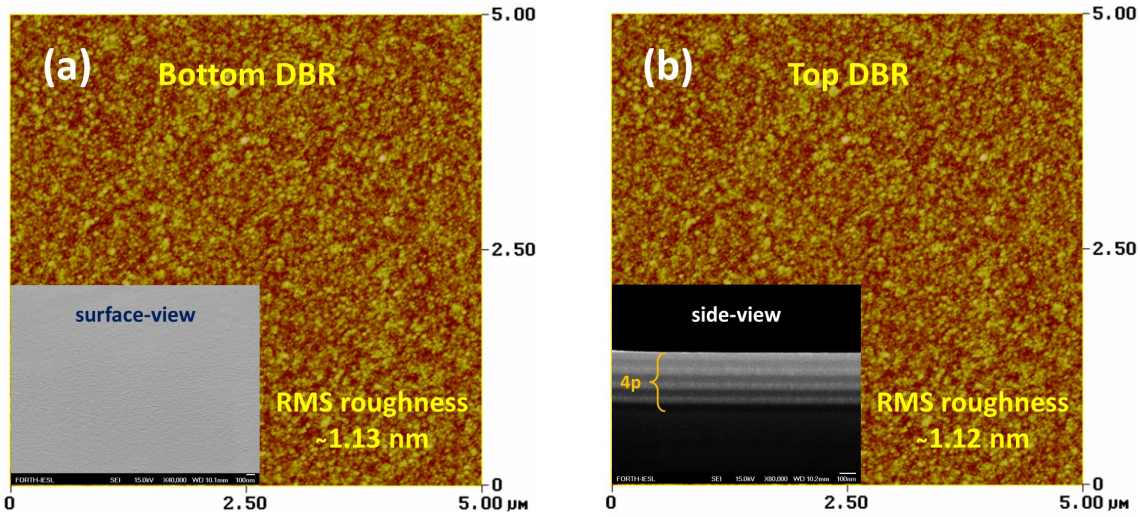

Figure 3.11: AFM images of a (a) bottom and a (b) top DBR deposited on Si substrate. The low values in RMS roughness illustrate a sufficient morphology for microcavity fabrication. The inset SEM images show (a) the surface of the bottom DBR while (b) the cross-section of the top DBR.

with the SiO_2/Ta_2O_5 system it is feasible to produce highly performing mirrors with a much smaller number of periods. Figure 3.10(c) presents a cavity mode obtained from a realized oxide $\lambda/2$ cavity (only top and bottom mirrors) along with the simulated curves. The oxide cavity was found to exhibit a Q-factor ($= \frac{\lambda}{\Delta\lambda}$) ~ 220, which is close to the theoretical value with zero losses $Q_{theor} \sim 260$.

The feasibility of having a pronounced cavity mode in a complete $3\lambda/2$ structure is further illustrated in Figure 3.10(d), where we compare the simulated cavity modes of "empty" microcavities, centered at 360 nm (λ_o), which are formed by combining different top DBRs with a $3\lambda/2$-cavity consisting of nitride QWs, along with a 10-pair SiO_2/Ta_2O_5 bottom DBR. From the graph, it is observed that the 4-pair SiO_2/Ta_2O_5 top DBR gives a Q-factor for the cavity mode close to 1000, which is comparable to that of the 8-pair HfO_2/Al_2O_3 DBR ($Q \approx 1400$). Even though, the 8-pair SiO_2/Ta_2O_5 top DBR can provide much higher Q-factors up to 5400, the large thermal strains were found to induce curving and damage in the fabricated microcavity devices. By considering the value of $Q = 1000$ and the relation $\tau_{cav} = \frac{Q\lambda_o}{2\pi c}$ we obtain a cavity lifetime of 0.2 ps. In addition, based on Equation 1.16, the effective length of a SiO_2/Ta_2O_5 top DBR mirror (L_{eff}^{top}) is 140 nm, while for a SiO_2/Ta_2O_5 bottom DBR (L_{eff}^{bottom}),

137 nm. These values correspond to a thickness which is almost one and a half alternating pairs ($L_{1-pair} \approx 100$ nm). Therefore, the overall effective cavity thickness (Equation 1.15) seems to be in the range of 480 nm. The AFM images presented in Figure 3.11 were acquired from the surface of a 10-pair bottom and a 4-pair top DBR mirror on Si and revealed an RMS roughness of 1.12 - 1.13 nm oven an area of 5 μm x 5 μm, which is a sufficient surface morphology for our microcavity needs. In the inset of Figure 3.11(a), it is given the SEM image of the mirror surface, while in the inset of Figure 3.11(b), the one acquired from the side, illustrating clearly the formation of the oxide layers on top of the Si substrate.

3.7 Fabrication of polar GaN/AlGaN membranes

Regarding the membrane separation, the as-grown samples were patterned into 1-μm-deep square mesas with various dimensions, from 45 μm x 45 μm up to 155 μm x 155 μm, using optical lithography and reactive ion etching similar to bulk GaN, in order to expose the lateral facets. The next step, as illustrated in Figure 3.12(a) for the sample with the "38-QWs", is the PEC-etching which was performed under steady state illumination by 3.5 mW of a 405-nm diode laser incident on the sample's front surface, along with an applied reverse-bias of 3.5 V. The total exposure time here for sufficient etching was approximately 40 minutes. Afterwards, the PEC-etched region was cleaned with deionized (DI) water and, the produced free-standing QW-containing membranes depicted in Figure 3.12(b), were then transferred individually with the use of a probe station, either on double-side-polished Sapphire template for optical characterization or on a bottom 10-pair SiO_2/Ta_2O_5 DBR deposited on a Si substrate (inset of Figure 3.12(b) and Figure 3.12(c)), as a first step for the fabrication of the complete microcavity.

In the optical and SEM images one can see the uniform separation of membranes, which can reach a lateral size up to 155 μm x 155 μm, illustrating the

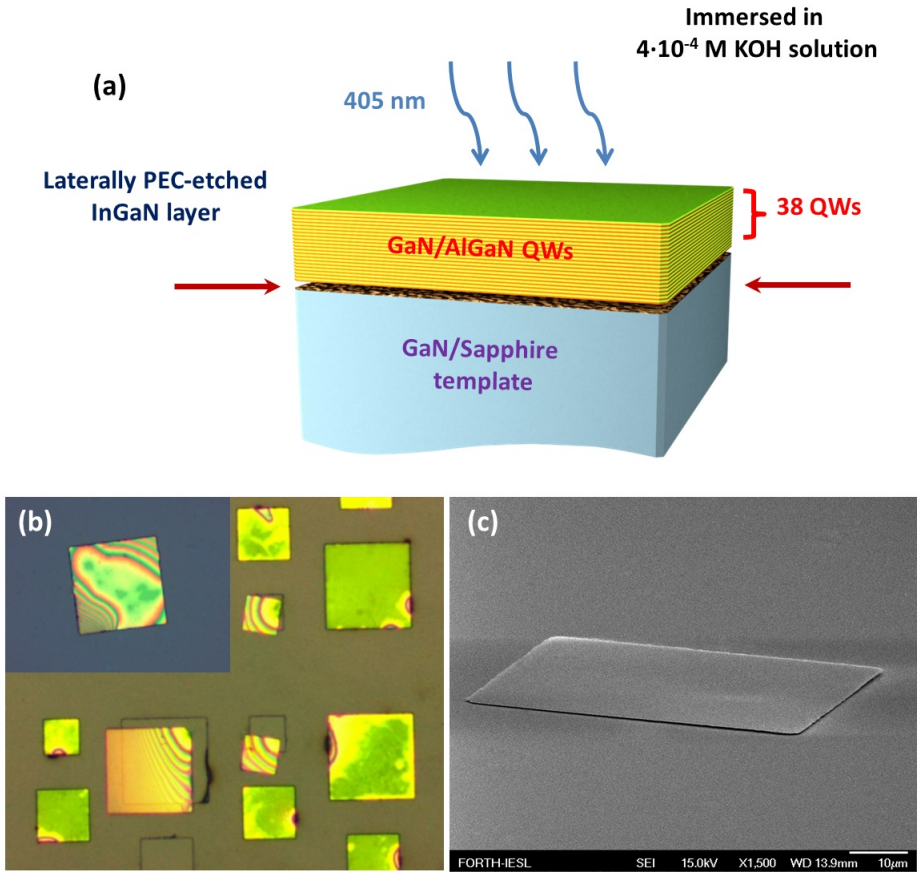

Figure 3.12: (a) Schematic of the PEC-etching method for the sample with "38 QWs". (b) Optical microscope image of the PEC-etched region with membranes varying from 45×45 μm^2 up to 155×155 μm^2. The inset shows a 38-QW-containing membrane transferred on a bottom-DBR/Si substrate. (c) SEM image of a similar transferred membrane on a bottom-DBR/Si substrate.

ability of the PEC-etching technique to produce ultra-thin high-quality films, but this time, with embedded GaN/AlGaN QWs. Based on the applied conditions and the long exposure time, similar to the work reported in [28], the resulting root-mean-square (RMS) roughness of the bottom-side etched surface should be considerably low ($\leq$ 1 nm). It should be noted here that the same conditions were applied in all three samples, namely "8", "10" and "38" QWs, and had similar results regarding the membrane fabrication apart from a variation in their colorization. More specifically, the membranes with few-QWs had a reddish color (inset image in Figure 3.13(a)) instead of the yellow-like observed for the multi-QW structure (inset image in Figure 3.13(b)), which is apparently due to a difference in the overall thickness similar to bulk GaN shown in Chapter 2.

Next, the photoluminescence of the free-standing membranes lying on a

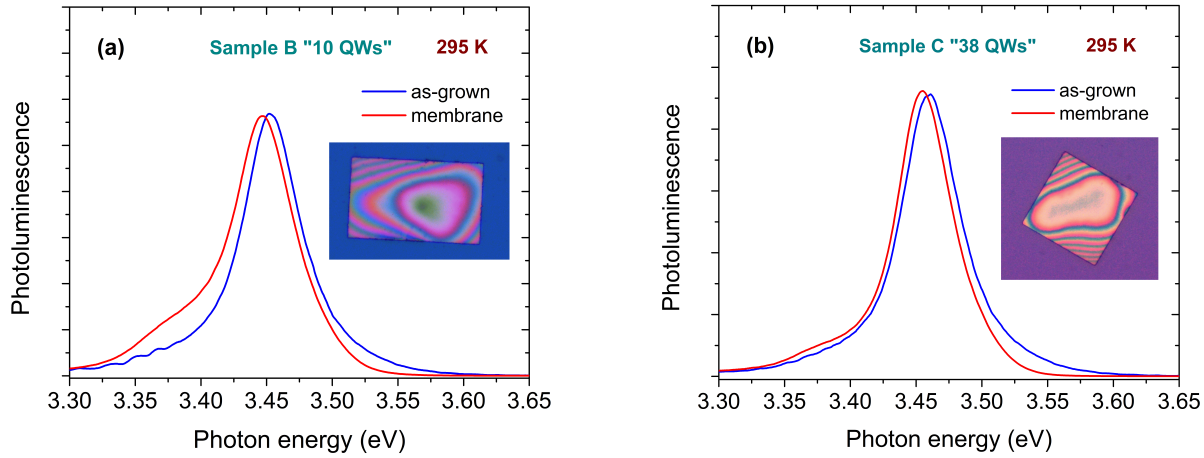

Figure 3.13: Photoluminescence spectra of the as-grown structures along with the emission of the bare membranes on Sapphire with (a) few (×10) and (b) multi (×38) GaN/AlGaN QWs at the temperature of 295 K. The insets are optical images of the corresponding membranes.

Sapphire template was recorded. For comparison purposes the room temperature PL emission of membranes is plotted here against the PL emission of the as-grown samples. Once again, here are presented only the "10" and "38" QWs. As indicated in the PL spectra of Figure 3.13, there is a small redshift in the PL emission of membranes compared to the PL peak of the as-grown samples. In the few QWs, the peak emission of the as-grown sample is at 3.4527 eV and after the membrane separation it is found 6 meV lower. A shift of 4 meV is found also in the multiple QWs where before etching the PL peak is centered at 3.4595 eV while the emission of free standing membrane is centered at 3.4553 eV. This result contradicts the expected blueshift due to the compressive strain imposed by the AlGaN layers after the release of membranes. One should think that initially the as-grown QW-layers are pseudomorphic on the thick GaN template, while the AlGaN layers feel tensile strain due to the lower lattice constant (Figure 1.1(b)). After the membrane detachment, and the release of the structures in a free-standing form, the AlGaN layers try to gain control until a new equilibrium (net-force zero) is reached in the system. In this case, the GaN layer is compressed and the PL emission should be blueshifted. Between the two samples discussed here, the effect should be more pronounced in the sample

with the few QWs as the AlGaN thickness is much larger compared to the GaN layers in the membrane. In the "38-QWs" sample, where the AlGaN and GaN thicknesses are equal in the membrane, we estimate that the blueshift due to the new compressive state in the QWs should be about 7 %. The previous is based on the estimation that the average superlattice lattice constant corresponds to $Al_{0.03}Ga_{0.97}N$. The compression is given by multiplying the 3 % with 2.4 % (= $\Delta\alpha/\alpha$ between GaN and AlN) $\approx$ 0.07 %. It is known from literature that 0.1 % compression, the GaN gap shifts by 10 meV [29]. Therefore, a compression of 0.07 % gives a shift of 7 meV. To really decide what is happening here we need further experiments. It should be referred here that the PL emission of the AlGaN barriers in the sample with the "10-QWs", positioned at 3.5627 eV (348 nm), was cut with a filter above the energy of 3.5424 eV (350 nm).

3.8 Optical density in QW-structures

By following the same absorption methodology, as for the bulk GaN films, an initial attempt is demonstrated here to extract similar parameters in the membranes with 8, 10 or 38 embedded GaN/AlGaN QWs. The analysis shown in Chapter 2 can be extended to GaN/AlGaN QWs with some minor modifications. For this purpose, room temperature micro-transmittance measurements were performed on the QW-containing membranes transferred on Sapphire. Similar to bulk GaN membranes, considering the sub-wavelength thickness, it is necessary for the analysis of the transmittance data to use a transfer matrix formulation taking into account the reflectivity coefficients at the air / nitride and nitride / sapphire or nitride / air interfaces, as well as the formation of standing wave effects inside the membranes. Then, it is possible to transform the normalized μ-T spectra into the optical density (OD) spectra for different membranes with varying number of QWs.

After the complete acquisition of the μ-T spectrum for each membrane, the starting point is to determine, along with the membrane thickness, an effective

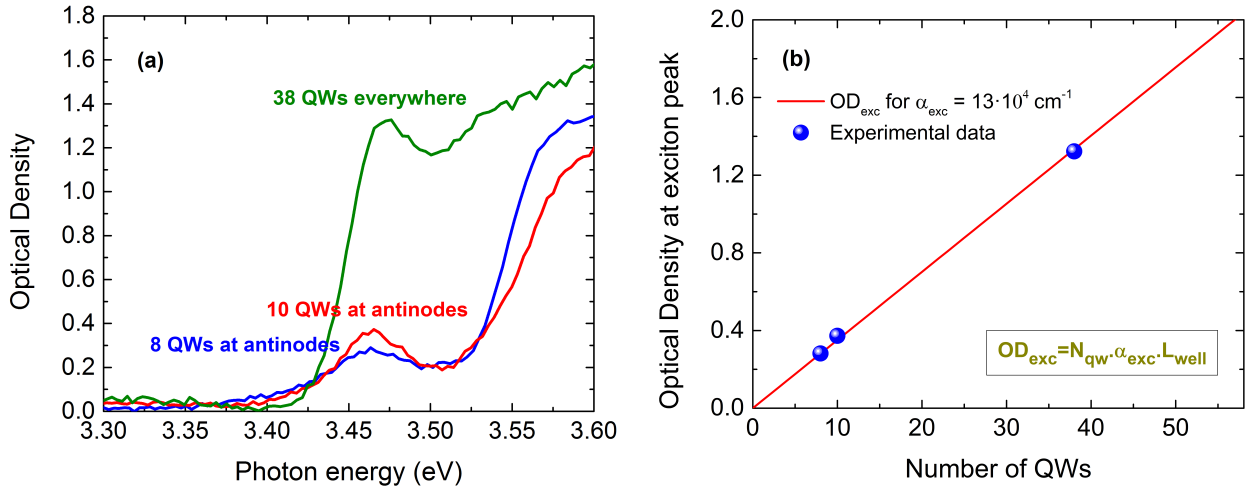

Figure 3.14: (a) Optical densities as deduced from the respective transmittance spectrums acquired at RT for three membranes containing 8, 10 and 38 GaN/AlGaN QWs. (b) Optical density at the exciton peak versus number of QWs. The fitting curve corresponds to an absorption coefficient of $13{\cdot}10^4\ cm^{-1}$ for the case of a 2.7-nm-thick GaN/$Al_{0.07}Ga_{0.93}N$ QW.

refractive index $n_{eff}(\lambda)$ for the GaN/AlGaN heterostructure. This is achieved by fitting the low-energy Fabry-Perot oscillations of the μ-T spectrum using Equation 2.4 and assuming a spectral dependence of $n_{eff}(\lambda)$ approximately equal to AlGaN [30]. Next, by inserting the experimental μ-T data and the corresponding fitted parameters in Equation 2.6, we deduce the optical density spectrum of the entire membrane. The derived optical density spectra for the "8", "10" and "38" QW-containing membranes are plotted in Figure 3.14(a) where we see that the pronounced excitonic peak at around 3.470 eV is coming from the temperature-induced merging of the A_{QW}+B_{QW} exciton peaks in the GaN/AlGaN QWs. More specifically, the pronounced A_{QW}+B_{QW} QW exciton peak can be seen that is considerably blueshifted and enhanced compared to the bulk case due to quantum confinement. In a QW-containing membrane, the optical density at the exciton peak can be written as

$$OD_{exc} = N_{qw} \cdot \alpha_{exc} \cdot L_{well} \tag{3.1}$$

where N_{qw} is the number of QWs, α_{exc} the effective exciton absorption coefficient

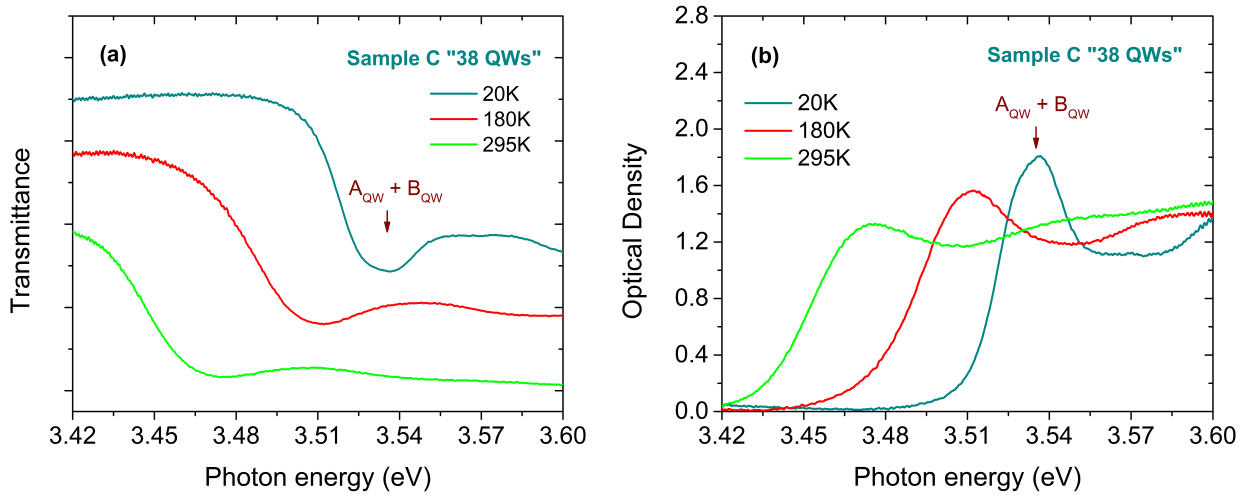

Figure 3.15: (a) Micro-transmittance spectra of a 2.7 nm GaN/AlGaN QW at 20, 180 and 295 K. (b) The optical density spectra extracted from the micro-transmittance data for the same temperatures.

in the QW material and L_{well} the well thickness.

As illustrated in Figure 3.14(b), the experimental OD_{exc} values for the three QW-containing membranes are found to be proportional to the number of QWs in the structure similar to what is expected. The slope of the fitting curve gives an OD_{exc} value per QW of about 3.5 %. For a well thickness of 2.7 nm, this leads to an absorption coefficient at the exciton peak of $13{\cdot}10^4\ cm^{-1}$. This value can be compared to the bulk one of $9{\cdot}10^4\ cm^{-1}$. The resulting absorption coefficient spectrum of the GaN/$Al_{0.07}Ga_{0.93}N$ (2.7 nm/2.7 nm) QWs can be obtained by dividing the OD spectrum with the number of the quantum wells and the thickness of the well.

Furthermore, temperature dependent μ-T measurements (Figure 3.15(a)) resulted in the OD spectra shown in Figure 3.15(b) for 20, 180 and 295 K, where we observe the evolution of the A_{QW}+B_{QW} QW absorption versus temperature. The presented μ-transmittance spectra have a constant offset in the plot for better visualization. Since the utilized cryostat had a lot of vibrations for the specific measurement, there is a small uncertainty in the obtained data as for the case of bulk GaN. Nevertheless, it is worth making a few comments based on the particular set of recorded data. At 20 K, the strong peak is coming from

the convolution of the A_{QW} and B_{QW} excitons at the energy position of 3.5350 eV with a maximum OD value of ~ 1.80. Despite the fact that it is difficult to distinguish the two main excitons, there is a visible feature at B_{QW} position exceeding the overall maximum peak indicating the B-state character. The position of the C_{QW} exciton cannot be clearly resolved here. As the temperature increases, the main A_{QW}+B_{QW} QW exciton peak broadens from 30 up to 45 meV due to phonon-assisted effects but its peak OD value remains at all temperatures higher than the bulk GaN, illustrating the robustness of the QW excitons up to ambient conditions, characterized by their high exciton binding energies and oscillator strengths.

Regarding the latter, an additional step was made to obtain the oscillator strength per unit area and per QW of the "A_{QW}+B_{QW}" QW exciton. Considering the demonstrations in Chapter 2, this was possible by performing a similar calculation. In the case of QWs, the oscillator strength is extracted per area and not per volume as was the case for the bulk GaN. Hence, the following relation is considered [31, 32]:

$$\frac{f_{qw}}{S} = \frac{2\varepsilon_o n_{eff} m_e c}{\pi e^2 \hbar} \cdot \frac{\int OD(E)dE}{N_{qw}} \tag{3.2}$$

The optical density integral is estimated by fitting the "A+B" QW exciton line with two Gaussians (Figure 3.14(a)), corresponding to the A_{QW} and B_{QW} excitons, distanced by 10 meV. For the QW-samples, the use of two Gaussians represents better the convolution of the "38 A_{QW}" and "38 B_{QW}" Lorentzian-like exciton response, considering the relative significance of the inhomogeneous broadening mechanisms compared to the homogeneous phonon-related ones in our QWs. The resulting value for the A_{QW}+B_{QW} QW exciton oscillator strength per unit area and per QW of the 2.7 nm GaN/AlGaN QW is found to be $4.5{\cdot}10^{13}$ cm^{-2}, in good agreement with previous reports for similar QWs that were based on polariton dispersion analysis [33, 35, 36]. The estimation of the oscillator strength value is of major importance for the simulation of the exciton

contribution in polariton branches, since it is included in the coupling constant (Equation 1.24), and our measurement of optical density allowed us to have a direct determination.

3.9 Robust strong coupling at ambient conditions

Considering the results of the previous sections, we have managed to obtain full microcavities by depositing 4-pairs of SiO_2/Ta_2O_5 as top DBR, on the membranes, sitting on a 10-pair SiO_2/Ta_2O_5 bottom DBR. A schematic of the complete structure is depicted in Figure 3.16(a), where is also shown the polariton formation inside the active region by the strong coupling of light with the exciton pair. According to the results shown in Figure 3.10, the 4 pairs of SiO_2/Ta_2O_5 provide sufficient optical confinement in our $3\lambda/2$-cavities and are able to bring the system in the strong coupling regime. The energy and momentum conservation between the photons inside the cavity and the ones emitted outside gives a one to one correspondence between energy and the angle (Equation 1.20), which allows us to have a visualization of the dispersion states inside the microcavity by recording the PL emission versus angle. Figure 3.16(b) illustrates a simplified experimental configuration for imaging the $k_{//}$ space emission pattern with the use of an aspheric and an imaging lens, having focal lengths f_a and f_i, at the entrance of a spectrometer in order to image and record the analyzed angle versus photon energy (Fourier plane) data with a nitrogen-cooled CCD camera. An example of the lower and upper polariton branches (energy dispersions) is presented in the schematic of Figure 3.16(c).

The polaritonic character (anticrossing behavior) in our cavities is confirmed by the discussed angle-resolved micro-photoluminescence (μ-PL) at low and room temperature conditions. In such a setup, the sample is excited at normal incidence with a continuous wave He-Cd laser emitting at 325 nm (E_{laser} = 3.8149 eV). Here, the excitation beam is focused down to a 9 μm spot by using an aspherical lens with a numerical aperture NA = 0.63. For the angle-dependent

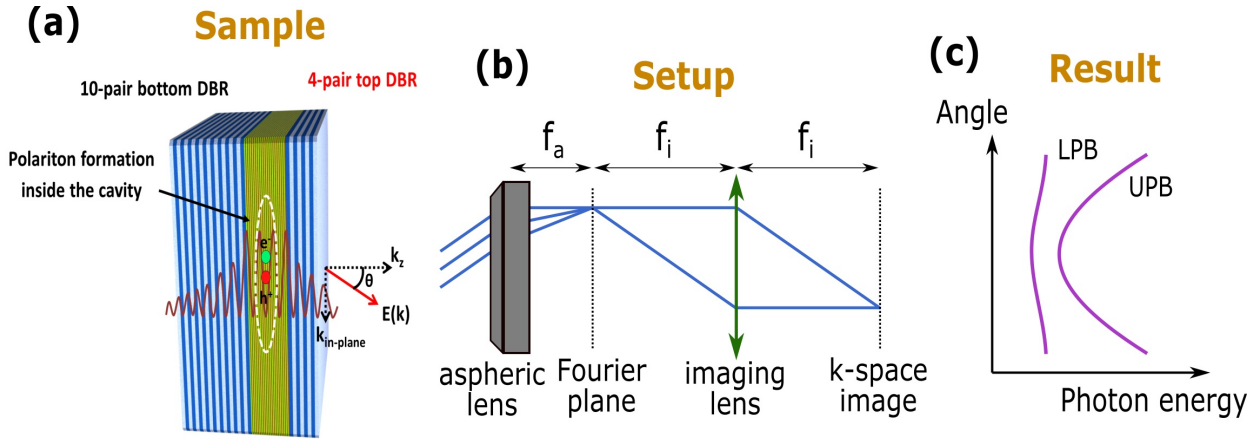

Figure 3.16: Illustration of (a) a $3\lambda_o/2n$-microcavity with a 4-pair top and a 10-pair bottom DBR mirror, exhibiting several antinodes of the electric field in the 38 QW-containing active region and forming polaritons in the strong coupling regime, (b) a k-space imaging setup for the acquisition of (c) the upper and lower polariton branches.

measurements, an imaging lens needs to be placed at a distance from the aspheric equal to $f_a + f_i$ (Figure 3.16(b)), so as to allow for PL imaging of the Fourier plane (k-space image) into the spectrometer located on the right hand side of the imaging lens (in the specific configuration) at a distance f_i. This way, it is possible to record simultaneously the emitted PL as a function of angle (Figure 3.16(c)). The range of the acquisition angles is limited by the NA of the system and for this reason lenses with high values of NA are typically used. In our case, we are able to read angles in the range of $\pm$ 39°. The excitation and collection paths, in the experimentally utilized setup (Appendix E), were through the same optical route with the use of a beam splitter.

To move on, in Figure 3.17(a) are presented the k-space imaging data recorded at 295 K for the "10 QW" microcavity, even though the flattening of the LPB at large angles is less pronounced, as a consequence of the smaller number of QWs and the larger negative detuning in this sample. To account for the observed polariton branches and estimate the Rabi splitting in the two samples, a linear Hamiltonian model (Section 1.7) is used to simulate the angle-dependent data at 295 K. In this model, the QW excitons interact with the cavity TE and TM modes (dotted lines) according to their respective coupling constants, forming in each case two polariton branches, which reproduce accurately the

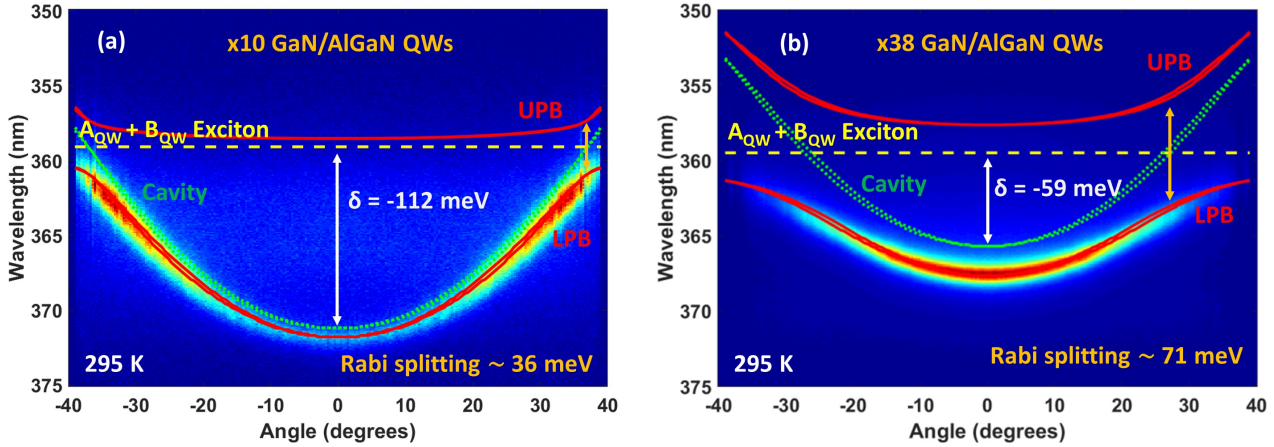

Figure 3.17: Angle-resolved polariton PL at room temperature from (a) a "10 QWs" microcavity with a Rabi splitting of 36 meV and (b) a "38 QWs" microcavity exhibiting a Rabi splitting of 71 meV. The exciton levels (dashed lines), the cavity modes (dotted lines), as well as the simulated lower- and upper-polariton branches (solid curves) are also shown.

experimental LPB dispersions. The zero angle emission of LPB is at 371.8 nm (3.3347 eV). The exciton state is at 359.1 nm (3.4526 eV) and the cavity mode placed at 371.2 nm (3.3401 eV), having a negative energy difference of -112 meV. Similar anti-crossing was obtained for the "38 QW" microcavity (Figure 3.17(b)). The depicted lower polariton branch (LPB) shows a clear anti-crossing behavior at large angles where the LPB flattens out towards the QW exciton emission (dashed line). The PL emission at zero angle ($k_{//} = 0$) is at 367.6 nm (3.3728 eV). The exciton line is positioned at 359.5 nm (3.4488 eV) while the cavity mode at 365.7 nm (3.3903 eV), giving a negative detuning of around -59 meV. The upper polariton branch (UPB) is not observed in either sample, something typical in nitride microcavities [1,2,10] most likely due to rapid decay of UPB polaritons to higher energy exciton and continuum states [37].

In these simulations, the thicknesses of the oxide layers of the mirrors are initially determined by fitting with a transfer matrix model the experimental reflectivity spectra of the bottom DBR/Si (Figure 3.10(a)), top DBR/Si (Figure 3.10(b)), as well as the $\lambda/2$ resonator formed by the combination of a top DBR on a bottom DBR/Si (Figure 3.10(c)). Additionally, the thickness of the membrane layer is defined, as explained earlier, based on the fitting of the μ-T spectra. This procedure is necessary in order to estimate with precision the cavity mode

position at k = 0 of the full microcavity. By knowing the cavity mode and QW exciton positions in each microcavity, it is then possible to sensitively fit the LPB dispersion with the Hamiltonian model, using the coupling constant as a sole adjustable parameter, assuming a reasonable value for the exciton linewidth. In the microcavities at hand, the coupling constants (g_o) that best reproduce the LPB dispersions are in the range of 18 meV for the "10 QWs" sample and of 36 meV for the "38 QWs" sample.

The smaller coupling constant in the "10 QWs" sample can be attributed to several reasons. First, is that in a $3\lambda/2$ cavity there exist antinodes not only at the center but also at the two DBR/membrane interfaces, where no QWs are present in the "10 QWs" case. Second, is that the active layer of the "10 QWs" sample is found by transmittance measurements a bit larger than nominal. This has as a consequence that the QWs are not positioned exactly at the field's antinodes, leading to a weaker coupling constant. Third, is that in the particular "10 QWs" microcavity, the top DBR is not centered at the right position due to increased oxide layer thicknesses, as deduced from the huge detuning. This leads to reduced DBR reflectivities at the wavelengths of interest, weakening further the coupling constant of the exciton-photon interaction. Knowing the coupling constants in the two samples, we have then estimated the respective Rabi splittings of the systems by the energy difference at the anti-crossing point between the calculated LPB and UPB dispersions (orange arrows). Thus, it was found to be 36 meV and 71 meV for the "10 QW" and "38 QW" microcavities, respectively. To our knowledge, these values set the state-of-the-art for nitride QW microcavities [2, 10, 33] and demonstrate the future potential of robust polariton structures.

3.10 Polariton lasing in multi-QWs

In this section, we analyze a power dependent study, performed with a Nd-YAG frequency-quadrupled pulsed laser at 266 nm ($E_{laser} = 4.66$ eV) with a

repetition rate of 7.58 kHz and a pulse width of 0.51 ns, for the optical excitation of a complete microcavity. The k-space imaging setup was aligned at 360 nm using the emission from the quantum wells, for which the spot size of the pulsed laser had an area of 60 μm × 10 μm. The elliptical profile here is due to the elongated waist of the laser beam. The excitation is non-resonant in order to create populations at higher energies and observe if the system can induce a macroscopic occupation in the polariton trap (polariton condensation) by increasing gradually the power. In this case, the optically generated populations are initially coherent but as they decay to lower energy states they lose their coherence completely due to phonon scattering. Finally, after some time (usually tens of ps), an incoherent population of polaritons has relaxed to the lower polariton branch. At this stage, the shape and properties of the lower polariton dispersion play an essential role to what will happen next. For the negatively detuned structures, discussed in the previous section, it was not possible in our power-dependent measurements to observe any polariton condensation in the trap. The main reasons for this are probably the relatively small Q-factor compared to the microcavity of reference [10] in combination with the rapid decay of excitons, which do not let the system to condense neither in the kinetic nor in the thermodynamic regime [34]. We believe that by increasing the top mirror pairs it will be possible to observe polariton lasing in our structure as observed in earlier work of our group [10].

As a next step, we decided to develop out of the same active regions, positively-detuned microcavities, by adjusting the thickness of the top DBR layers. As stated in the literature [38], increasing the detuning from negative values to zero or positive values has the advantage of faster relaxation rates and longer polariton lifetimes. This combination may be favorable for polariton condensation provided that the polariton trap does not become too swallow for the polaritons to thermally escape in to the exciton reservoir, especially at elevated temperatures. The previous statements can be confirmed by the k-space images of Figure 3.18, which were acquired from a positively-detuned ($\delta \sim 1.2$

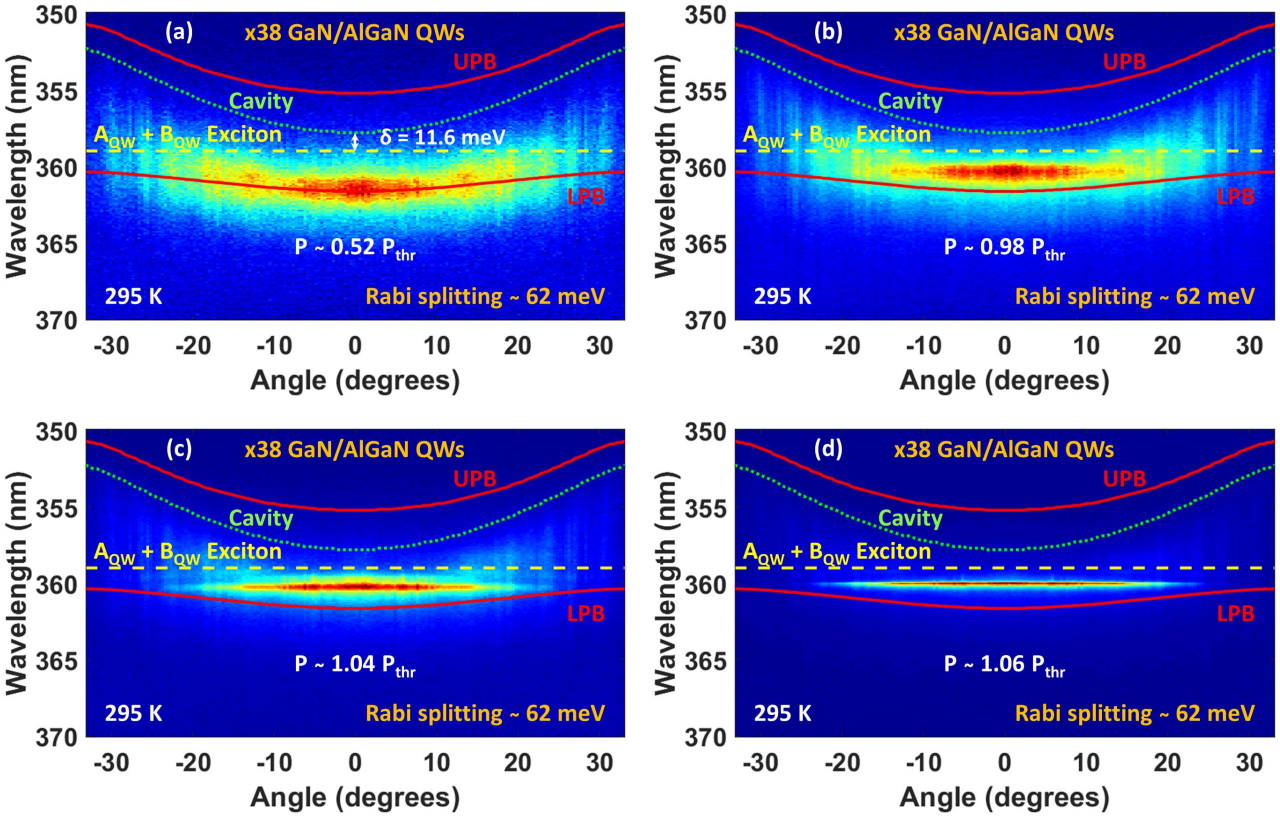

Figure 3.18: Room temperature k-space μ-PL imaging of a "38-QW" cavity under quasi-pulsed excitation at 266 nm with (a) $0.52P_{thr}$, (b) $0.98P_{thr}$, (c) $1.04P_{thr}$ and (d) $1.06P_{thr}$, where the power density threshold of polariton lasing is $\sim 4.5\ W/cm^2$.

nm (11.6 meV)) microcavity with "38" GaN/AlGaN QWs. At a power density of $0.52P_{thr}$ (Figure 3.18(a)), there is a large population of polaritons occupying the LP branch around $k_{//} \approx 0$. As the power increases to $0.98P_{thr}$ (Figure 3.18(b)), the distribution becomes narrower both in $k_{//}$ and energy along with significant blueshift due to polariton-polariton interaction mainly. Above threshold, at densities of 1.04 and 1.06 of P_{thr} (Figures 3.18(c-d)), the microcavity exhibits a narrowed-down in energy intense emission centered at $k_{//}$, characteristic of polariton lasing. In Figure 3.19 are given also the 3D k-space images for a range of excitation powers below and above threshold for better visualization of the progress of the condensate versus the power density.

To confirm our assertion of polariton lasing, the PL spectra at $k_{//} = 0$ versus excitation power are depicted in the same graph (Figure 3.20(a)), where is clearly visible the non-linear increase of the $k_{//} = 0$ PL intensity and the

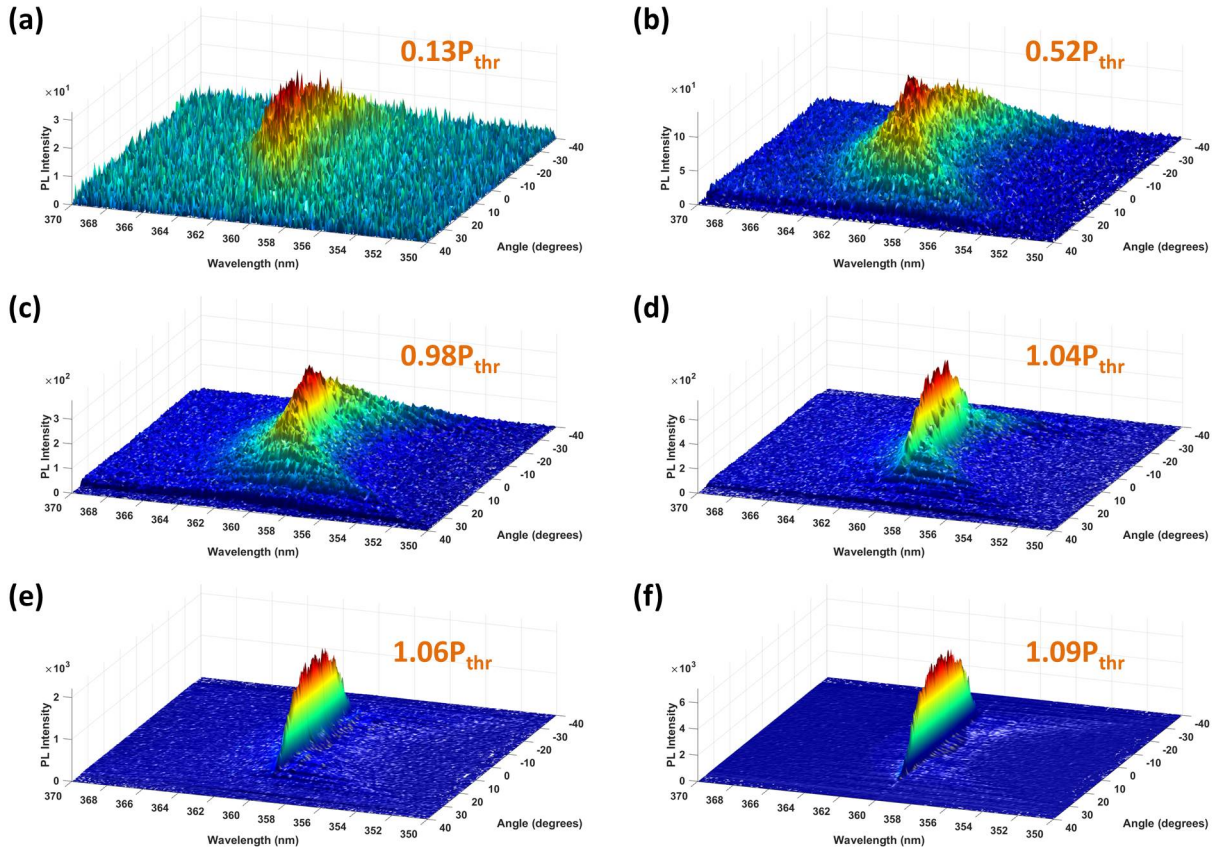

Figure 3.19: Room temperature k-space μ-PL imaging in 3D view of a "38-QW" microcavity under quasi-pulsed excitation at 266 nm with (a) $0.13P_{thr}$, (b) $0.52P_{thr}$, (c) $0.98P_{thr}$, (d) $1.04P_{thr}$, (e) $1.06P_{thr}$ and (f) $1.09P_{thr}$, where the power density threshold of polariton lasing is $\sim 4.5\ W/cm^2$.

drastic narrowing of the emission peak down to 2 meV (Figure 3.20(b)) as we cross the threshold power density (P_{thr}) of $\sim 4.5\ W/cm^2$, illustrating that this particular microcavity device is undergoing polariton lasing. It can be confirmed from the data that the lasing emission remains well below the bare exciton state (X) located at 359 nm (3.4536 eV) and cavity resonance (C) at 357.8 nm (3.4652 eV), respectively. In order to fit the LPB dispersion with the linear Hamiltonian model, as depicted with red lines in the figures, a coupling constant of 35 meV was utilized, which resulted in a Rabi splitting of 62 meV at $k_{//} = 0$. The previous calculation was in accordance with the transfer matrix method. The deduced polariton lifetime for the specific cavity is found to be $\tau_{pol} = 0.45$ ps, by considering the Equation C.7 and a decay time of 42 ps for the excitons

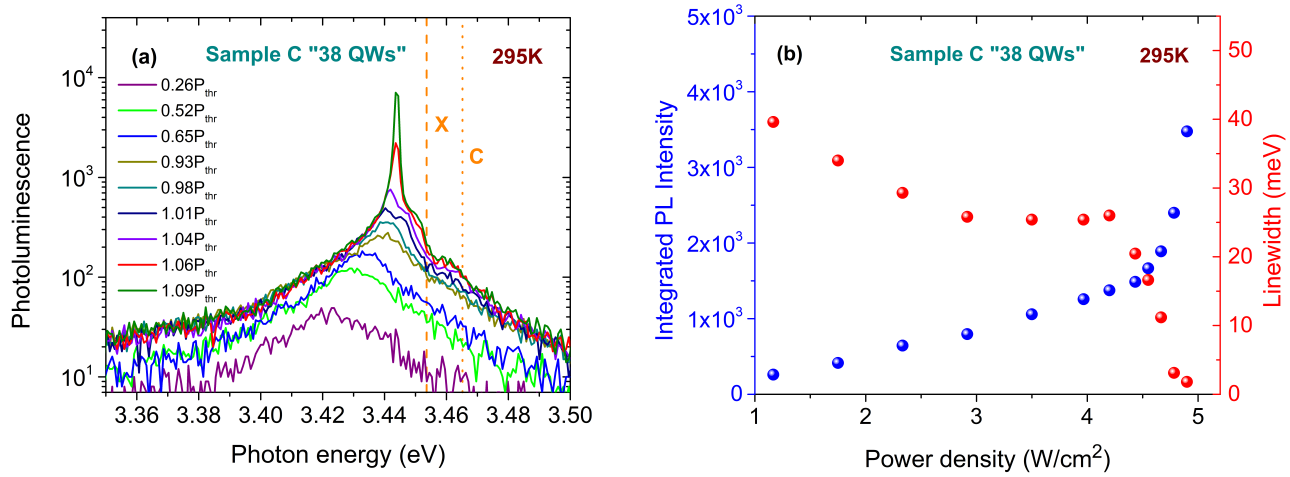

Figure 3.20: (a) Photoluminescence spectra at $k_{//} = 0$ versus excitation power and (b) the integrated $k_{//} = 0$ PL intensities versus the power densities in combination with the corresponding linewidth of the PL peaks.

at RT as extracted from the TRPL measurements. This τ_{pol} value is about double the value obtained for a negatively-detuned device with the same number of QWs and in combination with faster relaxation rates in positively-detuned microcavities, explains qualitatively how we were able to observe lasing here, in contrast to the negatively-detuned structures examined earlier.

In order to show the difference between polariton (strong coupling) and photonic (weak coupling) lasing, we present here the k-space image (Figure 3.21(a)) acquired from the same microcavity at a power density close to polariton lasing threshold, illustrating the different energy dispersions. Here, photonic lasing is powered from the cavity mode, as defined by the simulations of the structure, unlike the polariton lasing of Figure 3.18 which occurs 2.2 nm (21.6 meV) below the cavity mode. Moreover, the spread in wavevectors is much narrower ($\pm$ 3°) compared to the polariton laser where the $k_{//}$-spread was much larger ($\pm$ 10°). The comparison between the two, can be seen in the plot of Figure 3.21(b) for approximately similar excitation powers. As can be observed, polariton lasing occurs below the exciton energy (X) while photonic lasing above the cavity energy (C). Regarding the relatively large $k_{//}$-spread of the polariton-laser emission of Figure 3.18(d), we attribute it to some spatial confinement of the polariton condensate [34], based on which we can estimate

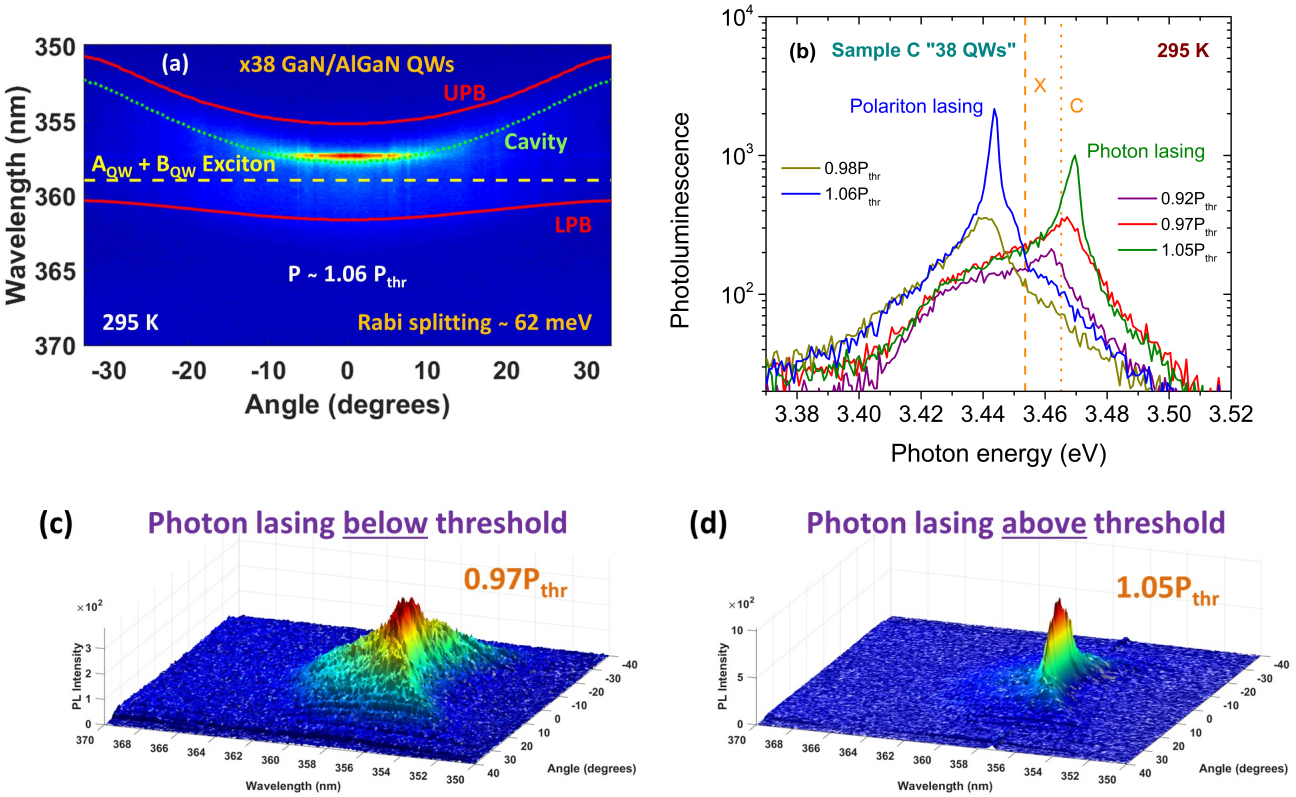

Figure 3.21: (a) RT k-space μ-PL imaging of a "38-QW" microcavity under quasi-pulsed excitation at 266 nm with $1.05P_{thr}$, (b) the PL of the photonic mode below and above lasing threshold along with the polariton lasing emission for $k_{//} = 0$ and (c-d) the 3D view of k-space μ-PL imaging at RT under quasi-pulsed excitation with (c) $0.97P_{thr}$, (d) $1.05P_{thr}$, where the P_{thr} of cavity lasing is $\sim 4.4\ W/cm^2$.

the radius of the condensate localization to be about 0.3 μm. In Figures 3.21(c-d) are given the 3D k-space images below and above threshold of photonic lasing for further demonstration of the previous.

A useful estimation for the exciton density per QW which are coupled can be made by taking the blueshift difference of the LPB up to threshold at $k_{//} = 0$. From low excitation until threshold, there is an overall shift of the PL peak by about 17 meV. This blueshift is mainly due to polariton-polariton scattering V_{int} and is enhanced here due to the strong excitonic component of the positively-detuned polaritons. We can obtain an estimate of the exciton density (n_{exc}^{2D}) based on the relation [2, 39, 40]

$$\Delta E = 6|X_o|^2 E_B \alpha_B^2 n_{exc}^{2D} \tag{3.3}$$

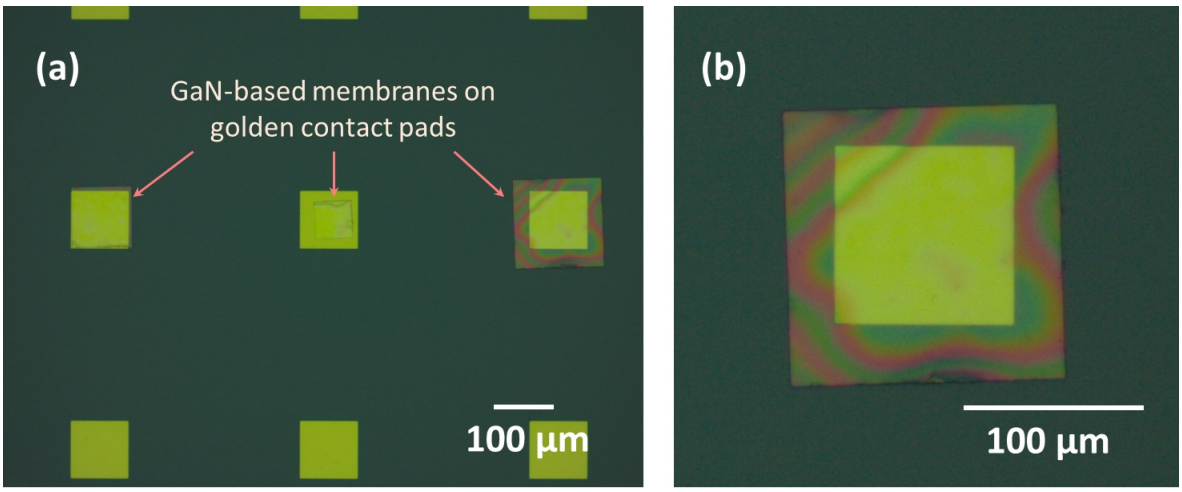

Figure 3.22: Optical image (a) with three 200-nm-thick GaN-based membranes of different size transferred on top of 100 μm × 100 μm square golden contact pads and (b) zoom of the 155 μm × 155 μm GaN-based membrane depicted on the right side of (a).

where $|X_o|^2$ (≈ 0.58) is the exciton fraction at $k_{//} = 0$, E_B (≈ 30 meV) is the binding energy and α_B (≈ 2.7 nm) is the Bohr radius of the exciton. Performing the above calculation, we get a value of $n_{exc}^{2D} \sim 2.23{\cdot}10^{12}$ cm^{-2} which remains below the Mott transition densities of 10^{13} cm^{-2}, reported for similar QWs [36], further asserting that we are in the strong coupling regime. Dividing the deduced exciton density by the number of QWs, we obtain a n_{exc}^{2D} per QW of $5.87{\cdot}10^{10}$ cm^{-2}.

3.11 Possibility of electrical injection

The feasibility to produce high quality GaN-based membranes that can be transferred individually onto precise regions of other substrates permitted us to transfer them on top of 100 μm × 100 μm golden contact pads as shown in the optical image of Figure 3.22(a). Additionally, in Figure 3.22(b) is presented the zoom of the 155 μm × 155 μm membrane depicted in Figure 3.22(a). Undoubtedly, this demonstrates that electrically injected all-dielectric polariton devices can be realized by considering the overall findings discussed in this chapter. In order to accomplish the specific fabrication, the active region must be

designed to operate as a p-n junction. At the same time, transparent conductive contacts are needed to allow the current injection while leaving intact the light propagation. The all-dielectric design can reduce considerably the current losses occurring in epitaxial mirror configurations where current is passing through the DBRs. Therefore, the successful fabrication and operation of an electrically injected polariton device with all-dielectric DBRs at ambient conditions will be a intriguing novelty in the field of polaritonics.

3.12 Conclusion

In summary, in this chapter we have reported the fabrication of high quality free-standing $3\lambda/2$-membranes, containing 8, 10 and 38 GaN/AlGaN QWs using the photo-electrochemical etching method. Micro-transmittance measurements on these QW-containing membranes allowed us to deduce an optical density per QW at the main exciton peak of our QWs, of about 3.5 % at room temperature. Complete microcavities have been fabricated by transferring first the membranes on a 10-pair SiO_2/Ta_2O_5 bottom DBR and by depositing next on top of them, a 4-pair SiO_2/Ta_2O_5 top DBR in an electron-gun deposition system. The produced microcavities exhibited robust polariton characteristics at ambient conditions, with a maximum Rabi splitting of 36 meV for the structure containing 10 QWs only at the antinodes of the active region while the value of 71 meV was achieved for the 38-QW-containing structure. In addition, in a positively detuned microcavity with 38-QWs as the active material, we observed polariton lasing at RT with a power density threshold of 4.5 W/cm^2. To our knowledge this is the lowest reported threshold density for a positively-detuned polar GaN-based microcavity. For the few QWs, it was not possible to observe stable polariton lasing, attributed to much weaker coupling strength due to misalignment of the DBR mirrors and increased membrane thickness. Nevertheless, the overall results further validate the PEC etching method as a means to obtain robust polaritonic devices operating at room temperature conditions.

Bibliography

[1] S. Christopoulos, G. Baldassarri Höger von Högersthal, A. J. D. Grundy, P. G. Lagoudakis, A. V. Kavokin, J. J. Baumberg, G. Christmann, R. Butté, E. Feltin, J.-F. Carlin, and N. Grandjean. *"Room-Temperature Polariton Lasing in Semiconductor Microcavities"*, Phys. Rev. Lett. 98, 126405 (2007).

[2] G. Christmann, R. Butté, E. Feltin, J.-F. Carlin, and N. Grandjean. *"Room temperature polariton lasing in a GaN/AlGaN multiple quantum well microcavity"*, Appl. Phys. Lett. 93, 051102 (2008).

[3] A. Das, J. Heo, M. Jankowski, W. Guo, L. Zhang, H. Deng, and P. Bhattacharya. *"Room Temperature Ultralow Threshold GaN Nanowire Polariton Laser"*, Phys. Rev. Lett. 107, 066405 (2011).

[4] P. Bhattacharya, T. Frost, S. Deshpande, M. Z. Baten, A. Hazari, and A. Das. *"Room Temperature Electrically Injected Polariton Laser"*, Phys. Rev. Lett. 112, 236802 (2014).

[5] Y.-K. Song, H. Zhou, M. Diagne, I. Ozden, A. Vertikov, A. V. Nurmikko, C. Carter-Coman, R. S. Kern, F. A. Kish, and M. R. Krames. *"A vertical cavity light emitting InGaN quantum well heterostructure"*, Appl. Phys. Lett. 74, 3441 (1999).

[6] R. W. Martin, P. R. Edwards, H.-S. Kim, T. Kim, I. M. Watson, M. D. Dawson, Y. Cho, T. Sands, and N. W. Cheung. *"Optical spectroscopy of GaN microcavities with thicknesses controlled using a plasma etchback"*, Appl. Phys. Lett. 79, 3029 (2001).

[7] F. Rizzi, P. R. Edwards, K. Bejtka, F. Semond, X. N. Kang, G. Y. Zhang, E. Gu, M. D. Dawson, I. M. Watson, and R. W. Martin. *"(In,Ga)N/GaN microcavities with double dielectric mirrors fabricated by selective removal of an (Al,In)N sacrificial layer"*, Appl. Phys. Lett. 90, 111112 (2007).

[8] K. Bejtka, F. Reveret, R. W. Martin, P. Edwards, A. Vasson, J. Leymarie, I. R. Sellers, and J. Y. Duboz. *"Strong light-matter coupling in ultrathin double dielectric mirror GaN microcavities"*, Appl. Phys. Lett. 92, 241105 (2008).

[9] G. Christmann, D. Simeonov, R. Butté, E. Feltin, J.-F. Carlin, and N. Grandjean. *"Impact of disorder on high quality factor III-V nitride microcavities"*, Appl. Phys. Lett. 89, 261101 (2006).

[10] R. Jayaprakash, F. G. Kalaitzakis, G. Christmann, K. Tsagaraki, M. Hocevar, B. Gayral, E. Monroy, and N. T. Pelekanos. *"Ultra-low threshold polariton lasing at room temperature in a GaN membrane microcavity with a zero-dimensional trap"*, Sci. Rep. 7, 5542 (2017).

[11] A. S. Barker Jr. and M. Ilegems. *"Infrared lattice vibrations and free-electron dispersion in GaN"*, Phys. Rev. B 7, 743 (1973).

[12] N. Grandjean, B. Damilano, S. Dalmasso, M. Leroux, M. Laügt, and J. Massies. *"Built-in electric-field effects in wurtzite AlGaN/GaN quantum wells"*, J. Appl. Phys. 86, 3714 (1999).

[13] F. Natali, D. Byrne, M. Leroux, B. Damilano, F. Semond, A. Le Louarn, S. Vezian, N. Grandjean, and J. Massies. *"Inhomogeneous broadening of $Al_xGa_{1-x}N/GaN$ quantum wells"*, Phys. Rev. B 71, 075311 (2005).

[14] B. Chwalisz, A. Wysmolek, R. Bozek, K. P. Korona, R. Stepniewski, W. Knap, K. Pakula, J. M. Baranowski, N. Grandjean, J. Massies, P. Prystawko, and I. Grzegory. *"Localization Effects in GaN/AlGaN Quantum Well - Photoluminescence Studies"*, Act. Phys. Pol. A 103, 573 (2003).

[15] Y. P. Varshni. *"Temperature dependence of the energy gap in semiconductors"*, Physica (Utrecht) 34, 149 (1967).

[16] I. Vurgaftman, J. R. Meyer, and L. R. Ram-Mohan. *"Band Parameters for III-V Compound Semiconductors and Their Alloys"*, J. Appl. Phys. 89, 5815 (2001).

[17] S. Chichibu, H. Okumura, S. Nakamura, G. Feuillet, T. Azuhata, T. Sota, and S. Yoshida. *"Exciton Spectra of Cubic and Hexagonal GaN Epitaxial Films"*, Jnp. J. Appl. Phys. 36, 1976 (1997).

[18] M. Gurioli, A. Vinattieri, M. Colocci, C. Deparis, J. Massies, G. Neu, A. Bosacchi, and S. Franchi. *"Temperature dependence of the radiative and nonradiative recombination time in $GaAs/Al_xGa_{1-x}As$ quantum-well structures"*, Phys. Rev. B 44, 3115 (1991).

[19] J.-F. Carlin, J. Dorsaz, E. Feltin, R. Butté, N. Grandjean, M. Ilegems, and M. Laügt. *"Crack-free fully epitaxial nitride microcavity using highly reflective AlInN/GaN Bragg mirrors"*, Appl. Phys. Lett. 86, 031107 (2005).

[20] J. Y. Zhang, L. E. Cai, B. P. Zhang, S. Q. Li, F. Lin, J. Z. Shang, D. X. Wang, K. C. Lin, J. Z. Yu, and Q. M. Wan. *"Low threshold lasing of GaN-based vertical cavity surface emitting lasers with an asymmetric coupled quantum well active region"*, Appl. Phys. Lett. 93, 191118 (2008).

[21] W. J. Liu, S. Q. Chen, X. L. Hu, Z. Liu, J. Y. Zhang, L. Y. Ying, X. Q. Lv, H. Akiyama, Z. P. Cai, and B. P. Zhang. *"Low Threshold Lasing of GaN-Based VCSELs With Sub-Nanometer Roughness Polishing"*, IEEE Photon. Technol. Lett. 25 (2013).

[22] A. Asahara, S. Chen, T. Ito, M. Yoshita, W. Liu, B. Zhang, T. Suemoto, and H. Akiyama. *"Direct generation of 2-ps blue pulses from gain-switched InGaN VCSEL assessed by up-conversion technique"*, Sci. Rep. 4, 6401 (2014).

[23] L. Gao, F. Lemarchand, and M. Lequime. *"Refractive index determination of SiO_2 layer in the UV/Vis/NIR range: spectrophotometric reverse engineering on single and bi-layer designs"*, J. Europ. Opt. Soc. Rap. Public. 8, 13010 (2013).

[24] L. Gao, F. Lemarchand, and M. Lequime. *"Exploitation of multiple incidences spectrometric measurements for thin film reverse engineering"*, Opt. Express 20, 15734 (2012).

[25] L. V. Rodríguez-de Marcos, J. I. Larruquert, J. A. Méndez, and J. A. Aznárez. *"Self-consistent optical constants of SiO2 and Ta2O5 films"*, Opt. Mater. Express 6, 3622 (2016).

[26] D. L. Wood, K. Nassau, T. Y. Kometani, and D. L. Nash. *"Optical properties of cubic hafnia stabilized with yttria"*, Appl. Opt. 29, 604 (1990).

[27] I. H. Malitson and M. J. Dodge. *"Refractive Index and Birefringence of Synthetic Sapphire"*, J. Opt. Soc. Am. 62, 1405 (1972).

[28] R. Jayaprakash, F. G. Kalaitzakis, M. Kayambaki, K. Tsagaraki, E. Monroy, and N. T. Pelekanos. *"Ultra-smooth GaN membranes by photo-electrochemical etching for photonic applications"*, J. Mater. Sci. 49, 4018 (2014).

[29] A. Shikanai, T. Azuhata, T. Sota, S. Chichibu, A. Kuramata, K. Horino, and S. Nakamura. *"Biaxial strain dependence of exciton resonance energies in wurtzite GaN"*, J. Appl. Phys. 81, 417 (1997).

[30] G. M. Laws, E. C. Larkins, I. Harrison, C. Molloy, and D. Somerford. *"Improved refractive index formulas for the $Al_xGa_{1-x}N$ and $In_yGa_{1-y}N$ alloys"*, J. App. Phys. 89, 1108 (2001).

[31] Y. Masumoto, M. Matsuura, S. Tarucha, and H. Okamoto. *"Direct experimental observation of two-dimensional shrinkage of the exciton wave function in quantum wells"*, Phys. Rev. B 32, 4275 (1985).

[32] Y. Yamamoto, F. Tassone, and H. Cao. *"Semiconductor Cavity Quantum Electrodynamics"*, Springer (2010).

[33] E. Feltin, G. Christmann, R. Butté, J.-F. Carlin, M. Mosca, and N. Grandjean. *"Room temperature polariton luminescence from a GaN/AlGaN quantum well microcavity"*, Appl. Phys. Lett. 89, 071107 (2006).

[34] R. Butté, J. Levrat, G. Christmann, E. Feltin, J.-F. Carlin, and N. Grandjean. *"Phase diagram of a polariton laser from cryogenic to room temperature"*, Phys. Rev. B 80, 233301 (2009).

[35] G. Christmann, R. Butté, E. Feltin, J.-F. Carlin, and N. Grandjean. *"Impact of inhomogeneous excitonic broadening on the strong exciton-photon coupling in quantum well nitride microcavities"*, Phys. Rev. B 73, 153305 (2006).

[36] G. Christmann, R. Butté, E. Feltin, A. Mouti, P. A. Stadelmann, A. Castilia, J.-F. Carlin, and N. Grandjean. *"Large vacuum Rabi splitting in a multiple quantum well GaN-based microcavity in the strong-coupling regime"*, Phys. Rev. B 773, 085310 (2008).

[37] S. Faure, T. Guillet, P. Lefebvre, T. Bretagnon, and B. Gil. *"Comparison of strong coupling regimes in bulk GaAs, GaN, and ZnO semiconductor microcavities"*, Phys. Rev. B 78, 235323 (2008).

[38] A. Kavokin, J. J. Baumberg, G. Malpuech, and F. P. Laussy. *"Microcavities"*,Oxford University Press (2017).

[39] F. Tassone and Y. Yamamoto. *"Exciton-exciton scattering dynamics in a semiconductor microcavity and stimulated scattering into polaritons"*, Phys. Rev. B 59, 10830 (1999).

[40] C. Ciuti, P. Schwendimann, B. Deveaud, and A. Quattropani. *"Theory of the angle-resonant polariton amplifier"*, Phys. Rev. B 62, R4825(R) (2000).

Chapter 4

Strong coupling in non-polar microcavities

This chapter focuses on the novel development of m-plane non-polar GaN/AlGaN membranes with multiple QWs for their incorporation in between all-dielectric DBR mirrors towards the demonstration of strong coupling regime and ultra-low polariton lasing at room temperature conditions. Moreover, due to in-plane polarization anisotropy it was possible to deduce the oscillator strength of the QW-excitons in the two orthogonal polarizations.

4.1 Introduction

Despite the novel achievements in polar polariton structures, the elimination of the quantum-confined Stark Effect in conjunction with the much larger optical matrix elements achieved in non-polar QWs presents an opportunity for further reduction in the polariton lasing threshold at ambient conditions as well as polarization-selective polariton dispersions. Initial investigations on non-polar microcavities focused on the growth of structures along the α-orientation ($[11\bar{2}0]$) with a first successful observation of strong coupling regime by Mastro et al. [1]. However, due to the marked difficulty in generating high quality structures, the α-direction was finally abandoned. During the subsequent years, the progress and commercial availability of adequate quality GaN bulk crystal in the m-axis ($[1\bar{1}00]$) [2] enabled the fabrication of improved m-plane microcavity structures, either hybrid [3, 4] or air-gap based [5, 6]. In the hybrid use, the epitaxial III-nitride bottom DBR mirrors pose a limitation in the performance of such microcavities as their limited index-difference gives a rather narrow reflectivity stop-band and necessitates a relatively large number of periods which usually affects adversely the optical quality of the active region. On the other hand, the

air-gap solution is not believed to be overall mechanically stable, while current injection schemes are not straightforward. To overcome these limitations, we have applied in the non-polar configuration our PEC-etching approach in order to fabricate a high-optical quality all-dielectric non-polar microcavity.

4.2 Novel demonstrations in this work

The successful growth of high-quality and free-of-internal-fields quantum wells in the m-orientation [7,8] motivated us to fabricate appropriate III-nitride structures with which we could apply the same PEC-etching approach to produce ultra-smooth membranes with embedded non-polar GaN/AlGaN quantum wells. In order to ensure the strong-coupling conditions in our structures, we designed the active medium to contain $\times 25$ $GaN/Al_{0.1}Ga_{0.9}N$ QWs in the whole active region, with well and barrier thicknesses being 5 nm and 3 nm, respectively. The 5-nm-thick well was chosen to keep the exciton inhomogeneous broadening at low levels, while at the same time maintaining sufficient confinement and the high recombination efficiencies of the non-polar quantum wells [10–12]. This possibility of increased well thickness does not exist in the polar QWs, due to the spacial separation of electron-hole wavefunctions induced by the large build-in fields in the polar orientation [13, 14]. Moreover, we increased the Al concentration to 10 % in order to limit significantly the thermal escape of excitons. In the produced microcavities, remarkable optical characteristics have been demonstrated, which are attributed to the utilization of dielectric top / bottom DBR mirrors and the high optical quality of the GaN-based membranes. In addition, by successfully transferring QW-containing non-polar membranes on Sapphire substrates, we were able to measure directly the oscillator strength of non-polar GaN/AlGaN QWs by applying our recently established standing wave approach given in Chapter 2.

It should be noted that apart from the enhanced optical properties, the non-polar GaN and AlGaN layers exhibit inherent birefringence and dichroism

phenomena, since the optical c-axis lies in the plane of the non-polar surface [15], and is responsible for the characteristic polarization selection rules along the two orthogonal in-plane directions (E//α and E//c). These effects are related to the complex refractive index and affect both the position of the photonic mode in a complete microcavity [16, 17] and the optical coupling with the quantum well excitons [18, 19]. As can be understood, a precise control is required in the design of non-polar nitride-based mirrors which aside from the limited stopband widths [16] are also exhibiting birefringence along the two polarizations [20]. On the other hand, the isotropic polarization-free oxide-based DBR mirrors used in this work with large stopbands and minimal absorption at the QW-emission wavelengths are an attractive alternative, considering that the polarization anisotropy is kept only inside the active region. Thus, the unique non-polar orientation leads to the generation of polarized-resolved polariton branches within the same single microcavity. Up to this work, there has not been in the literature a clear observation of polariton modes in both polarizations similar to our observations. Finally, the novel fabrication of robust all-dielectric non-polar microcavities in the present work led in addition to the observation of an ultra-low polariton lasing threshold at RT, with a threshold power density three times lower than previous state of the art. This result demonstrates the vast potential of non-polar nitride microcavities for further research and development towards ultra-efficient polaritonic devices.

4.3 Design and fabrication of m-plane GaN/AlGaN QWs

When growing a III-nitride structure along the [1$\bar{1}$00]-orientation (m-axis), the two orthogonal in-plane directions are the c-axis [0001] and the α-axis [11$\bar{2}$0] as depicted in the schematic of Figure 4.1(a). The α-axis [11$\bar{2}$0] mentioned in the introduction is also a non-polar orientation, but in this work we did not try to fabricate any samples. According to the work presented in the previous chapters, the design of the active region was performed with the use of the transfer matrix

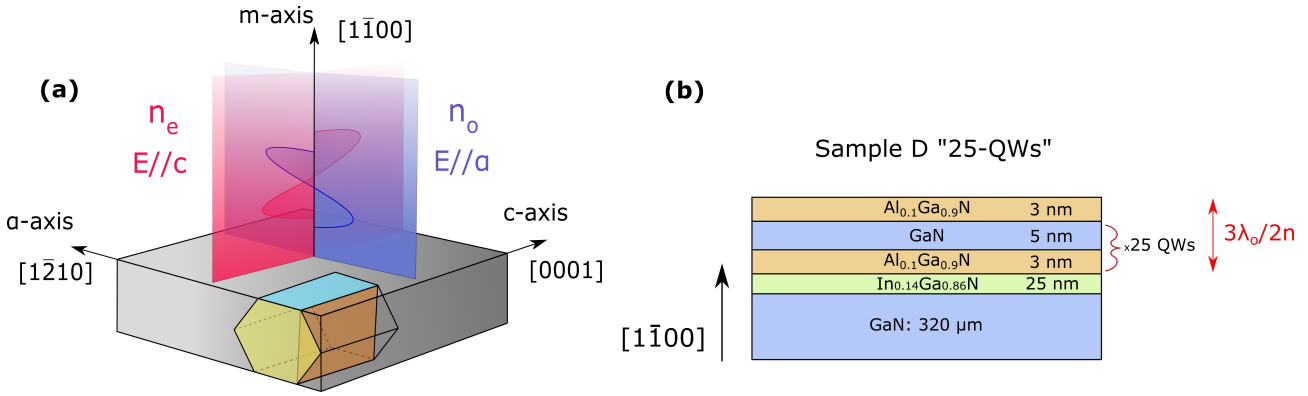

Figure 4.1: Illustration showing (a) the growth orientation along the [1$\bar{1}$00] orientation in conjunction with the birefringence rules in the two in-plane (c-, α-) crystallographic axes (reproduced from ref. [4]) and (b) the utilized design of "25 QWs" with 5 nm in the well (GaN) and 3 nm in the barrier (AlGaN) thickness spanned in the whole range of the active region. The 25-nm-thick InGaN layer is used as sacrificial layer in the PEC-etching approach.

method (TMM) (Appendix B) to evaluate the number and thicknesses of the quantum wells in a $3\lambda_o/2n$ ($\sim$ 200 nm) cavity and ensure for their enhanced coupling with the two antinodes of the electric field intensity inside the cavity due to the standing wave effect. The variables λ_o and n are being the exciton emission wavelength and average refractive index in the active medium at the same wavelength. In this growth orientation, the complex refractive index ($\tilde{n}$) (Appendix A) of the anisotropic GaN crystal depends strongly on the in-plane polarization. More specifically, both real (n) and imaginary (k) parts of the complex refractive index have altered characteristics in the two polaizations [16–19]. The effect on the real part of the index is named as double refraction or birefringence (n_o, n_e) where an incident ray of light is refracted differently in each polarization, while the effect on the imaginary part as dichroism (k_o, k_e) where the absorption of the exciton transitions is affected by the electric field polarization. The subscripts "o" and "e" in the two variables designate the ordinary and extra-ordinary polarizations (Figure 4.1(a)). It should be noted here that for c-axis grown GaN, a polarized incident ray entering along the optical axis (c-axis) of the GaN crystal does not feel birefringence.

In our simulations, the difference between the ordinary and extra-ordinary real refractive indices (Δn = n_e - n_o) has been considered to have an average

value of ~ 0.025 in all the layers of the active region, in agreement with previous works [17, 21]. For a positive linear birefringence ($n_e > n_o$), as in the case for the non-polar GaN crystal, the extraordinary ray is always traveling with a slightly slower velocity. Based on the literature [17], the ordinary ray is along the E//α polarization, while the extra-ordinary ray along the E//c. Theoretical investigations by other groups [3,19] have reported that the absorption coefficient ($\alpha \sim$ k) of each of the QW-exciton transitions depends critically on to the well thickness, Al-percentage in the barriers and strain condition of the QW-structure. Therefore, in order to properly design a non-polar microcavity, it is important to know the exciton oscillator strength in each polarization, something we achieved by performing micro-transmittance measurements on non-polar membranes, as will be discussed later on in this chapter.

To move on, in the TMM simulations we considered only the real part of the refractive index to make an initial optimal design for the non-polar structure, according to which we deduced an active region of $\times 25$ $GaN/Al_{0.1}Ga_{0.9}N$ QWs with a 5 nm well and 3 nm barrier thickness, spanning the entire 200-nm-thick membrane (Figure 4.1(b)). The simulated intensity profiles (I_o, I_e) of the electric field along with the corresponding refractive indices (n_o, n_e) in the E//α and E//c polarizations are plotted in Figures 4.2(a-b), assuming the active region is surrounded by a 4-pair top and a 10-pair bottom SiO_2/Ta_2O_5 DBR mirrors at the two sides. Furthermore, in Figures 4.2(c-d) are given the simulated angle-dispersed reflectance data, where we observe pronounced ordinary (C_o) and extra-ordinary (C_e) cavity modes at 360 nm (3.444 eV) and 361.6 nm (3.4287 eV), respectively. Even though, the electric field intensities (Figure 4.2(a-b)) do not seem to be affected, there is a non-negligible shift between the two cavity modes, as follows from the relation $3\lambda_o/2$n and $n_e > n_o$, which in the specific design resulted to be 1.6 nm (15.3 meV). Since the extra-ordinary real refractive index (n_e) is always higher, the C_e will be positioned in all cases at higher wavelengths ($C_e(\lambda_e) > C_o(\lambda_o)$). It should be recalled that the determined Q-factor in this device configuration is in the range of 1000.

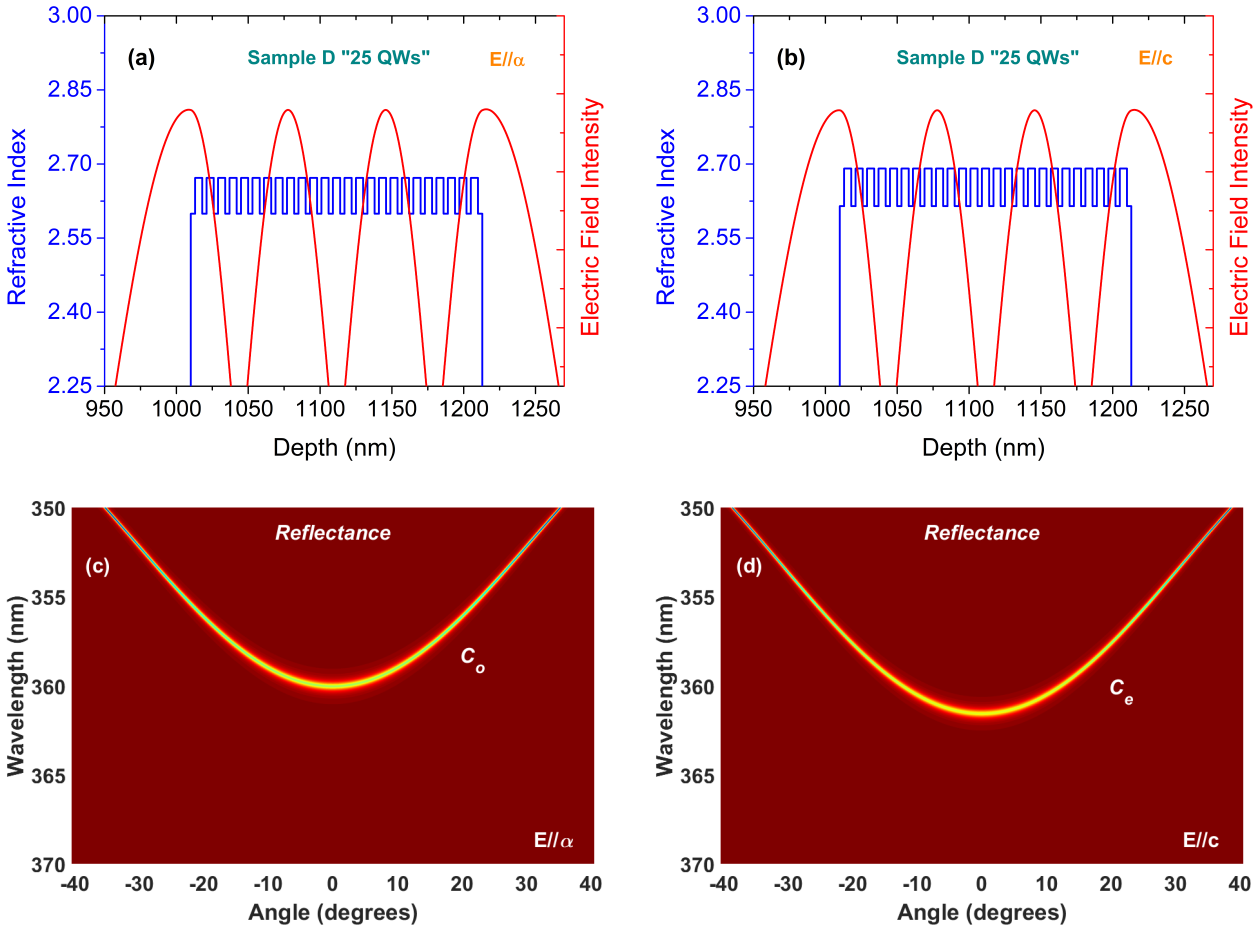

Figure 4.2: Refractive index and electric field intensity profile at (a) E//α and (b) E//c of an active region with 25 GaN/AlGaN QWs located in the whole range. The side regions of the simulated microcavity have a 4-pair top and 10-pair bottom SiO_2/Ta_2O_5 DBR mirrors (not shown). In (c) and (d) are presented the cavity modes in the dispersed reflectance spectra for the two in-plane polarizations denoted as E//α and E//c.

As suggested in the literature [22], the non-polar quantum wells offer the possibility to maintain the bandgap energies and exciton oscillator strengths of GaN wells unaffected by the Stark Effect. This allowed us to fabricate thicker quantum wells, while preserving high photoluminescence intensities compared to the identical polar-oriented QW-structures [10–12]. The reason behind the 5-nm-thick QWs adopted here, was to lower the inhomogeneous broadening due to QW width and alloy fluctuations, which are prominent in thin QWs [23]. On the other hand, the reduction in the exciton binding energy (E_B) is expected to be small [24]. In addition, the Aluminum content in the barrier layers was applied to be 10 % in order to increase the barrier height and reduce the thermal

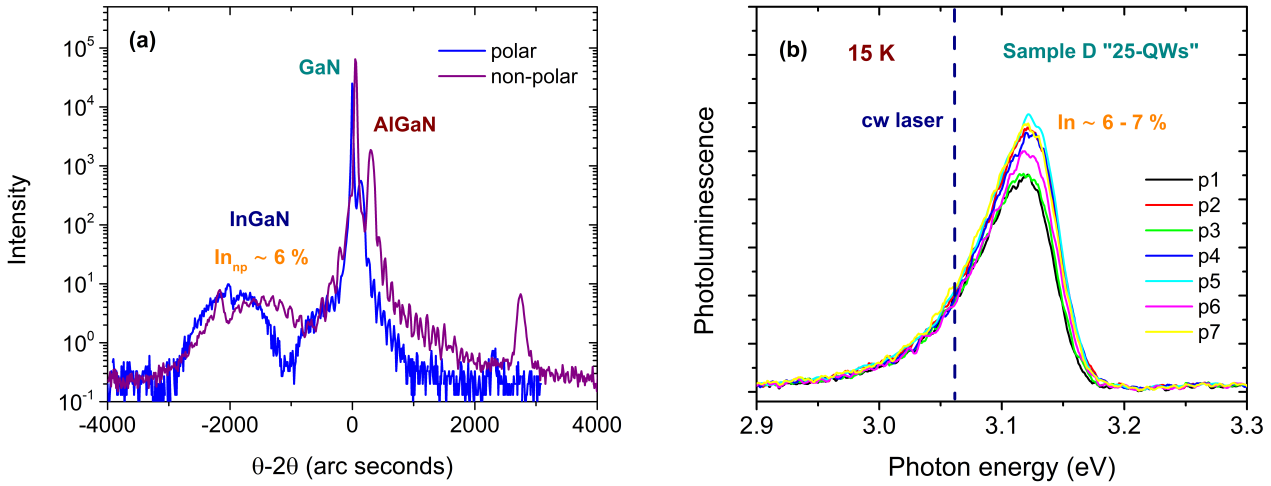

Figure 4.3: (a) X-Ray diffraction as acquired from the as-grown non-polar structure and (b) photoluminescence of the InGaN layer recorded from seven spots on the non-polar sample.

escape probability and dissociation of e - h pairs at room temperature conditions, without inducing too much strain in the overall superlattice structure [3].

To achieve superior optical quality, the non-polar GaN/AlGaN quantum wells were grown by plasma-assisted molecular beam epitaxy on commercial 320-μm-thick, nominally un-doped, m-plane crystalline GaN substrates acquired from Suzhou Nanowin Ltd. The particular free-standing [1$\bar{1}$00]-oriented (m-) substrates possess low dislocation densities ($\leq 10^6\ cm^{-2}$), several orders of magnitude lower than any non-polar heterostructure grown by heteroepitaxy, and minimal surface roughness in contrast to other suitable templates such as m-plane Al_2O_3 or γ-$LiAlO_2$ [25–28]. Once again here, the active region is separated from the GaN substrate by a 25-nm-thick InGaN sacrificial layer (Figure 4.1(b)), as optimized for the needs of the lateral bandgap-selective photo-electrochemical (PEC) etching [29]. The targeted Indium concentration in the InGaN layer was here also 14 % but as shown by X-ray diffraction (XRD) in a θ-2θ scan analysis (Figure 4.3(a)) and PL-mapping measurements at low temperature at seven different spots on the sample Figure 4.3(b), it was assessed to be around 6 - 7 %. To highlight the In-content variation between a polar and non-polar sample grown under the same conditions, in Figure 4.3(a) is shown the

XRD spectra from the two samples, the analysis of which gives a much higher ($\sim$ 18 %) In content for the polar sample, indicated by the more negatively in arc-seconds Indium XRD peak. Both measurements were performed by the equipment given in Appendix F.

As displayed in the plot of Figure 4.3(b), the InGaN's PL peak has an average energy of 3.115 eV (398 nm) at low temperatures, which is marginally higher than the laser energy used for PEC at 3.061 eV (405 nm). When moving at elevated temperatures, the emission of the sacrificial layer follows the expected temperature-induced shrinkage, reaching thus a central energy of $\sim$ 3.069 eV (404 nm), which is even closer to the laser's excitation energy (dashed-blue line). At the same time, during PEC-etching, the GaN/AlGaN QWs remain unaffected since their RT PL energy is centered around 3.444 eV (360 nm). It should be mentioned that incorporation of high Indium concentrations is not very feasible in the non-polar samples. On the other hand, in the c-plane structure of the same run, the In content was found much higher giving an average PL emission energy for InGaN at 2.666 eV (465 nm) ($\sim$ 17 % of Indium) in close agreement with XRD, demonstrating thus the high In-percentage contrast in the two orientations. Another remark on Figure 4.3(b) is the almost identical position of InGaN's PL peak emission at the different spots, illustrating a large uniformity of the non-polar InGaN layer over the sample. Even though the targeted concentration was not achieved, this was not a limiting factor to succeed the PEC-etching of the InGaN layer as we show later in the chapter.

4.4 Optical properties in the non-polar QWs

Next, the photoluminescence (PL) and the reflectivity (RFL) spectra were acquired in the as-grown samples to further evaluate the growth quality and optical characteristics of the bulk and QW excitons as a function of temperature. The optical excitation for the photoluminescence was made by a cw He-Cd Kimmon series laser at 325 nm and the reflectivity measurements using a Xenon

lamp (Appendix F). In Figure 4.4, we present a comparison of PL and RFL spectra at the bulk GaN and GaN/AlGaN QW exciton region for the two orthogonal polarizations (E//α and E//c) using a calcite Glan-Taylor prism, recorded at 15 K and 120 K. The polarized reflectance intensities are normalized to unity in order to determine the relative oscillator strengths among the two polarizations. In general, the non-polar orientation is characterized by enhanced PL intensities while RFL exhibits pronounced exciton features, demonstrating the marked interaction of non-polar excitons with the incident photons as well as the high optical quality of the m-plane quantum wells. More analytically, in Figure 4.4(a) showing E//α spectra at 15 K, we distinguish the bulk A_{GaN} and B_{GaN} excitons, located based on RFL spectrum at 3.479 eV and 3.484 eV, having an energy difference of 5 meV. These values and energy difference are in accordance with references [7, 8, 15, 30] for unstrained m-plane and α-plane bulk GaN, where both A_{GaN} and B_{GaN} exciton states are allowed in the E//α polarization. The relatively weak feature at 3.494 eV is potentially attributed to $A_{GaN}^{n=2}$ exciton state and is denoted by a dached arrow due to uncertainty. If this assignment is true, the 1s - 2s splitting is 15 meV and the corresponding Rydberg energy for the A-exciton is 20 meV, which is somewhat on the low side of exciton Rydberg values reported in the literature, which are between 22 and 26 meV [9]. Regarding QW-excitons, the allowed in this polarization A_{QW} exciton state is well resolved and positioned at 3.506 eV. A weaker C_{QW} feature is also visible at 3.529 eV.

Figure 4.4(b) illustrates the exciton transitions in the E//c polarization, where in this case the B_{GaN} (3.484 eV) and C_{GaN} (3.502 eV) bulk excitons are clearly visible and are separated by an energy difference of 18 meV. On the other hand, the A_{GaN} feature has disappeared indicating that the A_{GaN} has a strong in-plane polarization dependence. In similar works [15,30], C_{GaN} (3.502 eV) has been observed in both polarizations but with a much smaller component in E//α, however in our case, we do not have a very clear picture. In the plot of Figure 4.4(b), the allowed QW-states, are the B_{QW} at 3.514 eV and C_{QW} at 3.529 eV,

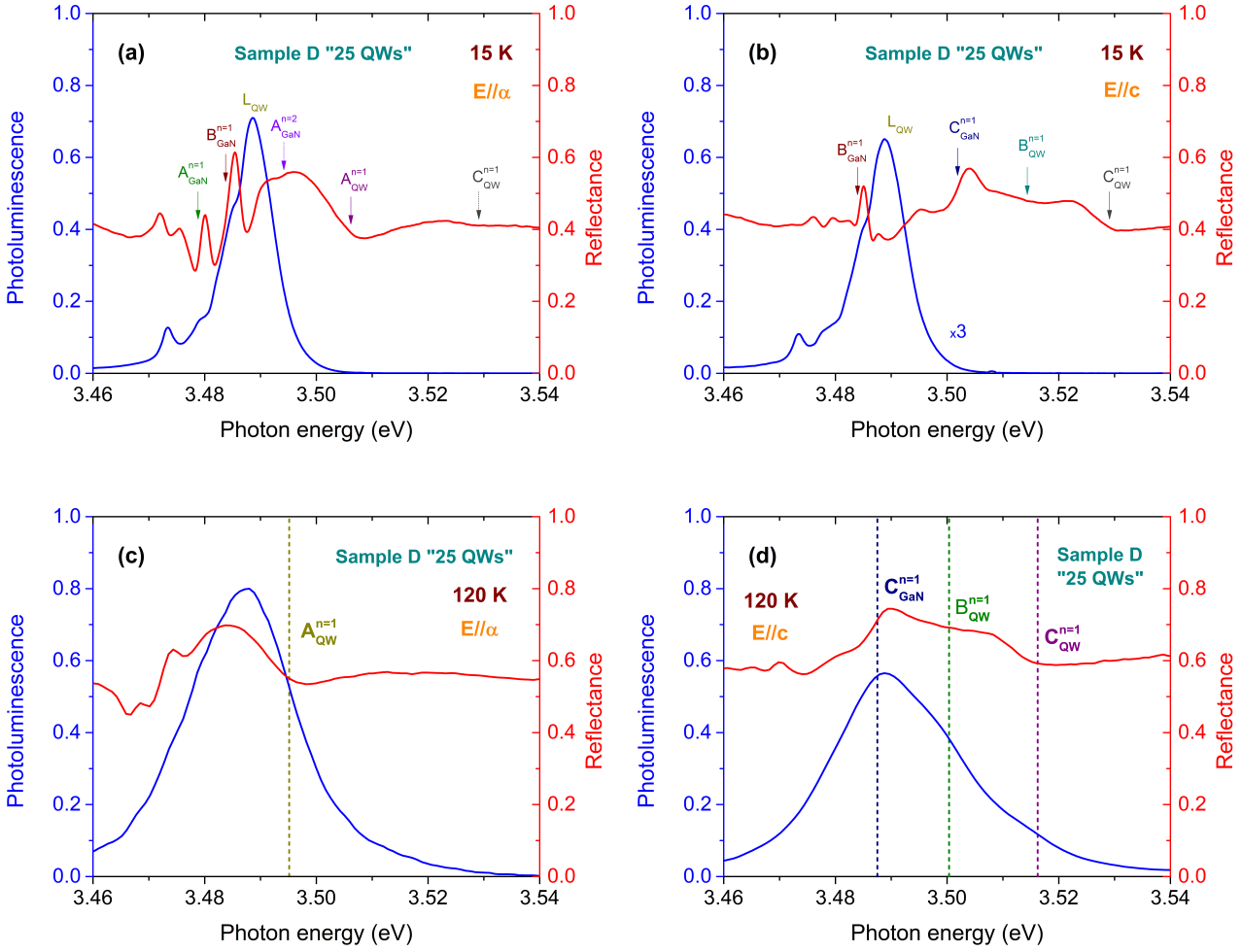

Figure 4.4: Photoluminescence and the corresponding reflectivity spectra of the as-grown structure in the (a) E//α and (b) E//c at the temperature of 15 K. (c-d) The same analysis at the temperature of 120 K.

confirming the fact that in the QW case the main A_{QW} and B_{QW} QW-states are both orthogonally polarized in contrast to the corresponding bulk states. This has been discussed by other groups [3, 4], in terms of strain effects and valence band mixing induced by the GaN / AlGaN lattice mismatch. Therefore, the Al composition is vital in determining the relative oscillator strengths of the QW-excitons. Moreover, the PL emission at cryogenic temperatures seems to be from localized A-exciton states (L_{QW}) since the corresponding peaks do not shift in energy in the two polarizations, while the emission seems to be strongly polarized along the E//α [18]. Please note that the PL spectrum in Figure 4.4(b) is multiplied $\times 3$ for better visibility. This is reasonable considering

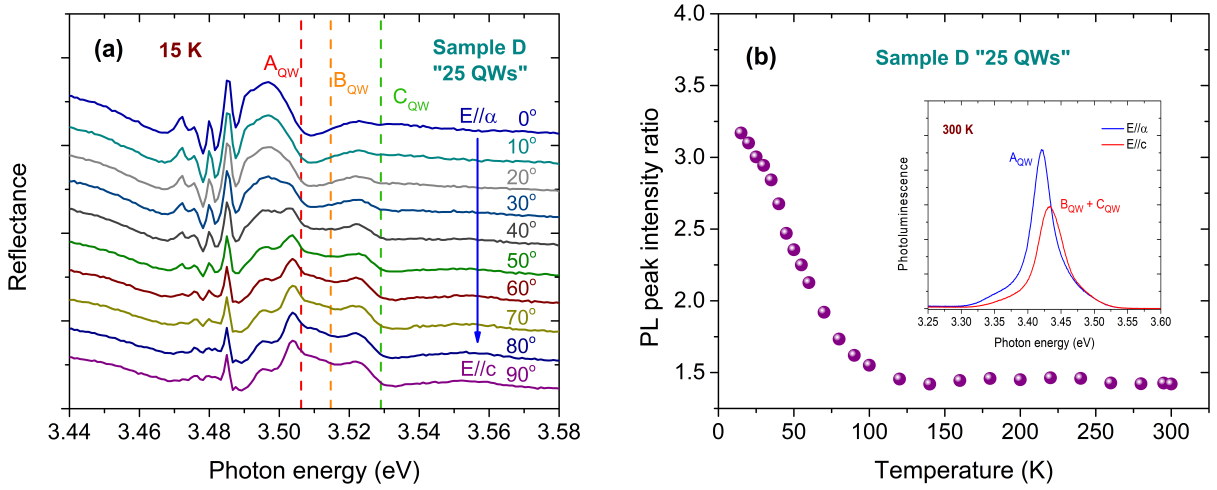

Figure 4.5: (a) Reflectivity spectrum of the as-grown m-plane structure as a function of the in-plane polarization at 15 K. (b) PL peak intensity correlation versus temperature between of the E//α and E//c. (Inset shows the room temperature photoluminescence in the two orientations).

that the A_{QW} exciton state is the lowest energetically state, and therefore, is better populated at low T. It should be also noted that as in the "$\times$38 polar" QWs, no PL emission related to the AlGaN (barrier) layer is observed, due to the superlattice structure. To move on, with increasing temperature, the QW emission peak approaches the free-exciton features as a result of thermally induced delocalization. This is evident in the PL / RFL spectra recorded at 120 K (Figures 4.4(c-d)), where the PL peak has now a significant overlap with the A_{QW}-feature seen in the RFL spectrum.

Figure 4.5(a) shows the reflectivity spectra at 15 K versus polarization angle in the angle range 0° (E//α) - 90° (E//c) with a step of 10 degrees. The position of each of the A_{QW}, B_{QW} and C_{QW} exciton states of the GaN/AlGaN QWs is denoted by colored dashed lines. By inspection of the RFL spectra, the exciton lines appear undeniably polarized in agreement with other reports [3,4]. Specifically, the A_{QW} exciton seems strongly polarized along E//α, with an intensity ratio $I_{E//\alpha}/I_{E\perp\alpha}$ as high as 10 while the B_{QW} and C_{QW} excitons appear clearly orthogonally polarized, along the E//c polarization. From these RFL spectra one can also qualitatively deduce that the B_{QW} exciton line appears significantly weaker than both the A_{QW} and C_{QW} exciton lines. These results are

in qualitative agreement with the k.p estimates of reference [3] for GaN/AlGaN QWs for Al-content (x_{Al}) $\simeq$ 5 - 10 %. In that work, x_{Al} is assumed to control the strain of the GaN layers, which strictly speaking is not the case in our-grown samples, where the GaN layers are lattice-matched to the GaN substrate. This is the case, however, of the free-standing $GaN/Al_{0.1}Ga_{0.9}N$ QW membranes, where the GaN samples feel a compressive strain, which is due to the presence of the AlGaN layers and is proportional to x_{Al}. In Figure 4.5(b) is given the PL peak intensity ratio for the E//α and E//c polarization versus temperature. At low T values, the PL peak intensity ratio is as high as $\sim$ 3.25. This ratio decreases gradually up to RT, reaching finally a value of approximately 1.4. In general, the PL intensity at E//α was more enhanced at all temperatures. As an additional information, it should be mentioned that the unpolarized PL of the m-plane sample was 2 orders more intense compared to the c-plane structure grown in parallel. The polar PL peak was also red-shifted due to the triangular well potential caused by the Stark effect. The inset image in Figure 4.5(b) shows the room temperature PL along the two in-plane polarizations, where the E//α component originates mainly from the dominant free A_{QW} excitons and the E//c from free B_{QW} + C_{QW} excitons. Apart, from the indicated higher luminescence intensity, the E//α polarization has also a smaller FWHM by 8 meV. In addition, the energy shift between the two PL peaks at RT is about 12 meV, close to the A_{QW} - B_{QW} exciton energy position difference.

Following the same analysis up to room temperature, we present in Figures 4.6(a-b) the analyzed PL peak position and FWHM values versus temperature from the acquired PL data in each polarization. Above a certain temperature of about 100 K, the PL peak obeys the bandgap energy shrinkage. Applying the Varshni model in both sets of PL data, the fitting for the PL res-shift results in α = 0.88 meV/K and β = 890 K parameters. However, the extrapolated at zero-temperature Varshni curves differ from the respective PL peak energies by as much as 12 meV in the E//α polarization and by 18 meV in the E//c polarization. This is a clear indication of localization process in potential minima

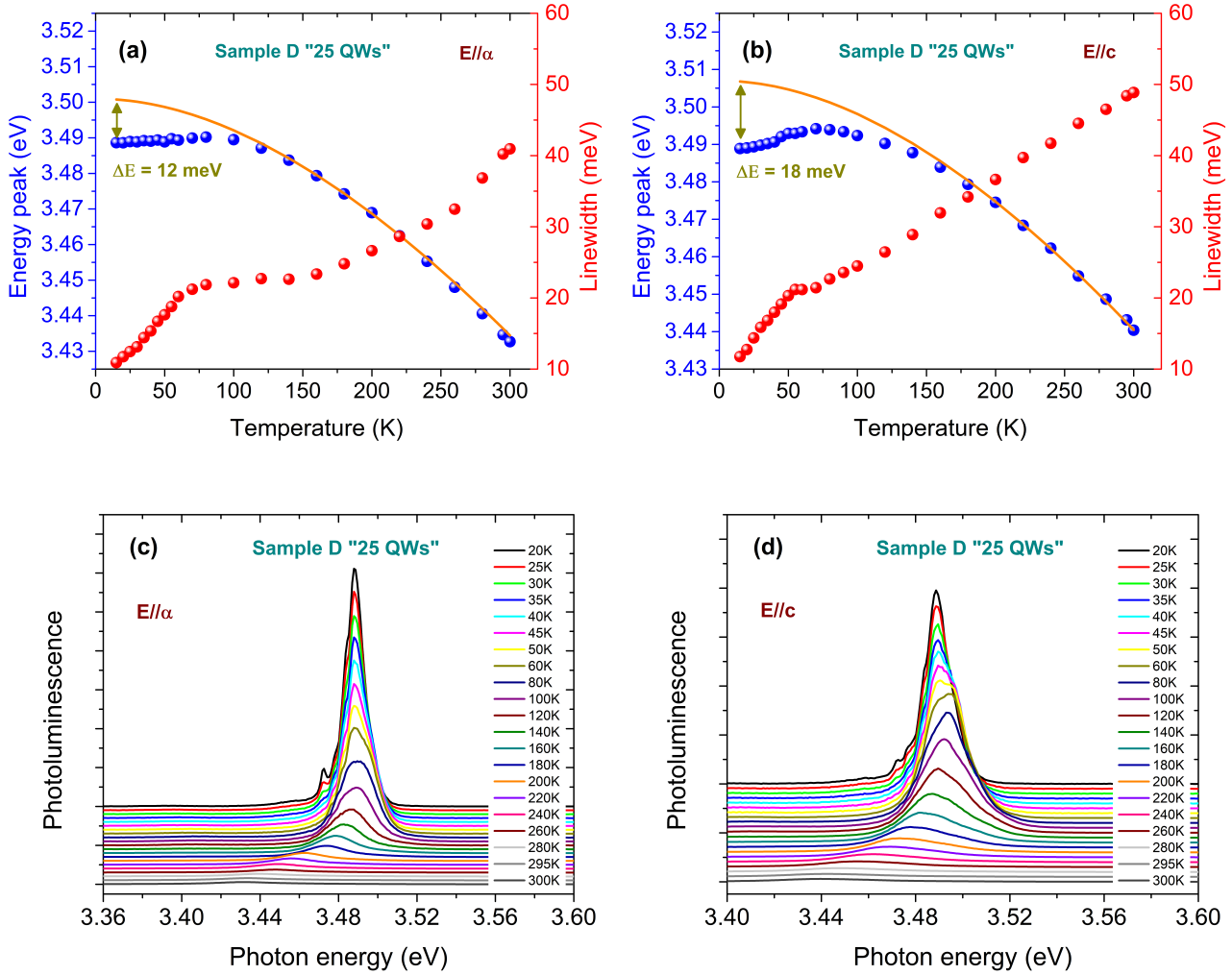

Figure 4.6: Energy peak along with PL linewidth versus temperature for (a) E//α and (b) E//c. The orange curves in the graphs are obtained based on the Varshni model. (c-d) Photoluminescence versus temperature at each of the two polarizations.

formed by well-width and barrier alloy fluctuations, in much the same way as observed in the polar quantum wells. Regarding non-polar QW-structures, it has been reported that localization effects are increasing as a function of the well thickness [12]. In addition, the energy positions indicated by the Varshni curves at zero temperature are not in perfect agreement with the determined QW excitons in the reflectance data of Figures 4.4(a-b). For instance, in the E//α, the Varshni energy at 0 K is 3.502 eV, whereas the A_{QW} exciton in RFL is rather 3.506 eV. This can be possibly attributed to the fact that the E//α PL peak contains additional contributions such as for instance from the GaN substrate,

red-shifting the observed PL peak positions. Even worse is the situation in the other E//c polarization, where in addition to the substrate PL one has to take into account the fact that the localized A_{QW} excitons are not fully polarized due to the localization process diluting the polarization selection rules.

By taking into account Figure 4.6(a) for better accuracy, the "de-trapping" temperature of the non-polar QW-excitons seems to occur at 100 ± 20 K. The FWHM in the two plots (Figures 4.6(a-b)) has a linear-like dependence within the localized temperature range similar to polar samples. The particularly narrow linewidth ($\sim$ 12 meV) at 15 K demonstrates the considerably minimized inhomogeneous broadening, owing to the relatively large well width and the high quality growth. Above 70 ± 20 K, there is an exponential like increase of the FWHM linewidth for E//α, likely due to thermal broadening of the A_{QW} exciton by LO-phonons. For E//c, the increase above 70 K is much more linear, likely due to the multiple lines (B_{QW} and C_{QW}). The 300 K FWHM value for E//α is about 40 meV, whereas for E//c is close to 50 meV. This is consistent with the multi-exciton nature of the PL emission in the E//c polarization. The PL curves in Figures 4.6(c-d) present the PL spectra as a function of temperature, from which were deduced the temperature evolution of PL peak position and FWHM linewidth illustrated in Figures 4.6(a-b).

4.5 Time-resolved photoluminescence in non-polar QWs

To have an estimate of the exciton decay times (τ_{exc}) in the as-grown non-polar GaN/AlGaN QWs, we performed time-resolved photoluminescence (TRPL) experiments in the temperature range of 5 K up to 300 K. Details of the experiment along with the utilized conditions are given in Appendix D. From the obtained TRPL curves, we have extracted the PL decay time as a function of temperature presented in the graph of Figure 4.7(a). At low temperatures, the lifetimes are approximately 160 ps, while as the temperature elevates up to 80 K there is a pronounced increase towards the prolonged value of 460 ps. Beyond 80

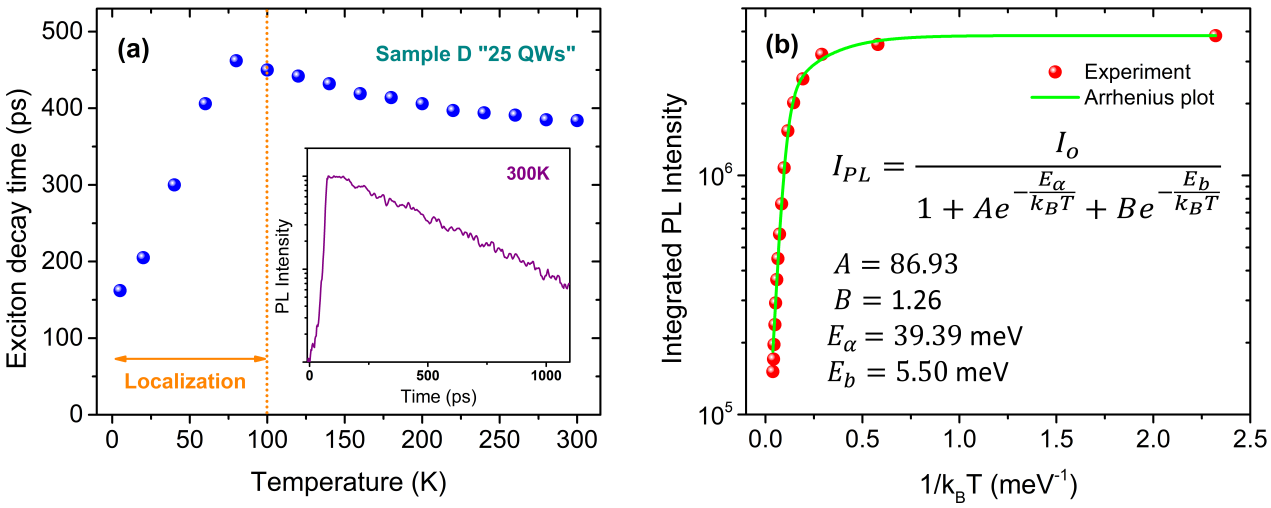

Figure 4.7: (a) Temperature dependence of non-polar QW-exciton lifetimes in the range from 5 K up to 300 K under low optical excitation. The inset shows the time-resolved photoluminescence decay curve of QW-excitons acquired at 300 K. (b) Arrhenius plot of the integrated PL intensity of the exciton peak obtained during the same TRPL experiment along with the extracted parameters.

K, the decay times remain roughly stable with a slight decrease, reaching 384 ps at RT. The rapid increase until 80 K is attributed to the delocalization and the fact that the thermally-delocalized (or else free) excitons exhibit longer lifetimes. The latter illustrates the major contribution of the energy traps in reducing the e-h recombination times. On the other hand, the high decay times from 80 K up to RT reflect the high optical efficiency and suppression of the non-radiative channels in the as-grown sample. The localization temperature is taken to be up to 100 K based on the data of Figure 4.6(a). The inset plot in Figure 4.7(a) exhibits a characteristic PL decay curve of the non-polar GaN/AlGaN excitons at RT. It should be referred here that similar behavior in the exciton lifetime versus the temperature has been reported in reference [31] for an α-plane oriented non-polar GaN/AlGaN heterostructure grown on a high quality GaN crystal.

In conjunction with TRPL measurements, further analysis was made by recording the PL spectra for the corresponding temperatures during the same experiment in order to calculate the spectrally-integrated PL intensities versus $1/k_B$T given in Figure 4.7(b). In the non-polar sample, it is visible that the integrated PL intensity decreases by only 1.5 orders of magnitude from cryogenic

temperatures up to RT, demonstrating the robust PL emission of non-polar QWs due to the elimination of internal fields in the QWs along with the reduced non-radiative channels within the structure. To have a better overview, we fitted the particular set of data with an Arrhenious curve considering two activation energies (inset of Figure 4.7(b)). The model gave an activation energy of E_a = 39.39 meV and the other of E_b = 5.50 meV. The first value cannot be attributed to the thermal escape of excitons above the AlGaN barriers, as it was the case in the polar sample. Perhaps the suppression of the over-the-barrier escape of carriers can be attributed to the increased energy barrier height (10 % Al) in this sample. The bandgap energy difference between the well and the barrier is considered to be in the range of 150 - 200 meV. On the other hand, the value of $\sim$ 40 meV is in the range of the binding energy (E_B) of the GaN/AlGaN QW excitons [3, 4]. A similar amount for the high temperature activation energy has been reported also in references [12, 31, 32]. This highlights the fact that at high temperatures the main non-radiative mechanism is due to exciton dissociation. Regarding, the smaller and less probable activation energy of 5.5 meV is believed to be a consequence of dissociation from the localized states since it has comparable energy with the 12 meV localization energy obtained by the Varshni fitting (Figure 4.6(a)).

Following the analysis given in reference [33], we decomposed the exciton decay times into radiative (τ_r) and non-radiative (τ_{nr}) terms as shown in Figure 4.8. Taking into consideration the delocalization of excitons (orange-dashed line in Figure 4.5(a)), we utilized as a fitting parameter the radiative efficiency at 100 K (n_o(100K)) instead of the one at 5 K, while its value ranged between 0.1 and 1 to account for wrong estimations in τ_r and τ_{nr}. For the n_o(100K) = 0.5, the exciton radiative decay at 300 K reaches an average value of 7.8 ns. On the other hand, the non-radiative decay had in general a converging behavior vs T, which for the same value of n_o(100K) the RT decay was 403 ps. Despite the domination of non-radiative channels at room temperature, non-polar QW excitons exhibit markedly high RT exciton lifetimes. For clarity, the RT τ_{exc}

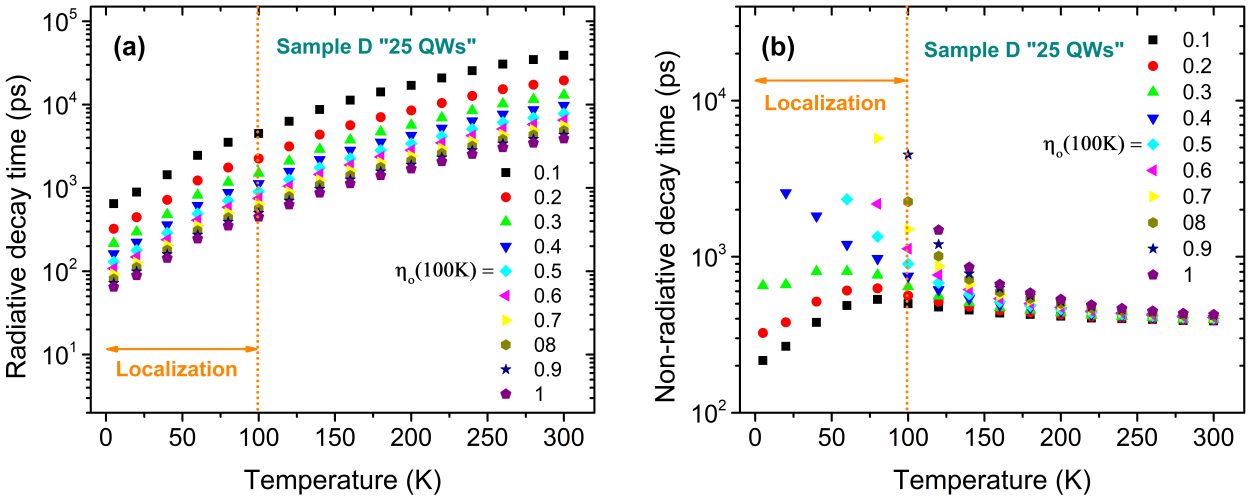

Figure 4.8: (a) Radiative (τ_r) and (b) non-radiative (τ_{nr}) lifetime variation as vs temperature for a range of η_o values from 0.1 up to 1.

value of $\sim$ 384 ps can be compared again to the polar one of $\sim$ 275 ps acquired in our best polar samples [34]. This is a clear sign that the as-grown m-plane samples are of sufficiently high optical quality in which defect-related processes (eg. dislocation density) are relatively limited, confirming hence partially the assumption that non-polar structures grown on high quality GaN substrates have enhanced characteristics.

4.6 Fabrication of non-polar GaN/AlGaN membranes

At this point, the surface of the as-grown sample was patterned into square mesas 1-μm-deep with an area of 45 μm x 45 μm up to 155 μm x 155 μm with the use of photolithographic and reactive ion etching process steps. This enables the lateral undercut PEC-etching of the non-polar InGaN layer for the separation of the non-polar structure into a thin membrane similar to the previous polar membrane fabrication. Especially for this work, the orientation of the photo-lithographic mask was such that the produced mesas edges follow the two vertical orientations (c- and α-axis) of the GaN crystal. These orientations were known from the rectangular shape of the GaN substrate as defined by the company's data-sheet characteristics. It should be mentioned here that an

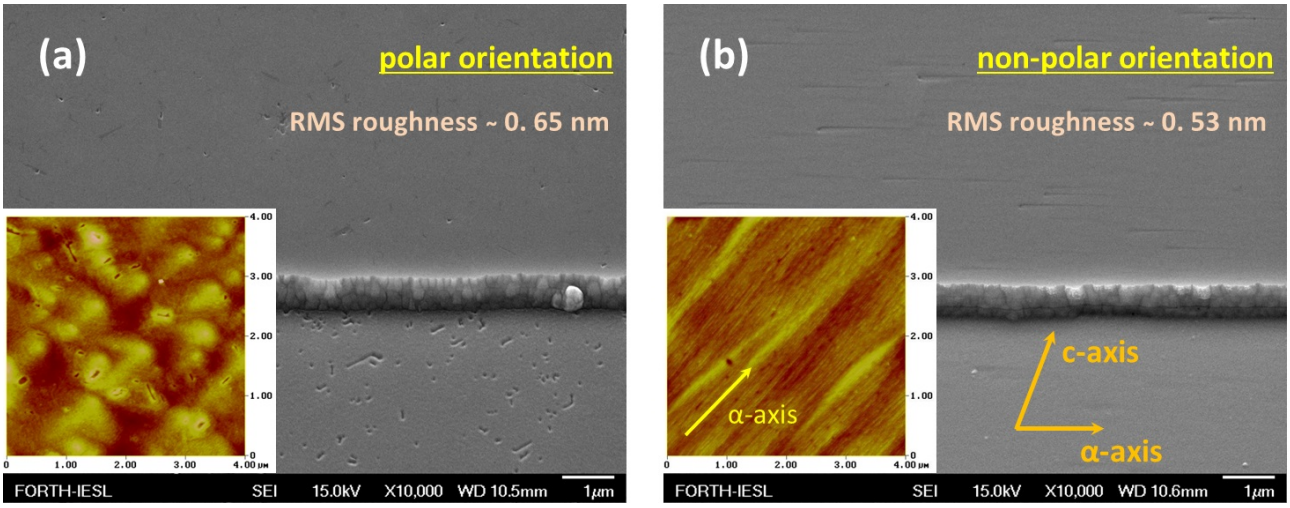

Figure 4.9: Scanning electron microscopy images of as-grown (a) polar [0001] and (b) non-polar [$1\bar{1}00$] GaN/AlGaN samples right after mesa patterning. The inset AFM images were acquired on the as-grown surfaces, revealing an RMS roughness of 0.65 nm (polar) and a 0.53 nm (non-polar) over an area of 4 μm x 4 μm. In the non-polar sample are indicated the in-plane orientations.

additional XRD analysis was performed in each of the two axis orientations prior to patterning, where the c-axis scan was obtained to have a FWHM of 0.028 angle degrees in contrast to the value of 0.024 measured along the α-axis (not shown). The particular low FWHM values indicate once again the high quality of the substrate in comparison to the growth on other substrates [26]. The ratio in the intensity of the XRD peaks was around 5 : 4. For visualization of the surface morphology, Figure 4.9 shows the scanning electron microscopy (SEM) images of a polar [0001] and non-polar [$1\bar{1}00$] oriented surfaces near the edge of the referred mesas. The inset AFM images acquired in the tapping mode gave a root-mean-square (RMS) roughness of 0.65 nm (polar) and 0.53 nm (non-polar) measured over an area of 4 μm x 4 μm. The polar sample does not seem to have any particular pattern on the surface. In contrast, the non-polar surface exhibits oriented stripes along the α-axis that are more distinct in the AFM image. The latter observation has been confirmed and discussed also by other experimental and theoretical reports [25,35] and is attributed to the reduced diffusion barrier, exhibiting Gallium atoms along the α-direction.

The etching procedure was performed once again by attaching the sample on an electrochemical cell with embedded diluted KOH ($4{\cdot}10^{-4}$ M) solution,

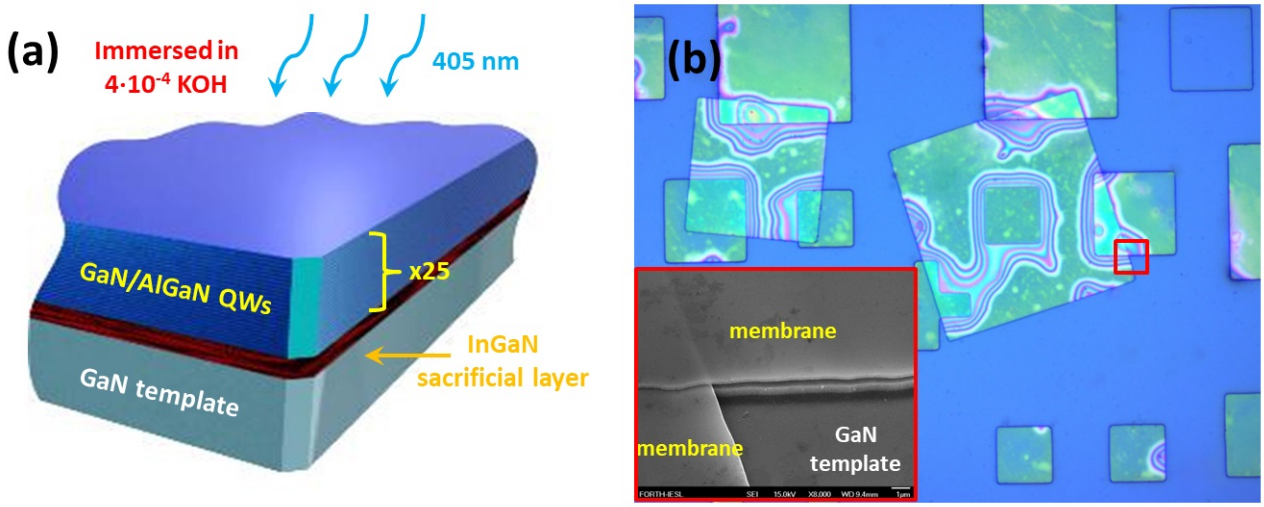

Figure 4.10: (a) Schematic of the bandgap-selective PEC-etching method for non-polar membrane separation. (b) Optical microscope image of a PEC-etched region with membranes varying from 45×45 μm^2 up to 155×155 μm^2. The inset SEM image shows the region indicated by the red square in the optical image.

allowing us to etch an active area of $7.8{\cdot}10^{-3}$ cm^2 by a continuous wave 405-nm diode laser illumination of around 4.5 mW, as shown in the illustration of Figure 4.10(a). The applied reverse bias for the successful non-polar membrane separation was around 4 V while the PEC-etching was left to run for an overall time of approximately 45 minutes. Despite the earlier XRD and PL observation that the InGaN layer did not have the desired In-percentage, the lateral etching of the sacrificial layer was able to occur without any problems in the specific non-polar sample as illustrated by the blueish-colored membranes which have left their original positions as shown clearly in Figure 4.10(b). The SEM image in the inset depicts the red-squared region marked in the optical image, where the membranes have been detached and shuffled during processing with other ones without breaking. This observation demonstrates the robustness of the non-polar membranes considering the fact that their total thickness is only $\sim$ 200 nm. The unintentional shuffling occurred when blowing the sample with nitrogen to remove the deionized (DI) water droplets, utilized after each PEC-etching experiment. It should be noted that the feasibility to obtain an ultra-low root-mean-square (RMS) roughness on the bottom-etched surfaces of

the free-standing III-nitride membranes offers a novel microcavity production in contrast to previous solutions that were encountered with low optical quality. Our non-polar PEC-etching achievement paves the way for even more efficient all-dielectric DBR GaN-based microcavities which could play a vital role in reduced polariton lasing thresholds compared to the already demonstrated in polar devices.

After PEC-etching, the free-standing non-polar membranes with embedded $\times 25$ $GaN/Al_{0.1}Ga_{0.9}N$ QWs were transferred one by one on other substrates by the already developed dry-transfer method with the use of a probe station. The transfer of membranes on double-polished Sapphire substrate allowed to perform polarization-resolved μ-photoluminescence (μ-PL) and μ-transmittance (μ-T) measurements. For microcavity fabrication, the membranes were transferred onto a bottom 10-pair SiO_2/Ta_2O_5 DBR deposited by e-beam evaporation on a Si substrate, which had been characterized earlier by reflectivity to confirm that the stopband is centered at the right wavelength position (Figure 3.10(a)). The polarized PL spectra of a bare membrane attached on a Sapphire substrate were obtained by utilizing a Glan-Taylor polarizer at the entrance of the spectrograph. The rotation of the polarizer from 0 up to 350 angle degrees with a step of 10 degrees revealed as expected a polarization dependence in the room temperature photoluminescence (contour plot in Figure 4.11(a)). In the specific data, the PL emission at 0° (and 180°) refers to E//c polarization while 90° (and 270°) refers to E//α. The drastic dependence arises from the already discussed anisotropic behavior of the A_{QW} (E//α) and B_{QW} (E//c) QW-excitons [3, 4]. The C_{QW} has also a contribution along the E//c polarization.

In Figure 4.11(a), the E//α and E//c polarizations are indicated by arrows, while the location of the two excitons with the dashed-dotted and dashed lines. It should be noted that the non-negligible decrease in the recorded PL emission at the range 180° - 350° resulted from a slight misalignment during the rotation of the polarizer and not from the non-polar sample itself. The PL peaks in the two polarizations have an energy difference of around 11 meV. As discussed earlier,

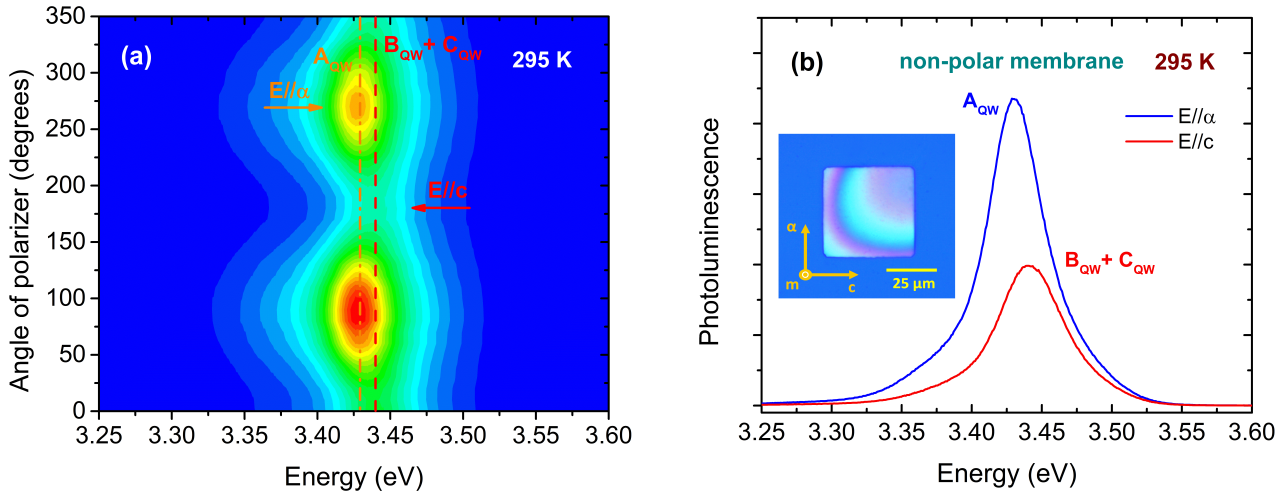

Figure 4.11: (a) Contour plot of the room temperature photoluminescence in non-polar membrane with embedded 25 GaN/AlGaN QWs by rotating a polarizer from 0 up to 350 degrees and (b) the photoluminescence only at the E//α and E//c polarizations. The inset is an optical of a transferred 45 μm x 45 μm non-polar membrane.

the low energy peak comes predominantly from free A_{QW} excitons, while the higher energy peak (E//c) is a mixture of B_{QW} and C_{QW} excitons. In contrast to the B_{QW} + C_{QW} peak, the A_{QW} exciton has obviously higher PL intensity as observed also in the as-grown structure, but here the respective ratio was a bit larger 9 : 4. The increased PL intensity of A_{QW} at RT is attributed to the higher occupancy of the thermally-de-trapped A_{QW} excitons. In the particular set of measurements, the FWHM of the two PL signals was measured to be 48 meV for the A_{QW} and 57 meV for the B_{QW} + C_{QW}.

In the work of Rossbach at al. [3], they performed k.p calculations for an m-plane GaN layer pseudomorphically grown on AlGaN to describe the relative oscillator strengths of the main exciton transitions. As it is clarified, there is a non-trivial modification in the oscillator strengths as a function of Al content due to the compressive strain affecting GaN. Based on their model for a $\sim$ 7 % Al and $1.7{\cdot}10^{-3}$ strain along the growth direction (ϵ_{mm}), the relative oscillator strengths of the QW excitons are distributed as 0.92 (A_{QW}), 0.05 (B_{QW}) and 0.04 (C_{QW}) for the E//α while 0.06 (A_{QW}), 0.87 (B_{QW}) and 0.11 (C_{QW}) for the E//c polarization. From our observations, it is believed that the referred values must be relatively close to the ones exhibited by our produced superlattice structure

when it is in the free-standing membrane form. From the stated polarization selection rules, it can be understood that the $B_{QW} + C_{QW}$ seem to have a small contribution to the PL signal in E//α and respectively the A_{QW} in the E//c. This could explain in part the relatively large FWHM in both polarizations. The inset optical image in Figure 4.11(b) shows a transferred 45 μm x 45 μm non-polar membrane. As indicated, the in-plane axes were designed to be parallel to the edges of the membranes.

4.7 Optical density in non-polar QWs

To derive the optical density (OD) and absorption coefficient of the $\times$25 non-polar $GaN/Al_{0.1}Ga_{0.9}N$ QWs and further evaluate their oscillator strength properties, we acquired the room temperature μ-transmittance spectra given in Figure 4.12(a) in the two in-plane polarizations (E//α and E//c) from membranes transferred on double-polished Sapphire substrates. As depicted in Figure 4.12(a), the μ-T spectra exhibit a Fabry-Perot oscillation behavior similar to the polar bulk and QW membranes discussed in Chapters 2 and 3, illustrating again the air / nitride / air configuration. Then, by employing the standing wave methodology developed in the previous chapters, it was possible to extrapolate the optical density spectra given in Figure 4.12(b). In Figure 4.12(a), the slight shift between the two spectra discrepancy in the transparent region is due to birefringence, while at the exciton absorption (3.47 - 3.48 eV) due to dichroism. Some contribution from chromatic aberration in the optical components is also present at lower energies ($\leq$ 2.6 eV). The fitting of the Fabry-Perot oscillations in the depicted μ-T spectra give a refractive index difference (Δn = n_e - n_o) of about 0.025 in the measured energy region. This value is compatible with other reports [17, 21]. Moreover, the fitting allowed also the estimation of the membrane thickness of 196 nm in this case, confirming that the fabricated non-polar membranes contain only the designed active region made of the "$\times$25 QWs". In connection with the reflectivity stopband of the bottom DBR, the

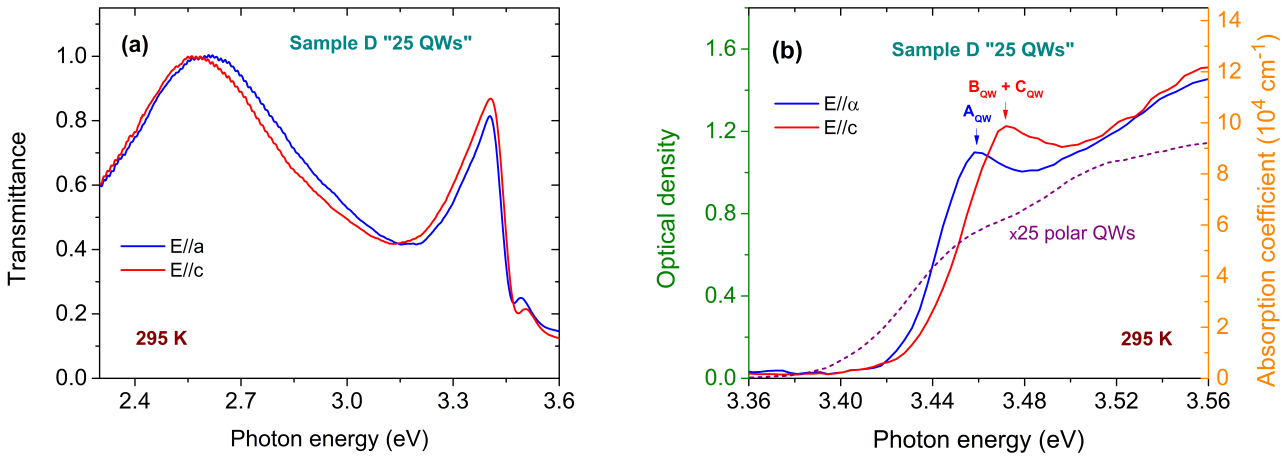

Figure 4.12: (a) Room temperature μ-transmittance spectra at E//α and E//c in a non-polar membrane with embedded $\times$25 GaN/AlGaN QWs. (b) The optical density spectra extracted from the data shown in (a). For comparison, the optical density in $\times$25 polar QWs is also shown in dashed line.

membrane thickness is a critical parameter for the design of the top DBR mirror, and thus, the fabrication of the complete microcavity in the following stage.

The extracted OD spectra shown in Figure 4.12(b) exhibit two excitonic features distanced by about 12 meV. Based on the polarization-resolved data discussed earlier, the lower-energy peak for E//α is attributed mainly to A_{QW} exciton while the higher energy for E//c to B_{QW} + C_{QW} excitons. The E//c peak appears sensibly stronger compared to the E//α configuration. This can be explained by the joint contribution of the to B_{QW} + C_{QW} exciton and possibly due to stronger overlapping with higher excited continuum states. The fitting of the excitonic peaks with Gaussian curves gives a FWHM linewidth of 37 meV for the E//α and 45 meV for the E//c polarization, which are slightly smaller than the ones obtained from the PL spectra. In addition, the integration of the OD(E) under the two Gaussian curves in combination with Equation 3.2 yielded an "ordinary" oscillator strength per 5-nm-thick non-polar GaN/AlGaN QW of $4.0{\cdot}10^{13}$ cm^{-2} and an "extra-ordinary" one of $5.6{\cdot}10^{13}$ cm^{-2}. These values are close to the $4.5{\cdot}10^{13}$ cm^{-2} obtained for the 2.7-nm-thick polar GaN/AlGaN QW (Chapter 3). The short-dashed line in Figure 4.12(b) corresponds to the unpolarized μ-T spectrum of an identical c-plane structure. From the polar

OD curve, it was difficult to extract the respective polar oscillator strength per 5-nm-thick QW. Undeniably, between the 5-nm-thick polar and non-polar QW-structures, the interaction of non-polar excitons with light outweighs that of polar excitons since the optical matrix elements are much larger based on the absence of the internal field. The relative mis-balance between the two polarizations is confirmed also by other researchers [11]. The OD_{exc} per QW in our case is attained to be 4.4 % for the ordinary electric field component and 4.9 % for the extra-ordinary one. On the right-hand scale in Figure 4.12(b), is depicted the absorption coefficient based on Equation 3.1, which is in average about $3.5{\cdot}10^4$ cm^{-1} lower than the result of $13{\cdot}10^4$ cm^{-1} found in the polar 2.7-nm-thick GaN/AlGaN QW case (Figure 3.14).

4.8 Anisotropic polariton emission at RT

To investigate the strong coupling regime in the $[1\bar{1}00]$ orientation, a final processing step is required to produce a fully-operational all-dielectric DBR microcavity device. This step is the e-beam deposition of a 4-pair SiO_2/Ta_2O_5 top DBR mirror on top of the non-polar GaN/AlGaN membranes lying on a 10-pair bottom SiO_2/Ta_2O_5, as shown in the previous chapter. By utilizing oxide alternating pairs, there is a remarkable photon-confinement in contrast to nitride-based DBR mirrors. The air-gap/nitride DBR mirror configuration is another alternative for a DBR with extreme refractive index contrast, however, earlier reports using this approach [17] have not been totally convincing. Note that in the particular microcavity configuration used here, the SiO_2 is the low refractive index oxide and is the initial layer placed in contact to both sides of the non-polar membrane. As demonstrated for the [0001]-oriented microcavities in Chapter 3, these dielectric mirrors are sufficient to enable robust polariton operation up to room temperature conditions by using only a few number of pairs in the top mirror. This occurs mainly due to the increased peak reflectivity values of the DBR mirrors ensuring an enhanced light confinement between the

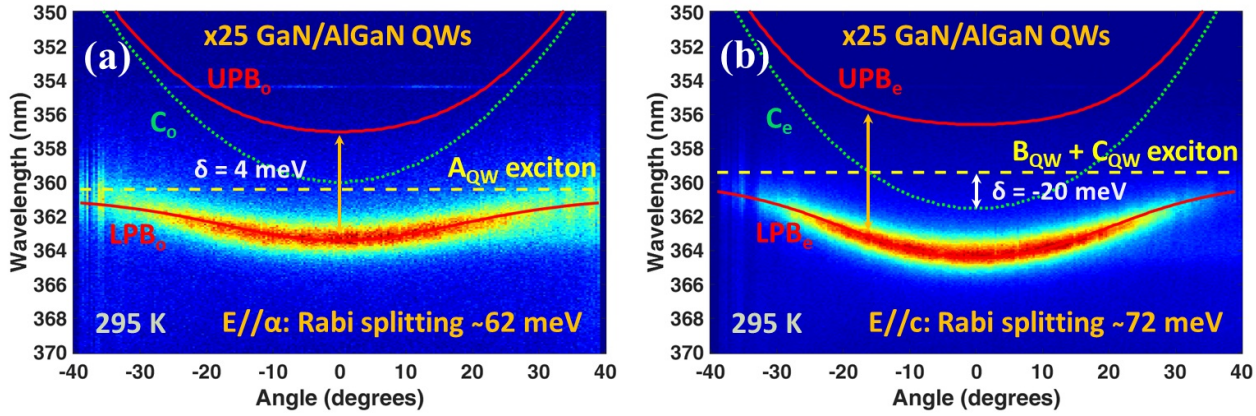

Figure 4.13: Room temperature k-space μ-PL imaging of a $3\lambda_o/2n$-microcavity with a 4-pair top and a 10-pair bottom DBR mirror exhibiting a Rabi splitting of (a) 62 meV in the E//α and (b) of 68 meV in the E//c polarization. The ordinary (C_o) and extraordinary (C_e) cavity modes (dotted lines), the polarized A and B exciton levels (dashed lines), as well as the simulated lower- and upper-polariton branches (solid curves) are also shown. The difference in the cavity modes arises due to birefringence of the non-polar GaN and AlGaN layers.

two DBR's. Additionally, the specific pair exhibits wide reflectivity stopbands and is thus an appropriate solution for polariton devices with high Rabi splitting values. The referred characteristics are enabled by the high index difference (Δn = 0.85) of the respective oxide materials. In the obtained non-polar GaN/AlGaN microcavities, room temperature angle-resolved μ-PL experiments took place by optically exciting the samples at normal incidence with a cw laser emitting at 325 nm (3.804 eV) focused down to a 9 μm spot in diameter while for the acquisition of the μ-PL signal, the standard k-space imaging setup described elsewhere (Appendix E) was utilized to record the far-field spectra with the use of an aspherical lens having a 0.63 numerical aperture (NA). The specific NA, as mentioned also in Chapter 3, allows for the observation of up to $\pm$ 39° angle spread in the Fourier plane.

As it appears in Figure 4.13, when the nitride cavity layers are grown in a non-polar direction, they exhibit polarization-resolved lower polariton branches (LPBs) in the k-space imaging, in accordance with the selection rules of the non-polar orientation. Similar to polar devices [34, 36–38], upper polariton branches (UPBs) were not observed in either polarization. At low angles, the dielectric materials of the DBRs have no anisotropy in comparison to GaN-based

DBR solutions where the non-negligible anisotropy at zero angle along with the reduced width in the reflectivity stopbands can impact adversely the strong coupling observations. The polariton emission was decoupled in the two in-plane electric field components (E//α and E//c), by placing a Glan-Taylor prism polarizer in the collection path just before the entrance of the spectrograph. Indeed, as experimentally confirmed in both configurations (Figure 4.13), there is a characteristic flattening or anti-crossing at large angles illustrating that the device operates under the strong coupling regime. The two lower polariton branches (LPB_o and LPB_e) can be fitted taking into account the anisotropic oscillator strength in the two polarizations. Specifically, LPB_o arises due to strong-coupling between the "A_{QW}" exciton peak (Figure 4.12(b)) and the "C_o" cavity mode (dashed curve in Figure 4.13(a)). Likewise, LPB_e occurs due to interaction between the "$B_{QW} + C_{QW}$" exciton peak (Figure 4.12(b)) with the "C_e" cavity mode. In Figure 4.13, the position of the A_{QW} QW exciton is taken to be at 360.4 nm (3.440 eV) while for the $B_{QW} + C_{QW}$ QW excitons at 359.4 nm (3.450 eV).

Based on birefringence effect of GaN, where $n_e = n_o$ +0.025, the C_e cavity mode is at significantly higher wavelength than C_o ($C_e(\lambda) > C_o(\lambda)$), changing the character of the two LPBs from negatively-detuned in LPB_e to slightly positively-detuned in LPB_o. This in combination with the 40 % higher oscillator strength of the $B_{QW} + C_{QW}$ exciton peak, explains the fact that the LPB_e is at larger wavelengths compared to LPB_o. In particular, the values of the lower polariton branches at zero angle are 363.4 nm (3.411 eV) for the "ordinary LPB" and 364.1 nm (3.402 eV) for the "extra-ordinary LPB". Taking into account the material's positive linear birefringence ($n_o < n_e$) in the TMM model, the best fittings for the expected ordinary (C_o) and extraordinary (C_e) cavity modes (dotted lines) were deduced to be at 360 nm (3.444 eV) and 361.6 nm (3.4287 eV) for $k_{//} = 0$ for a Δn of 0.025. Therefore, the wavelength difference between the two cavity modes resulted to be 1.6 nm (15.3 meV). Accordingly, the detunings for the two polarizations in the measured microcavity are 4 meV (E//α) and -20

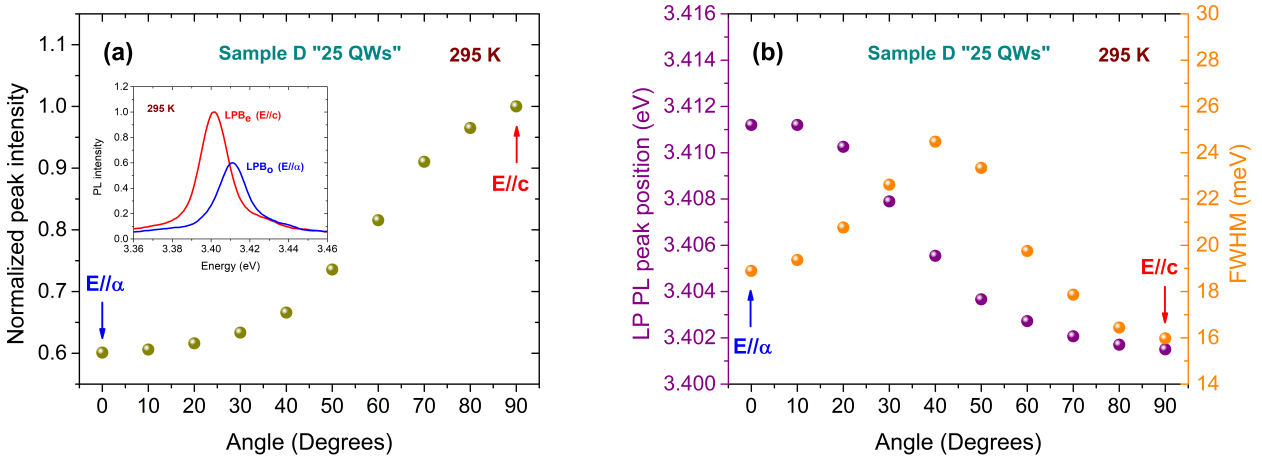

Figure 4.14: (a) Normalized μ-PL peak intensity at $k_{//} = 0$ as a function of the polarization angle. The inset shows the μ-PL at E//α and E//c. (b) Lower polariton peak position along with the corresponding FWHM at $k_{//} = 0$.

meV (E//c). By fitting the polariton dispersions of Figure 4.13 with the linear Hamiltonian model (Section 1.7), using a coupling constant of around 31 meV for the E//α and 37 meV for the E//c, the corresponding Rabi splittings are 62 meV for E//α and 72 meV for E//c.

Further analysis of polarization-resolved data are presented in Figure 4.14. In Figure 4.14(a) is plotted the normalized PL peak intensity as a function of polarization angle, from which we deduce that the PL peak almost doubles in the photon-like (E//c) LPB_e. One possible reason for this is the reduced lifetime (low Q-factor) of polaritons when they are more photonic. The inset plot of the same figure shows the μ-PL spectra of the two orthogonally-polarized LPBs at $k_{//} = 0$ where the LPB_e emission exceeds the LPB_o one. Additionally, in Figure 4.14(b) is presented the lower polariton (LP) PL peak position at $k_{//} = 0$ as a function of polarization angle. For the E//α polarization, the measured energy position of the PL peak is at higher energy and gradually falls around 10 meV to the energy position of the LPB_e polarized at E//c. In the same graph is given the FWHM of the μ-PL versus the polarization angle. The two branches seem to have almost 3 meV difference in their FWHM linewidth while the increased values around 45 degrees correspond to the mixed

emission branches. The above k-space imaging analysis shows that our produced non-polar structure has much more complex polariton characteristics than the previously studied polar devices of Chapter 3. To some extent, one can expect to engineer the polarized polariton branches by adjusting the oscillator strength of the A_{QW}, B_{QW} and C_{QW} QW excitons in the two polarizations [3] as well as the cavity detuning parameter. Apart from the original design, the polariton properties can be tuned by changing the lattice temperature which in our case means to work at cryogenic temperatures as discussed in the next section.

4.9 Anisotropic polariton emission at low T

When the microcavity devices are cooled at cryogenic temperatures with the use of a closed-cycle cryostat, the excitons and cavity modes are shifted towards higher energies, and thus, enable for the thermal tuning of the polariton branches. In contrast to the cavity modes, the excitons have usually a larger shift in energy and play the principal role in the overall detuning. The particular tuning increases the photon fraction at low T's or the exciton fraction at high T's and modifies the polariton branches from mainly photonic or mainly excitonic. To illustrate the main differences between c- and m-growth, in Figure 4.15, we present the unpolarized k-space μ-PL images of a polar ($\times$38 GaN/AlGaN) and a non-polar ($\times$25 GaN/AlGaN) $3\lambda_o/2n$ microcavity made by a 4-pair top and a 10-pair bottom DBR. In the polar sample (Figure 4.15(a)), the sharp LPB polariton curves at 100 K allow to distinguish the splitting of the TM / TE modes at large angles, between 25 - 35 degrees, which have been resolved here with a FWHM linewidth of 0.4 nm. These low FWHM values are consistent with the large negative detuning of this microcavity. In the same k-space image, the visible uncoupled excitons are also indicated by the yellow-dashed line at 354.6 nm (3.4965 eV). On the other hand, for the non-polar k-space image acquired at 200 K (Figure 4.15(b)), the distinct LPB_o and LPB_e have a wavelength difference of 0.7 nm (6.7 meV) at $k_{//} = 0$, while in the angle range of 25 - 35

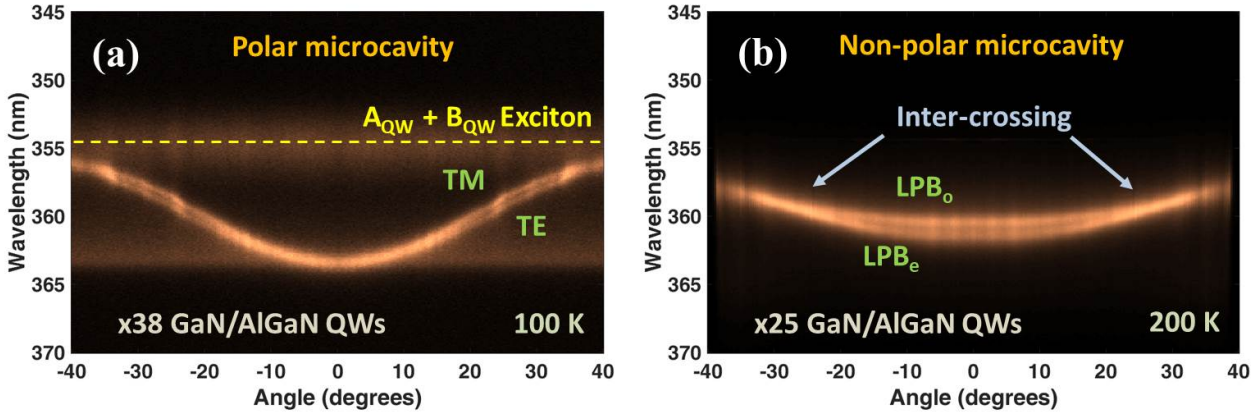

Figure 4.15: Unpolarized low temperature k-space μ-PL imaging of a (a) polar (×38 GaN/AlGaN QWs) and (b) non-polar (×25 GaN/AlGaN QWs) $3\lambda_o/2$n-microcavity with a 4-pair top and a 10-pair bottom DBR mirror. In the polar sample, the splitting at the angle range of 25 - 35 degrees arises due to TE / TM modes while in the non-polar sample at the same range there is a visible inter-crossing of the polariton modes. For the non-polar sample, the splitting at zero angle arises due to birefringence and dichroism of the GaN and AlGaN layers.

degrees indicated by the blue arrows, we observe an inter-crossing of the two polariton modes due to the previously discussed peculiar coupling of non-polar excitons with the cavity modes. Despite the fact that both structures have multiple QWs in the whole range of the active medium, as depicted in Figure 4.15, the uncoupled excitons are visible only at relatively low temperatures ($<$ 120 K).

4.10 Lasing in a non-polar microcavity

The successful non-polar microcavity fabrication and polariton observation from low to room temperature allowed us to go one step further in order to explore the possibility of polariton lasing in these microcavities. To investigate the possibility of having optical non-linearities in the $3\lambda_o/2$ microcavity, a power dependent quasi-continuous pulsed excitation was applied at normal incidence with a frequency-quadrupled Nd-YAG laser emitting at 266 nm (E_{laser} = 4.66 eV), with a repetition rate of 7.58 kHz and a 0.51 ns pulse-width. The excitation and collection was performed by the same k-space imaging setup which was aligned at the emission of GaN/AlGaN quantum well exciton states ($\sim$ 360

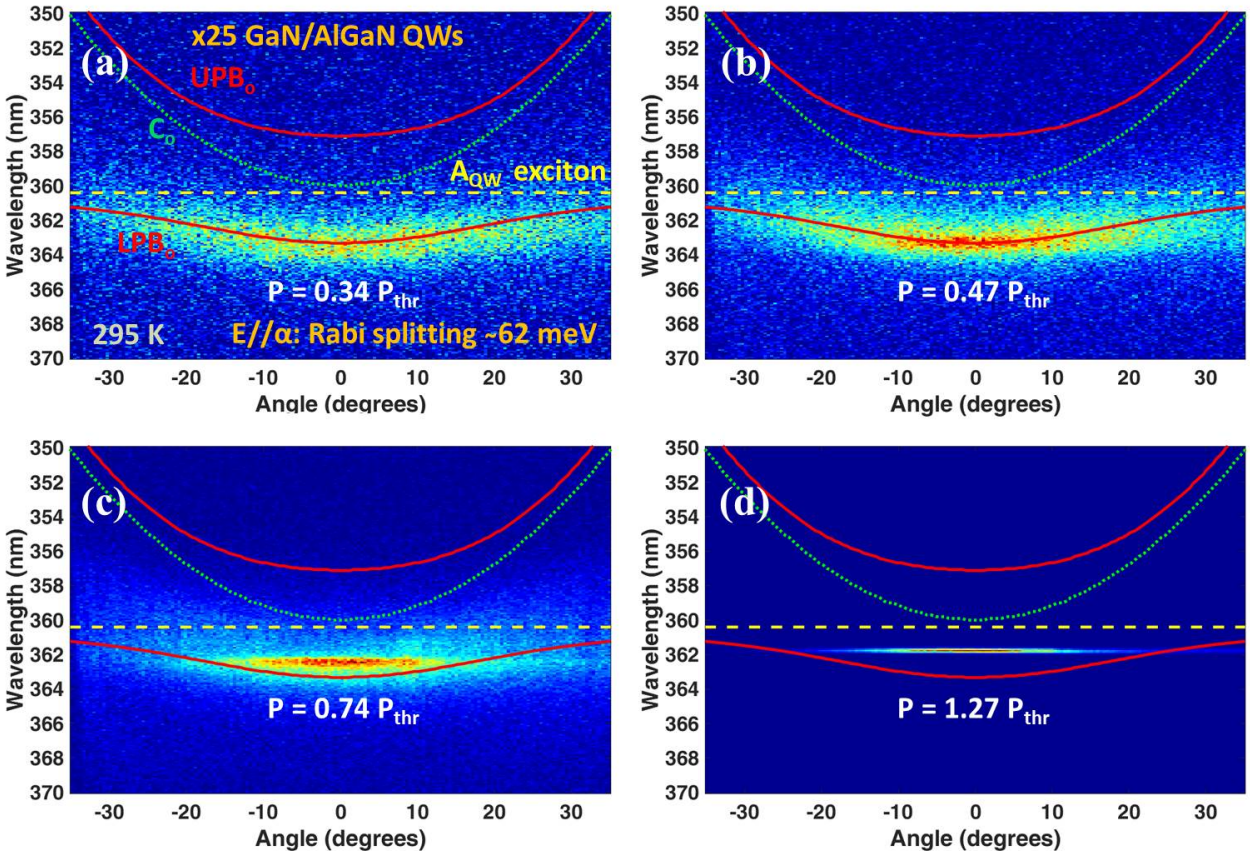

Figure 4.16: k-space μ-PL imaging acquired at RT in the E//α polarization from a 25-QW-containing $3\lambda_o/2$ microcavity under quasi-pulsed excitation by a frequency-quadrupled Nd-YAG laser emitting at 266 nm, under (a) $0.34P_{thr}$, (b) $0.47P_{thr}$, (c) $0.74P_{thr}$ and (d) $1.27P_{thr}$, with an ultra-low polariton lasing threshold of $P_{thr} = 1.5\ W/cm^2$.

nm). Further details on the excitation and collection path are given in Section 3.10 and Appendix E. In Figure 4.16 is shown the angle-resolved μ-PL of the lower polariton branch at the E//α polarization for the excitation powers (a) 0.34, (b) 0.47, (c) 0.74 and (d) 1.27 of the power density threshold (P_{thr}). Compared to our earlier achieved threshold of 4.5 W/cm^2 (Chapter 3 for $\delta > 0$ and reference [34] for $\delta < 0$), we demonstrate here that the non-polar device is capable of polariton condensation at the bottom of the trap with an even lower power threshold of 1.5 W/cm^2. At the powers of $0.47P_{thr}$ and $0.74P_{thr}$ (Figures 4.16(b-c)), the polaritons have started to massively occupy the lower energies of the LPB_o polariton branch with an obvious decrease in the linewidth. Further increase of the power above threshold ($1.27P_{thr}$), as

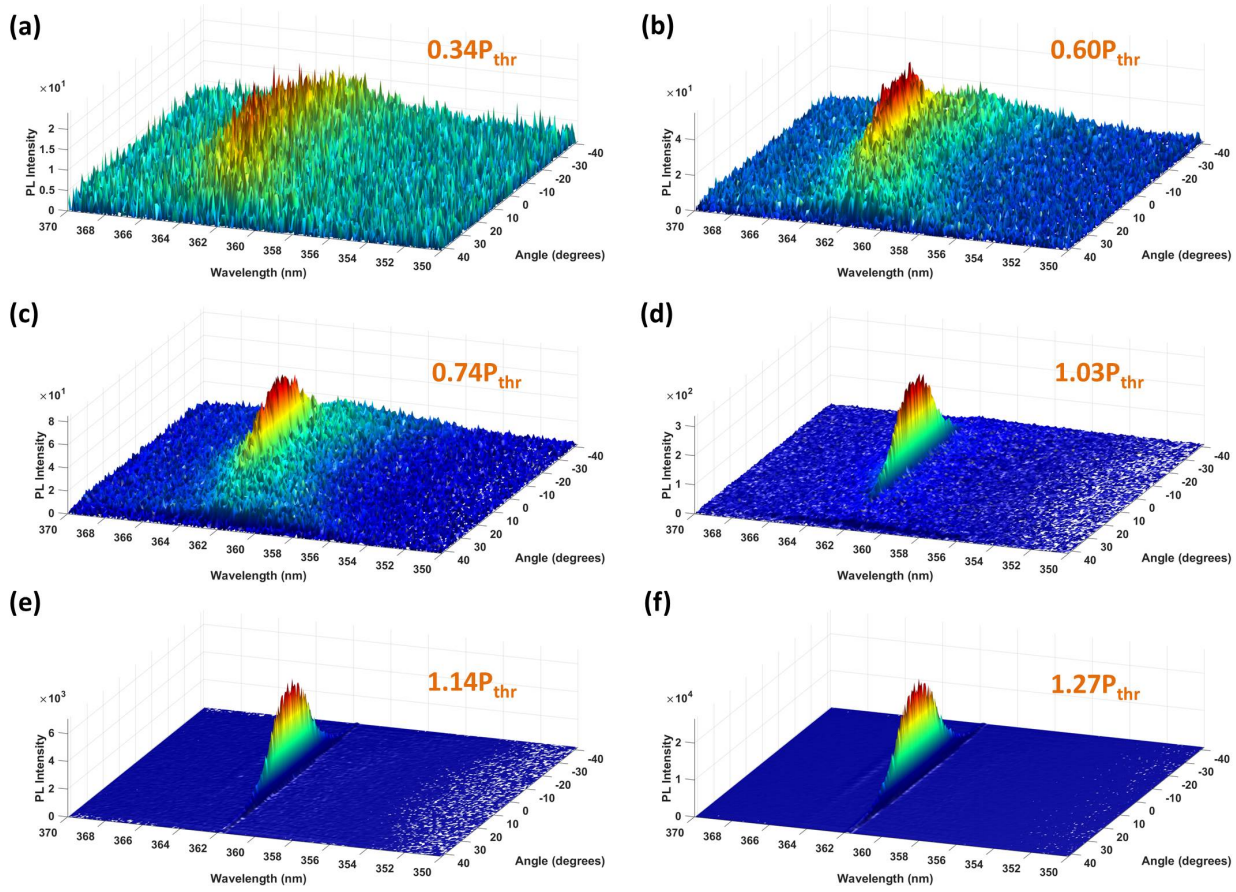

Figure 4.17: Angle-resolved μ-PL imaging acquired at ambient conditions in the E//α polarization from a 25-QW-containing $3\lambda_o/2$ microcavity under quasi-pulsed excitation by a frequency-quadrupled Nd-YAG laser emitting at 266 nm, under (a) $0.34P_{thr}$, (b) $0.60P_{thr}$, (c) $0.74P_{thr}$, (d) $1.03P_{thr}$, (e) $1.14P_{thr}$ and (f) $1.27P_{thr}$, where it is demonstrated ultra-low polariton lasing threshold of $P_{thr} = 1.5\ W/cm^2$.

presented in Figure 4.16(d), leads to polariton lasing emission at $k_{//} = 0$ which is remarkably sharp ($\sim$ 2 meV) and intense (Figures 4.17(d-f) and 4.18(b)). On the other hand, this non-linear behavior was not observed for the E//c polarization, which merits further understanding. It should be noted that due to the anisotropic oscillator strength and polariton dispersion characteristics in the non-polar microcavities, the polariton relaxation and recombination dynamics is different in each polarization. Similar to the polar devices discussed in Chapter 3, the LPB_o in our case is exciton-like due to the almost zero detuning, while LPB_e is photon-like due to the negative detuning (Figure 4.13). The 3D k-space images in Figure 4.17 depict the evolution of the LPB_o polariton condensate as a function of power density. By inspection, it is clear that the LPB_o condensate

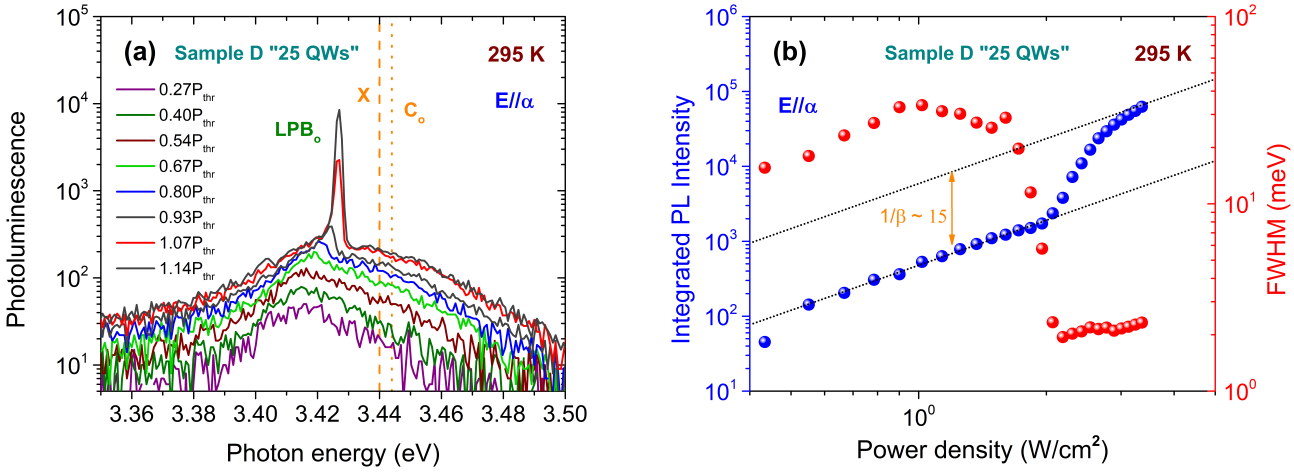

Figure 4.18: (a) PL intensity spectra at $k_{//} = 0$ for a range of excitation powers illustrating the polariton narrowing and non-linear increase of PL intensity under polariton lasing conditions. (b) The integrated PL intensity versus the excitation power density indicates a power threshold of 1.5 W/cm^2.

has a significant $k_{//}$-spread which extends to $\pm$ 10°. Similarly, large k-spreads of the polariton condensate have been observed in the positively detuned polar polariton laser of Chapter 3 (Section 3.10).

Our understanding of the experimental observations, is that the prolonged decay times due to the exciton-like nature of LPB_o in the E//α polarization provide the appropriate conditions for the creation of a large population of polaritons which is necessary for the macroscopic condensation and account for the observation of polariton lasing only in the E//α configuration. In addition, as has been already explained in Section 3.10 and reported also in other works [39], the slightly positive detuning ($\delta \sim$ 4 meV) provides much faster relaxation times, compared to the negatively-detuned ($\delta \sim$ -20 meV) branch, which further facilitate the system to pass in the condensation regime. In this device, based on Equation C.7 and the exciton decay time at RT of 384 ps, the polariton lifetime (τ_{pol}) at $k_{//} = 0$ of the LPB_o is calculated to be 0.40 ps, while the LPB_e-polaritons have 10 % less of mentioned lifetime. Such a small difference cannot by itself explain why it was not possible to observe polariton lasing in the LPB_e branch. Therefore, we believe that lasing action is achieved due to the slightly larger mass of polaritons "living" in the exciton-like branch since it

increases the scattering probability, which finally, enhances the energy transfer or loss among them. It is important that the trap's depth at $k_{//} = 0$ is still sufficient to prohibit the thermal escape of polaritons at RT. To have a better insight into the polariton's lasing properties, in Figure 4.18 are presented (a) the room temperature PL spectra for a range of excitation powers along with (b) the integrated PL intensity versus power density. Clearly, polariton lasing occurs below both the exciton state (X) positioned at 3.440 eV and the cavity resonance (C_o) positioned at 3.444 eV (Figure 4.18(a)). The threshold power density is 1.5 W/cm^2 as extracted from Figure 4.18(b). This ultra-low threshold is around three times lower than our earlier state-of-the-art values for polar microcavities. Experimentally, the spontaneous emission factor (β) is measured by the ratio of the integrated intensity above and below threshold indicated by the two parallel dotted-lines (Figure 4.18(b)) and represents the fraction of the spontaneous emission that contributes to lasing action [40]. The extrapolated $1/\beta$ parameter seems to have a surprisingly low value of 15 (Figure 4.18(b)). For an ideal thresholdless laser, the β should be unity, and thus, no S-like behavior would be observed in the graph of Figure 4.18(b). The latter simply would mean that all the spontaneous emission is utilized in the gain mechanism.

From the k-space imaging data of Figure 4.16 and the PL spectra of Figure 4.18(a), it is confirmed that the microcavity remains under the strong coupling regime, even at higher excitation powers, since the simulated ordinary cavity mode (C_o) is far away from the lasing emission wavelength at $k_{//} = 0$ at all powers. Considering the blueshift of the PL intensity peak up to threshold, which is more visible in Figure 4.18(b), we deduce a shift of around 8 meV (= ΔE). This highlights again the strong polariton-polariton interactions that account in part for the ultra-low lasing threshold. From this blueshift one can obtain the corresponding exciton density (n_{exc}^{2D}) using Equation 3.3. The applied parameters to deduce n_{exc}^{2D} were an exciton fraction at $k_{//} = 0$ of $|X_o|^2$ (≈ 0.53), a binding energy of E_B ($\approx$ 40 meV) and a Bohr radius for the exciton of α_B ($\approx$ 2.8 nm) which finally yielded to be around $8{\cdot}10^{11}$ cm^{-2}. As can be observed,

this number is smaller than in the polar microcavity (Section 3.10) while it is also far below the Mott transition density ($\sim 10^{13}\ cm^{-2}$) [41]. The division by the number of QWs, yields a n_{exc}^{2D} per QW of $3.2{\cdot}10^{10}\ cm^{-2}$.

4.11 Conclusion

To summarize, in this chapter we describe the design, growth and fabrication of $3\lambda/2$ non-polar GaN-based membranes that are free of internal fields for their use in all-dielectric microcavities, by implementing them in between two oxide-based DBR mirrors. By transferring the non-polar membranes on Sapphire and performing transmittance measurements, we were able to extrapolate the optical density per QW at the exciton peak (~ 4.6 % at RT) in the two orthogonal in-plane polarizations, considering also the standing wave effect. The microcavity fabrication procedure was based on the established methodology given in Chapter 3, where an InGaN sacrificial layer is utilized for the separation of the active region after being PEC-etched. In the all-dielectric DBR microcavity device, k-space μ-PL imaging experiments permitted the observation of an anisotropic polariton emission which is modified according to the polarization selection rules based on the birefringence and dichroism in the GaN and AlGaN layers. Evidently, the device exhibited enhanced room temperature characteristics in both active polarizations with Rabi splittings of 62 (E//α) and 72 (E//c) meV. Optical pumping of the $\times$25 GaN/AlGaN QW microcavities by a pulsed laser showed an ultra-low polariton threshold of 1.5 W/cm^2 at the E//α polarization, which is three times lower than the state-of-the-art value demonstrated previously by us in the polar orientation. Polariton lasing was not observed in the E//c probably due to the photon-like dispersion of the polariton branch which does not let the system to create sufficient population for the condensation. Despite the relatively thin 4-pair top DBR, the general outcome underscores the potential of novel non-polar nitride polariton devices and encourages the fabrication of ultra-efficient polariton lasers operating at ambient conditions.

Bibliography

[1] M. A. Mastro, E. A. Imhoff, J. A. Freitas, J. K. Hite, and C. R. Eddy Jr. *"Towards a polariton-based light emitter based on non-polar GaN quantum wells"*, Solid State Commun. 149, 2039 (2009).

[2] P. Waltereit, O. Brandt, M. Ramsteiner, A. Trampert, H. T. Grahn, J. Menniger, M. Reiche, R. Uecker, P. Reiche, and K. H. Ploog. *"Growth of M-Plane GaN($1\bar{1}00$): A Way to Evade Electrical Polarization in Nitrides"*, Phys. Status Solidi A 180, 133 (2000).

[3] G. Rossbach, J. Levrat, A. Dussaigne, G. Cosendey, M. Glauser, M. Cobet, R. Butté, N. Grandjean, H. Teisseyre, M. Bockowski, I. Grzegory, and T. Suski. *"Tailoring the light-matter coupling in anisotropic microcavities: Redistribution of oscillator strength in strained m-plane GaN/AlGaN quantum wells"*, Phys. Rev. B 84, 115315 (2011).

[4] J. Levrat, G. Rossbach, A. Dussaigne, G. Cosendey, M. Glauser, M. Cobet, R.l Butté, N. Grandjean, H. Teisseyre, M. Boćkowski, I. Grzegory, and T. Suski. *"Nonlinear emission properties of an optically anisotropic GaN-based microcavity"*, Phys. Rev. B 86, 165321 (2012).

[5] R. Tao, M. Arita, S. Kako, and Y. Arakawa. *"Fabrication and optical properties of nonpolar III-nitride air-gap distributed Bragg reflector microcavities"*, Appl. Phys. Lett. 103, 201118 (2013).

[6] R. Tao, M. Arita, S. Kako, K. Kamide, and Y. Arakawa. *"Strong coupling in non-polar GaN/AlGaN microcavities with air-gap/III-nitride distributed Bragg reflectors"*, Appl. Phys. Lett. 107, 101102 (2015).

[7] P. Misra, U. Behn, O. Brandt, H. T. Grahn, B. Imer, S. Nakamura, S. P. DenBaars, and J. S. Speck. *"Polarization anisotropy in GaN films for different nonpolar orientations studied by polarized photoreflectance spectroscopy"*, Appl. Phys. Lett. 88, 161920 (2006).

[8] R. Kucharski, M. Rudzinski, M. Zajac, R. Doradzinski, J. Garczynski, L. Sierzputowski, R. Kudrawiec, J. Serafinczuk, W. Strupinski, and R. Dwilinski. *"Nonpolar GaN substrates grown by ammonothermal method"*, Appl. Phys. Lett. 95, 131119 (2009).

[9] K. Kornitzer, T. Ebner, K. Thonke, R. Sauer, C. Kirchner, V. Schwegler, M. Kamp, M. Leszczynski, I. Grzegory, and S. Porowski. *"Photoluminescence and reflectance spectroscopy of excitonic transitions in high-quality homoepitaxial GaN films"*, Phys. Rev. B 60, 1471 (1999).

[10] M. D. Craven, P. Waltereit, J. S. Speck, and S. P. DenBaars. *"Well-width dependence of photoluminescence emission from a-plane GaN/AlGaN multiple quantum wells"*, Appl. Phys. Lett. 84, 496 (2004).

[11] H. Teisseyre, C. Skierbiszewski, B. Łucznik, G. Kamler, A. Feduniewicz, M. Siekacz, T. Suski, P. Perlin, I. Grzegory, and S. Porowski. *"Free and bound excitons in GaN/AlGaN homoepitaxial quantum wells grown on bulk GaN substrate along the nonpolar (11$\bar{2}$0) direction"*, Appl. Phys. Lett. 86, 162112 (2005).

[12] H.-M. Huang, C.-Y. Chang, Y.-P. Lan, T.-C. Lu, H.-C. Kuo, and S.-C. Wang. *"Ultraviolet emission efficiency enhancement of a-plane AlGaN/GaN multiple-quantum-wells with increasing quantum well thickness"*, Appl. Phys. Lett. 100, 261901 (2012).

[13] O. Ambacher, J. Smart, J. R. Shealy, N. G. Weimann, K. Chu, M. Murphy, W. J. Schaff, L. F. Eastman, R. Dimitrov, L. Wittmer, M. Stutzmann, W. Rieger, and J. Hilsenbeck. *"Two-dimensional electron gases induced by spontaneous and piezoelectric polarization charges in N- and Ga-face AlGaN/GaN heterostructures"*, J. Appl. Phys. 85, 3222 (1999).

[14] E. Kuokstis, C. Q. Chen, M. E. Gaevski, W. H. Sun, J. W. Yang, G. Simin, M. A. Khan, H. P. Maruska, D. W. Hill, M. C. Chou, J. J. Gallagher, and B. Chai. *"Polarization effects in photoluminescence of C- and M-plane GaN/AlGaN multiple quantum wells"*, Appl. Phys. Lett. 81, 4130 (2002).

[15] P. Misra, O. Brandt, H. T. Grahn, H. Teisseyre, M. Siekacz, C. Skierbiszewski, and B. Łucznik. *"Complete in-plane polarization anisotropy of the A exciton in unstrained A-plane GaN films"*, Appl. Phys. Lett. 91, 141903 (2007)

[16] T. Zhu, A. Dussaigne, G. Christmann, C. Pinquier, E. Feltin, D. Martin, R. Butté, and N. Grandjean. *"Nonpolar GaN-based microcavity using AlN/GaN distributed Bragg reflector"*, Appl. Phys. Lett. 92, 061114 (2008).

[17] R. Tao, M. Arita, S. Kako, and Y. Arakawa. *"Optical anisotropy of m-plane nitride air-gap distributed Bragg reflector microcavities"*, Phys. Status Solidi C 11, 840 (2014).

[18] B. Rau, P. Waltereit, O. Brandt, M. Ramsteiner, K. H. Ploog, J. Puls, and F. Henneberger. *"In-plane polarization anisotropy of the spontaneous emission of M-plane GaN/(Al,Ga)N quantum wells"*, Appl. Phys. Lett. 77, 3343 (2000).

[19] A. Arora and S. Ghosh. *"Polarization of emission from non-polar III-nitride quantum wells: The influence of confinement"*, J. Phys. D Appl. Phys. 47, 045101 (2014).

[20] D. M. Schaadt, O. Brandt, S. Ghosh, T. Flissikowski, U. Jahn, and H. T. Grahn. *"Polarization-dependent beam switch based on an M-plane GaN/AlN distributed Bragg reflector"*, Appl. Phys. Lett. 90, 231117 (2007).

[21] S. Shokhovets, R. Goldhahn, G. Gobsch, S. Piekh, R. Lantier, A. Rizzi, V. Lebedev, and W. Richter. *"Determination of the anisotropic dielectric function for wurtzite AlN and GaN by spectroscopic ellipsometry"*, J. Appl. Phys. 94, 307 (2003).

[22] P. Waltereit, O. Brandt, A. Trampert, H. T. Grahn, J. Menniger, M. Ramsteiner, M. Reiche, and K. H. Ploog. *"Nitride semiconductors free of electrostatic fields for efficient white-emitting diodes"*, Nature 406, 865 (2000).

[23] M. Gladysiewicz and R. Kudrawiec. *"Broadening of photoluminescence for inhomogeneous polar and non-polar InGaN/GaN quantum wells"*, Phys. Status Solidi C 9, 830 (2012).

[24] S. Schulz and E. P. O'Reilly. *"Excitonic binding energies in non-polar GaN quantum wells"*, Phys. Status Solidi C 7, 1900 (2010).

[25] R. Armitage and H. Hirayama. *"M-plane GaN grown on m-sapphire by metalorganic vapor phase epitaxy"*, Appl. Phys. Lett. 92, 092121 (2008).

[26] Q. S. Paduano, D. W. Weyburne, and D. H. Tomich. *"Growth and properties of m-plane GaN on m-plane sapphire by metalorganic chemical vapor deposition"*, J. Cryst. Growth 367, 104 (2013).

[27] P. Waltereit, O. Brandt, M. Ramsteiner, R. Uecker, P. Reiche, and K. H. Ploog. *"Growth of M-plane GaN ($1\bar{1}00$) on γ-$LiAlO_2$ (100)"*, J. Cryst. Growth 218, 143 (2000).

[28] S. Ghosh, P. Waltereit, O. Brandt, H. T. Grahn, and K. H. Ploog. *"Polarization-dependent spectroscopic study of M-plane GaN on γ-$LiAlO_2$"*, Appl. Phys. Lett. 80, 413 (2002).

[29] R. Jayaprakash, F. G. Kalaitzakis, M. Kayambaki, K. Tsagaraki, E. Monroy, and N. T. Pelekanos. *"Ultra-smooth GaN membranes by photo-electrochemical etching for photonic applications"*, J. Mater. Sci. 49, 4018 (2014).

[30] H. T. Grahn. *"Nonpolar-Oriented GaN Films for Polarization-Sensitive and Narrow-Band Photodetectors"*, MRS Bulletin 34, 314 (2009).

[31] P. Corfdir, J. Levrat, A. Dussaigne, P. Lefebvre, H. Teisseyre, I. Grzegory, T. Suski, J.-D. Ganière, N. Grandjean, and B. Deveaud-Plédran. *"Intrinsic dynamics of weakly and strongly confined excitons in nonpolar nitride-based heterostructures"*, Phys. Rev. B 83, 245326 (2011).

[32] C. B. Lim, A. Ajay, C. Bougerol, E. Bellet-Amalric, J. Schörmann, M. Beeler, and E. Monroy. *"Effect of Al incorporation in nonpolar m-plane GaN/AlGaN multi-quantum-wells using plasma-assisted molecular-beam epitaxy"*, Phys. Status Solidi A 217, 1600849 (2017).

[33] M. Gurioli, A. Vinattieri, M. Colocci, C. Deparis, J. Massies, G. Neu, A. Bosacchi, and S. Franchi. *"Temperature dependence of the radiative and nonradiative recombination time in $GaAs/Al_xGa_{1-x}As$ quantum-well structures"*, Phys. Rev. B 44, 3115 (1991).

[34] R. Jayaprakash, F. G. Kalaitzakis, G. Christmann, K. Tsagaraki, M. Hocevar, B. Gayral, E. Monroy, and N. T. Pelekanos. *"Ultra-low threshold polariton lasing at room temperature in a GaN membrane microcavity with a zero-dimensional trap"*, Sci. Rep. 7, 5542 (2017).

[35] V. Jindala and F. Shahedipour-Sandvik. *"Computational and experimental studies on the growth of nonpolar surfaces of gallium nitride"*, J. Appl. Phys. 107, 054907 (2010).

[36] S. Christopoulos, G. Baldassarri Höger von Högersthal, A. J. D. Grundy, P. G. Lagoudakis, A. V. Kavokin, J. J. Baumberg, G. Christmann, R. Butté, E. Feltin, J.-F. Carlin, and N. Grandjean. *"Room-Temperature Polariton Lasing in Semiconductor Microcavities"*, Phys. Rev. Lett. 98, 126405 (2007).

[37] G. Christmann, R. Butté, E. Feltin, J.-F. Carlin, and N. Grandjean. *"Room temperature polariton lasing in a GaN/AlGaN multiple quantum well microcavity"*, Appl. Phys. Lett. 93, 051102 (2008).

[38] S. Faure, T. Guillet, P. Lefebvre, T. Bretagnon, and B. Gil. *"Comparison of strong coupling regimes in bulk GaAs, GaN, and ZnO semiconductor microcavities"*, Phys. Rev. B 78, 235323 (2008).

[39] A. Kavokin, J. J. Baumberg, G. Malpuech, and F. P. Laussy. *"Microcavities"*, Oxford University Press, New York (2017).

[40] G. V. Soest and A. Lagendijk. *"β factor in a random laser"*, Phys. Rev. E 65, 047601 (2002).

[41] G. Christmann, R. Butté, E. Feltin, A. Mouti, P. A. Stadelmann, A. Castilia, J.-F. Carlin, and N. Grandjean. *"Large vacuum Rabi splitting in a multiple quantum well GaN-based microcavity in the strong-coupling regime"*, Phys. Rev. B 773, 085310 (2008).

Chapter 5

Fabrication of tranferrable DBR membranes

This chapter demonstrates the possibility to fabricate a complete microcavity structure operating in the strong coupling regime with the utilization of transferrable oxide-based DBR membranes as an upper mirror for an all-dielectric DBR planar cavity along with the implementation of GaN-based membranes as an active medium in between the mirrors.

5.1 Introduction

Distributed Bragg Reflectors (DBRs) have proven over the years to be an integral part of major optoelectronic devices, such as vertical-cavity surface emitting lasers (VCSEL's) [1], resonant-cavity light emitting diodes [2], and eventually polaritonic devices [3]. As already discussed in Chapter 1, a DBR is essentially a multilayered stack of high and low refractive index materials, with a quarter-wavelength (λ/4n) thickness in each layer, where λ is the wavelength of maximum reflectivity and n the layer's refractive index. The main advantage of DBR mirrors is their ability to exhibit high reflectivity values at any desired wavelength of the electromagnetic radiation spectrum by merely adjusting the thicknesses of the individual layers. In microcavity structures where the DBRs consist of the same semiconductor system as the active region of the device, both DBR and active region are typically synthesized in the same epitaxial run. In heterogeneous cases, e.g. a dielectric DBR grown on a semiconducting active region, the dielectric materials are generally deposited ex situ by evaporation or sputtering. However, the direct deposition of a DBR on the active region does not always lead to optimal results. In particular, in the case of an active medium consisting of an ultra-thin semiconducting membrane, having a thickness from a

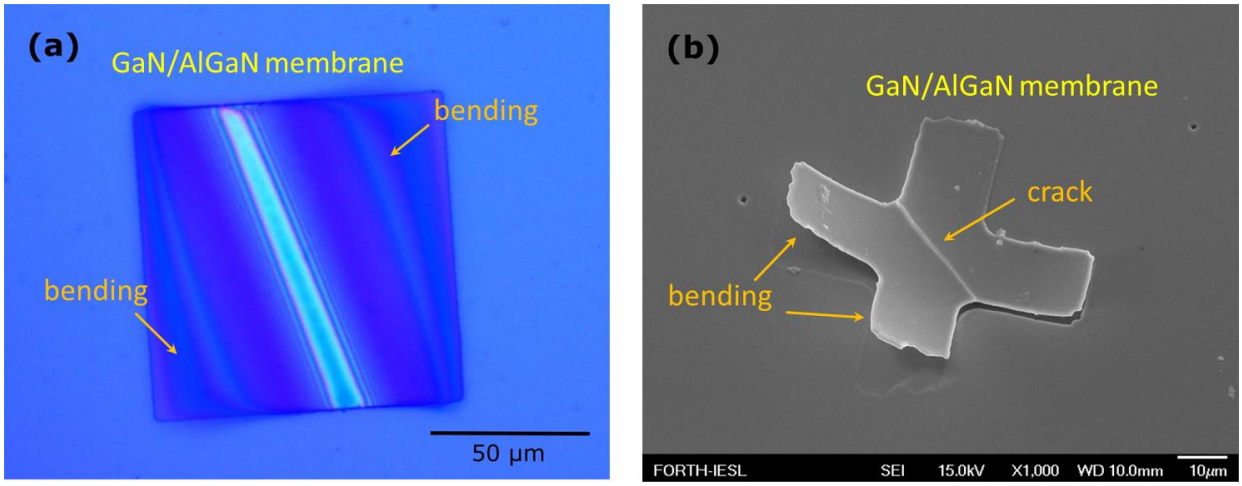

Figure 5.1: (a) Optical image of a rectangular-shaped and (b) a SEM image of a cross-shaped GaN/AlGaN membrane after the direct deposition of a 4-pair and an 8-pair top DBR at 300 °C. The thermally induced bending of the membrane is clearly visible in both cases which can lead even to cracks in the films.

few hundred nanometers down to the atomic mono-layer limit of two-dimensional systems, direct deposition of the top mirror may induce a bowing of the films due to the mismatch in thermal expansion coefficients or lattice parameters. Two examples are presented in Figure 5.1, which are clearly depicting the effect after the deposition of the top mirror on a rectangular and a cross-shaped GaN-based membrane having a thickness of 200 nm. Another example is the case of process-sensitive materials, e.g. organic thin films, where the DBR deposition process can lead to material degradation, often requiring an inorganic capping layer for protection [4, 5].

5.2 Conceptualization of DBR membranes

In order to cope with such issues, a novel fabrication process is introduced allowing us to produce planar microcavities without damaging the thin films based on *transferrable* high-quality DBR (t-DBR) membranes. The concept of t-DBR membranes is applicable to any semiconductor system and offers the possibility to incorporate such membranes with minimal thermal load as top DBR mirrors in vertical-cavity surface emitting devices. In contrast to previous reports, where t-DBR mirrors were fabricated by the sequential transfer of the

constituent DBR layers [6, 7], in our case the whole t-DBR is transferred as a block, which simplifies the manufacturing task. Another interesting feature of the t-DBR method is that several hundreds of DBR membranes are produced on the same wafer during a single deposition run. Such membranes can be stored and transferred on demand, depending on the specific microcavity design at hand. Additionally, an envisaged application for the t-DBRs is their use as diaphragms in high-sensitivity miniaturized pressure-sensor interferometers, owing to their submicron thickness [8].

As an example of the wide possibilities of the method, it is presented here the fabrication of novel GaN microcavities operating in the strong coupling regime at ambient conditions by using our t-DBRs. In previous chapters, it has been shown that GaN is a model system to observe robust polaritonic phenomena due to the large exciton oscillator strength of III-nitride semiconductors [9–12]. Therefore, seeking to obtain high-Q GaN microcavities, many research groups have explored several DBR combinations over the years. Specifically, the top and bottom DBRs can be all-nitride [13, 14], hybrid (i.e. one nitride, one dielectric) [9, 10], or all-dielectric [12, 15]. Air-gap DBR's are also an interesting variant [16,17], adding however significantly to the complexity of the fabrication process. Among the alternatives listed above, the all-dielectric case is undoubtedly the most appealing, since highly reflective and broadband dielectric mirrors can be achieved with a small number of periods as already illustrated in the previous chapters.

5.3 Current investigation

In this work, we report the fabrication of dielectric t-DBR membranes consisting of "$\times$4" and "$\times$8" alternating pairs of SiO_2/Ta_2O_5, where the specific quarter-wavelength layer thicknesses are designed for the operation in the near ultra-violet (UV) region. The DBR membranes are initially deposited on GaAs substrates. Then, they are detached by a standard GaAs wet-etching process and

are transferred on other templates for their use as top mirrors in cavities. Based on the successful fabrication and transfer of the "4-pair" DBR membranes, we demonstrate for the first time the realization of an all-dielectric "$\lambda/2$ oxide" microcavity showing a marked cavity mode at 380 nm, as well as a "$3\lambda/2$ complete" microcavity containing either $\times 38$ polar $GaN/Al_{0.07}Ga_{0.93}N$ or $\times 25$ non-polar $GaN/Al_{0.10}Ga_{0.90}N$ QWs, by utilizing the PEC-etched membranes shown in Chapters 3 and 4, exhibiting prominent strong coupling characteristics at room temperature conditions. The latter demonstrations strongly suggest that our t-DBR process can be a practical and versatile technique to produce efficiently planar nitride microcavities.

5.4 Fabrication of 4-pair DBR membranes

In order to fabricate the t-DBRs, a 2μm-thick poly-methyl-glutarimide (PMGI) layer was spinned on top of (100) semi-insulating GaAs substrates and cured at 200 $^{\circ}C$ (Figure 5.2(a)). The PMGI layer was photo-lithographically patterned into circular holes with diameters between 100 and 500 μm (Figure 5.2(b)). After patterning, a "4-pair" SiO_2/Ta_2O_5 top DBR mirror, with respective layer thicknesses of 67 and 45 nm, was deposited by electron beam evaporation at 150 $^{\circ}C$ (Figure 5.2(c)). As explained in Chapter 3, these oxides can produce a highly reflective DBR mirror with a minimal number of pairs. The reason to use the low deposition temperature at this stage was to prevent any PMGI degradation and preserve the structural integrity of the t-DBRs. Then, a lift-off step with the aid of N-methyl-pyrrolidone (NMP) solvent removed completely the PMGI layer, hence leaving intact DBR stacks in circular form on the GaAs surface (Figure 5.2(d)). Figures 5.2(e-f) present optical images of the sample's surface with a "4-pair" DBR mirror, before and after PMGI-removal.

The thus obtained mirrors on GaAs were then optically characterized by room temperature μ-reflectivity spectra (Figure 5.3), acquired by illuminating the DBR mesas with white light from a Xenon lamp source. The reflected

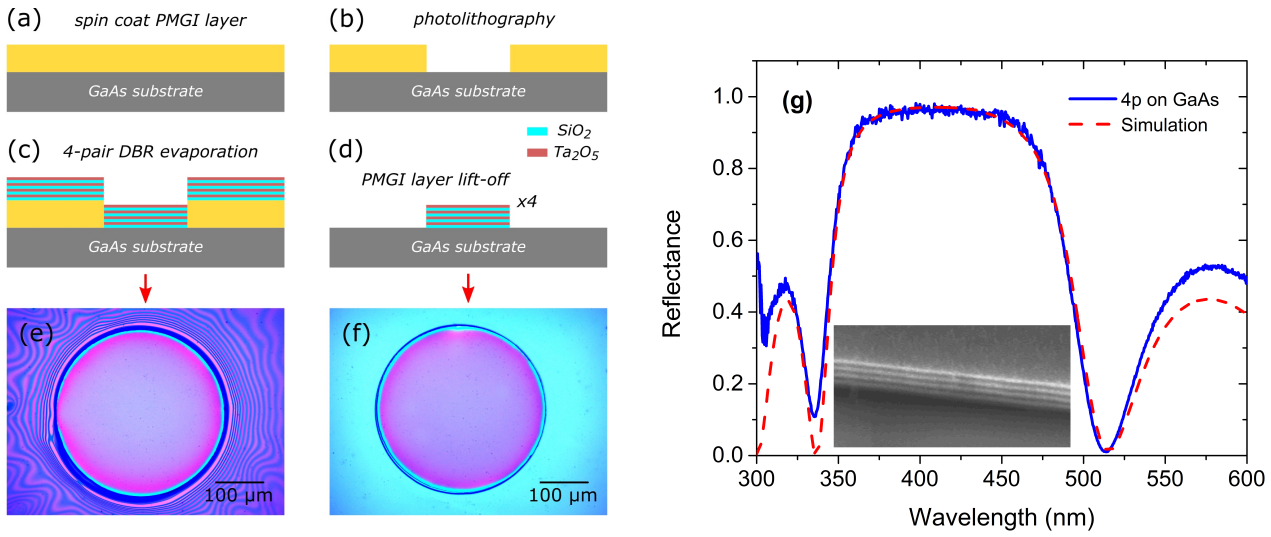

Figure 5.2: (a)-(d) Schematic illustrations of the initial processing steps for the fabrication of transferrable top DBR mirrors on GaAs. (e),(f) Top view optical images of a 4-pair SiO_2/Ta_2O_5 top-DBR mirror deposited on a patterned GaAs substrate, before and after the PMGI mask-layer lift-off. (g) Micro-reflectance spectrum of a 4-pair SiO_2/Ta_2O_5 DBR on a GaAs substrate in comparison with the simulated TMM data. Inset shows a SEM image of a transferred 4-pair DBR membrane, illustrating the uniformity of the evaporated layers.

light from the circular mesas was collected with x10 magnification and was spatially filtered with a 100 μm-diameter pinhole, at the entrance of a 0.5-meter, triple grating, imaging spectrograph, equipped with a liquid-nitrogen cooled charged-coupled device detector. The magnification (M = h_i/h_o) was achieved by placing an achromatic lens at a distance d from the sample (Figure 5.3), which is equal to its focal length (f_{achr}). Moreover, the numerical aperture (NA) of the specific lens is 0.16 based on the company's characteristics, allowing therefore the observation of an angle range $\sim \pm 9.2°$. In Figure 5.2(g), the normalized μ-reflectivity spectrum of a "4-pair" DBR stack on top of a GaAs substrate is compared to the calculated curve, obtained by TMM reflectivity simulations by using the refractive indices of the oxides (Figure 3.8), while the refractive index of GaAs is taken from reference [18]. High reflectivity values up to 97 % along with a wide stopband of about 150 nm are observed, in accordance with the theoretical data. The minor discrepancy between the experimental and simulated curves in the short-wavelength part of the given reflectance spectrum is due to the fact that bandgap-tail absorption effects in the oxide layers are not taken into account in the TMM model.

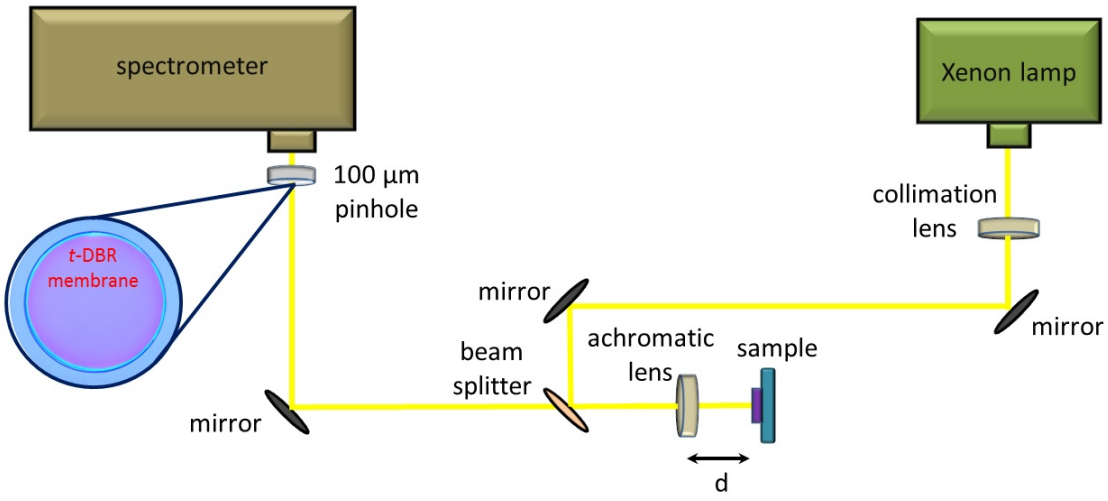

Figure 5.3: Schematic of the μ-reflectance setup, where collimated white light from a Xenon lamp illuminates the sample and an achromatic lens, placed at a distance d from the membrane, is utilized to magnify the membrane by a factor of 10 on a 100 μm pinhole at the entrance of the spectrograph. The pinhole is utilized for spatial filtering, as well as to drastically reduce the scattered light entering the spectrograph.

5.5 Transfer of DBR membranes

Following the successful top DBR deposition on GaAs, the next step was to cover the sample surface with a 1 μm-thick layer of polyimide (PI2525) (Figure 5.4(a)), which was subsequently cured on a hotplate at 300 $^{\circ}C$. The purpose of this polyimide layer was to mechanically support the circular DBR mesas during the removal of the GaAs substrate by a standard wet-etching process ($1H_3PO_4 : 1H_2SO_4 : 1H_2O_2 : 5H_2O$), as schematically shown in Figure 5.4(b). The etching of the GaAs substrate produced a few micron-thick polyimide membrane with several circular DBR membranes attached on its bottom surface. As depicted in the schematic of Figure 5.4(c) and in the optical image of Figure 5.4(e), the polyimide membrane was transferred with a fishing technique on the surface of an 8-pair SiO_2/Ta_2O_5 bottom-DBR, pre-deposited on a Sapphire substrate. In Figure 5.4(g) is presented the surface shown in (e) after the removal of the polyimide film, revealing the free-standing membranes.

It is worth noting here that the reason for transferring the polyimide layer containing the DBR membranes directly on a bottom DBR mirror was to obtain an "oxide $\lambda/2$" cavity in a simple one-step process. Other templates, such as for

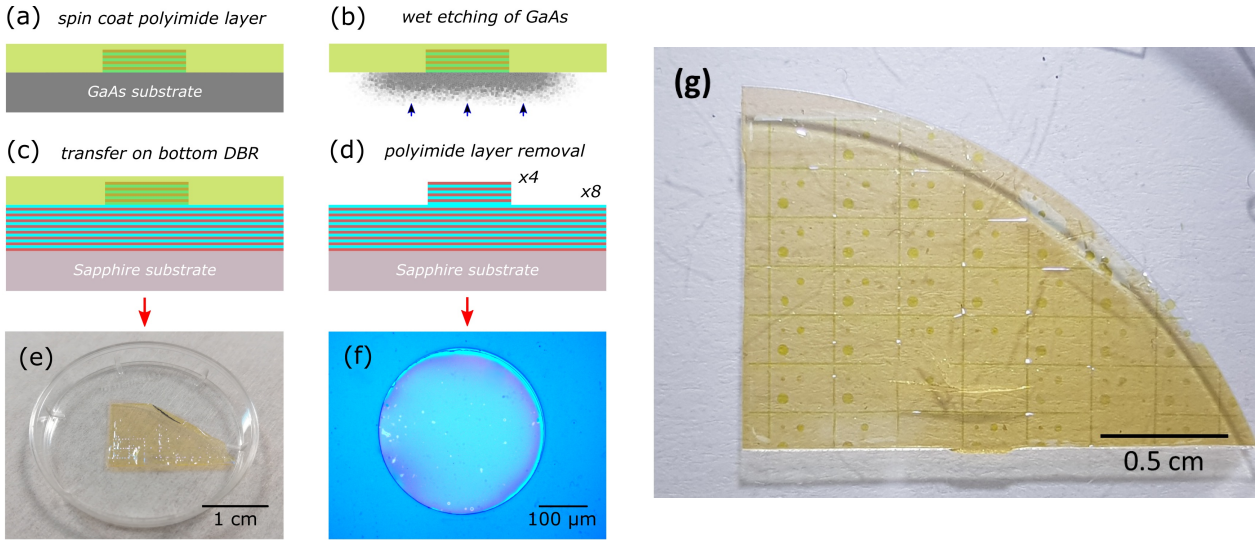

Figure 5.4: (a)-(d) Schematic illustrations of the final processing steps needed for the transfer of the membrane top DBR's on a pre-deposited bottom DBR/Sapphire template. (e) Optical image after fishing the DBR-containing polyimide membrane with the use of the previously mentioned template. (f) A free-standing SiO_2/Ta_2O_5 top DBR membrane transferred on the bottom DBR/Sapphire template. (g) Top-view optical image of the structure shown in (e), after the polyimide removal, depicting clearly the t-DBR membranes. Missing membranes from certain spots have been transferred on other templates for further experiments.

instance plain Sapphire, can be utilized as well when deemed necessary. In fact, we note here that the t-DBRs showed better adhesion on Sapphire compared to other templates, as testified by a uniform colorization under the microscope. By closer examination of Figure 5.4(e), it appears that most of the polyimide membrane is attached smoothly to the bottom DBR/Sapphire template, showing limited amount of wrinkles, apart from some edge regions where the membrane is folded and partially exfoliated. Further improvements of the fishing step would lead to a better adhesion of the polyimide film and to minimal mirror losses.

In a final fabrication step, oxygen plasma was used to remove completely the polyimide layer from all-around the DBR membranes and produce thus a structure similar to the configuration shown in Figure 5.4(d). An optical image of a 4-pair SiO_2/Ta_2O_5 top DBR membrane transferred onto an 8-pair SiO_2/Ta_2O_5 bottom DBR/Sapphire template is presented in Figure 5.4(f). From the optical image, it is evident that the DBR membranes can be transferred without any crack or major deformation, demonstrating the robustness of the individual oxide membranes in spite of their relatively small thickness of about 450 nm.

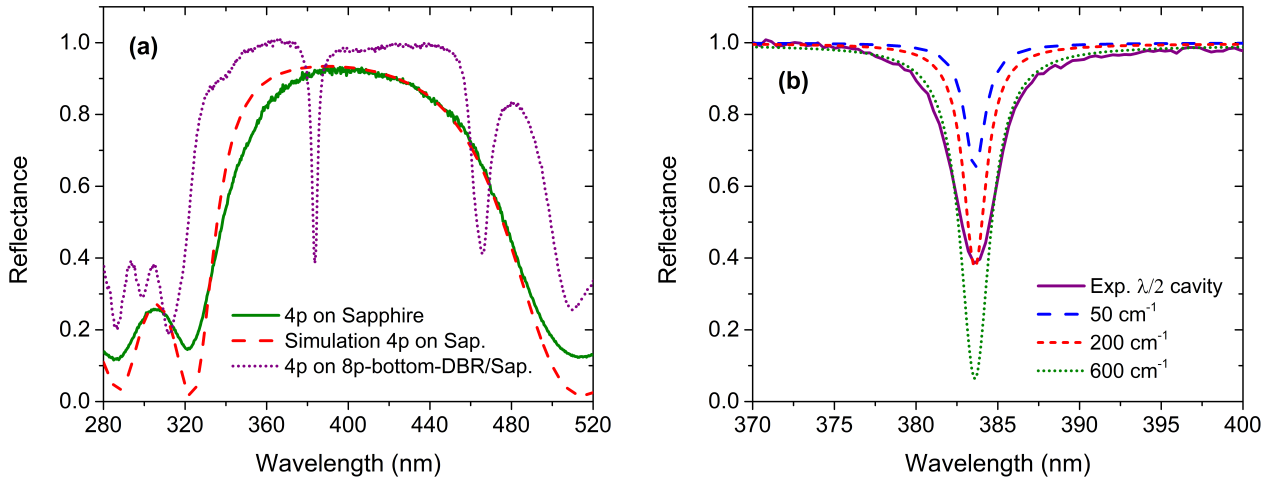

Figure 5.5: (a) Micro-reflectance spectra of the 4-pair top DBR membrane following transfer on Sapphire substrate (solid) along with the TMM simulation (dashed), while an additional transfer on an 8-pair bottom-DBR/Sapphire exhibits a fully-functional $\lambda/2$ oxide cavity with a distinct cavity mode (short-dotted). (b) A zoom around the experimental cavity mode of the $\lambda/2$ oxide cavity (solid) along with the simulation for 50 cm^{-1} (dashed), 200 cm^{-1} (short-dashed) and 600 cm^{-1} (short-dotted) mirror losses.

In Figure 5.5(a), we plot the μ-reflectivity spectrum from a "$\lambda/2$ oxide" cavity, formed simply by transferring a 4-pair top t-DBR on an 8-pair bottom DBR/Sapphire template (depicted in Figure 5.4(f)). The oxide cavity in this case forms a stopband with a maximum reflectivity near 99% and supports a strong cavity mode with a corresponding Q-factor ($\Delta\lambda/\lambda$) of about 110, illustrating that our t-DBR technique is capable to produce optically active microcavity structures. It should be noted that based on calculations the theoretical limit for the Q-factor in a "perfect" $\lambda/2$ oxide cavity is expected to be 240. Likely reasons for the reduced Q-factor in our case are surface roughness of the DBR's, imperfect adhesion of the top DBR, and mirror losses due to scattering effects.

At this stage, as regards the fabrication process, further experiments are needed to disentangle all the above mentioned mechanisms. Nevertheless, we note that the measured RMS roughness of a 4-pair SiO_2/Ta_2O_5 top DBR and an 8-pair SiO_2/Ta_2O_5 bottom DBR is merely 1.12 nm in both cases, which is too low to account for the reduced Q factor. Moreover, as an illustration of the role of mirror losses on the Q-factor, we compare in Figure 5.5(b) the experimental cavity mode with the simulated ones, for various levels of mirror losses in the

DBR layers. Apparently, mirror losses in excess of 600 cm^{-1} are needed to account for the observed Q-factor, which is considered to be an unrealistic value.

As additional characterization and applicability test of the t-DBR method, Figure 5.5(a) displays also the micro-reflectivity spectrum of a 4-pair top DBR transferred on plain Sapphire. In contrast to the reflectivity spectrum of Figure 5.2(g) for the same DBR on GaAs, the DBR on Sapphire is evidently "weaker", in the sense that the reflectivity reaches barely the 90% level and exhibits a rounded-shape stopband with a relatively narrower stopband of about 130 nm, in excellent agreement again with the TMM simulation. The Sapphire refractive index is taken from reference [19]. This behavior can be adequately understood considering the relatively small number of periods used in these DBRs, so that the template refractive index has a major influence on the overall reflectivity pattern.

5.6 Strong coupling at room temperature

In this preliminary development phase of our technique, we managed to position the "4-pair" top DBR membranes directly on top of 200-nm-thick films with embedded $GaN/AlGaN$ quantum wells, previously transferred one by one on a bottom DBR. The GaN-based membranes contained either $\times 38$ polar $GaN/Al_{0.07}Ga_{0.93}N$ QWs or $\times 25$ non-polar $GaN/Al_{0.10}Ga_{0.90}N$ QWs, as the ones presented in Chapters 3 and 4. The transfer of the individual t-DBR membranes and the GaN-based membranes was accomplished with the use of a probe tip taking advantage of the attractive van der Waals interaction between membrane and probe tip, similar to Figure 2.4. The specific method offers sufficient lateral precision in positioning a t-DBR on a GaN-based membrane, thus forming a complete planar microcavity device such as the one shown in the schematic of Figure 5.6(a) made out of the "$\times 38$ polar" QWs. The successful realization of such polariton devices is depicted in the optical image of Figure 5.6(b), where in this particular case, the transferred 4-pair t-DBR has a cross-like

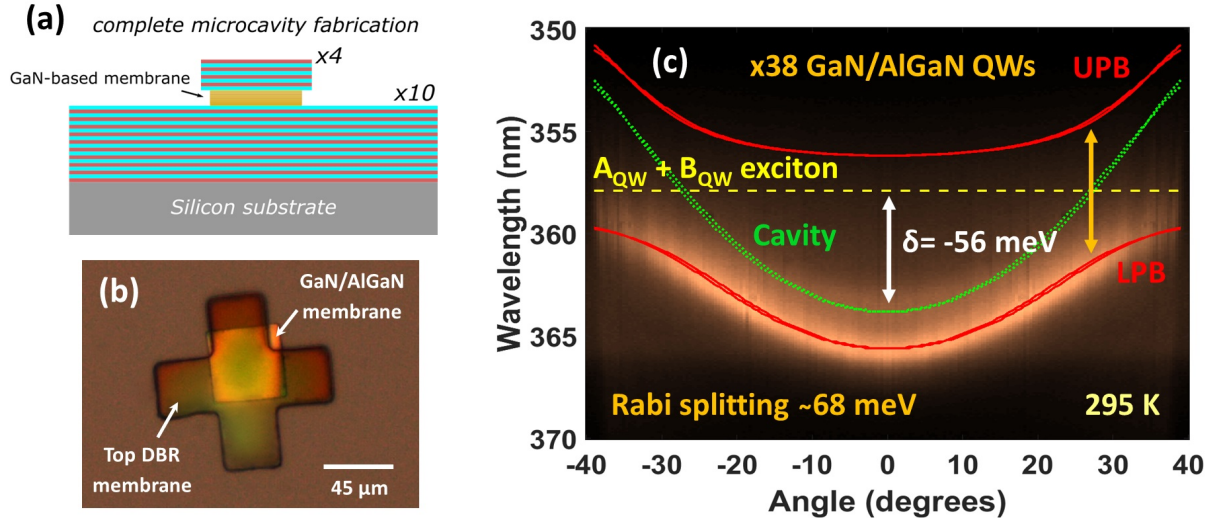

Figure 5.6: (a) A schematic of the fabricated $3\lambda/2$ GaN-based microcavity with 38 polar $GaN/Al_{0.07}Ga_{0.93}N$ QWs similar to the one shown in the optical image (b). The cross-like feature in the image is the 4-pair top-DBR mirror, while the yellowish layer underneath is the 38 polar GaN/AlGaN QW-containing membrane. (c) The k-space imaging data from the mentioned microcavity, demonstrating that the device remains in the strong coupling regime at RT with a Rabi splitting of 68 meV.

shape with lateral dimensions sufficient to cover the underneath nitride membrane while the bottom DBR was a 10-pair SiO_2/Ta_2O_5 on a Silicon substrate.

Interestingly, as suggested by the k-space imaging data of Figure 5.6(c) along with simulations based on transfer matrix and linear Hamiltonian model, the GaN-based microcavity obtained by the t-DBR approach exhibits a Rabi splitting of 68 meV and a coupling constant of 37 meV, i.e. numbers reassuringly close to the directly-deposited DBR case presented in Chapter 3. The "A_{QW} + B_{QW}" exciton state in this membrane is at 357.9 nm (3.4642 eV) while the photonic mode (C) at 363.8 nm (3.4080 eV), giving a detuning of -56 meV and a polariton emission at 365.6 nm (3.3912 eV) for the $k_{//} = 0$. Even though, the spectral linewidth in the discussed t-DBR structure was considerably larger compared to the structure obtained by direct deposition of Chapter 3, the flattening at large angles is still visible confirming that the device is able to operate in the strong coupling regime. According to our present understanding, the principal reason for the increased FWHM in this polariton device could be attributed to imperfect adhesion of the t-DBR membrane on the underneath GaN membrane, leading to small variations in cavity length.

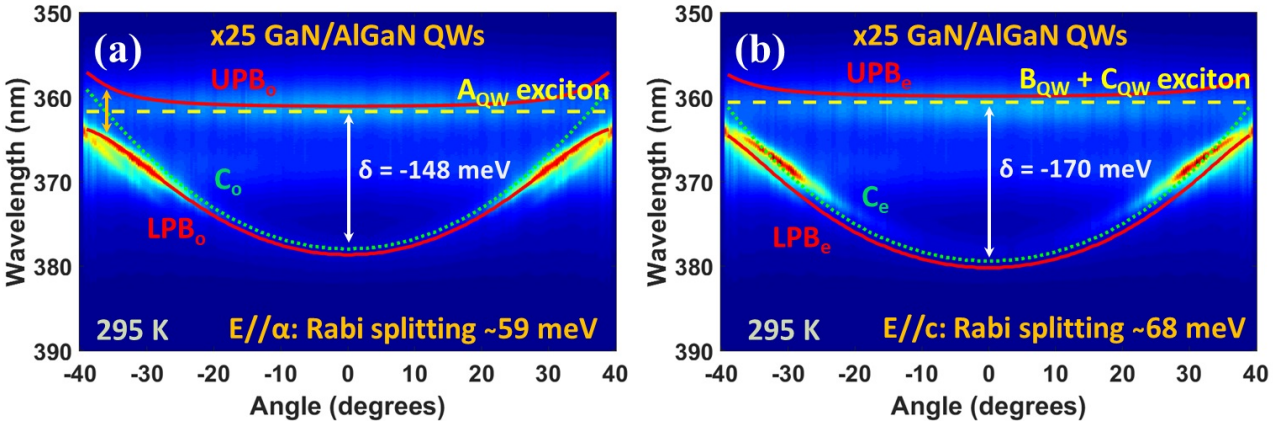

Figure 5.7: The k-space PL imaging data from a non-polar microcavity with 25 non-polar $GaN/Al_{0.10}Ga_{0.90}N$ QWs, demonstrating that the device remains in the strong coupling regime for both polarizations at room temperature with a Rabi splitting of (a) 59 meV for E//α and (b) 68 meV for E//c despite the large detunings.

A further study was made to produce an all-dielectric non-polar microcavity by placing a "non-polar" membrane with $\times$25 GaN/AlGaN QWs in between a "4-pair" $SiO_2/Ta2O_5$ t-DBR and an 8-pair bottom $SiO_2/Ta2O_5$ DBR mirror on Sapphire. The transferred t-DBR on top of the 200nm-thick non-polar GaN-based membrane had again a cross-shape similar to Figure 5.6(b). As indicated by the k-space images of Figure 5.7, obtained without the use of the Glan-Taylor polarizer, the strong coupling has been also achieved with distinct characteristics in the two orthogonal polarizations despite the large negative detunings. The two images show the same k-space data but with the corresponding simulated curve to each of the two polarizations E//α and E//c. The presented modelling is in accordance with the findings of Chapter 4, where the polarization resolved LPB_o results from the coupling of "A_{QW}" QW exciton state with the "ordinary" cavity mode (C_o) while LPB_e from the coupling of "$B_{QW} + C_{QW}$" QW excitons with the "extra-ordinary" cavity mode (C_e), while the two LPB's are having again an inter-crossing behavior. As follows from the positive birefringence ($\Delta n > 0$) in GaN (Chapter 4), the C_e is at higher wavelengths (or lower energy) compared to the (C_o). Moreover, in contrast to the case of the 10-pair on Silicon showed in Figure 5.6, the stopband of the 8-pair bottom DBR on Sapphire is better adjusted to that of the 4-pair t-DBR.

In the specific device, the narrower polariton branches result from the improved adhesion, demonstrating once again the feasibility of the t-DBR method to obtain high quality polaritonic devices.

Due to the large negative detunings, leading to a strong bottleneck effect, the polariton dispersions at small angles (or $k_{//}$ values) are less observable. This phenomenon occurs due to the rapid radiative decay of polaritons at high $k_{//}$'s before they manage to reach the bottom of the lower polariton branch. For this reason, the fitting for the simulation of the dispersion curves was based mostly on the emission at the higher angles, where it can be distinguished an inter-crossing of the ordinary and extra-ordinary branches, while maintaining a good matching at $k_{//} = 0$. As depicted, the simulated polariton curves appear to agree well with the data for both polarizations. As concerns the parameters for the simulations, in Figure 5.7(a), the A_{QW} exciton is at 361.7 nm (3.4278 eV) while the ordinary cavity mode (E//α) at 378 nm (3.28 eV), giving thus a negative detuning of -148 meV. The Rabi splitting at the anti-crossing point is obtained to be 59 meV with a coupling constant of 30 meV. For the ordinary branch (LPB_o), the minimum is at 378.7 nm (3.274 eV). On the other hand, in Figure 5.7(b), the $B_{QW} + C_{QW}$ exciton line is located at 360.6 nm (3.4383 eV) and the extra-ordinary cavity mode (E//c) seems to be at 379.4 nm (3.2679 eV), i.e. lower in energy than the ordinary one, resulting to an even larger negative detuning of -170 meV. The Rabi splitting at the anti-crossing point of the E//c polarization is estimated to be 68 meV with a coupling constant of 35 meV and is located slightly outside the range of our k-space imaging setup. Moreover, the minimum point of the LPB_e occurs to be at 380.2 nm (3.261 eV).

5.7 Fabrication of 8-pair DBR membranes

Following the developed methodology for the "4-pair" top DBR membrane we decided to take another step and fabricate an "8-pair" top t-DBR, since the peak reflectivity is expected to be higher, and therefore, it will be possible

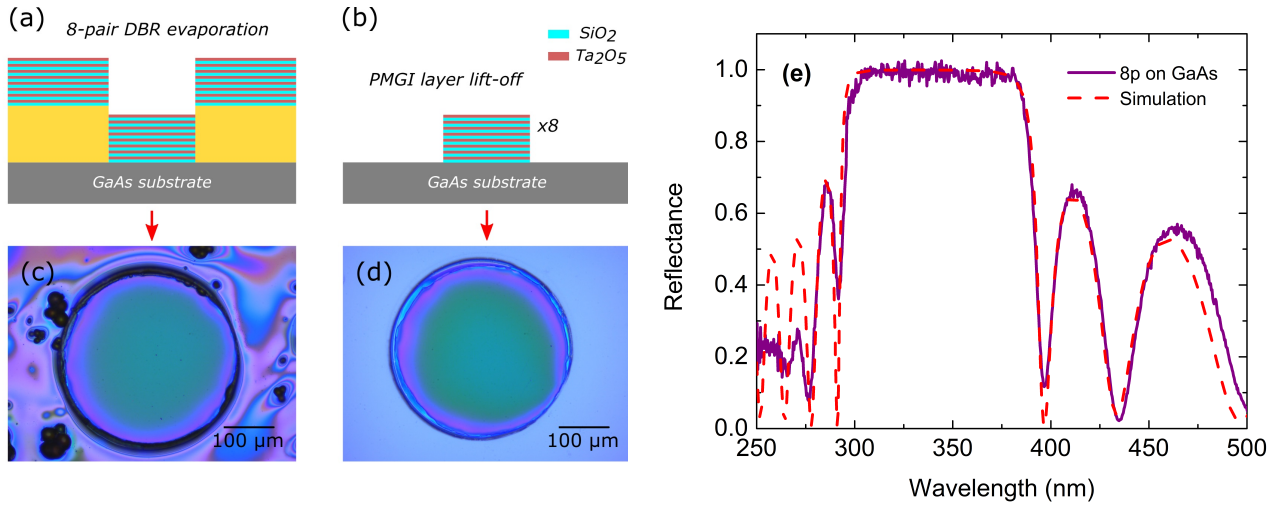

Figure 5.8: (a)-(b) Schematic illustrations of the 8-pair mirror evaporation on the pre-patterned GaAs substrate with a PMGI mask and the PMGI mask-layer lift-off. (c),(d) Top view optical images of an 8-pair SiO_2/Ta_2O_5 top-DBR mirror deposited on a patterned GaAs substrate for the two cases of (a-b). (e) Micro-reflectivity spectrum of an 8-pair SiO_2/Ta_2O_5 DBR on a GaAs substrate along with the simulated TMM data.

to succeed even better quality factors in the complete microcavity. In Figure 5.8(a-d) is depicted the process schematic along with the optical images of the evaporated DBR materials on the pre-patterned GaAs substrate before and after removal of the PMGI. It is worth noting that the larger deposition time induced some regional PMGI degradation as observed in Figure 5.8(c), but this created no problem in the t-DBR fabrication. In Figure 5.8(b) is presented the reflectance spectum as acquired from a DBR mirror on GaAs substrate, by utilizing the setup of Figure 5.3, along with the simulated curve by using the same refractive indices as in Figure 5.2(g). The results reflect clearly the close matching between the two curves with a normalized peak value close to 1. This time the "8-pair" spectrum is shifted to smaller wavelengths, since we tried to center it at 360 nm, compared to the "4-pair" t-DBRs (Figure 5.2(g)).

In the next step, we performed the wet etching process described in Figure 5.4 to remove the GaAs substrate and have the DBR membranes buried inside a polyimide layer that is ready to transfer onto another substrate with a fishing method. However, our experiments showed that even though the transfer can be safely done as before, it was not possible to achieve either a "$\lambda/2$" (only

oxide) or a "$3\lambda/2$" (with a semiconducting membrane) microcavity having good optical characteristics in the reflectance spectra. Further investigation is still needed in order to resolve this particular issue, which is possibly related to the thermal strain induced during cooling as we strongly believe it will be beneficial to utilize an "8-pair" mirror in microcavities based on the high quality reflectance spectrum shown in Figure 5.8(e) obtained on GaAs substrate.

5.8 Conclusion

In this work, we have demonstrated the fabrication of SiO_2/Ta_2O_5 t-DBR membranes for their use as transferrable upper mirrors in planar microcavities. The 4-pair DBR mirrors are first deposited by electron beam evaporation on a pre-patterned GaAs substrate and show high reflectivity values up to 97 % in the near UV region. Following removal of the GaAs substrate by chemical etching, the DBR stacks are released in membrane form, enabling thus their subsequent transfer and integration in vertical-cavity surface-emitting geometry devices. As an illustration, we have produced an all-dielectric $\lambda/2$ oxide microcavity with a well-defined cavity mode at 380 nm as well as a polar and non-polar GaN-based $3\lambda/2$ microcavity exhibiting marked strong coupling characteristics and Rabi splittings in the range of 59 - 68 meV at ambient conditions with the use of only 4-pair DBR membranes. The respective fabrication of an 8-pair top DBR mirror gave a high peak value close to 100 % and a broad stopband region prior to wet-etching of GaAs, while after the GaAs removal and transfer of the t-DBRs on other substrates, we did not achieve sufficient results possibly related to the large thermal strain in the t-DBR membrane, along with the GaAs removal and transfer process. Overall, further adjustments on the transferred membranes, such as for instance varying their relative size and roughness, will likely resolve several of the problems. We strongly believe that there is still plenty of room for improving the method t-DBR in order to produce high quality planar microcavities with even higher Q-factors.

Bibliography

[1] S. Kinoshita, K. Morito, F. Koyama, and K. Iga. *"Reproducible fabrication of AlGaAs/GaAs circular buried heterostructure (CBH) surface-emitting lasers with low thresholds"*, Electron. Lett. 24, 699 (1988).

[2] E. F. Schubert, Y.-H. Wang, A. Y. Cho, L.-W. Tu, and G. J. Zydzik. *"Resonant cavity light-emitting diode"*, Appl. Phys. Lett. 60, 921 (1992).

[3] C. Weisbuch, M. Nishioka, A. Ishikawa, and Y. Arakawa. *"Observation of the coupled exciton-photon mode splitting in a semiconductor quantum microcavity"*, Phys. Rev. Lett. 69, 3314, (1992).

[4] S. Sellner, A. Gerlach, F. Schreiber, M. Kelsch, N. Kasper, H. Dosch, S. Meyer, J. Pflaum, M. Fischer, B. Gompf, and G. Ulbricht. *"Mechanisms for the enhancement of the thermal stability of organic thin films by aluminum oxide capping layers"*, J. Mater. Res. 21, 455 (2006).

[5] A. Genco, G. Giordano, S. Carallo, G. Accorsi, Y. Duan, S. Gambino, and M. Mazzeo. *"High quality factor microcavity OLED employing metal-free electrically active Bragg mirrors"*, Org. Electron. 62, 174 (2018).

[6] W. Peng, M. M. Roberts, E. P. Nordberg, F. S. Flack, P. E. Colavita, R. J. Hamers, D. E. Savage, M. G. Lagally, and M. A. Eriksson. *"Single-crystal silicon/silicon dioxide multilayer heterostructures based on nanomembrane transfer"*, Appl. Phys. Lett. 90, 183107 (2007).

[7] M. Cho, J.-H. Seo, J. Lee, D. Zhao, H. Mi, X. Yin, M. Kim, X. Wang, W. Zhou, and Z. Ma. *"Ultra-thin distributed Bragg reflectors via stacked single-crystal silicon nanomembranes"*, Appl. Phys. Lett. 106, 181107 (2015).

[8] H. Bae and M. Yu. *"Miniature Fabry-Perot pressure sensor created by using UV-molding process with an optical fiber based mold"*, Opt. Express 20, 14573 (2012).

[9] S. Christopoulos, G. Baldassarri Höger von Högersthal, A. J. D. Grundy, P. G. Lagoudakis, A. V. Kavokin, J. J. Baumberg, G. Christmann, R. Butté, E. Feltin, J.-F. Carlin, and N. Grandjean. *"Room-Temperature Polariton Lasing in Semiconductor Microcavities"*, Phys. Rev. Lett. 98, 126405 (2007).

[10] G. Christmann, R. Butté, E. Feltin, J.-F. Carlin, and N. Grandjean. *"Room temperature polariton lasing in a GaN/AlGaN multiple quantum well microcavity"*, Appl. Phys. Lett. 93, 051102 (2008).

[11] P. Bhattacharya, T. Frost, S. Deshpande, M. Z. Baten, A. Hazari, and A. Das. *"Room Temperature Electrically Injected Polariton Laser"*, Phys. Rev. Lett. 112, 236802 (2014).

[12] R. Jayaprakash, F. G. Kalaitzakis, G. Christmann, K. Tsagaraki, M. Hocevar, B. Gayral, E. Monroy, and N. T. Pelekanos. *"Ultra-low threshold polariton lasing at room temperature in a GaN membrane microcavity with a zero-dimensional trap"*, Sci. Rep. 7, 5542 (2017).

[13] J. M. Redwing D. A. S. Loeber, N. G. Anderson, M. A. Tischler, and J. S. Flynn. *"An optically pumped GaN–AlGaN vertical cavity surface emitting laser"*, Appl. Phys. Lett. 69, 1 (1996).

[14] J.-F. Carlin. J. Dorsaz, E. Feltin, R. Butté, N. Grandjean, M. Ilegems, and M. Laügt. *"Crack-free fully epitaxial nitride microcavity using highly reflective AlInN/GaN Bragg mirrors"*, Appl. Phys. Lett. 86, 031107 (2005).

[15] K. Bejtka, F. Reveret, R. W. Martin, P. R. Edwards, A. Vasson, J. Leymarie, I. R. Sellers, J. Y. Duboz, M. Leroux, and F. Semond. *"Strong light-matter*

coupling in ultrathin double dielectric mirror GaN microcavities", Appl. Phys. Lett. 92, 241105 (2008).

[16] R. Sharma, Y.-S. Choi, C.-F. Wang, A. David, C. Weisbuch, S. Nakamura, and E. L. Hu. *"Gallium-nitride-based microcavity light-emitting diodes with air-gap distributed Bragg reflectors"*, Appl. Phys. Lett. 91, 211108 (2007).

[17] R. Tao, M. Arita, S. Kako, K. Kamide, and Y. Arakawa. *"Strong coupling in non-polar GaN/AlGaN microcavities with air-gap/III-nitride distributed Bragg reflectors"*, Appl. Phys. Lett. 107, 101102 (2015).

[18] A. D. Rakić and M. L. Majewski. *"Modeling the optical dielectric function of GaAs and AlAs: Extension of Adachi's model"*, J. Appl. Phys. 80, 5909 (1996).

[19] R. L. Kelly. *"Program of the 1972 Annual Meeting of the Optical Society of America"*, J. Opt. Soc. Am. 62, 1336 (1972).

Conclusions and future perspectives

Up to date the maturity in III-nitride fabrication technology has been remarkably improved as compared to the initial fabrication stages where the material quality was creating a number of drawbacks. The outcome of having a high quality GaN layer has intrigued many researchers towards the development of improved GaN-based polariton microcavities due to the high binding energy and oscillator strength of the GaN excitons opening the route for UV polariton emission at room temperature. Nevertheless, the fabrication of fully epitaxial, hybrid or even airgap-based microcavities has not yet found a solid ground to flourish, as there is still need to increase the efficiency of the polariton lasing devices. The utilization of ultra-thin III-nitrides as the active material, while having dielectric materials with a high refractive index contrast as top and bottom mirrors can be the ideal solution in decreasing the modal volume of the cavity while offering the possibility for electrical injection. The small active region is regarded to be one of the major parameters for achieving ultra-low lasing thresholds since less power is needed to excite the system. Therefore, the aim of this doctoral study was the fabrication of all-dielectric DBR microcavities based on ultra-smooth GaN-based membranes of approximately 200-nm-thick and 45 $\times$ 45 μm^2 - 155 $\times$ 155 μm^2 wide in the polar (c-) and non-polar orientation (m-) with the use of the photo-electrochemical etching technique. The separation can be succeeded by removing a sacrificial InGaN layer, which has proven a promising alternative to decrease etching-process imperfections and provide increased optical quality in the sub-micron-thick films. Utilizing low etching rates and high extents in time resulted in ultra-low rms roughness of the

etched surfaces. Apart from bulk GaN membranes, this method allowed to make novel high quality free-standing membranes with embedded GaN/AlGaN QWs only at antinodes and in the whole extent of the thin film along a polar and a non-polar orientation. Among the two, non-polar orientation is far superior since quantum-confined Stark effect is eliminated and there are no built-in fields inside the GaN/AlGaN quantum wells. This allowed to increase the well thickness from 2.7 to 5 nm in order to reduce inhomogeneous broadening by structural disorder, while at the same time increase further the PL intensity. The concentration of Al in the AlGaN barrier was kept in the range of 7 % (polar) and 10 % (non-polar) to minimize strain effects.

Special handle in the separation of the fabricated GaN-based membranes and their subsequent transfer onto Sapphire substrates, with a simple dry transfer method developed within the framework of this PhD, allowed us to perform μ-transmittance measurements. Then, following a comprehensive methodology considering the impact of the standing wave effects arising when light passes through the sub-wavelength-thick films, we deduced the absorption coefficient and oscillator strength in bulk and QW structures. Moreover, transferring the membranes on substrates with pre-deposited bottom dielectric DBRs, followed by a top mirror deposition by e-beam evaporation, complete optical microcavities can be produced. In our investigation, we utilized the SiO_2 (low index) and Ta_2O_5 (high index) as mirror oxides, which based on theoretical and experimental investigations yield large stopbands and high peak-values in the reflectivity spectra with only a small number of alternating pairs. For instance, 4 pairs in the top and 10 pairs in the bottom DBR provide a Q-factor of ~ 1000. AFM characterization of the mirror surfaces indicated an rms roughness in the range of 1 nm illustrating their feasibility as an integral part of microcavities. The analysis of the strong coupling regime was performed with a k-space imaging setup, where the particular all-dielectric DBR microcavities exhibited robust polariton lasing characteristics at RT in both growth orientations of the GaN crystal, with the m-orientation giving a significantly lower $P_{thr} = 1.5\ W/cm^2$.

Polariton lasing occurred in positively detuned microcavities, where the lifetime and scattering rate of polaritons are increased. This is a direct consequence of the enhanced exciton-fraction of the polaritons with the simultaneous decrease of relaxation time needed to reach the ground state of the lower polariton branch. Among the two growth orientations, the intrinsic polarization anisotropy of the m-orientation resulted in inter-crossed polarization-resolved polariton branches. The clear observation of the polariton branches obtained in our samples shows the high optical quality of the fabricated structures in comparison to other works, and therefore, illustrates the concrete advantages of this state-of-the-art fabrication and opens new perspectives such as for instance the study of polariton parametric scattering and its use as entangled photon pair source at ambient conditions. Compared to a direct mirror deposition which induces thermal load in the GaN/AlGaN membranes after cooling in the deposition chamber, an additional investigation aimed at the fabrication of transferrable dielectric DBR membranes for their use in all kinds of GaN-based polariton and VCSEL technology. Even though hundreds of oxide-based membranes are produced on a large wafer at once, such DBR membranes can be transferred to form a specific microcavity based "on demand". Mirrors made by 4 alternating pairs, around 450-nm-thick, were found to be able to produce pronounced cavity modes in a $\lambda/2$ oxide cavity and give strong-coupling effects in a $3\lambda/2$ GaN-based microcavity. To conclude, the major outcome of the current investigation was to illustrate future key points towards the fabrication of a GaN-based membrane with embedded p-n junction in the active material, whose simple transfer on appropriately patterned substrates can facilitate the current injection with direct contacts on the membranes, reducing thus resistance issues already observed in other device geometries. Such a demonstration will lead to new polariton LED and lasing devices with significantly reduced operation thresholds for their use in the UV spectrum.

Publications

Papers

- "*Improved GaN Quantum Well Microcavities for Robust Room Temperature Polaritonics*",
  Emmanouil A. Amargianitakis, F. Miziou, M. Androulidaki, K. Tsagaraki, A. Kostopoulos, G. Konstantinidis, E. Delamadeleine, E. Monroy, and N. T. Pelekanos, Phys. Status Solidi B 256, 1800716 (2019).

- "*Absorption in ultrathin GaN-based membranes: The role of standing wave effects*",
  E. A. Amargianitakis, R. Jayaprakash, F. G. Kalaitzakis, E. Delamadeleine, E. Monroy, and N. T. Pelekanos, J. Appl. Phys. 126, 083109 (2019).

- "*Transferrable dielectric DBR membranes for versatile GaN-based polariton and VCSEL technology*",
  E. A. Amargianitakis, S. Kazazis, G. Doundoulakis, G. Stavrinidis, G. Konstantinidis, E. Delamdeleine, E. Monroy, and N. T. Pelekanos, Microelectron. Eng. 228, 111276 (2020).

- "*Ultra-low polariton lasing threshold in all-dielectric non-polar GaN quantum well microcavities*",
  E. A. Amargianitakis, K. Tsagaraki, A. Kostopoulos, G. Konstantinidis, E. Delamadeleine, E. Monroy, and N. T. Pelekanos, (pending submission).

Conferences

- "*Improved GaN Quantum Well Microcavities for Robust Room Temperature Polaritonics*",
  Emmanouil A. Amargianitakis, F. Miziou, M. Androulidaki, K. Tsagaraki, A. Kostopoulos, G. Konstantinidis, E. Delamadeleine, E. Monroy, and N. T. Pelekanos, 34^{th} International Conference on Physics of Semiconductors (ICPS) 2018, Montpellier, France.

- "*Polariton lasing in non-polar GaN/AlGaN quantum well microcavities*",
  E. A. Amargianitakis, G. Stavrinidis, A. Kostopoulos, G. Konstantinidis, E. Delamadeleine, E. Monroy, and N. T. Pelekanos, 20^{th} International conference on Physics of Light–Matter Coupling in Nanostructures (PLMCN) 2019, Moscow - Suzdal, Russia.

- "*Transferrable dielectric DBR membranes for versatile GaN-based polariton and VCSEL technology*",
  E. A. Amargianitakis, S. Kazazis, G. Doundoulakis, G. Stavrinidis, G. Konstantinidis, E. Delamadeleine, E. Monroy, and N. T. Pelekanos, 45^{th} International Conference on Micro & Nano Engineering (MNE) 2019, Rhodes, Greece.

Appendix A

Complex Refractive Index

In optics, one of the most substantial parameters to describe a material's optical response is the refractive index [1, 2]. The refractive index is defined as the ratio of the velocity of light c in vacuum ($\approx 3{\cdot}10^8$ m/s) to the group velocity v in the medium. Combining the previous definition with Maxwell's equations [3], leads to a formula containing the relative complex permittivity $\tilde{\varepsilon}_r$ and the relative complex permeability $\tilde{\mu}_r$ describing classically the dispersion of light in a substance as

$$\tilde{n}(\lambda) = \frac{c_o}{v(\lambda)} = \sqrt{\tilde{\varepsilon}_r(\lambda)\tilde{\mu}_r(\lambda)} \tag{A.1}$$

Based on the previous equation, a complex refractive index is defined (in the case of non-magnetic materials, $\tilde{\mu}_r = 1$) to fully describe the material optical characteristics as

$$\tilde{n}^2(\lambda) = (n(\lambda) - ik(\lambda))^2 = \tilde{\varepsilon}_r(\lambda) = \varepsilon_r'(\lambda) - i\varepsilon_r''(\lambda) \tag{A.2}$$

where the imaginary part of the refractive index $k(\lambda)$ represents the attenuation of light when propagating through a material and is known in literature as extinction coefficient, while $\varepsilon_r'(\lambda)$ and $\varepsilon_r''(\lambda)$ are the real and imaginary part of the complex relative permittivity. The link between the discussed parameters is given through Kramers-Kroning relations [3] by the expressions

$$\varepsilon_r'(\lambda) = n^2(\lambda) - k^2(\lambda) \tag{A.3}$$

$$\varepsilon_r''(\lambda) = 2n(\lambda)k(\lambda) \tag{A.4}$$

Another useful quantity is the absorption coefficient and is related to the extinction coefficient as

$$\alpha(\lambda) = \frac{4\pi k(\lambda)}{\lambda} \tag{A.5}$$

where this parameter describes the decrease occurring on the light's intensity when passing through a medium.

The dispersion relations of the real and imaginary parts of the refractive index corresponding to a material can be deduced by performing spectroscopic ellipsometry (SE) measurements. As regards the real part of the refractive index, the transparent region of a semiconductor can be represented by a Cauchy or a Sellmeier relation [3, 4] as described below

$$Cauchy: \quad n(\lambda) = A + \frac{B}{\lambda^2} + \frac{C}{\lambda^4} + ... \tag{A.6}$$

$$Sellmeier: \; n(\lambda) = \sqrt{1 + \frac{F_1\lambda^2}{\lambda^2 - B_1} + \frac{F_2\lambda^2}{\lambda^2 - B_2} + \frac{F_3\lambda^2}{\lambda^2 - B_3}...} \tag{A.7}$$

where A, B and C are the Cauchy and F_1, F_2, F_3, B_1, B_2, B_3 are the Sellmeier constants.

Regarding the three major QW exciton entities A_x, B_x and C_x, they can be modeled as "oscillators" within a transfer matrix model (Appendix B) to simulate the energy dispersion of polaritons when light and matter are strongly

coupled. Considering the Drude-Lorentz damping oscillator model to account for the homogeneous dielectric behavior of eg. three QW-excitons [5–7] as

$$\tilde{\varepsilon}_r(E) = \tilde{\varepsilon}_r^B(E) + \tilde{\varepsilon}_{exc}^{hom}(E) = \tilde{\varepsilon}_r^B(E) + \sum_{j=1}^{3} \frac{e^2\hbar^2}{\varepsilon_o M_{exc} L_{well}} \frac{f_{x_j}^{qw}}{S} \frac{1}{E_{x_j}^2 - E^2 + i\gamma_{x_j}^{hom} E} \tag{A.8}$$

where $\tilde{\varepsilon}_r^B(E)$ represents the background dielectric constant, $f_{x_j}^{qw}/S$ is the oscillator strength of the excitonic transition per unit surface (for QWs), E_{x_j} corresponds to the energy of the j^{th} exciton, L_{well} is the thickness of the well material, ε_o is the vaccum permittivity, e the electron charge, M_{exc} is the exciton mass and $\gamma_{x_j}^{hom}$ is the homogeneous damping constant of exciton.

To account for inhomogeneous broadening due to interface roughness and/or AlGaN's alloy fluctuations, the effect can be represented by a Gaussian profile of the form

$$\varepsilon_{exc}^{inh}(E) = \frac{1}{\sigma\sqrt{2\pi}} e^{-\frac{(E-E_{x_j})^2}{2\sigma^2}} \tag{A.9}$$

where E_{x_j} is the energy of the central exciton and σ^2 is the variance with a $\gamma_{x_j}^{inh} = 2\sigma\sqrt{2ln2} \approx 2.35482\sigma$. For a more analytic description, the convolution of a Gaussian and a Lorentzian function can be modeled by a Voigt function

$$\tilde{\varepsilon}_{exc}^{total}(E) = \int_{-\infty}^{\infty} \varepsilon_{exc}^{inh}(E')\tilde{\varepsilon}_{exc}^{hom}(E, E')dE' \tag{A.10}$$

where for each value of E' around the central value E_{x_j} of a Gaussian distribution there is a Lorentzian contribution of each individual exciton. The main fitting parameters for a complete description of an exciton transition in the transfer matrix model (TMM) (Appendix B) are just the oscillator strength, the energy position and the two damping constants $\gamma_{x_j}^{hom}$ and $\gamma_{x_j}^{inh}$ [6, 7].

Bibliography

[1] B. E. A. Saleh and M. C. Teich. *"Electromagnetic Optics"*, Fundamentals of Photonics, Wiley-Interscience, New York (1991).

[2] M. Born, E. Wolf, A. B. Bhatia, P. C. Clemmow, D. Gabor, A. R. Stokes, A. M. Taylor, P. A. Wayman, and W. L. Wilcock. *"Basic properties of the electromagnetic field"*, Principles of Optics: Electromagnetic Theory of Propagation, Interference and Diffraction of Light, Cambridge University Press (1999).

[3] J. Mistrik, S. Kasap, H. E. Ruda, C. Koughia, and J. Singh. *"Optical Properties of Electronic Materials: Fundamentals and Characterization"*, Springer Handbook of Electronic and Photonic Materials, Springer Handbooks, Springer, Cham (2017).

[4] F. A. Jenkins and H. E. White. *"Dispersion"*, Fundamentals of Optics, McGraw-Hill, Inc. (1981).

[5] H. Kalt and C. F. Klingshirn. *"Oscillator Model of Strong Light-Matter Coupling"*, Semiconductor Optics 1. Graduate Texts in Physics, Springer, Cham (2019).

[6] R. Jayaprakash. *"Novel approaches for robust polaritonics"*, PhD Thesis, University of Crete (2015).

[7] G. Christmann. *"III-nitride Based Microcavities: Towards Polariton Condensation at Room Temperature"*, PhD Thesis, École polytechnique fédérale de Lausanne (2009).

Appendix B

Transfer Matrix Method

To describe light propagation in layered media, instead of solving every time Maxwell's equations analytically, it is convenient to use the advantageous tranfer matrix method (TMM) [1–3] supposing that the layers are isotropic, homogeneous and the surfaces of the materials are parallel to each other. The method considers an incident electromagnetic wave (TE or TM) at the surface of a multi-layered structure, where each layer constituting the structure is defined mathematically by a matrix, which accounts for the material's parameters. The multiplication can be made in simple steps and gives the characteristic overall matrix defining all the layers in the structure. The behavior of light at each layer / material depends exclusively on the complex refractive index ($\tilde{n}_m$) (Appendix A) and its thickness ($d_m = t_j$ - t_{j-1}), where m and j are integers denoting the number of the layers and the surfaces / interfaces. Bearing all this in mind, the respective equation expressing the amplitudes of the incident electric and magnetic field components to those after passing the entire structure is given by

$$\begin{pmatrix} \vec{E}_{1,d=0} \\ \vec{H}_{1,d=0} \end{pmatrix} = M_1 ... M_m \begin{pmatrix} \vec{E}_{m,d=t} \\ \vec{H}_{m,d=t} \end{pmatrix} \tag{B.1}$$

where M_m is the transmission matrix of each layer and has the following form

$$M_m = \begin{pmatrix} cos(\delta_m) & \frac{i}{\gamma_m} sin(\delta_m) \\ i\gamma_m sin(\delta_m) & cos(\delta_m) \end{pmatrix} \tag{B.2}$$

with a phase shift $\delta_m = \frac{2\pi}{\lambda}\tilde{n}_m d_m cos(\alpha_m)$ and α_m the angle of incidence at the m_{th} material. By taking into account the polarization of light, the following two cases are distinguished

$$\gamma_m = \tilde{n}_m cos(\alpha_m) \qquad for\ TE \tag{B.3}$$

$$\gamma_m = \frac{\tilde{n}_m}{cos(\alpha_m)} \qquad for\ TM \tag{B.4}$$

The relation connecting the angle of the incident ray to the one that is refracted is given by the Snell's law for refraction ($\tilde{n}_{m-1} sin(\alpha_{m-1}) = \tilde{n}_m sin(\alpha_m)$) and occurs due to the different values of the refractive indices between the two media. Note that in the TMM calculations we use the complex refractive index in the previous equation. The resulted expressions can be extracted by satisfying the tangential boundaries of $\vec{E}$ and $\vec{H}$ in Maxwell's equations for a light wave traveling from medium "$m-1$" to medium "m". Considering that incidence occurs from the air and that a substrate is utilized to host the structure, the complete matrix will have the form

$$M_{total} = \begin{pmatrix} M_{11} & M_{12} \\ M_{21} & M_{22} \end{pmatrix} = {D_{air}}^{-1} M_{structure} D_{substrate} \tag{B.5}$$

where the two D_i's, describing the refraction of light at the air / structure and the structure / substrate interface, can be calculated by

$$D_i = \begin{pmatrix} 1 & 1 \\ \frac{1}{\gamma_{m,i}} & -\frac{1}{\gamma_{m,i}} \end{pmatrix} \tag{B.6}$$

For the case that the particular structure is a distributed Bragg reflector (DBR) ($\delta_m = \frac{\pi}{2}$) with N alternating pairs, the matrix results to be

$$M_{DBR} = \Big(M_L M_H\Big)^N = \begin{pmatrix} (-\frac{n_H}{n_L})^N & 0 \\ 0 & (-\frac{n_L}{n_H})^N \end{pmatrix} \tag{B.7}$$

where L and H denote the low and the high refractive index material. Knowing the total matrix of a system, it is then possible to calculate the normalized reflectance and transmittance in the DBR from

$$R = |r|^2 = \left|\frac{M_{21}}{M_{11}}\right|^2 \tag{B.8}$$

$$T = \frac{\gamma_{m,sub}}{\gamma_{m,air}}|t|^2 = \frac{\gamma_{m,sub}}{\gamma_{m,air}}\left|\frac{1}{M_{11}}\right|^2 \tag{B.9}$$

with r and t referred to as the Fresnel's coefficients and M_{ij}'s the matrix elements. The absorbance results from the equation

$$A = 1 - R - T \tag{B.10}$$

To account for both polarizations in R and T the following relations should be utilized instead

$$R = \frac{R_{TE} + R_{TM}}{2} \tag{B.11}$$

$$T = \frac{T_{TE} + T_{TM}}{2} \tag{B.12}$$

which are basically the average of the TE and TM cases. The TMM approach can be applied to a thin film to analyze eg. transmittance spectra or even to more sophisticated structures such as a microcavity device for a nominal design for the operation at the desired wavelengths. More details for the simulation of GaN-based microcavities can be found in references [4, 5].

Bibliography

[1] S. A. Furman and A. V. Tikhonravov. *"Spectral Characteristics of Multilayer Coatings: Theory"*, Basics of Optics of Multilayer Systems (Atlantica Séguier Frontières, Gifsur-Yvette, France, 1992).

[2] L. A. Coldren and S. W. Corzine. *"Diode Lasers and Photonic Integrated Circuits"*, Wiley-Interscience, New York (1995).

[3] A. Kavokin, J. J. Baumberg, G. Malpuech, and F. P. Laussy. *"Microcavities"*, Oxford University Press (2017).

[4] R. Jayaprakash. *"Novel approaches for robust polaritonics"*, PhD Thesis, University of Crete (2015).

[5] G. Christmann. *"III-nitride Based Microcavities: Towards Polariton Condensation at Room Temperature"*, PhD Thesis, École polytechnique fédérale de Lausanne (2009).

Appendix C

Transformations

Describing the linear Hamiltonian of the exciton - photon system in the second quantization (Section 1.7), it is possible to utilize the following transformation to link the initial operators ($\hat{b}_{k_{//}}$, $\hat{a}_{k_{//}}$) to the lower and upper polariton operators ($\hat{P}_{k_{//}}$, $\hat{Q}_{k_{//}}$) for each in-plane wavevector

$$\begin{pmatrix} \hat{P}_{k_{//}} \\ \hat{Q}_{k_{//}} \end{pmatrix} = \begin{pmatrix} X_{k_{//}} & C_{k_{//}} \\ -C_{k_{//}} & X_{k_{//}} \end{pmatrix} \begin{pmatrix} \hat{b}_{k_{//}} \\ \hat{a}_{k_{//}} \end{pmatrix} \tag{C.1}$$

where the new Hamiltonian results to have the following form [1]

$$\hat{H}_{pol} = \sum_{k_{//}} E_{LP,k_{//}} (\hat{P}^{\dagger}_{k_{//}} \hat{P}_{k_{//}}) + \sum_{k_{//}} E_{UP,k_{//}} (\hat{Q}^{\dagger}_{k_{//}} \hat{Q}_{k_{//}}) \tag{C.2}$$

with $\hat{P}^{\dagger}_{k_{//}}$, $\hat{Q}^{\dagger}_{k_{//}}$ being the creation and $\hat{P}_{k_{//}}$, $\hat{Q}_{k_{//}}$ the annihilation operators of the lower and upper polaritons, respectively. The $E_{LP,k_{//}}$ and $E_{UP,k_{//}}$ are the energy dispersions of the polation branches given in Section 1.7. The parameters $X_{k_{//}}$ and $C_{k_{//}}$ are named as Hopfield coefficients [2] and they are calculated by the equations below for each $k_{//}$ as

$$|X_{k_{//}}|^2 = \frac{1}{2}\left(1 + \frac{\delta_{k_{//}}}{\sqrt{\delta^2_{k_{//}} + 4g_o^2}}\right) \tag{C.3}$$

$$|C_{k_{//}}|^2 = \frac{1}{2}\left(1 - \frac{\delta_{k_{//}}}{\sqrt{\delta^2_{k_{//}} + 4g_o^2}}\right) \tag{C.4}$$

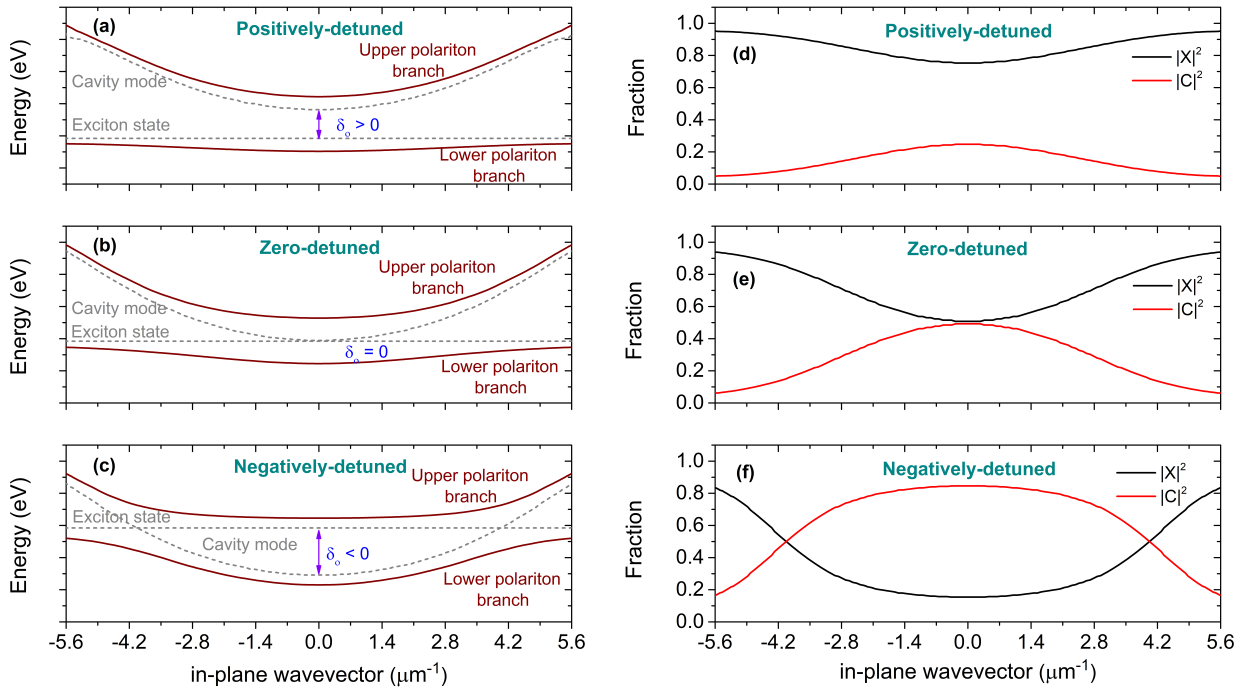

Figure C.1: Polariton eigenenergies and the corresponding Hopfield coefficients $|X_{k_{//}}|^2$ and $|C_{k_{//}}|^2$ at (a, d) $\delta_o > 0$, (b, e) $\delta_o = 0$ and (c, f) $\delta_o < 0$.

where $|X_{k_{//}}|^2$ and $|C_{k_{//}}|^2$ reflect the excitonic and photonic contributions (or else fractions) for each $k_{//}$ of the polariton branches, fulfilling the condition that their sum is always unity. The term $\delta_{k_{//}}$ is the energy difference (detuning) of the exciton state and cavity mode at a given in-plane wavevector and g_o the coupling constant given by Equation 1.24. Depending on the value of the detuning, the polariton branches can be more photonic or more excitonic, as can be seen in Figure C.1. Additionally, due to the particular characteristics, the polariton effective masses can be obtained by the relations

$$\frac{1}{m_{LP,k_{//}}} = \frac{|X_{k_{//}}|^2}{M_{exc}} + \frac{|C_{k_{//}}|^2}{m_{cav}} \tag{C.5}$$

$$\frac{1}{m_{UP,k_{//}}} = \frac{|C_{k_{//}}|^2}{M_{exc}} + \frac{|X_{k_{//}}|^2}{m_{cav}} \tag{C.6}$$

where M_{exc} is the effective mass of the exciton and m_{cav} is the effective mass of the photon in the cavity. By making a rough calculation one can see that the effective polariton mass m_{pol} is of the order $10^{-4}M_{exc} = 10^{-5}m_e$, since the photonic mass is always much smaller, and hence plays a dominant role in the system.

Accordingly, the effective lifetimes of polaritons in the two branches are given by

$$\frac{1}{\tau_{LP,k_{//}}} = \frac{|X_{k_{//}}|^2}{\tau_{exc}} + \frac{|C_{k_{//}}|^2}{\tau_{cav}} \tag{C.7}$$

$$\frac{1}{\tau_{UP,k_{//}}} = \frac{|C_{k_{//}}|^2}{\tau_{exc}} + \frac{|X_{k_{//}}|^2}{\tau_{cav}} \tag{C.8}$$

where τ_{exc} is the effective exciton decay time and τ_{cav} is the effective cavity-photon lifetime ($\approx$ 0.2 - 1 ps). Typically, the effective polariton decay time τ_{pol} is of the order of ps and depends mostly on the Q-factor of the cavity, since it is usually much smaller than the exciton decay time ($\approx$ 50 - 500 ps). In addition, analogous equations hold also for the linewidths of the polariton branches by considering the respective parameters.

Bibliography

[1] H. Deng, H. Haug and Y. Yamamoto. *"Exciton-polariton Bose-Einstein condensation"*, Rev. Mod. Phys., 82, 1489 (2010).

[2] J. J. Hopfield. *"Theory of the Contribution of Excitons to the Complex Dielectric Constant of Crystals"*, Phys. Rev., 112, 1555 (1958).

Appendix D

Time-resolved photoluminescence

Time-resolved photoluminescence (TRPL) is an experimental technique to investigate the recombination dynamics of semiconductor structures through their temporal evolution. Multiple effects are possible to be analyzed with the TRPL method such as the quantum confined Stark Effect (QCSE), the screening and the time decays of the carriers. The necessary tools to acquire a time resolved PL decay curve are mainly three: (a) a short pulse laser, (b) an ultra-fast detector and (c) a closed-helium-flow cryostat to perform measurements at low temperatures. More specifically, the technique works as follows, an initial pulse excites the sample and the fast detector analyzes the photoluminescence decay signal in combination with a computer storing the data. The whole procedure is completed before the second pulse excites the sample again. Each time a pulse excites the sample, the detector repeats the same procedure over and over again and gives a statistical average of the counts per unit of time. A high number of repetitions lead to a lower statistical error in the measurement.

In an as-grown sample, without microcavity, the observed PL lifetime $\tau_{PL}(T)$ is basically related to the exciton recombination inside the QWs and is related to the exciton radiative lifetime $\tau_r(T)$ and the non-radiative lifetime $\tau_{nr}(T)$ through the following equation [1]

$$\frac{1}{\tau_{PL}(T)} = \frac{1}{\tau_r(T)} + \frac{1}{\tau_{nr}(T)} \tag{D.1}$$

Moreover, the integrated photoluminescence at a temperature T is expressed as

$$I_{PL}(T) = \frac{I_o}{\eta_o}\frac{\tau_{PL}(T)}{\tau_r(T)} = \frac{I_o}{\eta_o}\eta(T) \tag{D.2}$$

with I_o being a normalization factor which depends on the photoexcited carriers and η_o is the radiative efficiency at T = 0 K, while $\eta(T)$ is the radiative efficiency at a temperature T. As a result, the expressions for the $\tau_r(T)$ and $\tau_{nr}(T)$ are decoupled as

$$\tau_r(T) = \frac{I_o}{\eta_o I_{PL}(T)}\tau_{PL}(T) = \frac{\tau_{PL}}{\eta(T)} \tag{D.3}$$

$$\tau_{nr}(T) = \left(\frac{I_o}{I_o - \eta_o I_{PL}(T)}\right)\tau_{PL}(T) = \left(\frac{1}{1-\eta(T)}\right)\tau_{PL} \tag{D.4}$$

In order to deduce the decay times as a function of the temperature, it is often assumed that at low temperatures only radiative recombination occurs since the non-radiative recombination processes are much slower, therefore I_o is taken as $I_{PL}(0K)$. Hence, the integrated PL intensity can be normalized to unity at T = 0 K ($\eta(0K) = 1$), while in order to relax this assumption one has just to consider a lower value of n_o (< 1) in Equation D.2. The time decay of the carriers can be affected by structural defects inside the crystal such as non-uniformity and well-width fluctuations leading to localized excitons at low temperatures. As the temperature rises, the thermally-induced de-trapping of the excitons allows them to move and find non-radiative defects leading to an overall degradation of the PL intensity.

To perform low T measurements, the sample is mounted in a closed-cycle helium cryostat in combination with a temperature controller to adjust the sample's temperature (Appendix F). In this work, the sample was excited by a Mira femtosecond laser oscillator which was powered by a Verdi laser and gives pulses at a repetition rate of 76 MHz (1 pulse every 13 ns) giving enough

time to the system to relax before the arrival of a new pulse. For the sample's excitation, it was utilized the third harmonic (3ω) of the laser's beam with the use of a tripler which gave a wavelength at $\lambda = 266$ nm, representing a non-resonant excitation energy, i.e well above the bandgap of the well and barrier materials of the fabricated QW structure. The average excitation power was maintained at an average power density of 4 W/cm^2 by using appropriate neutral density filters in the path. The latter value was kept low in order to eliminate any exciton-exciton interaction effects. Furthermore, a bandpass filter with 280 nm cut-off was placed at the entrance of the spectrometer to cut most of the back-scattered laser beam. With the use of a beam splitter, a portion of the Mira's beam triggered the streak camera synchronously with the portion of pulse that was hitting on the sample. Finally, the time-resolved PL spectra were analyzed and recorded with the use of a spectrometer in combination with the Streak camera, giving a time resolution of a few ps. Additional information about the particular setup configuration and measurements can also be found in reference [2].

Bibliography

[1] M. Gurioli, A. Vinattieri, M. Colocci, C. Deparis, J. Massies, G. Neu, A. Bosacchi, and S. Franchi. *"Temperature dependence of the radiative and nonradiative recombination time in $GaAs/Al_xGa_{1-x}As$ quantum-well structures"*, Phys. Rev. B 44, 3115 (1991).

[2] R. Jayaprakash. *"Novel approaches for robust polaritonics"*, PhD Thesis, University of Crete (2015).

Appendix E

k-space PL-imaging setup

The Fourier plane (or k-space) imaging was realized with the setup presented in Figure E.1, which enables the PL imaging at different temperatures with the use of a closed-circuit cryostat along with a temperature controller. A laser source is utilized to optically pump the sample that is mounted inside (or in front of) the cryostat at normal incidence. The incident beam is directed with UV mirrors and a beam splitter, and finally is, focused with an aspheric (objective) lens on the sample. A varying neutral density filter in this path was used to adjust the excitation power of the laser. Then, the collection of the PL signal is acquired with the use of an imaging lens at $d_i = f_2 = 200$ mm from the Fourier plane, on the left-hand side of the aspheric lens ($d_a = f_3 = 8$ mm) with focal length 8 mm. The numerical aperture (NA) of the particular aspheric lens is ~ 0.63 and allows for an angle-range PL acquisition of $\pm\ 39°$. The collection is made with an additional lens ($f_1 = 100$ mm) to direct the signal in front of a spectrometer, where the analyzed spectrum was then recorded by a nitrogen-cooled CCD camera connected to a computer. The focal length of the specific collection lens depends on the magnification needed to fill the pixels of the CCD. The use of a pinhole, installed on a translational stage, at the left-sided focal point of the imaging lens permitted the spatial filtering of the signal. Moreover, a filter (< 350 nm) was used to cut the unwanted back-scattered laser emission. Since the QW-emission is at ~ 360 nm, the alignment and focus of the setup was adjusted for this wavelength. Figure E.2 depicts the real setup.

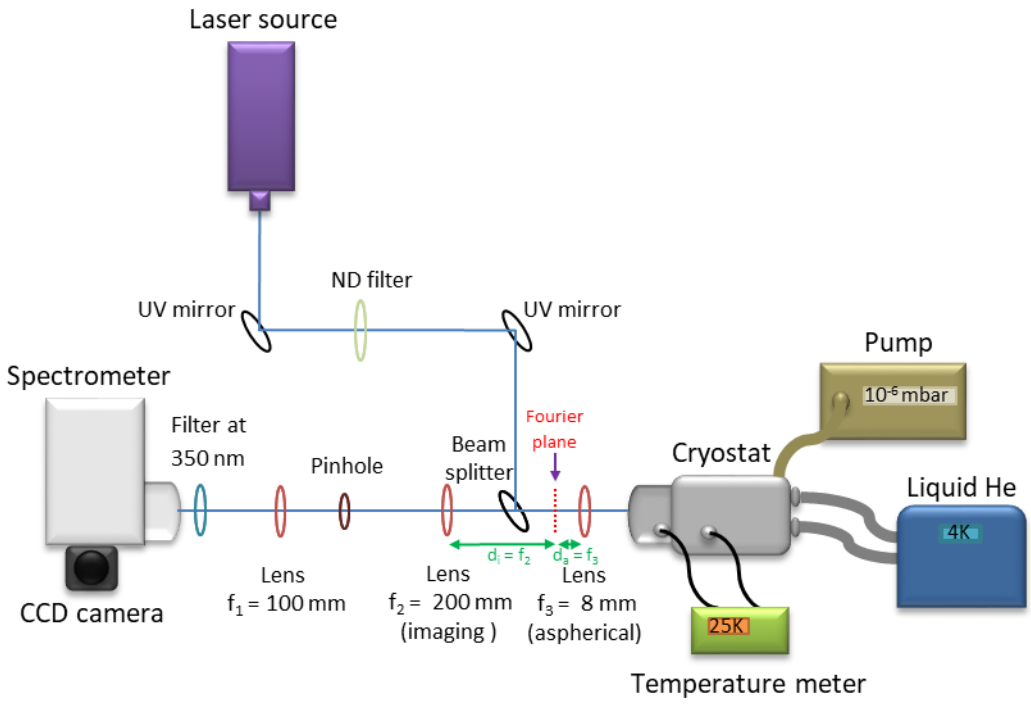

Figure E.1: Schematic of the k-space μ-PL imaging setup for data acquisition from low up to room temperature.

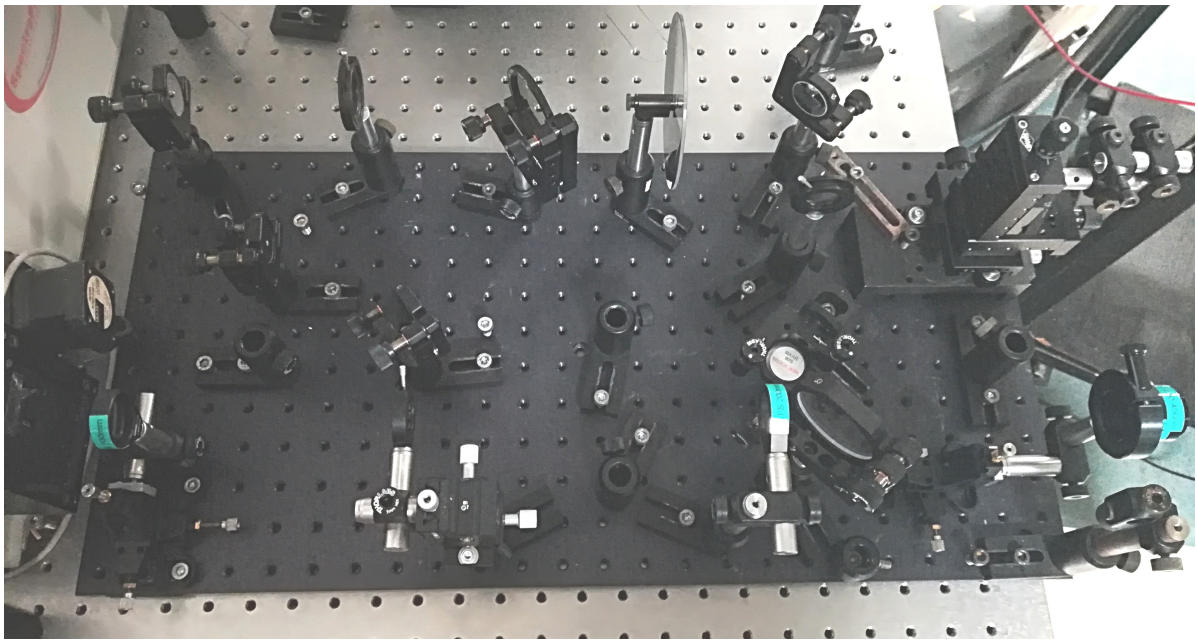

Figure E.2: The utilized k-space μ-PL imaging setup for data acquisition from low up to room temperature.

Appendix F

Experimental Equipment

A) Optical sources:

- A fibre coupled, collimated Mikropack light source, which is equipped with a deuterium (UV) and halogen lamp (visible and IR). This source was utilized in reflectivity experiments.
- A 150 W Xenon Hamamatsu lamp. The specific lamp was utilized in reflectivity and transmission experiments.
- A Kimmon IK series, continuous wave, He-Cd laser with emission at 325 nm. The measured maximum output power was at 32 mW with a beam divergence of 0.92 mrad. The particular laser was utilized as an excitation source in photoluminescence experiments.
- A Nanolase, frequency quadrupled, pulsed, Nd-YAG (neodymium-doped yttrium aluminium garnet; $Nd : Y_3Al_5O_{12}$) laser with emission wavelength at 266 nm. Its pulse-width is 0.51 ns and has a repetition rate of 7.58 kHz. The separation of the 266 nm beam from the other harmonics was possible with a quartz prism. The average power at 266 nm was about 0.4 mW. This laser was utilized in non-resonant optical excitation of GaN/AlGaN microcavities for the demonstration of polariton lasing.
- A diode laser with emission at 405 nm and a maximum output power of about 9.5 mW. This laser was utilized mainly as an optical source in photo-electrochemical etching experiments.

- A Mira-900 series, pulsed, tunable Ti : Sapphire laser, with a tuning range of 700 - 1000 nm and a pulse-width about 200 fs, where the repetition rate is 76 MHz. The Mira-900 laser is followed by a tripler stage, transforming the 800 nm pulses into the 266 nm 76 Mhz fs pulses used as source of excitation in the TRPL measurements.

B) Spectrometer:

- An Acton SpectraPro, 0.5 meter focal length, triple grating and imaging spectrograph, with a resolution of 0.02 nm at 435.8 nm and an accuracy of $\pm$ 0.02 nm. The three gratings are the following: (1) 150 grooves/mm, blazed at 300 nm (2) 600 grooves/mm, blazed at 300 nm and (3) 2400 grooves/mm, blazed at HUV (holographic UV). The spectrograph is equipped with a liquid nitrogen cooled charge-coupled device (CCD), having a width of 1024 pixels and a height of 256 pixels.

C) Streak camera:

- All the TRPL measurements are made on a Hamamatsu M5675 streak camera, equipped with four different time range options, based on the sweep voltage used to deflect the light. Time range "1" corresponds to the highest resolution whereas time range "4" to the lowest one. When all conditions are optimal, the temporal resolution of this particular streak camera can be as low as $\approx$ 2 ps. Under normal operating conditions, however, the temporal resolution is less than 10 ps.

D) Low temperature apparatus:

- For the temperature-dependent measurements, the samples were placed in an APD helium closed-circuit cryostat. The setup is equipped with a Scientific Instruments, series 5,500 temperature controller, which allowed the control of sample temperature from 15 K to 300 K.

E) Power source:

- For the PEC process, a Keithley 6517A was utilized to apply a bias in the setup while at the same time measure the response in current. The particular power supply has a built-in ± 1 kV voltage source and the capability to measure currents in the range 1 fA - 20 mA. An additional feature is the built-in IEEE 488 interface which allows programming it with a computer interface.

F) Atomic Force Microscopy:

- The surface imaging and topographical analysis, cross-sectional profiles and roughness measurements were performed with a Multimode AFM connected to a Nanoscope IIIa controller. The particular AFM is featured with Contact, Tapping and Non-contact modes with 2 piezoelectric scanners: a normal for 125 × 125 μm^2 max scan size and a high precision for 5 × 5 μm^2 max scan size. The resolution is 1 $\mathring{A}$ in z-axis while 10 nm in x- and y-axis.

G) X-Ray Diffraction:

- For the investigation of the structure of crystalline solids the x-ray diffraction (XRD) measurements were performed with a BEDE D1 Triple Axis High Resolution XRD (HR-XRD) equipped with a Siemens - Sealed X-ray tube [CuKa radiation (2 kW)] source and a scintillation detector for single crystal analysis.

H) Scanning Electron Microscope:

- The presented scanning electron images (SEM) images were acquired with a FE-SEM, JEOL JSM-7000F equipped with INCA microanalysis system with featured capabilities High Resolution Scanning Electron Microscopy (HR-SEM) and Energy Dispersive X-ray Spectroscopy (EDS). Its source is a Schottky type field-emission (T-FE) gun with Zr/O tungsten emitter providing a beam voltage range of 0.5 - 30 kV with a resolution of 1.2 nm at 15 kV and 3.0 nm at 1 kV.